

Université du Québec  
Institut National de la Recherche Scientifique  
Centre Énergie, Matériaux et Télécommunications

**TIME- AND SPECTRAL-DOMAIN HOLOGRAPHY FOR HIGH-SPEED  
PROCESSING OF OPTICAL SIGNALS**

Par

María del Rosario Fernández Ruiz

Thèse présentée pour l'obtention du grade de  
*Doctorat en Télécommunication, Ph.D.*

**Jury d'évaluation**

Examineur externe	Christophe Caloz École Polytechnique de Montréal
Examineur externe	Jérôme Genest Université Laval
Examineur interne	Luca Razzari INRS-EMT
Directeur de recherche	José Azaña INRS-EMT
Co-Directeur de recherche	Alejandro Carballar University of Seville



*A mis padres y a Juanma*



# Acknowledgements

The successful realization of a work like the one presented in this Thesis is the result of multiple factors. Of course determination, perseverance and hard work are fundamental. But it couldn't be possible without the support, guidance and encouragement of significant people around us. In my case, I have been tremendously lucky to have the right people close to me offering their support, guidance and encouragement. This dissertation wouldn't be complete without their names in it.

First of all, I want to express my gratitude to my supervisors, Prof. José Azaña and Prof. Alejandro Carballar. I truly appreciate their guidance, counsel and willingness to take time to discuss my research. They have taught me valuable lessons to become better researcher and scientific professional. It has been an honor to work with both of them and learn so much from them.

I would like to deeply thank my dear husband Juanma for his support, help, care, motivation and his mere company. He is my my best friend and my companion in life. No amount of words is enough to express my gratitude for his patience and for always being there.

I also thank my parents, Juan and Josefina, for their love and support throughout my life. They have walked with me along good and difficult times, and during this path, they have taught me to always think big and work hard to achieve my goals. Their precious advice for life will always accompany me.

I shall not forget my dear group members. I specially thank Prof. Ming Li for introducing me the wonder of the experimental work in the laboratory. I thank Mauri, Hamed, Luis, Lei, Jeonhyun, Reza Maram, Bo, and Reza Ashrafi for their help, stimulating discussions and collaborations, but most importantly, for their friendship. To all of them, thank you for your generosity sharing with me not only your scientific knowledge but also your culture and your experiences. Thank you for making me feel I was part of a new, big family.

I thank Prof. Sophie LaRochelle and her group members, specially Dr. Mansour Dastmalchi and Dr. Lixian Wang, at Université Laval for their assistance on the fabrication of our fiber Bragg grating devices and for their ideas and priceless suggestions on the projects in which we have collaborated. I would like to express my gratefulness to Prof. Martin Rochette for being an excellent teacher and for our discussion on the nonlinear-optics-based project in this dissertation. It is always a pleasure to share time and ideas with such excellent and reputable professionals.

Finally, I thank the Natural Sciences and Engineering Research Council of Canada (NSERC), le Fonds Québécois de la Recherche sur la Nature et les Technologies (FQRNT), and Institut National de la Recherche Scientifique – Énergie, Matériaux et Télécommunications (INRS-EMT), for providing the funding which allowed me to undertake this PhD research.



# Abstract

The ever-increasing traffic data requirements in telecommunication services lead to a continuous need for higher transmission capabilities. In this scenario, fiber-optic communications have proven to be a very promising way of achieving such high bitrates. Nowadays, wavelength division multiplexing (WDM) systems support transmission capabilities of about 10 Tbps, through multiplexing of several hundred wavelengths with a single channel bit rate of  $\sim 40$  Gbps. For pre- and post- processing of information, WDM requires opto-electronic signal conversion circuits individually set and operated for each different wavelength channel; therefore this evolution leads to an impractical increase of circuitry complexity and power consumption. Moreover, with the transmission-capacity increase in WDM systems, coherent technologies have attracted a large interest over the recent years. The motivation lies in finding methods for achieving the growing bandwidth demand with multilevel complex modulation formats. To implement high-order complex (amplitude and phase) modulation formats, the optical in-phase and quadrature (IQ) components of the information signal need to be synthesized, processed and detected independently, additionally requiring proper synchronization of these two IQ optical paths.

Therefore, in spite of the fact that the combination of WDM and coherent technologies enables a more efficient use of the available spectrum, it also hinders the required circuitry in the transmitter, receiver and intermediate network nodes. In this Thesis, we present and experimentally demonstrate new concepts and signal processing techniques that remarkably simplify the required electro-optical circuitry (and consequently the power consumption) in coherent optical systems. Furthermore, we also develop new ultrafast all-optical signal processors, able to process the information directly in the optical domain at ultrafast speeds (ideally, with speeds into the THz regime). These optical processing systems are becoming increasingly important for a myriad of scientific and engineering applications, including not only high-speed optical telecommunications but also optical computing systems, ultrafast biomedical imaging, or ultrafast measurement and characterization systems. Their fundamental goal is to avoid current electronic-based processing, which severely limits the operation speeds below a few tens of GHz and entails a bottleneck for the effective use of the high bandwidth intrinsic to optics.

The problem of simultaneously controlling the amplitude and phase of a complex electromagnetic signal has long been solved in the spatial domain. Holography was developed as a lensless interferometric imaging system that was able to record and subsequently reconstruct the original complex-valued information signal, in spite of the recording medium being sensitive to intensity-only variations. Holographic systems have been widely applied in a vast number of fields, such as 3D imaging, spatial-domain signal processing, microscopy or security. The basics of classical (spatial domain holography) are reviewed in Chapter 3, paying special attention to those concepts that will serve as foundations for the original ideas presented through this work.

In this Thesis, we propose and formulate for the first time, to the best of our knowledge, the exact time-domain counterpart of spatial domain holography, by means of the space-time duality. This method, which is described in Chapter 4, enables simultaneous control of the amplitude and phase of a temporal optical waveform with complex envelope using a simple setup composed of devices sensitive to intensity-only or phase-only variations. To prove its effectiveness, several applications of time-domain holography are experimentally demonstrated and the results are presented in this dissertation. First, as a proof of concept, we demonstrate generation of complex-modulated optical waveforms using a simple setup mainly composed of an electro-optical intensity modulator and a band-pass filter. Then, these complex-envelope waveforms are detected (in amplitude and phase) using a heterodyne scheme based on an intensity-only photodetector. Additionally, we propose and implement a simplified scheme to perform electro-optical temporal phase conjugation. This holographic method greatly simplifies previous electro-optical approaches, avoiding the need for detection and subsequent processing of the phase of the optical signal prior to the electronic-based conjugation process. Instead, the proposed approach uses intensity-only photodetection and modulation components, combined with a band-pass filter, thus reducing the complexity and potential cost of the setup, minimizing errors and simplifying the procedure. Finally, we demonstrate wavelength conversion of complex-envelope optical signals based on time-domain holography. In this case, an all-optical approach based on nonlinear cross-phase modulation is used. This technique exhibits important advantages with respect to all previous approaches that typically use four-wave mixing, as it avoids the stringent phase-matching condition and requires at least one order of magnitude less power in the employed pump signals.

Using the Fourier-transform property of duality between the time domain and the frequency domain, we also propose and formulate, for the first time, the concept of spectral-domain holography, which is described in Chapter 5. This novel concept enables the simultaneous control of the amplitude and phase of an optical spectral response by just manipulating the amplitude spectrum. Spectral-domain holography is applied to the design of two kinds of signal processors. First, we implement complex-valued and non-symmetrical optical pulse shaping using a scheme based on time-domain spectral shaping, which achieves temporal resolutions in the sub-picosecond regime but has been typically restricted to symmetric and intensity-only pulse shaping operations. In this scheme, the modulating signal that performs the spectral shaping is a spectral hologram, enabling the synthesis of complex-envelope output waveforms using a setup identical to that of previous spectral shaping methods. The proposed methodology can be considered as the time-domain counterpart of (spatial domain) Vander-Lugt filters. Then, we apply spectral-domain holography to the implementation of non-minimum-phase optical pulse processors using fiber Bragg gratings (FBGs) operating in transmission, which can be considered as optical linear filters with a minimum-phase spectral response. In this case, the complex-valued spectral response of the target filter is encoded in an amplitude-only spectral response (the spectral hologram). The use of FBGs operating in transmission has well-known advantages with respect to the reflective configuration. In this Thesis, we present and experimentally demonstrate an additional extraordinary advantage: an FBG operating in transmission is able to implement signal processing functionalities with bandwidths well in the THz regime (one order of magnitude higher than conventionally achieved bandwidths) thanks to the degree of freedom available in choosing the spectral phase in reflection. In particular, we propose the use of a quadratic spectral phase in reflection, which translates into a linear chirp, allowing the increase of the grating's operation bandwidth without increasing the grating spatial resolution.

The novel concepts of time- and spectral-domain holography can be foreseen as powerful tools for the development of new techniques for the generation, measurement and processing of ultrafast

complex-envelope optical temporal waveforms. In this Thesis, we have demonstrated interesting methods aimed at (i) simplifying the current required setup in coherent systems, and (ii) allowing the implementation of simpler, arbitrary ultrafast optical signal processing devices, which are key components for future, low power-consumption high-capacity telecommunication networks. Moreover, the vast number of applications of spatial-domain holography allows us to predict a similar broad range of applications for the time/spectral-domain holography.



# Résumé

## A. Introduction

La demande toujours croissante de la quantité de débit pour les services de télécommunications entraîne un besoin de capacités supérieures de transmission de données. Dans ce contexte, les fibres optiques ont démontré la possibilité d'obtenir de telles performances. De nos jours, le multiplexage de longueurs d'ondes (WDM pour *wavelength division multiplexing*) permet d'obtenir des débits d'environ 10 Tbps, via le multiplexage de centaines de longueurs d'onde, avec un débit par canal de 40 Gbps [1]. Pour de tels systèmes, des circuits opto-électroniques adaptés à chaque longueur d'onde sont nécessaires pour le traitement de l'information en entrée et en sortie de fibre optique. Ceci induit une complexification intense des circuits et une augmentation de l'énergie consommée. De plus, avec l'augmentation des débits de données grâce aux systèmes WDM, les technologies cohérentes ont attiré un intérêt certain ces dernières années [2]. Cette thèse est motivée par le besoin de méthodes pour simplifier et/ou améliorer les systèmes qui combinent les techniques WDM et les formats de modulations à plusieurs niveaux complexes. Afin d'implémenter des formats de modulation complexes (amplitude et phase) d'ordres supérieurs, les composantes optiques en phase et en quadrature (IQ) de l'information doivent être synthétisées, traitées et détectées de façon indépendante, ce qui demande une synchronisation entre chemins optiques de ces deux IQ composantes.

Ainsi, malgré le fait que la combinaison des technologies WDM et cohérentes permet une utilisation plus efficace du spectre disponible, cela complique des circuits indispensables aux différents nœuds de transmission, réception et intermédiaires du réseau. Dans cette thèse, nous présentons et démontrons de nouveaux concepts et techniques pour le traitement du signal qui simplifient considérablement les circuits électro-optiques (et par conséquent, diminuent la consommation d'énergie) dans les systèmes optiques cohérents. De plus, nous avons aussi développé un nouveau procédé tout optique ultra-rapide pour le traitement de l'information directement dans le domaine optique à une vitesse extrêmement élevée (idéalement, de l'ordre du THz) par l'utilisation de Réseaux de Bragg sur Fibre Optique (RDBF, ou FBG par ses sigles en anglais, *fiber Bragg gratings*). Ces processeurs optiques deviennent de plus en plus importants pour une myriade d'applications scientifiques, non seulement pour la télécommunication optique ultrarapide mais également pour les systèmes de calcul optiques, l'imagerie biomédicale ultra rapide ou encore les systèmes de caractérisation ou de mesure à grande vitesse. Le but fondamental de ces processeurs optiques est d'éviter tout circuit électronique qui limite drastiquement les vitesses d'opérations à une dizaine de GHz et représente un goulot d'étranglement pour l'utilisation pratique des larges bandes passantes intrinsèques à l'optique.

Le contrôle simultané de l'amplitude et de la phase de l'enveloppe complexe d'un signal optique est maîtrisé depuis longtemps dans le domaine spatial. L'holographie fût développée comme un sys-

tème interférométrique d'imagerie sans lentille pouvant enregistrer, et par conséquent reconstruire, le signal complexe original malgré un support d'enregistrement sensible uniquement aux variations d'intensité lumineuse [3-5]. Les systèmes holographiques sont appliqués dans des systèmes variés, de l'imagerie 3D au traitement des signaux en domaine spatial en passant par la microscopie ou la sécurité [6].

Dans cette thèse, l'équivalent temporelle de l'holographie spatiale traditionnelle est formalisé et démontré expérimentalement. Ce concept implique l'enregistrement, la génération et/ou le traitement d'un signal optique temporel complexe (amplitude et phase) via des systèmes optiques de modulation et/ou détection de variations d'intensité uniquement. Les procédures résultantes basées sur l'holographie simplifient considérablement les approches actuelles pour traiter des tâches similaires de génération et de traitement. En utilisant des relations de dualité des transformées de Fourier entre le domaine temporel et fréquentiel, le concept d'holographie en domaine spectral est présenté, formalisé et démontré. Ce concept novateur permet le contrôle simultané de l'amplitude et de la phase de la réponse spectrale par l'unique manipulation de l'amplitude du spectre. L'holographie en domaine spectral est appliquée à la conception de deux types de traitement du signal, génération programmable et reconfigurable de la forme d'une impulsion optique arbitraire (complexe) basée sur un filtre électro-optique (EO) et un traitement ultra-rapide de signaux arbitraires basé sur des filtres tout optiques à phase minimale (MP).

## B. Contributions originales

- Proposition et démonstration expérimentale du concept d'holographie temporelle comme contrepartie exacte en temps de l'holographie classique (spatiale). Deux démonstrations expérimentales sont présentées pour valider ce concept : (i) génération et détection de signaux optiques complexes modulés, et (ii) la conjugaison de la phase temporelle des signaux. Ces deux exemples sont basés sur un montage EO inspiré par l'architecture de l'holographie spatiale. Les composants EO nécessaires pour le montage utilisé (modulateur et photo détecteur) sont sensibles uniquement aux variations d'intensité [7,8], simplifiant de façon significative les approches antérieures pour les applications impliquant la modulation, détection et conjugaison de signaux optiques à enveloppe complexe.
- Proposition et démonstration expérimentale d'une méthode tout optique pour l'application de l'holographie temporelle. Le processus de modulation est effectué par l'utilisation de la modulation de phase croisée (XPM pour *cross phase modulation*). La méthode proposée est validée via l'implémentation d'un système de conversion de longueur d'onde complexe, évitant ainsi la nécessité de satisfaire la condition d'accord de phases et réduisant la puissance du signal pompe nécessaire d'au moins un ordre de grandeur par rapport aux précédents convertisseurs de longueur d'onde basés sur l'effet du mélange à quatre ondes (MQO, ou FWM pour *four wave mixing*) [9].
- Proposition et démonstration expérimentale de la contrepartie temporelle des filtres de Vander-Lugt. Ces filtres reposent sur l'équivalent temporel des filtres optiques spatiaux de Fourier et font usage d'un « hologramme spectral » pour implémenter une fonction de transfert complexe. Ceci diffère des méthodes antérieures limitées aux fonctions de transfert réelles. Cette proposition est validée par la génération des formes d'impulsion à enveloppe complexe avec une résolution dans la gamme de la picoseconde [10].

- Proposition et démonstration expérimentale d'un modèle de RDBF pour le traitement de signaux optiques à phase minimale avec une bande passante dans le régime des THz, surpassant largement les limites des bandes passantes typiques des RDBF ( $\sim 200$  GHz). Cette méthode est démontrée via une modélisation numérique de différentiateurs optiques d'ordres arbitraires [11,12] et la démonstration expérimentale d'un générateur d'impulsions carrées avec une résolution de l'ordre de la picoseconde [11,13].
- Proposition et démonstration expérimentale d'une méthode de conception de RDBF qui permet l'implémentation des systèmes de traitement de signaux optiques à phase non minimale en utilisant des RDBF en transmission. Cette méthode permet de surmonter la restriction sur la phase minimale pour les RDBF en transmission par l'holographie spectrale. Cette proposition est validée par la démonstration expérimentale d'un transformateur de Hilbert photonique avec une bande passante de 5 THz implémenté dans un RDBF en transmission [14,15].

Les articles publiés dans des journaux évalués par des paires [7-15] avec un haut facteur d'impact (comme « Optics Letters », « Optics Express » ou « IEEE Photonics Technology Letter ») combinés avec les 20 présentations lors de conférences renommées (comme « CLEO » , « ECOC » ou « OFC » en incluant deux présentations invitées) portant sur les résultats de cette thèse démontrent l'originalité et l'importance de ces contributions.

## C. Revue de l'holographie (spatiale) classique

Avant de présenter les concepts novateurs présentés dans cette Thèse, une brève revue de la littérature sur l'holographie spatiale est menée en portant une attention particulière sur les concepts fondamentaux nécessaires pour les travaux présentés.

L'holographie spatiale est un procédé à deux étapes pour produire une image introduite par D. Gabor en 1949 [3]. Cette technique utilise l'interférence produite entre une onde de référence et la lumière diffractée ou diffusée par un objet. De cette façon, toute l'information (i.e. l'amplitude et la phase) de l'onde diffractée ou diffusée peut être enregistrée et par conséquent reconstruite, malgré le fait que le support d'enregistrement (e.g. un film photosensible) ne réponde qu'à l'intensité lumineuse [3-5]. Plusieurs années après, les hologrammes générés par ordinateur (CGH) ont été introduits [16], ouvrant la possibilité de générer et de traiter des images sans objets réels. Dans ce cas, le patron d'interférence désiré, i.e. l'hologramme, est calculé par ordinateur et transféré à la couche photosensible via un système d'impression ou de lithographie.

Dans un système d'holographie spatiale (voir Fig. 1), l'information complexe d'une onde monochromatique inconnue  $e_S(x, y)$  (avec  $x$  et  $y$  représentant les variables spatiales transverses à la propagation de la lumière,  $z$ ) peut être enregistrée par son interférence avec une onde de référence,  $e_{LO,1}(x, y)$ . Le front d'onde contenant l'information se propage avec un angle ( $\theta_y$ ) par rapport au front d'onde de référence. Les variations d'intensité du patron d'interférence  $i_H(x, y)$  sont enregistrées sur une couche photosensible. Le patron d'interférence peut également être généré par ordinateur, e.g. en simulant le processus d'interférence, et est référé comme CGH [16]. L'information complexe (i.e. l'amplitude et la phase) de l'onde originale peut alors être retrouvée par illumination de la couche d'enregistrement avec la même onde de référence  $e_{LO,2}(x, y) = e_{LO,1}(x, y)$  (dans le plan holographique,  $z = z_0$ ). Comme présenté sur la Fig. 1, le champ transmit à travers de la couche est diffracté en plusieurs ordres à différents angles. L'angle de propagation  $\theta_y$  est relié à la fréquence

de l'onde  $\nu_y = \sin(\theta_y)/\lambda_0$ , où  $\lambda_0$  est la longueur d'onde du signal de référence et de celui contenant l'information. Ainsi, pour des valeurs de  $\theta_y$  suffisamment élevées (i.e. une fréquence spatiale suffisamment grande), le front d'onde original peut être effectivement récupéré sans recouvrement avec les autres ordres [5].

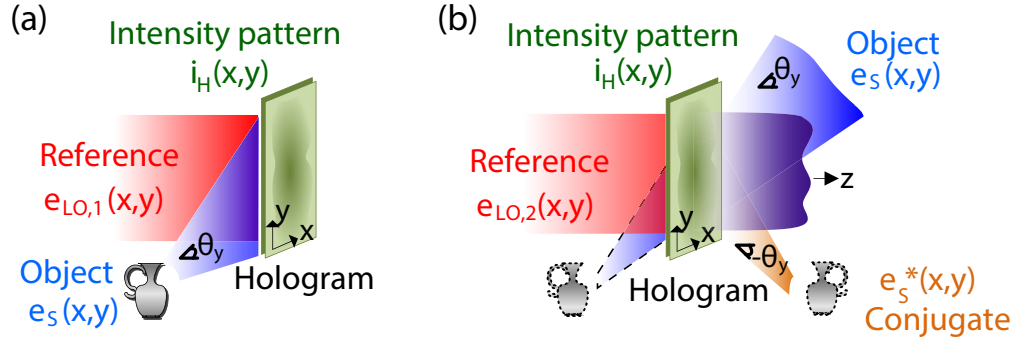


Figure 1 – (a) Étape d'inscription du signal et (b) étape de récupération de l'information en holographie classique.

Comme mentionné précédemment, l'holographie a des applications dans de nombreux domaines [6]. Une application particulièrement intéressante de l'holographie implique l'utilisation d'un filtre optique complexe spatiale utilisant des masques spatiaux sensibles uniquement à l'intensité, i.e. les filtres Vander-Lugt [17]. Ces filtres ont été développés dans les années 1960 pour généraliser les filtres optiques de Fourier traditionnels, à savoir les systèmes  $4f_l$  (où  $f_l$  est la longueur focale des lentilles utilisées) [18]. Les masques spatiaux typiques utilisés en optique de Fourier peuvent appliquer une modulation de l'intensité ou de la phase dans le plan de Fourier du système  $4f_l$  ce qui implique que seule une réponse impulsionnelle du filtre réelle et symétrique peut être introduite. Vander Lugt a alors proposé d'implémenter une fonction de filtrage complexe en utilisant un dispositif holographique. Il s'agit d'inscrire sur une couche photosensible le patron d'interférence entre la fonction de transfert complexe désirée et un signal de référence (voir Fig. 2(a)). Ainsi la couche photosensible contient l'information complexe de la fonction filtrante désirée. Afin de traiter n'importe quel signal, un système à deux lentilles équivalent au système  $4f_l$  doit être mis en place, en positionnant le masque holographique au plan de Fourier, comme présenté sur la Fig. 2(b).

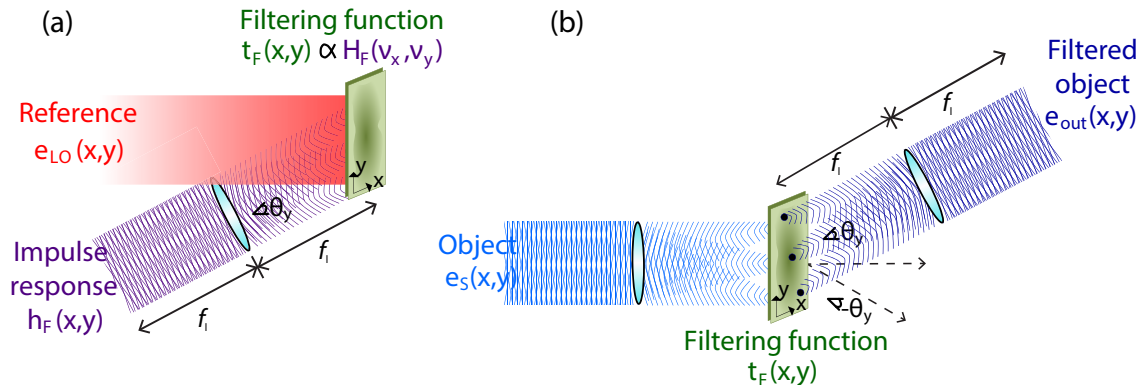


Figure 2 – Filtre de Vander-Lugt : (a) Enregistrement de l'hologramme, qui contient l'information de la fonction de transfert complexe du filtre et (b) procédé de filtrage de signaux basé sur la concaténation de deux systèmes de transformés de Fourier.

Dans la suite, on établit une analogie entre les traitements d'informations complexes encodées dans des formes d'ondes spatiales et des procédés équivalents pour des ondes temporelles, i.e., des ondes dans lesquelles l'information est contenue dans les variations temporelles.

## D. Holographie Temporelle

### D.1. Formalisme Mathématique

Inspiré par la dualité espace-temps [19], nous définissons la contrepartie temporelle de l'holographie spatiale ci-après. Lors de l'étape d'enregistrement, l'interférence entre le signal optique contenant l'information  $e_S(t)$  et une onde continue (OC, ou CW pour *continuous wave*) servant de signal de référence  $e_{LO,1}(t)$  est obtenue par un couplage optique (CO) et l'intensité du patron d'interférence  $i_H(t)$  est la suivante :

$$\begin{aligned} i_H(t) &= |e_S(t) + j e_{LO,1}(t)|^2 \\ &= |e_S(t)|^2 - |e_{LO,1}(t)|^2 + 2|\hat{e}_S(t)| |e_{LO,1}(t)| \sin(\omega_i t + \phi_S(t) - \phi_{LO,1}), \end{aligned} \quad (1)$$

où  $j = \sqrt{-1}$ ,  $e_S(t) = \hat{e}_S(t) \exp\{j\omega_S t\}$  est la représentation analytique du signal optique contenant l'information, avec  $\hat{e}_S(t) = |\hat{e}_S(t)| \exp\{j\phi_S(t)\}$  l'amplitude complexe de l'enveloppe,  $\omega_S$  représente la fréquence optique, et  $e_{LO,1}(t) = i_{LO,1}^{1/2} \exp\{j\omega_{LO,1} t + \phi_{LO,1}\}$  est le signal de référence OC, où  $i_{LO}$  est l'intensité optique constante,  $\omega_{LO,1}$  est la fréquence optique du signal de référence,  $\omega_i = \omega_S - \omega_{LO,1}$  est une fréquence intermédiaire et  $\phi_{LO,1}$  est une phase constante arbitraire. L'interferogramme temporel  $i_H(t)$  peut être interprété comme l'équivalent temporel de l'hologramme spatial et par conséquent peut être considéré comme un « hologramme temporel ». Pour la récupération de l'information, le même signal de référence  $e_{LO,2}(t) = e_{LO,1}(t)$  est utilisé comme porteuse dans le procédé de modulation temporel, typiquement la modulation de l'amplitude, qui est proportionnel à l'hologramme  $i_H(t)$  [7].

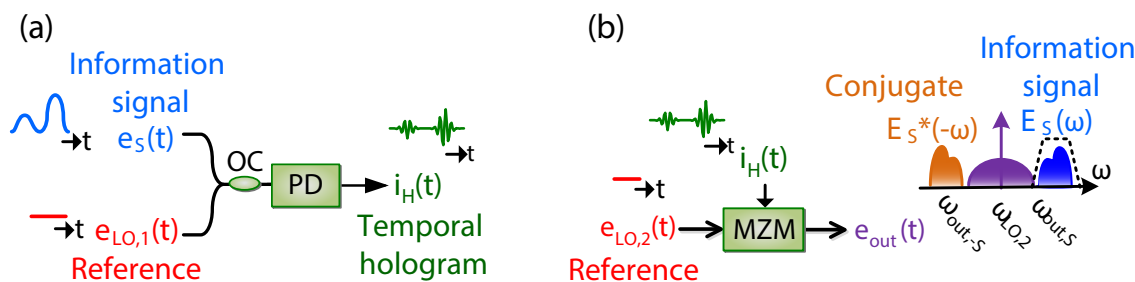


Figure 3 – (a) Génération d'hologramme temporel; (b) Récupération de l'information complexe. OC, couplage optique; PD, photo détecteur; MZM, Modulateur Mach-Zehnder. Seule l'enveloppe complexe du signal temporel est représentée.

Un exemple graphique du procédé est présenté sur la Fig. 3, dans lequel une approche EO est utilisée. Dans ce cas, l'hologramme temporel est généré via une photodiode conventionnelle (PD). L'hologramme temporel  $i_H(t)$  peut également être conçu par ordinateur puis généré par un Générateur d'Onde Programmable (GOP, ou AWG pour *arbitrary waveform generator*), lors d'un procédé que nous pouvons appeler Génération par Ordinateur d'Hologramme Temporel (CGTH). La récupération de l'information complexe s'effectue par l'utilisation d'un modulateur Mach-Zehnder

(MZM). Le spectre du signal en sortie du MZM est représenté sur la Fig. 3(b). Comme dans le cas de l'holographie spatiale (Fig. 1), le signal optique généré est composé de (i) une composante DC consistante en un signal de référence et d'un terme résultant de la convolution du signal original avec son conjugué, (ii) d'une version atténuée du signal original complexe  $e_S(t)$  centrée en  $\omega_S$  et (iii) d'une version atténuée du signal original conjugué centrée à  $2\omega_{LO,1} - \omega_S$  (en fixant  $\omega_{LO,1} = \omega_{LO,2}$ ). Ainsi, l'information complexe d'intérêt peut être facilement extraite de l'onde modulée en filtrant simplement le signal spectral correspondant, i.e. via un Filtre Optique Passe-Bande (FOPB, ou BPF pour *band-pass filter*). Si le signal conjugué est à la place filtré (sélectionné), la Conjugaison Temporelle de la Phase (CTP) est alors obtenue. Cette dernière opération est utile pour l'inversion spectrale à mi-longueur (ISML), permettant la compensation de la dispersion chromatique d'ordre pair et de diverses détériorations non-linéaires induites par la propagation de la lumière sur de longues distances dans les fibres optiques pour la télécommunication [20]. Il est possible d'aligner le terme conjugué à la longueur d'onde du signal original, obtenant ainsi un système CTP conservant la longueur d'onde. Dans ce but, le signal de référence utilisé lors du procédé de récupération  $e_{LO,2}(t)$  doit être différent de celui utilisé pour enregistrer le signal, en particulier,  $\omega_{LO,2} = 2\omega_S - \omega_{LO,1}$ . En général, le signal résultant peut être centré à une fréquence quelconque (procédé de conversion de longueur d'onde), en choisissant pertinemment la fréquence centrale de  $e_{LO,2}(t)$ , e.g. le signal de sortie non-conjugué sera centré à  $\omega_{out,S} = \omega_{LO,2} + \omega_S - \omega_{LO,1}$ , et le signal de sortie conjugué à  $\omega_{out,-S} = \omega_{LO,2} - \omega_S + \omega_{LO,1}$  [8].

Il faut noter que lorsque les deux premiers termes à droite de l'équation 1 (composante DC) ne présentent aucun intérêt, le terme de convolution impose une bande passante de détection/modulation au moins quatre fois plus élevée que celle du signal contenant l'information. Ce terme peut être négligé dans le cas d'une intensité de référence suffisamment élevée, i.e. lorsque  $i_{LO,1} \gg |\hat{e}_S(t)|^2$ , menant alors à une diminution significative (divisé par deux) des besoins en bande passante [7]. Cette observation peut rapidement être exploitée pour réduire la demande en bande passante dans le cas typique de la détection optique hétérodyne de phase par une PD unique.

L'approche EO représente une méthode directe pour l'implémentation de l'holographie temporelle puisque utilisant des systèmes sensibles aux variations d'intensité dans le temps. Bien que cette approche permette de réduire la complexité des circuits et d'éviter le besoin d'une synchronisation précise entre les composants en phase et ceux en quadrature de phase d'un signal complexe pour n'importe quel schéma de génération ou de détection, l'électronique impose une limitation intrinsèque dans la bande passante du système.

Pour dépasser cette limitation, un nouveau schéma a été développé pour l'utilisation de l'holographie temporelle dans le domaine tout optique [9]. Ceci repose sur une modulation de la phase uniquement, au lieu de l'amplitude, pour graver l'information du signal complexe dans une OC  $e_{LO,2}(t)$  qui va servir de sonde. La modulation en phase tout-optique est effectuée par procédé XPM dans une Fibre Optique Hautement Non-Linéaire (FOHNL, ou HNLF pour *highly nonlinear fiber*). Comme dans le cas EO, l'hologramme temporel,  $i_H(t)$ , est généré via l'interférence entre  $e_S(t)$  et  $e_{LO,1}(t)$ . Cependant, dans ce cas, aucune PD n'est utilisée lors de la génération du signal d'intensité, comme présenté sur la Fig. 4(a). À la place, le signal d'interférence agit comme signal de pompe à l'étape XPM et sa puissance est définie comme suit :

$$P_{pump}(t) = i_H(t) \cdot A_{eff}, \quad (2)$$

où  $A_{eff}$  est la surface effective du guide d'onde dans lequel le mode de propagation est transmis (une FOHNL dans cette configuration).

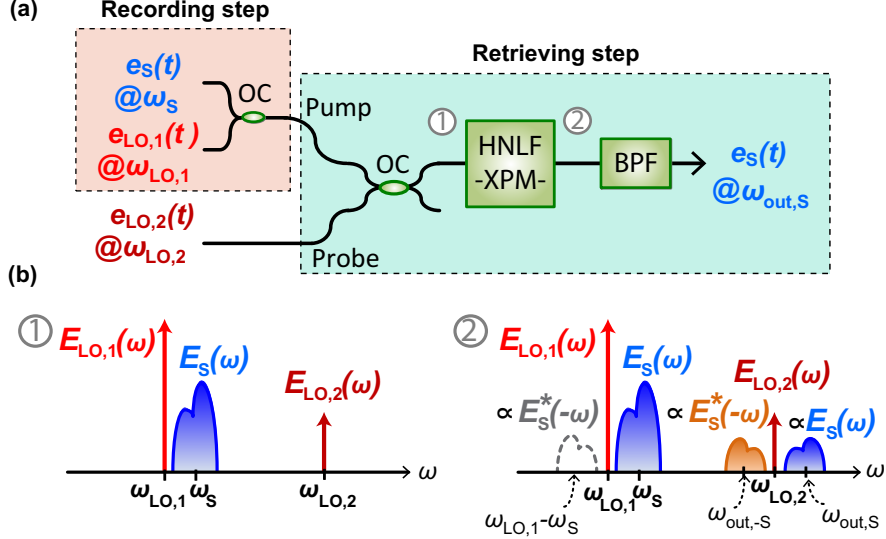


Figure 4 – (a) Schéma de production d’holographie temporelle basé sur XPM. Dans ce cas ,les procédés d’enregistrement et d’extraction sont concaténés; (b) Spectre avant et après propagation dans la FOHNL (HNLN).

Les signaux de pompage et de sonde se propagent tous deux dans la FOHNL, et l’expression du signal de référence après l’étape de XPM est :

$$e_{out}(t) = e_{LO,2}(t) \cdot \exp \left\{ j 2\gamma i_H(t) A_{eff} L \right\}, \quad (3)$$

où  $\gamma$  est le coefficient non linéaire et  $L$  représente la longueur de la fibre. Comme observé dans l’équation 3, le signal de modulation est intrinsèquement proportionnel à l’intensité du signal de pompage sans aucune étape de photo détection. Si  $2\gamma L A_{eff} i_{LO,1}^{1/2} |\hat{e}_S(t)| \ll \pi$ , le procédé est dans les limites de la *modulation de phase à bande étroite* et la modulation de la phase se comporte de manière identique à la modulation de l’intensité (à noter que l’approximation suivante peut être utilisée :  $e^{j\varepsilon} \sim (1 + j\varepsilon)$  si  $\varepsilon \ll \pi$ ). Ainsi, comme présenté sur la Fig. 4(b), la modulation de la phase élargie le spectre de la sonde de manière équivalente à un procédé de modulation de l’intensité. Deux composantes proportionnelles à  $e_S(t)$  et  $e_S^*(t)$  sont générées aux fréquences  $\omega_{out,S}$  et  $\omega_{out,-S}$  et peuvent être extraites via un FOPB.

## D.2. Application de l’holographie temporelle

L’holographie temporelle trouve des applications immédiates dans (i) la génération de profils temporels complexes (amplitude et phase); (ii) la conjugaison temporelle d’une forme d’onde temporelle existante et (iii) la conversion en longueur d’onde de signaux optiques à enveloppes complexes. Dans la suite, nous présentons la démonstration expérimentale de ces trois applications, utilisant soit l’approche EO (pour les applications (i) et (ii)) ou l’approche tout optique (pour l’application (iii)).

### D.2.1. Synthèse et détection de signaux optiques à enveloppe complexe

La première application présentée cible la synthèse de signaux temporels à enveloppe complexe par modulation d'intensité de lumière OC [7]. En particulier, deux signaux optiques à enveloppe complexe sont visés afin de démontrer la viabilité du concept : (i) une succession de 16 impulsions gaussiennes avec une phase quadratique arbitraire dans le but de démontrer que la technique proposée peut générer des ondes optiques avec des phases purement arbitraires évoluant dans le temps, et (ii) un signal optique pour une application plus concrète, un flux de 1024 symboles à 3 Gbps au format de modulation d'amplitude en quadrature à 16 états (16-QAM).

Le schéma présenté dans cette partie prend en compte l'étape d'enregistrement du procédé d'holographie temporel EO décrite précédemment dans laquelle le signal électrique variant en amplitude  $i_H(t)$  est conçu numériquement par CGTH. La figure 5 présente le montage expérimental ainsi que l'évolution du signal à travers des différentes étapes.

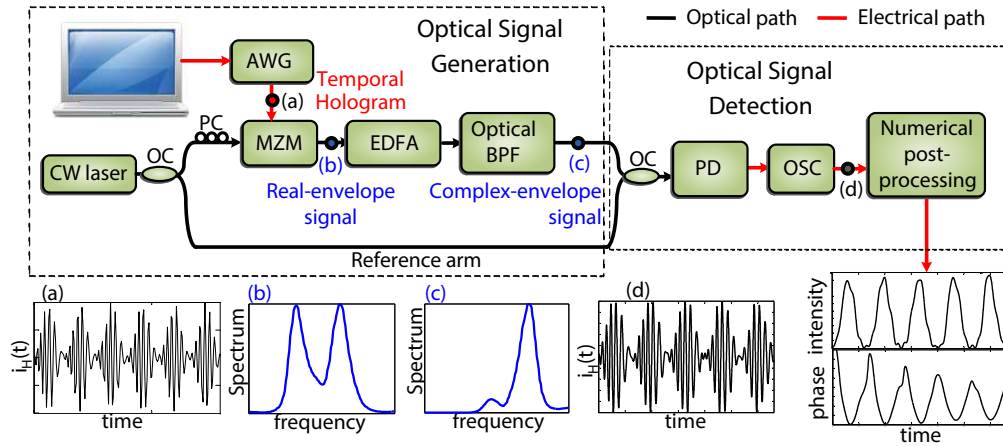


Figure 5 – Montage utilisé pour générer un signal optique à enveloppe complexe basé sur le concept de CGTH, i.e. utilisant un MZM unique et un FOPB. Cette figure montre également l'évolution des signaux en fonction du temps (en noir) et en fréquence (bleue) le long du montage. Le chemin optique est représenté par des lignes noires, alors que le signal électrique est représenté par des lignes rouges. AWG, générateur électrique d'onde aléatoire; CW, onde continue; MZM, modulateur Mach-Zenhdler; EDFA, amplificateur sur fibre dopée à l'Erbium; BPF, filtre optique passe-bande ; PD photo détecteur; OSC, oscilloscope en temps réel.

Le signal d'information  $e_S(t)$  est centré à  $f_S = \omega_S/2\pi = 193.385$  THz. Un laser OC génère un signal de référence centré à  $f_{LO,1} = \omega_{LO,1}/2\pi = 193.381$  THz, qui est alors divisé par un 10/90 CO pour une utilisation ultérieure lors de la synthèse et donc dans le procédé de détection. La lumière OC agit comme porteuse pour un MZM à 10 GHz (avec un biais de 5.1 V, coïncidant avec son point de transmission minimale) où le signal modulé,  $i_H(t)$ , a une bande passante de 9.6 GHz (à une intensité maximale de 1%).  $i_H(t)$  est généré par un GOP-7122C de Tektronix (taux de prélèvement de 24 GSps). Le signal de sortie du MZM (point  $b$  sur la Fig. 5) est proportionnel à  $i_H(t)$  et centré sur  $\omega_{LO,1}$ . Ainsi le signal correspondant au spectre de  $e_S(t)$ , qui est décalé de  $-\omega_i$  ( $f_i = (\omega_S - \omega_{LO})/2\pi = 4.5$  GHz) par rapport à  $\omega_{LO,1}$ , apparaît centré à  $\omega_S$ . Après l'étape d'amplification, le signal modulé résultant est filtré par un filtre adaptable (Santec OTF-350) centré à  $\omega_S$  et l'onde à enveloppe complexe est alors générée (point  $c$  sur la Fig. 5). Finalement, l'intensité et la phase du signal résultant sont mesurées par le système décrit ci-dessus d'enregistrement holographique via un PD unique à 10 GHz. Les pertes dans la partie supérieure de la Fig. 5 introduisent intrinsèquement

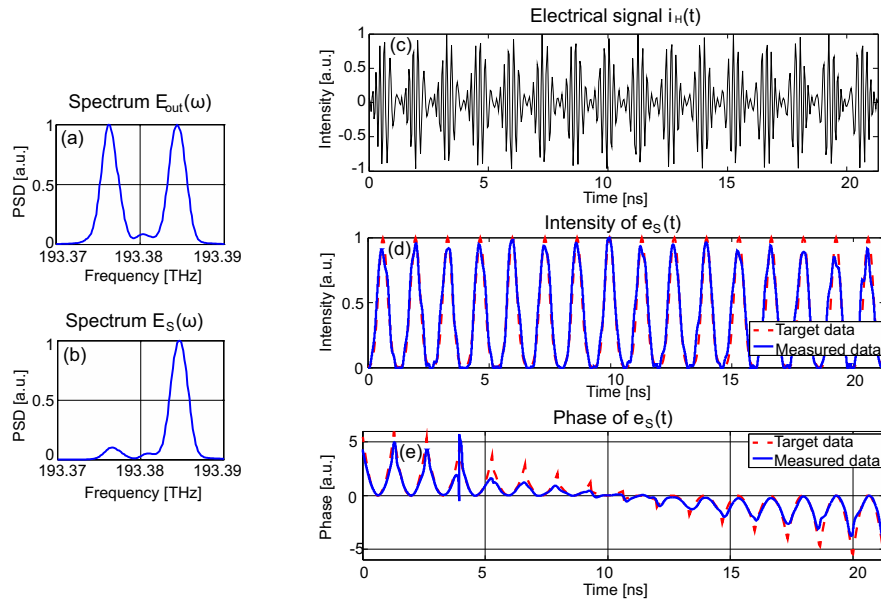


Figure 6 – Séquence de 16 impulsions gaussiennes avec une phase quadratique différentes entre elles. (a) Densité de puissance spectrale (PSD) du signal optique après la modulation d'intensité; (b) PSD du signal optique après le filtre; (c) Signal électrique généré par GOP; (d) Intensité de l'onde à enveloppe complexe générée (en bleu) et l'intensité ciblée (rouge); (e) Phase de l'onde générée (en bleu) et la phase ciblée (rouge).

une différence de puissance suffisante pour satisfaire la condition établie plus tôt ( $i_{LO,1} \gg |\hat{e}_S(t)|^2$ ), conduisant à l'augmentation de la bande passante mentionnée précédemment.

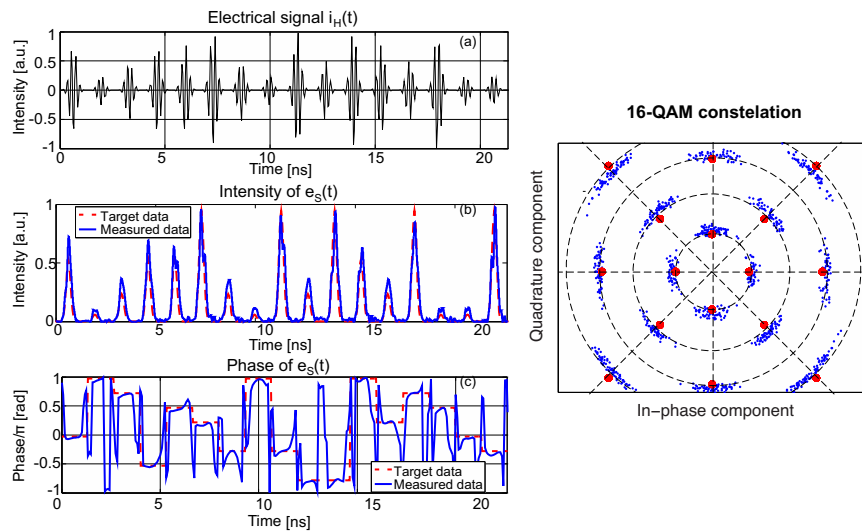


Figure 7 – Flux de données optiques, 1024 symboles au format 16-QAM. (a) Une partie de l'hogramme temporel conçu numériquement généré par GOP; Profils (b) d'intensité et (c) de phase du signal optique à enveloppe complexe généré (ligne bleue) et le flux de donnée visé (ligne rouge); (d) Constellation du flux de donnée généré (points bleu) et constellation idéale (points rouge) d'un signal 16-QAM.

La figure 6 présente les résultats de génération de données de 16 impulsions optiques gaussiennes avec une phase quadratique différente combinées avec le spectre mesuré avant et après le FOPB. La

figure 7 présente la génération d'un flux de données optiques de 1024 symboles à 3 Gbps modulé en 16-QAM (en intensité et en phase) et la constellation résultante, confirmant que l'onde à enveloppe complexe voulue est correctement générée.

### D.2.2. Conjugaison temporelle de la phase

La deuxième application démontrée est le CTP du signal optique à enveloppe complexe généré dans la section précédente. Le montage utilisé est présenté sur la Fig. 8 et comprend la concaténation des étapes de détection et de reconstruction de l'holographie. Dans ce cas, deux signaux de référence différents sont utilisés dans ces deux étapes pour conserver la longueur d'onde. Ainsi la fréquence centrale de  $e_{LO,2}(t)$  est modifiée de façon à obtenir  $\omega_{out,-S} = \omega_S$  [8], i.e.  $f_{LO,2} = \omega_{LO,2}/2\pi = 193.389$  THz.

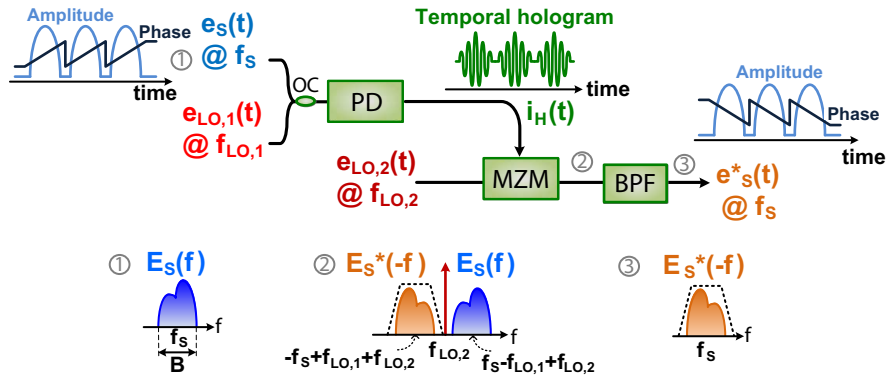


Figure 8 – Montage utilisé pour générer CTP basé sur le concept de l'holographie temporelle.

Une étape d'enregistrement identique à celle utilisée dans la section précédente est utilisée afin de mesurer l'amplitude et la phase du signal résultant à  $\omega_S$ . Les résultats obtenus sont présentés sur la Fig. 9 et 10 respectivement dans le cas d'une suite d'impulsions gaussiennes à phase quadratique différente entre elles et un flux de données modulé en 16-QAM. Les résultats ainsi obtenus présentent un excellent accord entre le signal conjugué et celui idéalement attendu, confirmant la génération d'une version conjuguée d'un signal prédéfini.

Le système EO fournit des opérations CTP de façon simple et directe, réduisant de façon significative la complexité des anciens montages EO pour CTP qui demandent typiquement (i) la détection des composantes en phase et en quadrature du signal, (ii) la conjugaison de ces derniers dans le domaine électrique et (iii) la modulation d'un signal optique OC utilisant les composantes en phase et en quadrature traités auparavant et synchronisés. Ainsi, le schéma proposé réduit effectivement la complexité, le coût potentiel du système global et minimise les erreurs.

### D.2.3. Conversion en longueur d'onde de signaux optiques à enveloppe complexe

La dernière application présentée de l'holographie temporelle est la conversion de longueur d'onde d'un signal à enveloppe complexe par l'utilisation de l'holographie temporelle tout optique [9]. Le montage utilisé est présenté sur la Fig. 11. Dans ce cas, le signal d'entrée  $e_S(t)$  est une série d'impulsions gaussiennes avec un taux de répétition de 10 GHz avec une largeur à mi-hauteur (FWHM) de 2.2 ps, générée par un Laser en Mode Actif Bloqué (LMAB, ou AMLL pour *active mode locked laser*) et dispersée par une fibre optique monomode (FOM, ou SMF pour *single mode*

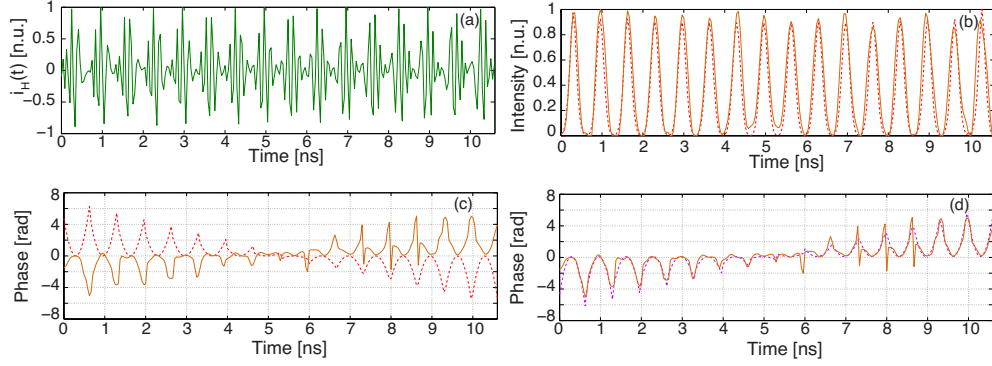


Figure 9 – (a) Hologramme temporel du signal d’entrée après détection; (b) Intensité détectée du signal conjugué (ligne pleine orange), comparée avec le profil d’intensité du signal d’entrée (ligne en pointillé rouge); (c) Phase détectée du signal conjugué (ligne pleine orange) et phase du signal d’entrée (ligne en pointillé rouge), et (d) Comparaison entre le signal de sortie détecté (ligne orange pleine) et la phase du signal idéal conjugué en entrée (ligne en pointillé violette).

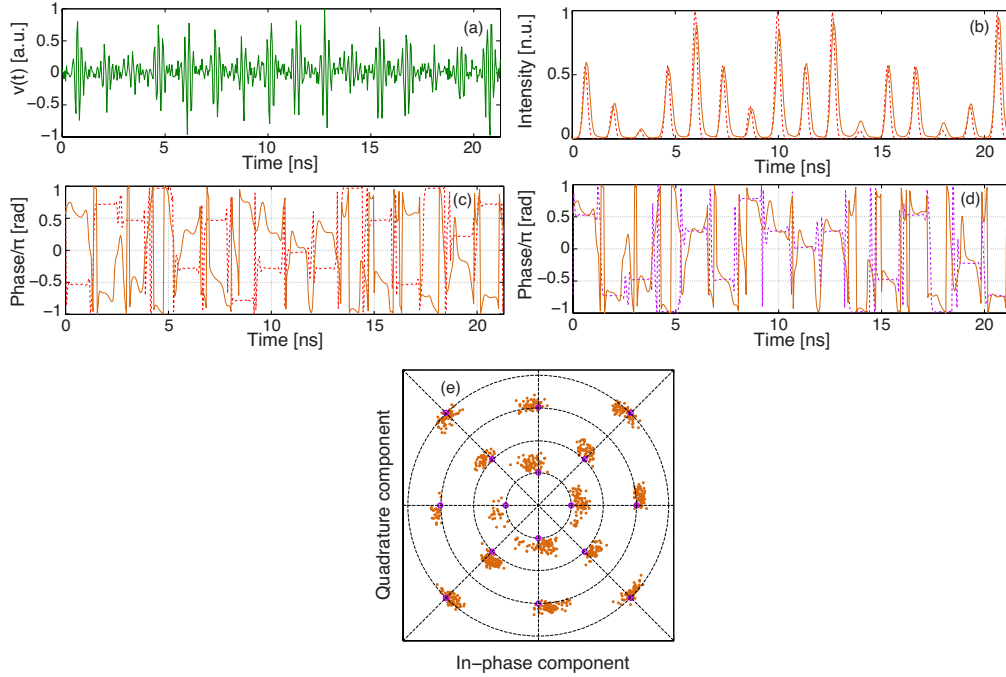


Figure 10 – (a) Hologramme temporel du signal d’entrée; (b) Intensité détectée du signal conjugué (ligne pleine orange), comparée avec le profil d’intensité du signal d’entrée (ligne en pointillé rouge); (c) Phase détectée du signal conjugué (ligne pleine orange) et phase du signal d’entrée (ligne en pointillé rouge); (d) Comparaison entre le signal de sortie détecté (ligne orange pleine) et la phase du signal idéal conjugué en entrée (ligne en pointillé violette), and (e) Constellation en sortie (les cercles violets représentent les positions idéales des symboles).

fiber) de longueur 1 km (FWHM final de 27.5 ps). Les signaux de référence  $e_{LO,1}(t)$  et  $e_{LO,2}(t)$  sont deux OC. La puissance moyenne des trois signaux impliqués dans ce procédé sont : 0.4 dBm pour le signal d’information  $e_S(t)$ , 13 dBm pour le signal de référence  $e_{LO,1}(t)$  et 3 dBm pour  $e_{LO,2}(t)$ . Les caractéristiques de la FOHNL sont  $\gamma = 11.3 \text{ W}^{-1}\text{km}^{-1}$ ,  $L = 1015 \text{ m}$ , la longueur d’onde à dispersion nulle est 1545 nm et la pente de la dispersion  $S_0$  (@ 1545 nm) =  $0.017 \text{ ps/nm}^2/\text{km}$ .

La figure 12 montre le spectre des impulsions et les variations temporelles du signal converti en longueur d'onde dans le cas (a) d'un décalage négatif de 17 nm de  $e_S(t)$ , (b) d'un décalage positif de 17 nm de  $e_S(t)$  et (c) d'une conversion supérieure de 10 nm de  $e_S^*(t)$ . Les ondes temporelles en sortie ont alors été mesurées en utilisant un oscilloscope optique à échantillonnage à 500 GHz (Exfo PSO-101). Dans tous les cas, les largeurs des impulsions obtenues coïncident avec celles des impulsions initiales, prouvant que la phase quadratique induite par la dispersion est conservée avec une efficacité de conversion de  $\sim 20$  dB. Ce résultat est cohérent avec les raisonnements précédents qui se reposent sur les MQO mais nécessitant une énergie inférieure d'un ordre de magnitude à celui du signal pompe  $e_S(t)$  et du signal sonde  $e_{LO,2}(t)$ .

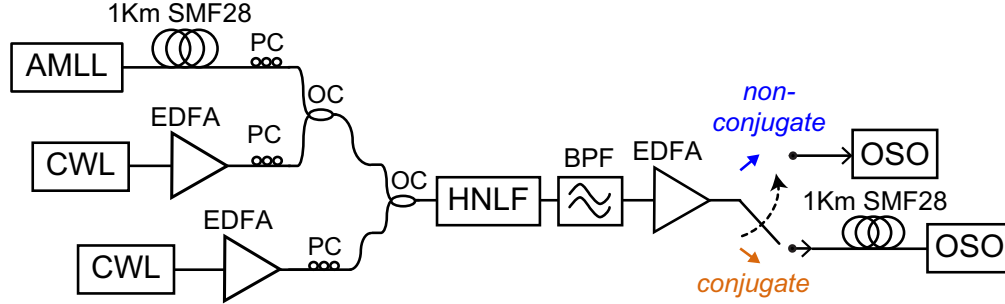


Figure 11 – Montage expérimental de la conversion en longueur d'onde du signal reposant sur le XPM pour des signaux à enveloppe complexe. AMLL : laser en mode actif bloqué; PC, contrôleur de polarisation; CWL, laser continu; EDFA, amplificateur sur fibre dopée à l'Erbium; OSO, oscilloscope optique à prélèvement; OC, coupleur optique; SMF, fibre monomode.

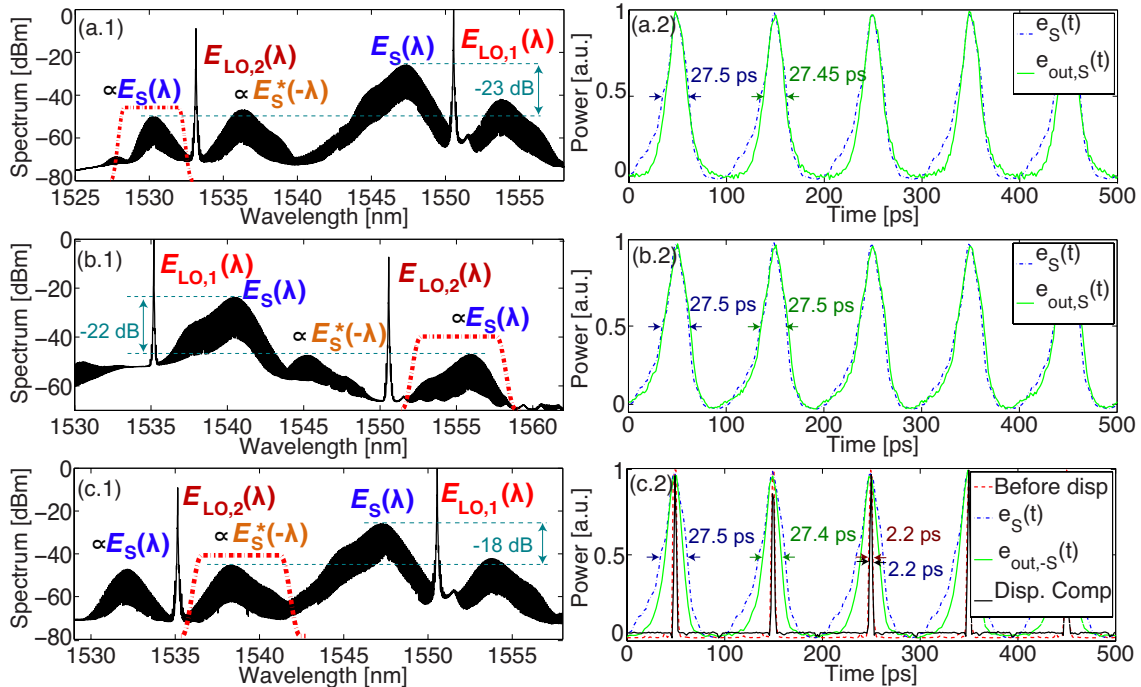


Figure 12 – (a) Décalage négatif de  $e_S(t)$ ; (b) décalage positif de  $e_S(t)$ ; (c) décalage négatif de  $e_S^*(t)$ ; a-c (1) Spectre après FOHNL; a-b (2) signal temporel après FOPB (ligne verte) vs. signal d'entrée (ligne en pointillé bleue); c (2) signal de sortie du LMAB (ligne rouge) et après compensation de la dispersion (ligne noire).

La méthode proposée pour la conversion en longueur d'onde de signaux à enveloppe complexe reposant sur l'holographie temporelle fournit des avantages intéressants comparés aux méthodes traditionnelles reposant sur le MQO : (i) la condition d'accord de phase n'est plus nécessaire; (ii) cela rend possible une bonne efficacité de conversion pour une large gamme de longueurs d'onde, fournissant une efficacité symétrique pour les décalages négatifs et positifs, et (iii) une puissance inférieure d'un ordre de grandeur est nécessaire pour les signaux utilisés dans ce processus. Les méthodes classiques reposant sur la XPM sont limitées à la conversion de signaux dont l'information est contenue seulement dans la variation de l'amplitude.

## E. Holographie en domaine spectral

En utilisant la propriété de dualité entre le domaine temporel et le domaine fréquentiel de la transformée de Fourier, nous proposons et formulons, pour la première fois, le concept d'holographie en domaine spectral. Le terme « holographie en domaine spectral » a déjà été utilisé dans la littérature mais pour définir des systèmes où des filtres dans le domaine spatial sont utilisés pour traiter des signaux temporels à enveloppe complexe. Dans cette thèse, l'holographie en domaine spectral est appliquée à la conception de deux types de systèmes de traitement du signal qui sont : le filtrage optique reposant sur la mise en forme de spectre dans le domaine temporel (MFSDT, ou TDSS pour *time-domain spectral shaping*) [10] et sur des RDBF utilisés en transmission [14,15]. Dans les deux cas, l'utilisation de concepts d'holographie permet de s'affranchir des limitations imposées par le filtrage associées à ces processus, i.e., des réponses spectrales réelles dans le cas de filtres reposant sur la MFSDT et des réponses spectrales à phase minimale dans le cas de RDBF en transmission. Pour la suite, le terme « holographie en domaine spectral » est utilisé par soucis de cohérence.

### E.1. Formalisme Mathématique

Dans le cas d'un système physiquement réalisable qui est linéaire et invariant dans le temps (LTI) avec une fonction de transfert  $H_F(\omega')$  (où  $\omega' = \omega - \omega_0$ ,  $\omega$  étant la fréquence angulaire optique et  $\omega_0$  étant la fréquence de l'onde porteuse). L'enveloppe complexe correspondante s'obtient comme  $\hat{h}_F(t) = \mathcal{F}^{-1}\{H_F(\omega')\}$ .  $H_F(\omega')$  doit être délimitée dans une fenêtre spectrale de durée  $\Delta\omega_F$ . Sa réponse impulsionnelle doit être causale (ou, en d'autres termes, la réponse impulsionnelle doit être nulle pour des valeurs négatives de temps). Aussi, la réponse doit être elle-même limitée dans une fenêtre temporelle de durée  $\Delta t_F$  et centrée à  $t_C > \Delta t_F/2$ . Un hologramme spectral peut être généré par le procédé équivalent en fréquence de l'étape d'enregistrement de l'holographie temporelle, où la fonction de transfert de la cible interfère avec le signal de référence. Dans ce cas, le signal de référence doit avoir une enveloppe temporelle instantanée  $\hat{h}_{Ref}(t) = A \cdot \delta(t - t_D)$  (centré sur  $\omega_0$ ), avec  $\delta(t)$  étant la fonction de Dirac. Ainsi, l'hologramme spectral est défini comme l'intensité du patron d'interférence entre le signal et la référence,

$$\begin{aligned} P_{Hol}(\omega') &= |H_F(\omega') + H_{Ref}(\omega')|^2 \\ &= |H_F(\omega')|^2 + A^2 + 2A|H_F(\omega')| \cos\left(t_p\omega' + \angle H_F(\omega')\right), \end{aligned} \quad (4)$$

où  $t_p = t_D - t_C$  est le délai entre la fonction  $h_F(t)$  et la référence  $h_{Ref}(t)$ .

Dans le domaine temporel, l'hologramme spectral est définie par l'expression suivante :

$$\hat{p}_{Hol}(t) = \hat{h}_F(t) \otimes \hat{h}_F^*(-t) + A \cdot \delta(t) + A\hat{h}_F(t - tp) + A\hat{h}_F^*(-t - tp). \quad (5)$$

Afin d'éviter toute superposition temporelle entre les différents composants du signal de sortie,  $t_p$  doit être défini comme  $t_p > 3\Delta t_F/2$  (on peut observer que la durée du « terme ambiguë » est deux fois celle de la fonction visée). Il est possible de réduire par deux la durée temporelle de l'hologramme spectral si la constante  $A \gg |\hat{h}_F(t)|$ , puisque le premier terme de l'équation 4 peut être négligé. Ce procédé peut être vu comme la contrepartie du processus employé dans la Section D pour réduire la bande passante nécessaire pour l'holographie temporelle. Dans ce cas, on génère des franges dans le domaine spectral, et la réponse visée peut être obtenue à partir de la réponse totale de sortie en utilisant un processus de portillonnage temporel.

## E.2. Holographie en domaine spectral pour le profilage spectral à valeurs complexes

La technique de profilage spectral pour le filtrage dans le domaine spatial a inspiré, de par la dualité espace-temps, une méthode extrêmement prometteuse pour implémenter des processeurs d'impulsions temporelles reconfigurables électroniquement sur fibre optique avec une résolution dans la gamme des sub-picosecondes [19]. Cette méthode est dénommée MFSDT et emploie (i) un milieu dispersif au lieu d'une diffraction spatiale pour séparer temporellement les composantes spectrales de l'impulsion initiale, (ii) un modulateur EO pour effectuer le processus de filtrage désiré dans le domaine temporel au lieu d'un masque spatial ou d'un Modulateur en Domaine Spatial (MDS) dans le cas du domaine spatial, et (iii) un deuxième milieu dispersif opposé au premier pour réassembler les composantes spectrales de l'impulsion initiale. La principale limitation des montages implémentant MFSDT concerne le fait qu'il est possible de contrôler uniquement l'intensité temporelle des profils de l'onde en sortie, et typiquement, la synthèse de forme temporelle doit strictement être symétrique. La figure 13(a) présente le diagramme d'un système MFSDT typique.

Des impulsions optiques avec une forme véritablement programmable (en amplitude et phase) peuvent être obtenues en concevant le signal modulateur  $H_{hc}(t)$  comme un hologramme spectral. Le principe général peut être interprété comme la contrepartie temporelle des filtres Vander-Lugt [10,17]. Dans les notations suivantes, nous employons les lettres majuscules pour les signaux proportionnels aux profils spectraux et les lettres minuscules pour des signaux proportionnels aux profils temporels, sans tenir compte de leur domaine de définition ( $t$  pour le domaine temporel et  $\omega$  pour le domaine fréquentiel).

Supposons que le signal en entrée est une impulsion transformée gaussienne limitée, définie comme  $e_S(t) = \hat{e}_S(t) \exp\{j\omega_0 t\}$ , où,  $\hat{e}_S(t) = \exp\{-t^2/2T_0^2\}$ ,  $T_0$  est la largeur à 1/e-hauteur au maximum et  $\omega_0$  est la fréquence de l'onde porteuse. L'enveloppe de la réponse impulsionnelle temporelle du filtre est  $\hat{h}_F(t)$  (à  $\omega_0$ ). Le signal en entrée est premièrement dispersé dans un milieu avec une fonction de transfert  $H_{\Phi}(\omega') = \exp\{-j\Phi\omega'^2/2\}$  où  $\Phi$  est la dispersion chromatique. Le signal dispersé est modulé en amplitude par un signal radiofréquence (RF)  $H_{hc}(t)$ , et la transformée de Fourier à la sortie du modulateur s'écrit comme suit :

$$E_M(\omega') \propto [E_S(\omega') \cdot H_{\Phi}(\omega')] \otimes h_{hc}(\omega), \quad (6)$$

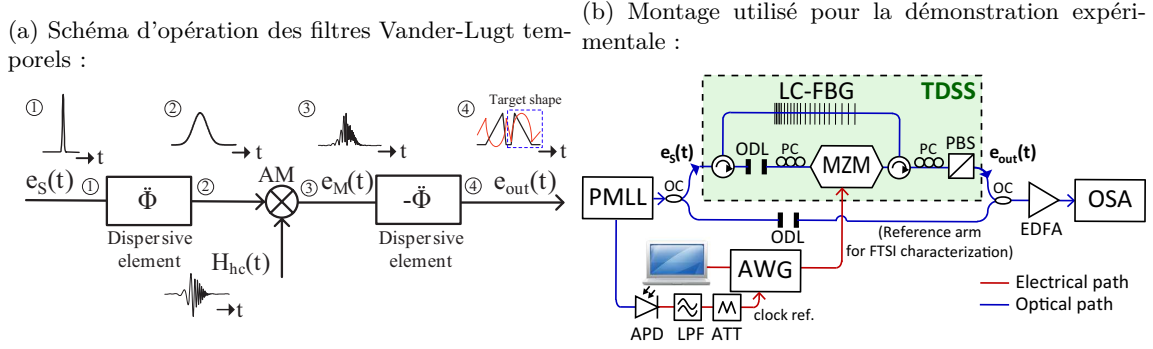


Figure 13 – (a) Schéma d'opération des filtres Vander-Lugt temporels, reposant sur le MFSDT avec un hologramme spectral comme signal de modulation. AM : modulateur d'amplitude. (b) Montage utilisé pour la démonstration expérimentale de mise en forme d'impulsion reposant sur des filtres de Vander-Lugt temporels ; la caractérisation du signal de sortie est effectué par interférométrie spectrale à transformée de Fourier (FTSI). Pour simplicité, les signaux temporels sont représentés par leurs enveloppes complexes. PMLL : laser en mode bloqué passif; OC : coupleur optique; ODL : ligne optique à délai; PC : contrôleur de polarisation; PBS : séparateur de faisceau polarisé; LC-FBG : réseau de Bragg à pas variable; EDFA : amplificateur sur fibre dopée à l'Erbium; APD : photodiode à avalanche; BPF : filtre passe-bande; ATT : atténuateur.

où  $\otimes$  fait référence à une convolution,  $E_S(\omega') = \mathcal{F}\{\hat{e}_S(t)\}$  et  $h_{hc}(\omega) = \mathcal{F}\{H_{hc}(t)\}$ . La dérivation dans la section E.1 nous donne l'expression du signal modulé :

$$H_h(t) \propto H_F(t) \exp\{-j\omega_p t\} + H_F^*(-t) \exp\{j\omega_p t\}, \quad (7)$$

qui est nommée comme  $H_h(t)$  au lieu de  $H_{hc}(t)$  puisqu'une étape supplémentaire est effectuée après la dernière opération qui est présentée dans la suite. Dans l'équation 7, les composantes en intensité ont été négligées puisque l'hologramme est conçu par ordinateur et ne sont donc pas utiles pour l'application visée. Le paramètre  $\omega_p$  est choisi pour éviter toute superposition entre les deux termes qui composent  $H_h(t)$ .

Quand le signal en entrée dispersé est modulé en amplitude avec  $H_h(t)$  (signifiant que dans l'équation 6 :  $h_{hc}(\omega) = \mathcal{F}\{H_h(t)\}$ ) et se propage ensuite à travers un milieu avec une dispersion chromatique  $-\ddot{\Phi}$ , le signal résultant en sortie est proportionnel à  $e_S(t) \otimes h_{hc}(t) \exp\{-j t^2/2\ddot{\Phi}\}$ , et présente alors un terme de phase temporel additionnel quadratique qui empêche d'obtenir le profil de phase désiré en sortie (voir Annexe A pour la démonstration mathématique). Afin de supprimer ce terme de phase indésirable, un terme de phase quadratique proportionnel à  $H_{\ddot{\Phi}}(\omega)$  doit être ajouté au spectre de  $H_h(t)$ , i.e.  $h_h(\omega)$ . Cependant, le signal modulé (l'hologramme spectral) doit toujours être une fonction à valeur réelle. Ainsi, les termes de phase ajoutés aux deux bandes latérales spectrales de  $H_h(t)$  doivent être de signes opposés, de façon que la phase spectrale totale soit une fonction de symétrie impaire (obtenant ainsi une transformée de Fourier à valeurs réelles) :

$$h_{hc}(\omega) \propto h_F(\omega - \omega_p) \exp\left\{j \frac{\ddot{\Phi} \omega^2}{2}\right\} + h_F^*(-\omega - \omega_p) \exp\left\{-j \frac{\ddot{\Phi} \omega^2}{2}\right\}. \quad (8)$$

En remplaçant l'équation 8 dans l'équation 6 et supposant que le spectre est confiné dans un domaine spectral réduit de façon que  $T_0 \omega_m \ll 1$ , où  $\omega_m$  est la fréquence maximale de  $H_{hc}(t)$ , le

spectre du signal optique modulé,  $E_M(\omega')$ , peut être approximé comme :

$$E_M(\omega') \propto E_S(\omega') H_{\ddot{\Phi}}(\omega') \left[ H_F(\omega') \exp\{j \ddot{\Phi} \omega_p \omega'\} + H_F^*(\omega') \exp\{-j \ddot{\Phi} \omega_p \omega'\} \otimes \exp\{-j \ddot{\Phi} \omega'^2/4\} \right]. \quad (9)$$

Finalement, le signal optique modulé se propage à travers un deuxième milieu dispersif avec une dispersion de  $-\ddot{\Phi}$ , comme présenté sur la Fig. 13(a). À la sortie, l'enveloppe complexe de l'onde temporelle résultante peut être écrite comme :

$$\hat{e}_{out}(t) \propto \hat{e}_S(t) \otimes h_F(t - \ddot{\Phi} \omega_p) + \hat{e}_S(t) \otimes h_F^*(-t - \ddot{\Phi} \omega_p) \exp(-j t^2 / \ddot{\Phi}). \quad (10)$$

L'équation 10 montre que le signal de sortie est composé de deux termes, un proportionnel à l'onde temporelle désirée (premier terme de l'équation). Les deux termes sont décalés temporellement entre eux; ainsi la fenêtre d'opération temporelle du système  $\Delta T_{out}$  est divisée par deux par rapport au cas où la réponse impulsionnelle d'un système est symétrique et en intensité. Le produit temps-bande passante (TBP)<sup>1</sup> de filtres Vander-Lugt temporels est directement proportionnel au produit  $\omega_m \cdot \ddot{\Phi}$ . La portion désirée du signal temporel de sortie peut être filtrée dans un procédé de portillonnage temporel, si besoin.

Les capacités du schéma proposé sont démontrées avec succès en synthétisant deux différentes ondes temporelles avec un intérêt pratique, dont une impulsion à forme triangulaire asymétrique avec une phase parabolique, et une séquence d'impulsion à 4-bit 16-QAM. La figure 13(b) montre le montage utilisé pour la démonstration expérimentale du plan proposé. Le bras supérieur de l'interféromètre de Mach-Zehnder représente le montage MFSDT (Fig 13(a)), dans lequel les deux milieux dispersifs opposés sont implémentés en utilisant le même RDBF avec un pas linéaire (PL-RDBF, ou LC-FBG pour *linearly chirped FBG*) utilisé par ses deux extrémités (ils fonctions en réflexion), et les modulations d'amplitudes sont implémentées via un MZM décentré à son point de transmission minimal. L'interféromètre est utilisé pour caractériser le champ à enveloppe complexe en sortie du dispositif de mise en forme d'impulsion des mesures de spectres optiques via l'utilisation d'un algorithme d'interférométrie spectrale à transformée de Fourier (ISTF, ou FTSI pour *Fourier transform spectral interferometry*) [21].

Le signal initial  $e_S(t)$  est généré par un laser en mode bloqué passif (LMBP, ou PMLL pour *passive mode locked laser*). Celui-ci consiste en une suite d'impulsion optique de type gaussienne avec une FWHM de 2 ps avec un taux de répétition de 10 MHz, centré à  $\lambda_0 = 2\pi c_0 / \omega_0 = 1545$  nm. Le PL-RDBF fourni une dispersion équivalente à 120 km de FOM, i.e.  $\ddot{\Phi} \propto -2600$  ps<sup>2</sup>, tout le long de la bande optique C de télécommunication. L'hologramme spectral est généré par le GOP-7122C fourni par Tektronix.

Les figures 14 et 15 présentent l'hologramme spectral désigné et les résultats obtenus pour les deux ondes synthétisées. La résolution temporelle des ondes en sortie a été mesurée comme l'inverse de la largeur à 1% du maximum de la réponse spectrale de l'impulsion correspondante, considérant que les impulsions en entrée et en sortie sont toutes deux à phase constante. Dans les deux exemples présentés, nous estimons une résolution temporelle de  $\delta t_{out} \sim 6.7$  ps, très proche de la résolution temporelle de l'impulsion initiale de  $e_S(t)$ , laquelle est  $\sim 5.8$  ps. Un relatif bon accord entre les ondes obtenues et les résultats idéalement attendus peut être observé sur ces graphiques.

---

<sup>1</sup>Le TBP est typiquement utilisé comme figure de mérite pour les systèmes de mise en forme d'impulsion.

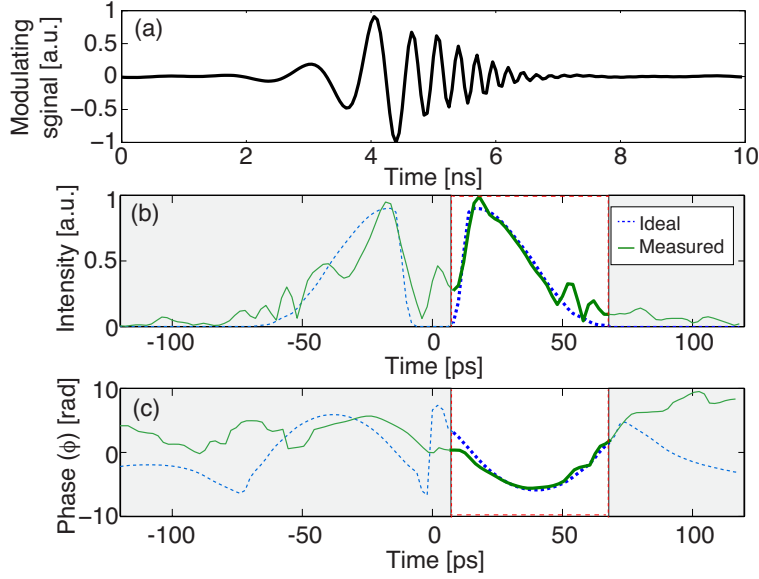


Figure 14 – Impulsion triangulaire asymétrique avec une phase parabolique : (a) hologramme spectrale  $H_{hc}(t)$  ; (b) intensité temporelle du signal de sortie; et (c) phase temporelle du signal de sortie : ciblée (ligne bleue en pointillé) et mesurée (ligne verte pleine).

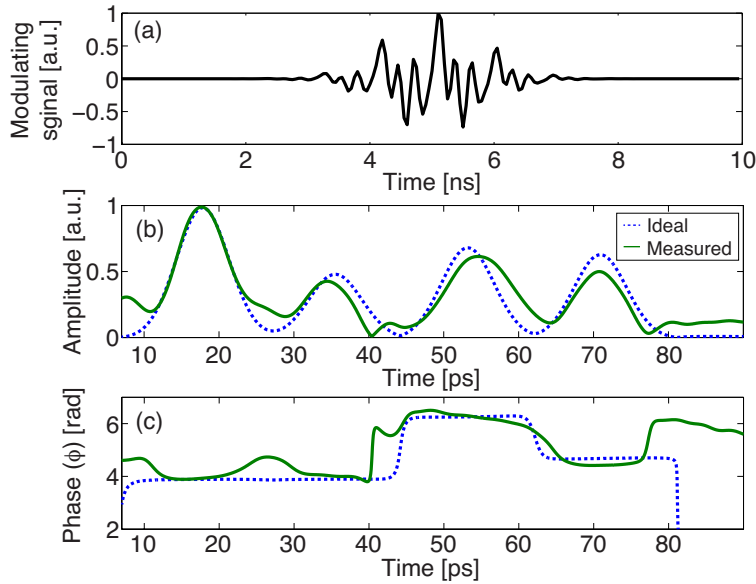


Figure 15 – Code 4-bit 16-QAM : (a) hologramme spectral  $H_{hc}(t)$  ; (b) amplitude temporelle du signal de sortie, seulement la partie droite du signal de sortie est présentée, correspondant de l'impulsion cible mise en forme; (c) phase temporelle du signal de sortie : ciblée (ligne bleue en pointillé) et mesurée (ligne verte pleine).

### E.3. Holographie dans le domaine spectral pour des processus à phase non-minimale reposant sur des RDBF en transmission

Les RDBF se sont révélés être une technologie critique pour un large éventail d'applications dans les communications optiques et dans les systèmes de capteurs de par leurs faibles couts, les faibles pertes optiques engendrées, et leur haute compatibilité avec les systèmes tout optiques. Cependant,

la caractéristique la plus remarquable des RDBF est leur extraordinaire flexibilité pour la conception de filtres optiques avec n'importe quelle forme de réponse spectrale passe-bande lorsqu'utilisés en réflexion. Les implémentations reposant sur des RDBF spécialement apodisés ont une bande passante limitée  $< 200$  GHz, par les limitations pratiques dans le maximum de changement d'indice de réfractons ( $< 10^{-3}$ ) et dans la résolution du profil d'apodisation ( $> 100 - 200\mu\text{m}$ ). Quand le réseau est utilisé en transmission, la complexité et le coût du système global sont réduits puisqu'il n'est pas nécessaire d'employer un circulateur ou un coupleur pour séparer le signal de sortie de celui en entrée. De plus, la phase de la réponse en transmission est souvent plus résistante aux imperfections dans la structure du réseau que celle de la réponse en réflexion [22]. Dans cette thèse, nous démontrons une nouvelle méthode d'opération de RDBF opérant en transmission qui fournit une augmentation de la bande passante d'au moins un ordre de grandeur comparé aux RDBF en réflexion (dans le régime THz). Malgré cela, la réponse spectral en transmission est une fonction à phase minimale [23], ce qui limite sévèrement les applications possibles dans cette configuration. Avec l'utilisation de l'holographie en domaine spectral, nous étendons les capacités des RDBFs en transmission, de façon à ce que des systèmes à phases non-minimale puissent aussi être implémentés dans cette configuration.

### E.3.1. Augmentation de la bande passante des RDBF

Dans la suite, une approche est proposée pour augmenter la bande passante d'un RDBF en transmission. Celle-ci consiste en l'exploitation du degré de liberté disponible lors de la résolution de la réponse spectrale en phase de la réflexion du RDBF.

Le problème en question concerne le concept des filtres optiques linéaires fournissant une fonction de transfert spectrale à phase minimale,  $H_{ideal}(\omega')$ , tout au long d'une bande passante extrêmement large (où  $\omega' = \omega - \omega_0$ ).  $H_T(\omega')$  et  $H_R(\omega')$  déterminent respectivement les réponses en transmission et en réflexion. Puisque le processus en question repose sur les RDBF en transmission,  $H_T(\omega')$  doit être proportionnel à  $H_{ideal}(\omega')$  le long de la bande passante utilisée. Dans un filtre à phase minimale (e.g. RDBF à transmission), la phase spectrale de la réponse du filtre est nécessairement déterminée par l'amplitude de la réponse spectrale via une transformation de Hilbert. De plus, dans une RDBF, la transmittivité ( $T = |H_T(\omega')|^2$ ) et la réflectivité ( $R = |H_R(\omega')|^2$ ) sont reliés par la relation suivante :  $T = 1 - R$ , par le principe de conservation d'énergie. Ainsi, les caractéristiques de  $|H_T(\omega')|$  imposent uniquement les fonctions  $\angle\{H_T(\omega')\}$  et  $|H_R(\omega')|$ . Ainsi, d'après les caractéristiques de l'amplitude de la transmission désirée  $|H_T(\omega')|$ , les problèmes de conception se réduisent à la synthèse de RDBF fournissant l'amplitude de la réponse  $|H_R(\omega')|$ , sans contrainte additionnelle sur la phase de la réponse  $\angle\{H_R(\omega')\}$ . Ainsi, la phase de la réflexion de la RDBF peut être fixée de façon adéquate pour obtenir un concept de réseau le plus simple possible en accord avec les caractéristiques ciblées.

La phase spectrale de la réflexion, qui se traduit en une variation linéaire de la période, augmente la bande passante du réseau : comme la composante fréquentielle en réflexion le long du réseau dépend de la période, la bande passante de la réponse spectrale en réflexion, i.e. la bande passante correspondante rejetée en transmission, peut être sensiblement supérieure que dans le cas des réseaux à périodes uniformes [11]. La réponse en réflexion du RDBF qui doit être synthétisée peut être exprimée mathématiquement :

$$H_R(\omega') = W(\omega') \sqrt{R_{max} \left( 1 - |H_T(\omega')|^2 \right)} \exp \left\{ j \left( \frac{1}{2} D \omega'^2 + \tau_{shift} \omega' \right) \right\}, \quad (11)$$

où  $R_{max}$  est le maximum de la réflexion;  $D$  est le paramètre dispersion ( $s^2$ ) ou de façon équivalente, la pente du retard de groupe;  $W(\omega')$  représente une fonction fenêtrée qui est introduite car la réflexion d'une RDBF doit être une fonction passe-bande limitée; et  $\tau_{shift}$  est le temps de retard, qui se traduit dans le terme linéaire de phase dans l'équation 11, afin d'obtenir un système causal.

D'après les caractéristiques de la réflexion définies par l'équation 11, la méthode proposée obtient la perturbation du réseau en utilisant un algorithme de synthèse RDBF par couche basé sur la Théorie des Modes Couplés (CMT) combiné avec la Méthode de Transfert de Matrices (TMM) [24]. Les études numériques ont montrées que les caractéristiques du réseau apodisé résultant peuvent être moins contraignantes et donc plus facilement réalisables en augmentant de façon adéquate la valeur spécifique du paramètre de dispersion ( $D$ ). Plus grand le paramètre de dispersion est, plus long le réseau sera et plus petit sera le pic maximum de la modulation de l'indice de réfraction.

### E.3.2. Processeurs ultrarapides à phase minimale à base de RDBF en transmission

Dans cette Section, nous présentons la conception de deux processeurs optiques à phase minimale, un différenciateur optique à ordre arbitraire et un dispositif de mise en forme d'impulsion rectangulaire.

- *Différenciateur optique à ordre aléatoire :*

Un différenciateur optique est un processeur optique qui fournit en sortie la dérivation de l'enveloppe complexe du signal optique d'entrée. La fonction de transfert idéale peut être exprimée comme :

$$H_{ideal,dif}(\omega') \propto (j \cdot \omega')^N, \quad (12)$$

où  $N$  est l'ordre de dérivation.

Nous avons conçu un différenciateur tout optique d'ordre  $N = 1$  avec une bande passante  $B = 2$  THz (largeur à 1% de l'amplitude maximale spectrale) utilisant l'approche décrite dans la Section E.3.1 [11]. Lors de la conception, l'équation 11 est utilisée avec un paramètre de dispersion  $D$  fixé à  $80 \text{ ps}^2$ ;  $\tau_{shift} = 1.356 \text{ ns}$  et  $R_{max}$  est à  $99.9999\%$ . Dans ce cas, aucune fenêtre temporelle n'est nécessaire ( $W(\omega') = 1$ ) puisque la fonction de transfert est une fonction passe-bande. La figure 16 montre l'apodisation du réseau, le profil des périodes et, après une évaluation numérique de l'effet des erreurs potentiels provenant du procédé de fabrication, la réponse spectrale en transmission.

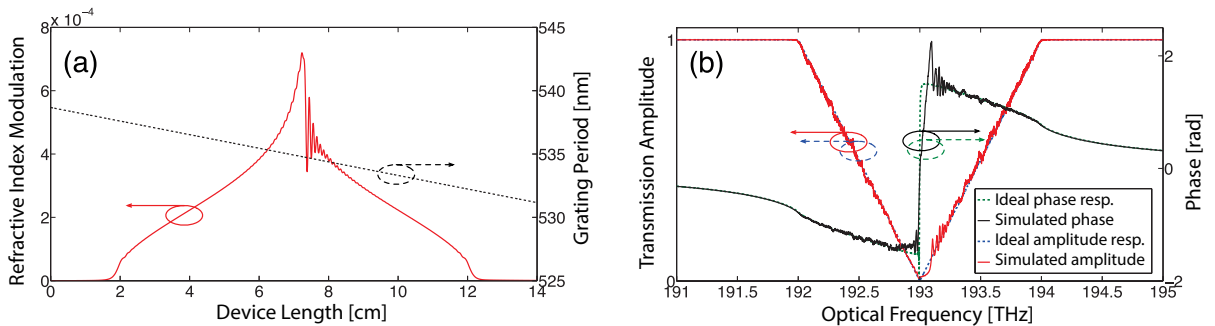


Figure 16 – (a) Profils d'apodisation (ligne pleine rouge) et de période (ligne en pointillé noir); (b) amplitude (ligne bleue en pointillé) et la phase (ligne verte en pointillé) de la réponse spectrale en transmission voulue comparée à l'amplitude (ligne rouge pleine) et la phase (ligne noire solide) de la réponse spectrale en transmission avec les contraintes de fabrication.

La figure 17(a) présente la caractérisation temporelle du dispositif en considérant une impulsion de type gaussien avec un FWHM de 1 ps. Le graphique présente un excellent accord entre le signal idéalement attendu en sortie et celui effectivement obtenue à partir du réseau conçu. Pour une analyse plus détaillée des performances, nous avons calculé le TBP du différentiateur pour un coefficient de corrélation croisée ( $C_C$ ) supérieur à 90% (voir Fig. 17(b)). Le TBP résultant est  $\sim 420$ , un ordre de magnitud plus grand que les différentiateurs proposés précédemment reposant sur les RDBF.

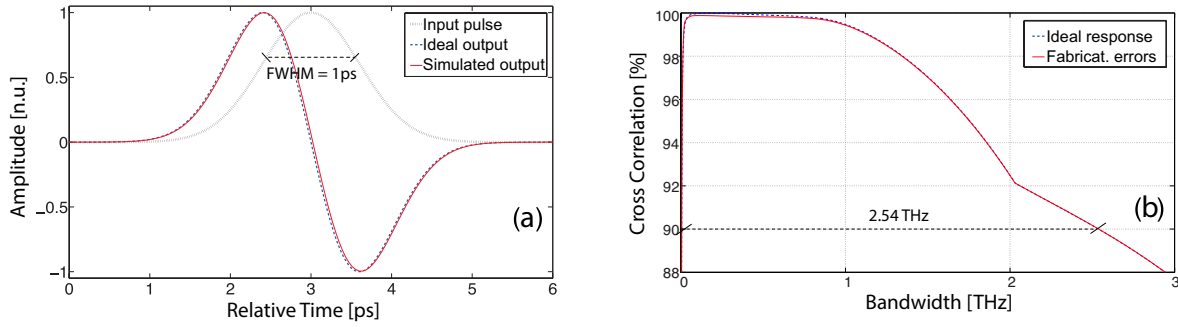


Figure 17 – (a) Impulsion de type gaussien en entrée (ligne noire en pointillé) et comparaison entre le signal en sortie idéal (ligne bleue en tiret) et celui obtenue numériquement (ligne rouge pleine) ; (b) coefficient de corrélation croisée entre l’onde de sortie temporelle idéale et numériquement obtenue en fonction de la bande-passante à 3 dB d’une impulsion gaussienne pour la conception original (ligne bleue en tiret) et la conception perturbée considérant les potentiels erreurs de fabrication (ligne rouge solide).

Finalement, la conception de différentiateurs optiques à 2 THz à ordre supérieur (jusqu’à  $N = 4$ ) est également proposée avec la même méthodologie [12]. Le profil d’apodisation résultant est représenté sur la Fig. 18(a). Tous les paramètres sont fixés à des valeurs identiques à celles de l’exemple précédent. La figure 18(b) présente la réponse temporelle en sortie du réseau comparée à celle idéalement attendue. Les simulations numériques offrent des valeurs de TBP similaires à celle obtenue avec le différentiateur de premiers ordre.

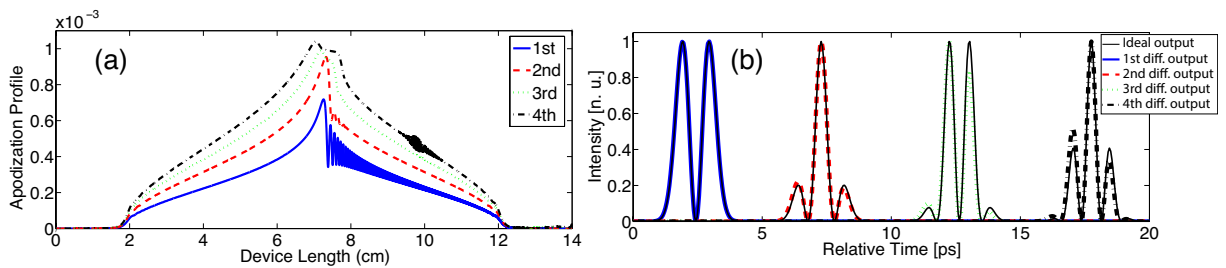


Figure 18 – (a) Profils d’apodisation considérant une résolution réaliste spatiale (limitée à 0.5 mm) (b) Intensité en sortie des différentiateurs optiques reposant sur des RDBF.

- *Dispositif de mise en forme d’impulsion rectangulaire:*

Un dispositif de mise en forme d’impulsion rectangulaire fourni une impulsion optique avec une enveloppe de forme rectangulaire. En considérant une impulsion en entrée suffisamment étroite, la fonction de transfert du dispositif de mise en forme rectangulaire peut être approximée par :

$$H_{ideal,ft}(\omega') = \text{sinc}(\omega' \cdot \tau_{FWHM}/2\pi), \quad (13)$$

où la fonction sinc est définie comme  $\text{sinc}(\pi\omega')/(\pi\omega')$  et  $\tau_{FWHM}$  est la durée de l'impulsion temporelle rectangulaire de sortie.

Nous présentons la démonstration expérimentale d'un dispositif d'une mise en forme à 2 ps reposant sur une RDBF en transmission ( $\tau_{FWHM} = 2$  ps) avec une bande passante à 5 THz [13]. Pour la fabrication du PL-RDBF, un masque de phase de longueur 14.5 cm a été utilisé avec une période de 1064.05 nm (i.e. longueur d'onde de Bragg  $\lambda_0 = 2\pi c_0/\omega_0 = 1544.87$  nm) et une augmentation de la période le long du réseau de 2.5 nm/cm. Ces paramètres fixent la dispersion du réseau à  $D = 33.77$  ps<sup>2</sup>. Le RDBF a été fabriqué dans le laboratoire de la professeure Sophie LaRoche à l'Université Laval. Appliquant l'outil de synthèse CMT-TMM à la réponse en réflexion prescrite (équation 11 avec les paramètres définies ci-dessus), les profils d'apodisation et de période, présentés respectivement dans les Figs. 19(a) et (b) sont obtenus. Les figures 19(d) et (e) montrent respectivement la réponse en amplitude et en phase du réseau modulées et mesurées.

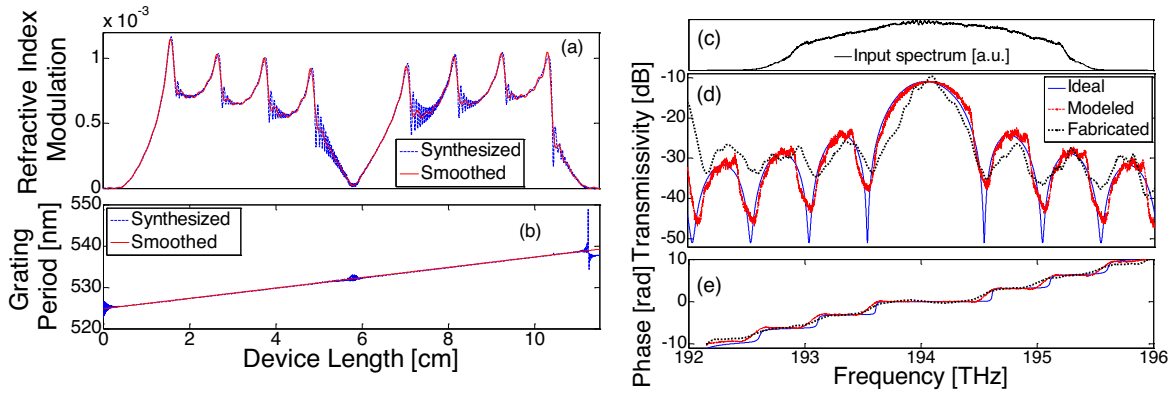


Figure 19 – Profils d'apodisation des RDBF obtenus (a) et période (b) de la synthèse (ligne bleue) et profils lissés adaptés aux contraintes de fabrication, i.e., résolution spatiale  $\geq 1$  mm (ligne rouge); (c) spectre du signal en entrée; (d) transmission et (e) phase de la transmission : idéales (ligne bleue), simulées considérant les contraintes de fabrication (ligne rouge) et mesurées du dispositif fabriqué (ligne noir en pointillé).

Pour la caractérisation dans le domaine temporel, un schéma ISTF a été implémenté [21]. L'impulsion en entrée a un FWHM de 400 fs et son spectre est présentée sur la Fig. 19(c). Les ondes temporelles en entrée et en sortie sont présentés sur la Fig. 20, validant le comportement du réseau fabriqué comme un dispositif de mise en forme d'impulsion rectangulaire.

On note que de nombreux autres dispositifs de mise en forme d'impulsions optiques à phase minimale, e.g. parabolique, triangulaire, dispositifs de mise en forme d'impulsion de Nyquist avec des résolutions de l'ordre du sub-picoseconde peuvent être implémentés sur un RDBF en transmission via l'utilisation de cette technique de conception.

### E.3.3. Holographie spectrale pour l'implémentation de processus ultrarapide à phase non-minimale reposant sur les RDBF en transmission

Si un système de traitement de signaux optiques à phase minimale avec une bande passante de l'ordre du THz est implémenté en utilisant un RDBF en transmission, seule la réponse en amplitude désirée doit être spécifiée dans l'algorithme décrit dans la suite. Cependant, si le système en question est à phase non-minimale, i.e., ses réponses en amplitude et en phase doivent être traitées

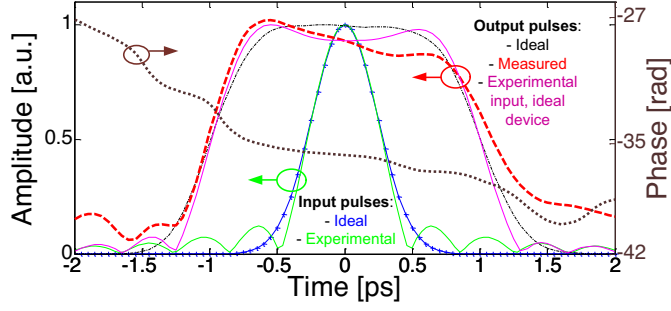


**Figure 20** – Impulsion idéale en entrée (ligne bleue en croix) ; impulsion expérimentale en entrée (ligne verte en pointillé) ; impulsion idéale en sortie (ligne noire en point) ; l’impulsion rectangulaire en sortie mesurée (ligne rouge en tiret) ; impulsion en sortie obtenue numériquement d’après l’impulsion en entrée expérimentale et la réponse idéale du réseau (ligne violette pleine) ; phase de l’impulsion mesurée (ligne pointillée).

indépendamment, et ses opérations peuvent être limitées dans une fenêtre bien définie en temps, il est possible d’utiliser l’holographie en domaine spectral pour implémenter des systèmes à phase non-minimale par l’utilisation de RDBF en transmission [14].

Le système optique à phase non-minimale (en négligeant le délai) de départ peut être décrit entièrement par sa fonction de transfert  $H_{NMP}(\omega')$  (domaine fréquentiel) ou par sa réponse impulsionnelle  $\propto \hat{h}_{NMP}(t)$  (domaine temporel). Pour la conception de l’hologramme spectral, nous considérons le signal de référence  $\hat{h}_{Ref}(t) = A \cdot \delta(t - t_D)$ . La réponse spectrale de l’hologramme spectral est :

$$P_{Hol}(\omega') = A^2 + AH_{NMP}(\omega') \exp \{ j t_p \omega' \} + AH_{NMP}^*(\omega') \exp \{ - j t_p \omega' \}. \quad (14)$$

où le terme de convolution est omis afin de réduire la durée temporelle du processeur optique. Si  $P_{Hol}(\omega')$  est implémenté par un RDBF opérant en transmission, l’amplitude de la réponse spectrale à phase minimale peut être  $H_{MP}(\omega') = P_{Hol}(\omega')$ , tandis que la phase est donnée par une relation de transformation de Hilbert . Il a été observé que la composante  $AH_{NMP}^*(\omega') \exp \{ - j t_p \omega' \}$  dans l’équation 14 est annulée après effet de la phase minimale sur la réponse du système global. Ainsi le système MP résultant a une réponse impulsionnelle avec une enveloppe complexe :

$$\hat{h}_{MP}(t) \propto A\delta(t) + \hat{h}_{NMP}(t - t_p); \quad (15)$$

et par conséquent, une fonction de transfert :

$$H_{MP}(\omega') = A + H_{NMP}(\omega') \exp \{ - j t_p \omega' \}. \quad (16)$$

Ce résultat concorde avec une propriété bien connue qui établit que n’importe quelle fonction temporelle avec un pic dominant autour ou proche de l’origine, est soit une fonction à phase minimale ou proche d’en être une [25]. La réponse du système avec la fonction de transfert  $H_{MP}(\omega')$  peut être synthétisée par des RDBF opérant en transmission.

Afin de valider cette technique, nous avons démontré l’implémentation d’un transformateur de Hilbert photonique (PHT) avec une bande passante de l’ordre du THz dans une RDBF en

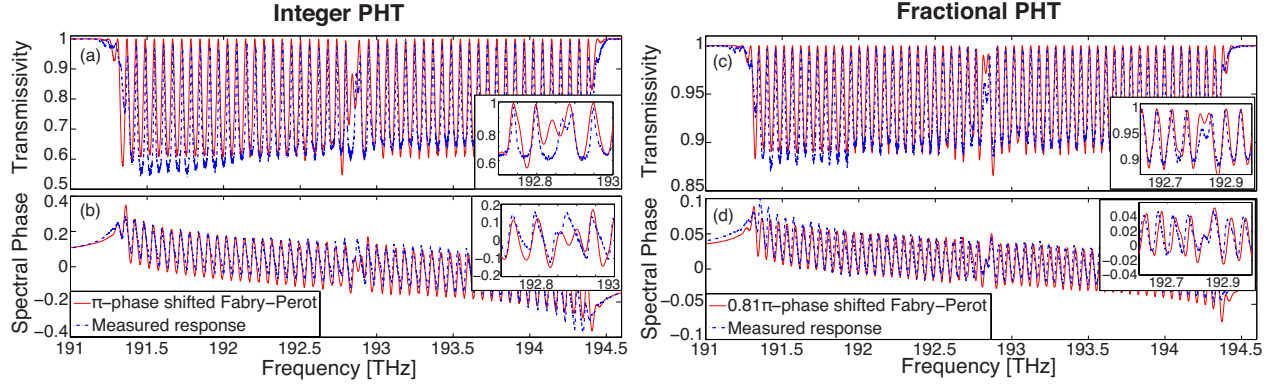


**Figure 21** – (a) Transmittivité simulée pour un transformateur de Hilbert photonique (PHT) à fabriquer (ligne rouge) et transmittivité du dispositif fabriqué (ligne bleue en tiret); (b) phase minimale simulée (ligne rouge) et phase mesurée en transmission (ligne bleue en tiret); (c) transmittivité simulée pour le PHT fractionné ( $P = 0.81$ ) à être fabriqué (ligne rouge) et transmittivité mesurée du dispositif fabriqué (ligne bleue en tiret); (d) phase minimale simulée (ligne rouge) et phase mesurée en transmission (ligne bleue en tiret).

transmission [15]. Un PHT est un processus de traitement d'impulsion qui fournit la transformée de Hilbert d'une impulsion optique incidente. La fonction de transfert d'un PHT à un ordre quelconque est définie comme

$$H_{ideal,PHT}(\omega') \propto \begin{cases} e^{-jP\pi/2} & \text{if } \omega > \omega_0, \\ 0 & \text{if } \omega = \omega_0, \\ e^{jP\pi/2} & \text{if } \omega < \omega_0, \end{cases} \quad (17)$$

où  $P$  est l'ordre fractionné. Dans le cas particulier de  $P = 1$ , le PHT est entier.

En particulier, nous avons ciblé l'implémentation de PHT entier et fractionné ( $P = 0.81$ ) avec une bande passante de 3 THz, utilisant un PL-RDBF avec  $L = 7$  cm et  $D = 34.24$  ps<sup>2</sup>. Ces RDBF ont également été fabriqués dans le laboratoire de Prof. Sophie LaRochelle. La figure 21 montre la transmittivité et la phase minimale correspondante des dispositifs fabriqués comparées avec celles idéalement visées. La transmittivité des réseaux présente la réponse attendue de type interférométrique, où les sauts en phase sont encodés dans les variations en amplitude de la réponse spectrale.

La figure 22 présente la caractérisation temporelle des PHT entiers (à gauche) et fractionnés (à droite) pour différentes impulsions en entrée (leurs FWHM sont indiqués sur la figure) effectuée avec un montage reposant sur ISTF [21]. L'évaluation de la performance du PHT entier montre un TBP de 7.8 et celle du dispositif fractionné, un TBP de  $\sim 17.9$ .

## F. Conclusions

Dans cette Thèse, deux nouveaux concepts ont été présentés et démontrés pour la première fois à notre connaissance. Il s'agit de *l'holographie en domaine temporel* et de *l'holographie en domaine spectral*. Ces concepts peuvent être perçus comme de puissants outils pour le développement de nouvelles techniques pour la génération, la mesure et le traitement d'ondes optiques temporelles ultrarapides.

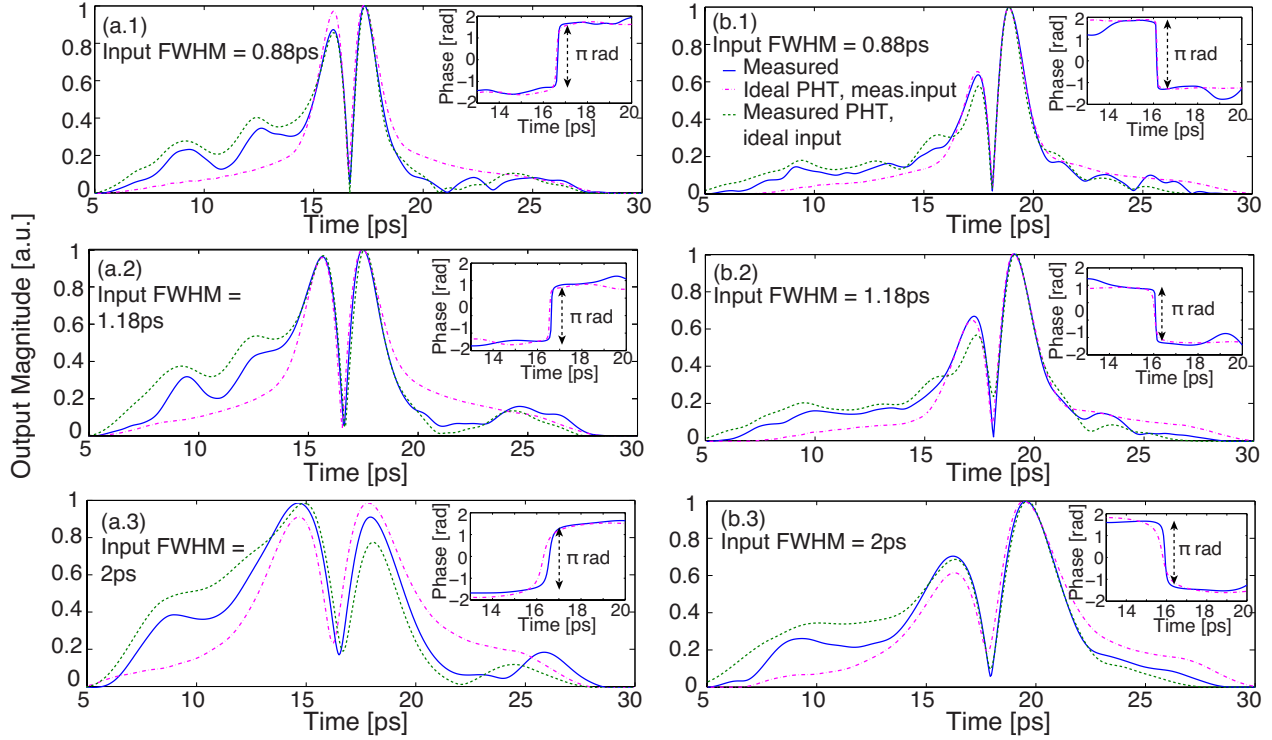


**Figure 22** – Composante transformée de Hilbert mesurée en sortie des PHT (ligne bleue) entiers (a) et fractionné (b) pour des impulsions de type gaussien mesurées avec un FWHM de (1) 0.88 ps; (2) 1.18 ps et (3) 2 ps. La sortie correspondante simulée d’un PHT idéal entier et fractionné à 0.81 (ligne rose en pointillé et tiret) sont également représenté pour comparaison. Les phases temporelles en sortie (simulées et mesurées) sont présentées dans les encadrés. Les lignes vertes en tiret présentent les sorties simulées des RDBF fabriqués (en utilisant les réponses spectrales mesurées dans la Fig. 21) en supposant une impulsion en entrée idéalement gaussienne.

L’holographie temporelle s’impose comme un processus efficace pour le contrôle simultané de l’amplitude et de la phase de signaux temporels. Elle a été utilisée pour démontrer expérimentalement la synthèse, le traitement (e.g. CTP ou conversion en longueur d’onde) et détection d’onde optique avec motifs de modulations aléatoires complexes (amplitude et phase) simplifiant ainsi de façon significative les techniques existantes. D’un autre côté, l’holographie en domaine spectral a été utilisée afin d’étendre les domaines d’applications de systèmes de traitements de signaux déjà connues. En particulier, la mise en forme d’impulsions à valeur complexe a été obtenue via l’utilisation de filtres optiques MFSDT, qui ont été typiquement limités à la mise en forme d’impulsions à valeurs réelles. De plus, des traitements à phase non minimale ont été implémentés grâce à l’utilisation de RDBF en transmission (limité aux fonctionnalités à phase minimale). En ce qui concerne ces nouveaux composants, nous avons proposé une nouvelle méthodologie de conception de RDBF pour obtenir des dispositifs tout optiques ultrarapides (dans le régime THz) de traitement de signaux, surpassant ainsi les limitations typiques en bande passante ( $< 200$  GHz).

De plus, le grand nombre d’applications dans l’holographie en domaine spatial nous permet de prévoir une quantité similaire et varié d’applications pour l’holographie temporelle/spectrale. Ainsi ce projet pourrait représenter une étape marquante pour le développement de nouveaux systèmes optiques plus efficaces dans le domaine de la communication, du traitement de l’information et au-delà.

## G. Références

- [1] H. Ishikawa, *Ultrafast all-optical signal processing devices*, Wiley, United Kingdom (2008).
- [2] K. Kikuchi, *Coherent optical communications: Historical perspective and future directions*, Optical and Fiber Communications reports 6, Springer-Verlag Berlin Heidelberg (2010).
- [3] D. Gabor, “A new microscope principle,” *Nature*, **161**, 777-778 (1949).
- [4] D. Gabor, G. W. Stroke, D. Brumm, A. Funkhouser, and A. Labeyrie, “Reconstruction of phase objects by holography,” *Nature*, **208**, 1159-1162 (1965).
- [5] E. N. Leith and J. Upatnieks, “Reconstructed wavefronts and communication theory,” *Journal of the Optical Society of America*, **52**, 1123-1128 (1962).
- [6] P. Hariharan, *Optical holography: principles, techniques and applications*, Cambridge University Press, Cambridge, UK (1984).
- [7] M. R. Fernández-Ruiz, M. Li, and J. Azaña, “Time-domain holograms for generation and processing of temporal complex information by intensity-only modulation processes,” *Optics Express*, **21** (8), 10314–10323 (2013).
- [8] M. R. Fernández-Ruiz and J. Azaña, “Temporal phase conjugation based on time-domain holography,” *Optics Letters*, **40**, 127–130 (2015).
- [9] M. R. Fernández-Ruiz, L. Lei, M. Rochette, and J. Azaña, “All-optical wavelength conversion based on time-domain holography,” *Optics Express*, **23**, 22 847–22 856 (2015).
- [10] M. R. Fernández-Ruiz, J. Huh, and J. Azaña, “Time-domain Vander-Lugt filters for in-fiber complex (amplitude and phase) optical pulse shaping,” *Optics Letters*, in preparation.
- [11] M. R. Fernández-Ruiz, A. Carballar, and J. Azaña, “Design of ultrafast all-optical signal-processing devices based on fiber Bragg gratings in transmission,” *Journal of Lightwave Technology*, **31**, 1593–1600 (2013).
- [12] M. R. Fernández-Ruiz, J. Azaña, and A. Carballar, “Ultrafast all-optical Nth-order differentiators based on transmission fiber Bragg gratings,” in *IEEE Photonics Conference (IPC), WCC3*, pp. 656–657 (2012).
- [13] M. R. Fernández-Ruiz, M. Li, M. Dastmalchi, A. Carballar, S. LaRochelle, and J. Azaña, “Picosecond optical signal processing based on transmissive fiber Bragg gratings,” *Optics Letters*, **38**, 1247–1249 (2013).
- [14] M. R. Fernández-Ruiz, A. Carballar, and J. Azaña, “Arbitrary time-limited optical pulse processors based on transmission fiber Bragg gratings,” *IEEE Photonics Technology Letters*, **26**, 1754–1757 (2014).
- [15] M. R. Fernández-Ruiz, L. Wang, A. Carballar, M. Burla, J. Azaña, and S. LaRochelle, “THz-bandwidth photonic Hilbert transformers based on fiber Bragg gratings in transmission,” *Optics Letters*, **40**, 41–44 (2015).
- [16] B. R. Brown and A. W. Lohmann, “Complex spatial filtering with binary masks,” *Applied Optics*, **5**, 967-969 (1966).

- [17] A. B. Vander Lugt, "Signal detection by complex spatial filtering," *IEEE Transactions Information Theory*, **10**, 139-145 (1964).
- [18] B. E. A. Saleh, and M. C. Teich, *Fundamentals of Photonics*, John Wiley & Sons, Inc. (1991).
- [19] B. H. Kolner, "Space-time duality and the theory of temporal imaging," *IEEE Journal of Quantum Electronics*, **30**, 1951-1963 (1994).
- [20] G. S. He, "Optical phase conjugation: principles, techniques and applications," *Progress on Quantum Electronics*, **26**, 131-191 (2002).
- [21] Y. Park, F. Li and J. Azaña, "Characterization and optimization of optical pulse differentiation using spectral interferometry," *IEEE Photonics Technology Letters*, **18**, 1798-1800 (2006).
- [22] K. Hinton, "Dispersion compensation using apodized Bragg fiber gratings in transmission," *Journal of Lightwave Technology*, **16**, 2336-2347 (1998).
- [23] L. Poladian, "Group-delay reconstruction for fiber Bragg gratings in reflection and transmission," *Optics Letters*, **22**, 1571-1573 (1997).
- [24] R. Feced, M. N. Zervas, and M. A. Muriel, "An efficient inverse scattering algorithm for the design of non uniform fiber Bragg gratings," *IEEE Journal of Quantum Electronics*, **35**, 1105-1115 (1999).
- [25] A. Ozcan, M. J. F. Digonnet, and G. S. Kino, "Characterization of fiber Bragg gratings using spectral interferometry based on minimum-phase functions," *Journal of Lightwave Technology*, **24**, 1739-1757 (2006).

# Contents

<b>Acknowledgements</b>	<b>v</b>
<b>Abstract</b>	<b>vii</b>
<b>Résumé</b>	<b>xi</b>
<b>Contents</b>	<b>xxxvii</b>
<b>List of Figures</b>	<b>xli</b>
<b>Abbreviations</b>	<b>xlix</b>
<b>1 Introduction</b>	<b>1</b>
1.1 Optical signal processing for coherent systems . . . . .	1
1.2 Nonlinear optical signal processing . . . . .	5
1.3 Linear optical signal processing . . . . .	8
1.3.1 Space-time duality . . . . .	11
1.3.2 Fiber grating structures . . . . .	14
1.3.2.1 Fiber Bragg gratings (FBG) . . . . .	16
1.3.2.2 Long period gratings (LPG) . . . . .	18
1.4 Optical pulse shaping . . . . .	20
1.4.1 Nonlinear optical pulse shaping . . . . .	20
1.4.2 Linear optical pulse shaping . . . . .	21
<b>2 Motivation and organization of the Thesis</b>	<b>27</b>
2.1 General motivation . . . . .	27
2.2 Original contributions . . . . .	29
2.3 Thesis organization . . . . .	31
<b>3 Review of classical space-domain holography</b>	<b>33</b>
3.1 Introduction to space-domain holography . . . . .	33
3.2 Mathematical formalism of space-domain holography . . . . .	34
3.3 Computer-generated holograms . . . . .	38
3.4 Vander-Lugt filters . . . . .	39
3.5 Conclusions . . . . .	42
<b>4 Time-domain signal processing based on holographic concepts</b>	<b>43</b>
4.1 Introduction to time-domain holography . . . . .	43
4.2 Mathematical formalism of time-domain holography . . . . .	44
4.3 Electro-optical approach . . . . .	47

4.3.1	Computer-generated temporal holograms . . . . .	49
4.4	All-optical approach . . . . .	50
4.5	Applications of time-domain holography . . . . .	53
4.5.1	Generation and detection of complex-envelope optical signals . . . . .	53
4.5.1.1	Arbitrary chirped Gaussian pulses . . . . .	55
4.5.1.2	16-QAM modulated data stream . . . . .	57
4.5.2	Temporal phase conjugation . . . . .	59
4.5.2.1	Arbitrary chirped Gaussian pulses . . . . .	61
4.5.2.2	16-QAM modulated data stream . . . . .	62
4.5.3	Wavelength conversion of complex-envelope optical signals . . . . .	64
4.6	Conclusions . . . . .	71
<b>5</b>	<b>Spectral-domain signal processing based on holographic concepts</b>	<b>73</b>
5.1	Introduction to spectral domain holography . . . . .	73
5.2	Mathematical formalism of spectral domain holography . . . . .	75
5.3	Electro-optical approach: time-domain Vander-Lugt filters . . . . .	78
5.3.1	Application of time-domain Vander-Lugt filters as pulse shapers . . . . .	84
5.4	Spectral-domain holography for the design of arbitrary optical filters based on minimum-phase structures . . . . .	88
5.4.1	Increasing the operation bandwidth of fiber Bragg gratings . . . . .	90
5.4.2	Applications of ultra-broadband transmissive FBGs as MP processors . . . . .	92
5.4.2.1	Arbitrary order optical differentiators . . . . .	92
5.4.2.2	Ultra-fast flat-top (rectangular) pulse shapers . . . . .	98
5.4.3	Spectral-domain holography for the design of non-MP optical filters on transmissive FBGs . . . . .	101
5.4.4	Applications of ultra-broadband transmissive FBGs as non-MP processors . . . . .	105
5.4.4.1	Ultrafast photonic Hilbert transformers . . . . .	105
5.5	Conclusions . . . . .	111
<b>6</b>	<b>Conclusions</b>	<b>113</b>
6.1	Conclusions of the Thesis . . . . .	113
6.2	Future perspectives . . . . .	117
	<b>References</b>	<b>121</b>
<b>A</b>	<b>Auxiliary mathematical demonstrations for the analysis of time-domain Vander-Lugt filters</b>	<b>137</b>
A.1	Time-domain Vander-Lugt filter using a simple spectral hologram . . . . .	138
A.2	Time-domain Vander-Lugt filter using a prechirped spectral hologram . . . . .	139
<b>B</b>	<b>Design of arbitrary filters based on fiber Bragg gratings</b>	<b>143</b>
B.1	Analysis of fiber Bragg gratings . . . . .	144
B.1.1	Coupled-mode theory (CMT) . . . . .	145
B.1.2	Multi-layer based on transfer-matrix method (ML-TMM) . . . . .	149
B.2	Synthesis of fiber Bragg gratings . . . . .	151
B.2.1	Coupled-mode theory (CMT) . . . . .	151
B.2.2	Multi-layer based on transfer-matrix method (ML-TMM) . . . . .	152
B.3	Discussion on the applicability of CMT and ML techniques and conclusions . . . . .	154

<b>C</b>	<b>Associated publications</b>	<b>157</b>
C.1	Journal articles . . . . .	157
C.2	International conference papers . . . . .	158
C.3	Book chapters . . . . .	159
C.4	Other publications not directly related with the Thesis . . . . .	159
C.4.1	Journal articles . . . . .	159
C.4.2	Conference papers . . . . .	159



# List of Figures

Fig. 1.1	Scheme of the expected growth in the number of devices connected to the Internet network by 2020. The number of connected devices will exceed 50 million by then. IoT: Internet of Things. Figure reproduced from Ref. [2]. . . . .	2
Fig. 1.2	Schematic of space domain (a) and time domain (b) optical signal processing. In space domain processing, information is encoded in the spatial distribution of light, which propagates in free space. In the time domain, information is encoded in temporal variations, and light typically propagates through a guiding medium, such as an optical fiber or waveguide. This Figure illustrates an example of intensity modulation of light in spatial domain (a) using a spatial light modulator (SML), and in time domain (b) using an intensity temporal modulator (IM). . . . .	4
Fig. 1.3	Example of the evolution of the spectrum of three input optical signals (centered at different carrier wavelengths) in their propagation along a HNLF (1 km-long). New frequency components are generated due to the effect of $\chi^{(3)}$ . The simulation has been carried out solving the nonlinear Schrödinger equation by using the split-step Fourier method [19]. . . . .	7
Fig. 1.4	Procedures for implementing time-domain optical linear filters: (a) inspired in spatial-domain filters, such as the one in the inset, and implemented for time-domain processing following the space-time duality, and (b) based on discrete components, e.g., ring resonators or fiber gratings. The system in (a) is time-variant, but when assuming synchronization between the modulating electrical signal and the modulated optical input, it can be considered as an optical filter. . . . .	10
Fig. 1.5	Schematic illustrating the angles of propagation of a traveling plane wave with wavevector $\vec{k}$ . . . . .	12
Fig. 1.6	Schematic diagram of the duality between spatial paraxial diffraction and first-order temporal dispersion: (a) Propagation of a plane wave through a rectangular aperture in free space. For simplicity, the problem has been reduced to the $x$ -axis in the illustration. The same behavior would be observed in the $y$ -axis. (b) Propagation of a temporal rectangular pulse through a first-order dispersion medium. . . . .	12
Fig. 1.7	(a) Conventional space lens; (b) Time lens implemented with a phase modulator driven by a quadratic voltage. . . . .	14
Fig. 1.8	Schematic of the sinusoidal perturbation at the core of an optical fiber, creating a fiber grating. The lower figure depicts light coupling to a counter-propagating mode. . . . .	15

Fig. 1.9	Schematic diagram of a fiber Bragg grating (FBG), indicating two operation possibilities: the reflection mode and the transmission mode. $\omega_0$ is the Bragg angular frequency, $\omega_0 = 2\pi c_0/\lambda_0$ . . . . .	17
Fig. 1.10	Schematic diagram of a long-period fiber grating (LPG), indicating two operation possibilities, the core-to-core mode and the core-to-cladding mode. In the figure, coupling to a higher-order cladding mode (LP <sub>05</sub> ) is assumed. . . . .	19
Fig. 1.11	Schematic of a spatial-domain filter for time-domain optical pulse shaping. The optical pulses are pre- and post- converted to the spatial-domain by means of diffraction gratings. . . . .	22
Fig. 1.12	Schematic design of a single unit-cell lattice filter, at the top of the figure, and example of an $N$ -unit cell filter, at the bottom. Figure reproduced from Ref. [134]. . . . .	24
Fig. 1.13	(a) Conceptual diagram of the pulse shaping technique based on the concept of temporal coherence synthesization; (b) Examples of synthesized temporal waveforms: flat-top, parabolic, triangular and trapezoidal pulse; (c) Schematic of a single stage of the multi-stage interferometric setup for pulse shaping based on this concept. B: 50:50 beam splitter; M: Mirror. Figure reproduced from Ref. [52] . . . . .	25
Fig. 3.1	(a) Signal recording step and (b) signal retrieval step in classical holography. The figure represents the geometry proposed by Leith and Upatnieks, from which the information signal and its conjugate appear angularly separated from the reference and ambiguity components. . . . .	36
Fig. 3.2	Spectral content of (a) information signal $e_S(x, y)$ , (b) hologram, and (c) hologram considering that $i_{LO} \gg  e_S(x, y) ^2$ . . . . .	37
Fig. 3.3	The hologram can be created by computationally modeling the interference pattern between an object and a reference plane wave, and transferring the result to a transparency. . . . .	38
Fig. 3.4	Spatial filtering process. The first lens generates the Fourier transform of the object wave; in the Fourier plane (at twice the focal length $f_l$ of the lens), an amplitude or phase mask modulates the traveling wave; finally a second lens in the same configuration at the previous one generates the Fourier transform of the modulated wave. The total system performs the operation of convolution. For simplicity, the coordinates in all the planes have been labeled as $(x, y)$ . . .	41
Fig. 3.5	Vander-Lugt filter: (a) Recording of the hologram, which contains information on the amplitude and phase of the complex-valued filter transfer function and (b) signal filtering process based on the concatenation of two Fourier-transforming systems and placing the hologram in the Fourier plane. . . . .	42
Fig. 4.1	Implementation of the concept of time-domain holography as the temporal counterpart of spatial-domain holography. (a) Generation of the temporal hologram; (b) Retrieval of the complex information signal. For the sake of simplicity, the optical temporal signals are represented by their amplitude envelope. OC, optical coupler; PD, photodetector; MZM, Mach-Zehnder modulator. . .	48

Fig. 4.2	The temporal hologram can be created by computationally modeling the interference pattern between the information signal and a reference CW signal, and generating this interference pattern via an arbitrary waveform generator (AWG). . . . .	50
Fig. 4.3	(a) Scheme for performing time-domain holography based on XPM. In this case, both the recording and the retrieving processes are concatenated; (b) Spectra before and after the highly nonlinear fiber (HNLF): Blue components represent the information signal, the yellow component represents the conjugated signal and the dashed grey component represents the conjugated signal resulting from four wave mixing (FWM) between the pump's components. . . . .	52
Fig. 4.4	Setup used to generate optical complex-envelope optical signals based on the concept of CGTH, i.e, using a single MZM and a BPF. The figure also shows the signal in time (black) and frequency (blue) along the setup. The optical path is represented by black lines, whereas the electrical path is represented by red lines. AWG, arbitrary waveform generator; CW, continuous wave; MZM, Mach-Zehnder modulator; EDFA, Erbium-doped fiber amplifier; BPF, band pass filter; PD, photodetector; OSC, real-time oscilloscope. . . . .	55
Fig. 4.5	16-symbol sequence of arbitrary chirped Gaussian pulses. (a) Power spectral density (PSD) of the optical signal after the intensity modulation; (b) PSD of the optical signal after the band pass filtering; (c) Electrical signal $i_H(t)$ generated by the AWG; (d) Intensity of the generated waveform (solid blue line) and target intensity (dashed red line); (e) Phase of the generated complex-envelope waveform (solid blue line), obtained by applying off-line digital signal processing to the electrical interferogram measured in the detection process, and target phase profile (dashed red line). . . . .	56
Fig. 4.6	1024-symbol 16-QAM optical data stream. (a) A portion of the numerically designed temporal hologram, shown over 16 consecutive symbols, as generated by the electrical AWG; (b) Intensity and (c) phase profiles of the generated complex-envelope optical signal (solid blue line) and target data stream (dashed red line) over the signal portion (16 symbols) shown in (a); (d) Constellation of the generated data stream (blue points) and ideal constellation of a 16-QAM signal. . . . .	58
Fig. 4.7	Scheme to perform TPC based on time-domain holography. The scheme comprises the concatenation of the detection and reconstruction steps of holography, in this case using two different reference signals in each step. . . . .	60
Fig. 4.8	Power spectral density of (a) the real optical signal after the modulation process; (b) the complex-envelope optical signal after the BPF. The spectrum of the input signal $e_S(t)$ is nearly coincident with (b). . . . .	61

Fig. 4.9	TPC of a 16-symbol sequence of arbitrary chirped Gaussian pulses. (a) Temporal hologram of the input signal after the detection process; (b) Detected intensity of the conjugated signal after modulation and band-pass filtering (solid orange line), compared with the intensity profile of the input signal (dashed red line); (c) Detected phase of the conjugated signal after modulation and band-pass filtering (solid orange line) and phase of the input signal (dashed red line), and (d) Comparison between the detected output phase (solid orange line) and the phase of the ideally conjugated input (dashed purple line). . . . .	62
Fig. 4.10	TPC of a 1024-symbol 16-QAM optical data stream. (a) Temporal hologram of the input signal; (b) Detected intensity of the conjugated signal; (c) Detected phase of the conjugated signal (orange line); (d) Comparison between the detected phase (orange line) and phase of the ideally conjugated input (dashed purple line), and (e) Output constellation (purple circles represent the symbol's ideal positions). . . . .	63
Fig. 4.11	Scheme of the central frequency of the signals involved in the wavelength conversion process and nomenclature given to the spectral separation between signals to develop the equations of phase-matching condition (Eqs. 4.12 and 4.13). . . . .	66
Fig. 4.12	Results from the numerical simulation of the proposed scheme (no phase-matching) (a) Spectrum at the output of the HNLF; dashed red line represents the applied numerical BPF (b) Resulting temporal waveform after the BPF (green line); transform-limited input before propagation through the SMF (red line); input chirped signal to be conjugated (blue line); wavelength-converted output after compensating the dispersion from the SMF (black line). . . . .	68
Fig. 4.13	Results from the numerical simulation of the proposed scheme (a) Spectrum at the output of the HNLF; dashed red line represents the applied numerical BPF. (b) Resulting temporal waveform after the BPF (green line); transform-limited input before propagation through the SMF (red line); input chirped signal to be conjugated (blue line); wavelength-converted output after compensating the dispersion from the SMF (black line). . . . .	69
Fig. 4.14	Experimental setup of the XPM-based wavelength converted scheme for complex-envelope optical signals. AMLL: Active mode-locked laser; PC: Polarization controller; CWL: Continuous-wave laser; EDFA: Erbium-doped fiber amplifier. OSO: Optical sampling oscilloscope. . . . .	69
Fig. 4.15	(a) Down-conversion of $e_S(t)$ ; (b) Up-conversion of $e_S(t)$ ; (c) Down-conversion of $e_S^*(t)$ ; a-c (1) Spectrum after HNLF; a,b (2) Temporal signal after BPF (green line) vs input signal (dashed blue line); c (2) includes output from AMLL (red line) and signal after dispersion compensation (black line). . . . .	70
Fig. 4.16	Conversion efficiency of the XPM-based wavelength converter scheme as a function of the wavelength shift $\Delta\lambda$ , for the cases of down-conversion (solid blue line) and up-conversion (dashed black line). . . . .	71

Fig. 5.1	(a) Temporal width of the output signal resulting from convolving the input signal to be processed with the impulse response of the spectral hologram; (b) Temporal width of the output signal if the terms proportional to the intensity of the target impulse response and reference signal are not considered in the generation of the spectral hologram. . . . .	77
Fig. 5.2	(a) Spatial domain spectral shaping setup, and (b) time-domain spectral shaping (TDSS) setup. $f_l$ is the focal length of the lenses. . . . .	79
Fig. 5.3	Schematic of operation of the TDSS system. Vander-Lugt filters are based on this configuration, but using a spectral hologram as the modulating signal. AM: amplitude modulation. . . . .	80
Fig. 5.4	Setup employed for the experimental demonstration of pulse shapers based on time-domain Vander-Lugt filters. The setup includes the time-domain Vander-Lugt filter in the upper arm of an interferometry configuration (inside the green rectangle); the interferometry configuration is employed for characterization of the output shaped signal via Fourier transform spectral interferometry (FTSI). PMLL: passive mode-locked laser; OC: optical coupler; ODL: optical delay line; PC: polarization controller; PBS: polarization beam splitter; LCFBG: linearly-chirped fiber Bragg grating, EDFA: Erbium-doped fiber amplifier; APD: avalanche photodiode; LPF: low pass filter; ATT: attenuator. . . . .	85
Fig. 5.5	Asymmetric triangular pulse with parabolic phase: (a) spectral hologram $H_{hc}(t)$ ; (b) temporal intensity of the output signal; and (c) temporal phase of the output signal: target (dotted blue line) and measured (solid green line) output. The spectral hologram was designed so that the right-hand side of the temporal output (highlighted and marked with a dashed red line) matches the target profile. . . . .	86
Fig. 5.6	4-symbol 16-QAM code: (a) spectral hologram $H_{hc}(t)$ ; (b) temporal amplitude of the output signal, just right-hand side is shown; (c) temporal phase of the output signal: target (dotted blue line) and measured (solid green line) output. . . . .	87
Fig. 5.7	First-order optical differentiator based on an FBG in transmission: (a) Apodization (red solid line) and period (black dashed line) profiles considering realistic spatial resolution (limited to 0.3 mm) and linearly chirped phase mask; (b) Specified transmission spectral response, amplitude (dotted blue line) and phase (dotted green line) compared to fabrication-constrained transmission spectral response, amplitude (solid red line) and phase (solid black line); (c) Ideal transmissivity in dB (dotted blue line) and fabrication-constrained transmissivity in dB (solid red line). . . . .	95
Fig. 5.8	First-order optical differentiator based on an FBG in transmission: Grating apodization profiles and device lengths obtained for different values of the dispersion parameter. . . . .	95

Fig. 5.9	First-order optical differentiator based on an FBG in transmission: (a) Input Gaussian-like pulse (dotted black line) and comparison between the ideal output (dashed blue line) and the numerically obtained output from a differentiator assuming fabrication constrains (red solid line); (b) Cross-correlation coefficient between the ideal and the numerically obtained temporal output waveform as a function of the 3 dB-bandwidth of an input Gaussian pulse for the original design (blue dashed line) and the perturbed design considering potential fabrication errors (red solid line). . . . .	97
Fig. 5.10	$N^{th}$ -order optical differentiators (up to $N = 4$ ) based on FBGs in transmission: (a) Apodization profiles considering realistic spatial resolution (limited to 0.5 mm); (b) Time-domain intensity outputs from practical FBG-based differentiators. . . . .	97
Fig. 5.11	Flat-top pulse shaper based on an FBG in transmission: Obtained grating apodization profile (a) and period (b) from synthesis (blue line) and smooth profiles adapted to fabrication constraints, i.e., spatial resolution $\geq 1$ mm (red line); (c) Input signal spectrum; (d) transmissivity and (e) transmission phase response: ideal (blue line), simulated considering fabrication constraints (red line) and measured from fabricated device (dotted black line). . . . .	99
Fig. 5.12	Flat-top pulse shaper based on an FBG in transmission: Temporal signals from FTSI; ideal input pulse (crossed blue line); experimental input pulse (dotted green line); ideal output pulse (dotted-dashed black line); measured flat-top output pulse (dashed red line); output pulse obtained numerically from the experimental input pulse and the ideal grating response (solid purple line); phase of the measured output pulse (dotted line). . . . .	100
Fig. 5.13	(a) Phasor diagram of $H_{NMP}(\omega')$ ; (b) Phasor diagram of $H_{MP}(\omega')$ , illustrating how its phase varies only between $-\pi/2$ and $\pi/2$ . . . . .	103
Fig. 5.14	PHT based on an FBG in transmission: (a) Reflectivity and (b) Group delay. The dashed black line represents the specified spectral response and the red line represents the spectral response of an FBG-based $\pi$ -phase shifted Fabry-Perot structure. . . . .	107
Fig. 5.15	PHT based on an FBG in transmission: (a) Simulated transmissivity of the integer PHT to be fabricated (red line) and measured transmissivity of the fabricated device (dashed blue line); (b) Simulated minimum phase (red line) and measured phase in transmission (dashed blue line); (c) Simulated transmissivity for the fractional ( $P = 0.81$ ) PHT to be fabricated (red line) and measured transmissivity of the fabricated device (dashed blue line); (d) Simulated minimum phase (red line) and measured phase in transmission (dashed blue line). . . . .	108

Fig. 5.16	PHT based on an FBG in transmission: Measured Hilbert-transformed output component of the fabricated integer (a) and fractional (b) PHTs (blue line) for the measured Gaussian-like input pulses with a FWHM of (1) 0.88 ps; (2) 1.18 ps and (3) 2 ps. The corresponding simulated output of an ideal integer PHT and a 0.81-order fractional PHT (dotted-dashed pink line) are also represented for comparative purposes. The insets show the corresponding (simulated and measured) temporal output phases. The dashed green lines show the simulated output from the fabricated FBG (using the measured spectral responses in Fig. 5.15) assuming an ideal Gaussian input. . . . .	109
Fig. 5.17	PHT based on an FBG in transmission: Cross-correlation coefficient between the output of the measured PHT and an ideal PHT vs. the temporal FWHM (or 3dB bandwidth) of an input Gaussian pulse; (a) integer PHT; and (b) fractional PHT. The position of the input pulses in the temporal characterization is marked by a blue cross. . . . .	110
Fig. 5.18	PHT based on an FBG in transmission: Amplitude (blue line) and phase (dashed purple line) of the spectrum of the isolated Hilbert transformed pulse at the output of the integer PHT. Orange line shows the input pulse: (a) Integer PHT; and (b) 0.81-order fractional PHT. . . . .	111
Fig. B.1	Nomenclature for the optical waveforms at the two extremes of an FBG of length $L$ . . . . .	146
Fig. B.2	Schematic of the division into layers of a non-uniform FBG for its analysis using CMT. The complete grating structure is divided into layers containing few periods, and each layer is treated as a uniform FBG. The analysis of the complete structure is done based on TMM. The propagating waves' dependence with the angular frequency has been omitted in the figure for simplicity. . . .	148
Fig. B.3	Schematic for division into layers of a non-uniform FBG for its analysis using ML-TMM. The complete grating structure is divided into layers with a length at least one order of magnitude shorter than the minimum value of the period, and each layer is treated as medium of constant refractive index. The analysis of the complete structure is done based on TMM. The optical waves' dependence with the angular frequency has been omitted in the figure for simplicity. . . .	149
Fig. B.4	Schematic of the two elements that compose the whole grating structure for its analysis following ML-TMM. . . . .	150
Fig. B.5	(a) Layout of the division of the FBG in layers and the contribution to the total sampled impulse response; (b) The calculation of the refractive index of each layer is obtained from the non-recursive component of the impulse response in this layer. To this purpose, the total sampled impulse response is decomposed into the recursive component and the non-recursive component, where the total impulse response and its non-recursive component are known. . . . .	153



# Abbreviations

A/D	Analog-to-digital
AMLL	Active mode-locked laser
AWG	Arbitrary waveform generator
BPF	Band pass filter
CGH	Computer-generated hologram
CGTH	Computer-generated temporal hologram
CMT	Coupled-mode theory
CW	Continuous wave
D/A	Digital-to-analog
DSP	Digital signal processing
EO	Electro-optics
EVM	Error vector magnitude
FBG	Fiber Bragg grating
FTSI	Fourier transform spectral interferometry
FWHM	Full-width at half maximum
FWM	Four-wave mixing
HNLF	Highly nonlinear fiber
IoT	Internet of Things
IQ	In-phase and quadrature
LC	Linearly chirped
LHS	Left hand side
LPF	Low pass filter
LPG	Long period grating

LTI	Linear and time invariant
ML	Multi-layer
MP	Minimum phase
MSSI	Mid-span spectral inversion
MZM	Mach-Zehnder modulator
OC	Optical coupler
OE	Opto-electronics
OFC	Optical frequency comb
OFDM	Orthogonal frequency division multiplexing
OOK	On-off keying
OPO	Optical parametric oscillator
OSA	Optical spectrum analyzer
OTDM	Optical time division multiplexing
OVA	Optical vector analyzer
PBS	Polarization beam splitter
PC	Polarization controller
PD	Photodetector
PHT	Photonic Hilbert transformer
PIC	Photonic integrated chip
PMLL	Passive mode-locked laser
PSD	Power spectral density
QAM	Quadrature amplitude modulation
RF	Radio frequency
RHS	Right hand side
SBS	Stimulated Brillouin scattering
SLM	Spatial light modulator
SMF	Single-mode fiber
SOA	Semiconductor optical amplifier
SPM	Self-phase modulation

SRS	Stimulated Raman scattering
SSB	Single sideband
TBP	Time-bandwidth product
TDSS	Time-domain spectral shaping
TMM	Transfer-matrix method
TPC	Temporal phase conjugation
UV	Ultraviolet light
UWB	Ultra-wide band
WDM	Wavelength division multiplexing
XPM	Cross-phase modulation
ZDW	Zero dispersion wavelength



# Chapter 1

## Introduction

### 1.1 Optical signal processing for coherent systems

The technological advances of the last decades have completely changed our way of perceiving the world. We are continuously surrounded by technology, e.g. when watching TV, reading the news through an electronic device, sharing data online, etc. Technology improves our lives, not only by enabling an easier, faster way of communicating with our peers, but also in many different areas, such as in medicine, agriculture, environmental studies or astrophysics, to name just a few. Within this frame, signal processing is a powerful enabler technology that has played a key role in reaching the current degree of technological maturity.

Considerable research has allowed a fast development of electronic-based analog and digital signal processing systems. However, the available processing capacity and speed of electronic systems is not enough to cope with current demands, particularly in the area of communications. Telecommunication networks need an ever-increasing bandwidth for networking applications such as data and video sharing, cloud computing, or data collection systems. It is estimated that the Internet traffic is growing by 40 percent annually [1]. This increase is not solely due to the information shared by people using cell phones, tablets or computers. Nowadays, countless devices embedded with sensors can connect and communicate their state via the Internet, e.g, toothbrushes, stovetops and millions of other devices that now have IP addresses. This situation has led to a new concept, the *Internet of things* (IoT), which is aimed to extend the benefits of the Internet access, i.e., con-

stant connectivity, remote control ability, data sharing, and so on, to goods in the physical world. Today, there are more connected devices than there are human beings on the planet. Estimates show that there will be over 50 billion connected devices by 2020 (Fig. 1.1) [2].

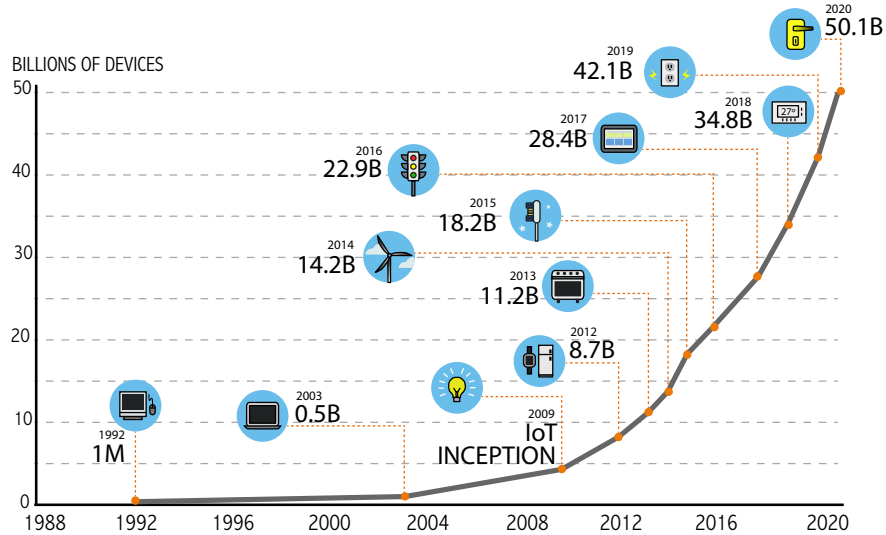


**Figure 1.1 – Scheme of the expected growth in the number of devices connected to the Internet network by 2020. The number of connected devices will exceed 50 million by then. IoT: Internet of Things. Figure reproduced from Ref. [2].**

To meet this increasing demand, technologies able to provide higher network capacity and processing speeds in a sustainable, energy efficient fashion are fundamental. Optics communications have proven to be a good solution to increase the data transmission rate and speed of communications systems. Recent progress in the development of new optical fibers, together with the use of signal multiplexing techniques, have enabled transmissions that reach the record of 255 Tbps on a multicore core fiber through 1 km of fiber [3]. However, the bandwidth per channel in wavelength division multiplexing (WDM) systems is still limited to 40 GHz in commercial systems due to the speed of electronic components employed for processing of information signals at the transmitter and receiver of communication network links.

The transmission-capacity increase achieved by WDM systems relaunched the interest in coherent technologies over recent years. The motivation lies in increasing the spectral efficiency and making better use of the capacity of currently existing fiber infrastructure by using multi-level complex modulation formats. While the spectral efficiency of binary modulation formats, e.g., on-off keying (OOK), is limited to 1 bit/s/Hz/polarization -which is called the Nyquist limit-, modulation formats with  $M$  bits of information per symbol can achieve a spectral efficiency up to  $M$  bit/s/Hz/polarization [4]. Also, the use of phase information extends the symbol distance on

the constellation diagram or IQ (in-phase vs. quadrature) plane, what leads to a longer unrepeated transmission distance. Another important advantage of coherent communications is the post-signal-processing capabilities available at the coherent receiver. All the information on the complex amplitude of the transmitted optical signal is recovered after detection, and signal-processing functions acting on the optical carrier, such as filtering, chromatic dispersion compensation and polarization-mode dispersion compensation, can be performed by customized electrical digital signal processing (DSP) circuits after detection [4].

The combination of WDM and coherent systems imposes the need for opto-electronic (OE) signal conversion circuits, individually set and operated for each different wavelength channel and the management of the amplitude and phase (or the in-phase and quadrature components) of the electromagnetic signal in an independent fashion. In general, the synthesis of high-order complex (amplitude and phase) modulation formats requires the use of two properly synchronized electro-optic (EO) modulation sub-systems (IQ modulators) [5], balanced arms with controlled phase lags [6], or schemes that require a number of perfectly identical devices for a good performance<sup>1</sup> [7, 8]. Therefore, the evolution to higher spectral efficient channels entails an impractical increase of circuitry complexity and power consumption. Furthermore, the use of individual circuits for each wavelength may lead to an asymmetric processing of the different channels.

All-optical signal processing arises as a promising solution to help electronics deliver high data capacities, reducing OE-EO conversions and taking advantage of the high bandwidth intrinsic to optics. It is based on the premise of exploiting the capabilities of switching speed and parallelism offered by light to process the information at a high data rate. Moreover, the development of higher-capacity systems for ultrafast processing of complex-envelope (amplitude and phase) optical signals provides a platform for the development of new applications, e.g., those ones requiring the analysis of huge dataset, such as geophysical data processing, drug discovery or environment and climate modeling [9]. One promising approach to implement optical signal processors involves using design strategies similar to the ones used for the implementation of current electronic signal processors. Hence, photonic counterparts of fundamental devices that form “basic building blocks” in electronic circuits have been designed and realized. Some examples of these building blocks are: wavelength converters, optical multiplexers/demultiplexers, optical differentiators/integrators, optical systems

---

<sup>1</sup>For example, a quad-parallel Mach-Zehnder optical modulator (QPMZM) is a device that generates 16-QAM-modulated signals. It requires four EO phase modulators and three  $\pi/2$  phase shifters.

performing multicasting, equalization, correlation, digital-to-analog (D/A) and analog-to-digital (A/D) conversion, optical logic gates, all-optical tunable delays or optical clock recovery, among others [10, 11].

The concept of *optical signal processing* encompasses a number of operations on the information encoded in a traveling light wave. This concept has been traditionally classified into two main categories, depending on whether the information is encoded in the spatial distribution of light (typically propagating in free space) or in its temporal variation. Thus, we can talk about spatial domain or temporal domain signal processing. Historically, the study and evolution of optics have been mainly focused on the spatial nature of light, and therefore, classical optics have greatly contributed to the development of the spatial-domain optical signal processing [12, 13] (see Fig. 1.2(a)). The invention of the laser, together with the emergence of low loss optical fibers and semiconductor optical devices have contributed to the upswing of temporal optical signal processing [12]. Nowadays, telecommunication systems mainly use time-domain signals and as such, they are the main focus of interest in this Thesis.

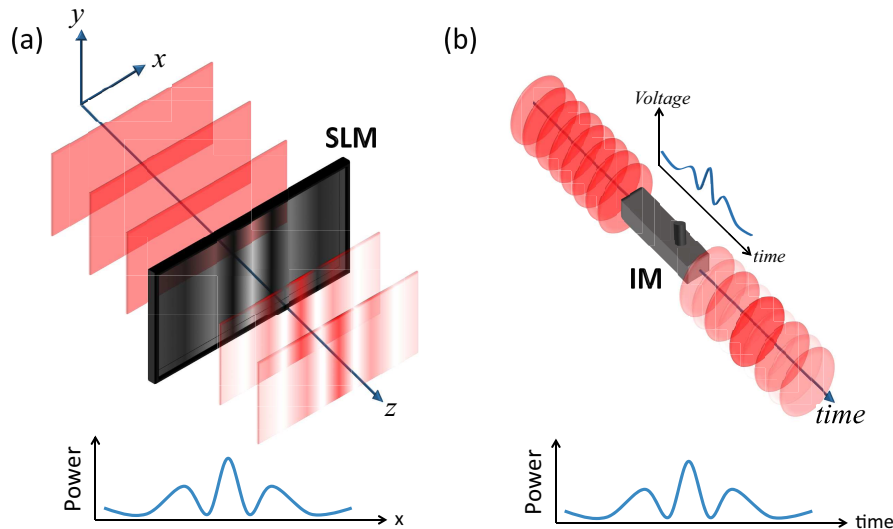


**Figure 1.2** – Schematic of space domain (a) and time domain (b) optical signal processing. In space domain processing, information is encoded in the spatial distribution of light, which propagates in free space. In the time domain, information is encoded in temporal variations, and light typically propagates through a guiding medium, such as an optical fiber or waveguide. This Figure illustrates an example of intensity modulation of light in spatial domain (a) using a spatial light modulator (SML), and in time domain (b) using an intensity temporal modulator (IM).

Temporal optical signal processors can be broadly categorized into nonlinear or linear processors, depending on whether they make use of optical nonlinear effects to perform their operation.

Nonlinear optics describes the behavior of light when propagating in a nonlinear medium, i.e., a medium in which the polarization density  $\vec{P}$  responds nonlinearly to the electric field  $\vec{E}$ . This nonlinear dependence is typically observed in optical fibers when the intensity of the propagating field is very high. Within the context of optical signal processing, nonlinear effects are mainly employed for the realization of *all-optical* processors implementing functionalities that require one or several optical beams to interact with each other; for example, the modulation of an optical signal using another optical beam, or all-optical demultiplexing and sampling [14, 15]. On the other hand, we refer to optical linear processors as those ones that use discrete components to perform the target functionality in such a way that the system satisfies the principle of superposition [16].

A fundamental review of both nonlinear and linear signal processors is presented in the following Sections. Finally, we conclude this introductory Chapter with an outline of the state-of-the-art of a particularly interesting application of optical signal processing of high relevance for this dissertation, namely, optical pulse shaping.

## 1.2 Nonlinear optical signal processing

The development of ultrafast pulsed lasers made the generation of picosecond and femtosecond optical pulses readily feasible [17]. For many applications requiring optical pulses in the (sub)picosecond regime, as optical metrology, advanced microscopy, image processing, or optical computing, techniques based on EO processing are not suitable due to the operation bandwidth limitations imposed by electronics [18]. Nonlinear optical signal-processing devices enable all-optical operations at ultrahigh speeds, i.e. down to the femtosecond regime [19]. Although further progress in nonlinear signal processing needs to be achieved for practical viability, recent advances in quasi-phase matched materials, semiconductor optical amplifiers, photonic crystal media and highly nonlinear fibers have enabled more efficient nonlinear signal processing with relatively lower powers and small device sizes [20].

When a sufficiently high power optical signal propagates through a dielectric medium, the optical properties of this one, e.g., the refractive index and the absorption coefficient, exhibit a dependence on the intensity of the propagating wave. As a consequence, new frequency components can be

generated as light propagates along the medium, and also photons can interact to each other through the matter [12].

In this Section, we focus on nonlinear effects that occur in centrosymmetric (with a center of symmetry) media such as the silica glass ( $\text{SiO}_2$ ), as those are the nonlinear effects that appear in optical fibers and, as such, they can be readily employed to implement in-fiber all-optical signal processors. The nonlinear effects in centrosymmetric media, also called *Kerr media*, are governed by the third term in the Taylor expansion of the polarization density  $\vec{P}$  with respect to the optical field  $\vec{E}$  [19].

$$\begin{aligned}\vec{P} &= \varepsilon_0[\chi^{(1)}:\vec{E} + \chi^{(2)}:\vec{E}\vec{E} + \chi^{(3)}:\vec{E}\vec{E}\vec{E} + \dots] \\ &\simeq \varepsilon_0[\chi^{(1)}:\vec{E} + \chi^{(3)}:\vec{E}\vec{E}\vec{E}] = \varepsilon_0\chi^{(1)}:\vec{E} + \vec{P}_{NL},\end{aligned}\tag{1.1}$$

where  $\varepsilon_0$  is the vacuum permittivity,  $\chi^{(p)}$  is the  $p^{\text{th}}$  order susceptibility and  $\vec{P}_{NL}$  is the nonlinear polarization component.

Depending on the number of optical waves (i.e., at different carrier frequencies) that propagate together through a Kerr medium, third harmonics and sums and differences of triplets frequencies, as well as modulation interactions between them can be generated. The most general case involves the study of the effects induced by the propagation of three different input waves. The nonlinear processes that concern the generation of new frequency components must satisfy the frequency matching condition (Eq. 1.2a) and the phase matching condition (Eq. 1.2b):

$$\omega_{out} = \pm\omega_1 \pm \omega_2 \pm \omega_3,\tag{1.2a}$$

$$\beta_{out} = \pm\beta_1 \pm \beta_2 \pm \beta_3,\tag{1.2b}$$

where  $\omega_q$  and  $\beta_q$  are the carrier angular frequency and propagation constant of each optical wave. The dispersion characteristic of optical fibers makes that phase matching between the newly generated frequency components is not easily achieved, limiting the efficiency of nonlinear processes such as third-harmonic generation ( $\omega_1 = \omega_2 = \omega_3$ ,  $\beta_1 = \beta_2 = \beta_3$ ) or four-wave mixing (FWM). Most of the nonlinear effects in optical fibers therefore originate from nonlinear refraction, a phenomenon referring to the dependence of the refractive index to the intensity of the light propagating through the medium. This dependence leads to interesting nonlinear effects; the two most widely studied

are self-phase modulation (SPM) and cross-phase modulation (XPM). Nonlinear refraction involves the spectral spreading of an optical signal due to a phase modulation process. Therefore, the newly generated frequency components do not need to satisfy the phase matching condition [19].

Figure 1.3 shows an illustrative example of propagation of three input signals (two continuous waves (CW) at 1543 nm and 1547 nm, and one train of Gaussian-like pulses at 1539 nm) through a 1 km-long highly nonlinear fiber (HNLF), that is, a specialty fiber with a high nonlinear coefficient<sup>2</sup> and typically small group velocity dispersion. In the example, the parameters of the standard HNLF from OFS [21] are employed. We can observe how new spectral components are generated along the light propagation due to the effect of  $\chi^{(3)}$ . In particular, the spectral broadening of the signal at 1539 nm is attributed to SPM, the spectral broadening of the two CW waves is attributed to XPM induced by signal at 1539 nm (train of pulses), and the components around 1551 nm are attributed to FWM of the three input signals.

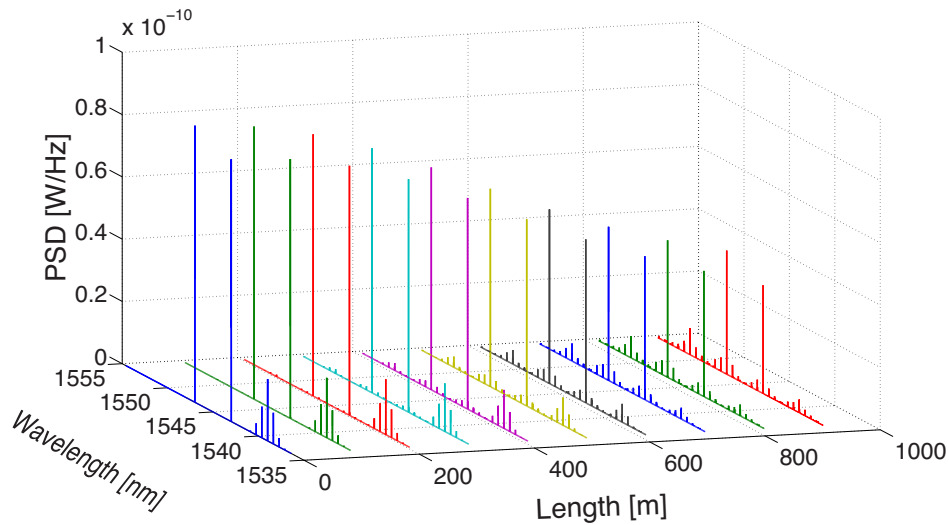


**Figure 1.3 – Example of the evolution of the spectrum of three input optical signals (centered at different carrier wavelengths) in their propagation along a HNLF (1 km-long). New frequency components are generated due to the effect of  $\chi^{(3)}$ . The simulation has been carried out solving the nonlinear Schrödinger equation by using the split-step Fourier method [19].**

For all the above-mentioned nonlinear effects, there is no exchange of energy between the electromagnetic field and the dielectric medium. In another class of observed nonlinear effects, there is a transfer of energy between the optical field and the medium. The most important effects in this category are stimulated Raman scattering (SRS) and stimulated Brillouin scattering (SBS) [19].

<sup>2</sup>The nonlinearity of an optical fiber is more practically expressed using the nonlinear coefficient  $\gamma$ .  $\gamma$  proportional to the real part of  $\chi^{(3)}$  and inversely proportional to the effective area of the fiber.

A vast number of all-optical signal processing operations have been investigated and experimentally demonstrated based on the above-mentioned nonlinear effects. Among the most relevant operations, we can mention wavelength conversion of intensity-only signals based on XPM [14, 22–24] or complex-envelope signals based on FWM [25–30]; optical demultiplexing and sampling for optical time division multiplexing (OTDM) bit streams based on XPM [15, 31] or FWM [32]; optical regeneration based on SPM [33, 34], XPM [35] or FWM [36]; optical performance monitoring [37, 38]; impairments compensation via time or spectral phase conjugation based on FWM [39–42]; and all-optical pulse shaping [18, 43–45].

To date, the high degree of control required on the characteristics of the input signals (e.g., power, central frequency, state of polarization, etc.) involved in a nonlinear processing operation has hindered their application beyond a well-controlled laboratory environment. In general, optical signal processing based on optical nonlinear effects is not energy efficient, and high optical powers are commonly required. An additional drawback of nonlinear techniques is that highly nonlinear fibers or waveguides with customized dispersion profiles are needed for an efficient processing, making the system costly and bulky. Moreover, the implementation of more complex systems relying on the concatenation of two or more nonlinear optical signal processors may notably degrade the information signal. This degradation might be caused by the reduction of the signal-to-noise ratio (associated to the low energy efficiency of these processors and the requirement of amplification stages), and/or by the inclusion of spurious frequency components in the bandwidth of the information signal.

### 1.3 Linear optical signal processing

Linear systems are those that possess the property of superposition. Thus, the output of a linear processor to an input consisting of the weighted sum of several signals is simply the superposition, that is the weighted sum of the response of the processor to each of those signals [16]. Among linear systems, we are particularly interested in those that have the property of time-invariance, as many physical processes possess this property (on the time scale of interest) and they can be analyzed in a far simpler fashion. A system is time-invariant if a time shift in the input signal causes the same time shift in the output signal. Fourier analysis provides a set of powerful tools and insights for

the design and understanding of systems that have the properties of linearity and time-invariance (LTI) [16].

The output of an LTI system can be easily computed by decomposing the input into a linear combination of simpler, basic signals and providing the system's response to each of these basic signals. For example, any input signal can be represented as a set of shifted unit impulses. The response of the system to an input temporal impulse provides the impulse response function  $h(t)$ , with  $t$  being the time variable, which completely characterized the LTI system: knowing the response to this function, the response to any arbitrary input signal can be obtained. Alternatively, the system can be described by the corresponding frequency response (spectral transfer function)  $H(\omega)$ , i.e., the frequency-domain representation of the device's temporal impulse response using a Fourier transformation, where  $\omega$  is the angular frequency variable. An excellent reference on the fundamentals of linear signal processing is Ref. [46]. There is a myriad of interesting optical signal processing functionalities that can be described by an LTI system response, e.g., optical pulse shapers, optical differentiators, integrators, pulse processors such as Fourier or Hilbert transformers or dispersive media, among many others.

Nowadays, two main procedures are employed to implement time-domain linear optical signal processors, usually referred to as optical temporal filters: (i) the development of time-domain analogs of well-known spatial-domain filters, in which the filtering operation is carried out in the time domain via modulation processes (Fig. 1.4(a))<sup>3</sup>, and (ii) the design of temporal filters based on discrete components, e.g. ring resonators, interferometers or fiber gratings, where the filtering operation is carried out by directly shaping the signal's spectrum (Fig. 1.4(b)) [11, 47–55]. In this classification, we have only considered systems that perform the processing operation directly in the time-domain. There exists another kind of optical, temporal signal processors based on bulky, spatial-domain setups that pre- and post- convert the spectral information of the signal to waves with different propagation angles in the spatial-domain for its processing. An example of these signal processors will be provided in Section 1.4.2.

Time-domain equivalents of spatial-domain optical filters have been identified and created owing to the so-called space-time duality [56, 57]. The general space-time duality theory builds upon the

---

<sup>3</sup>These systems are time-variant due to the use of a modulation process. However, assuming synchronization between the modulating and modulated signals and certain restrictions on the temporal duration of the modulating signal, the total scheme acts as an optical filter and can be described by an impulse response over a defined temporal window.

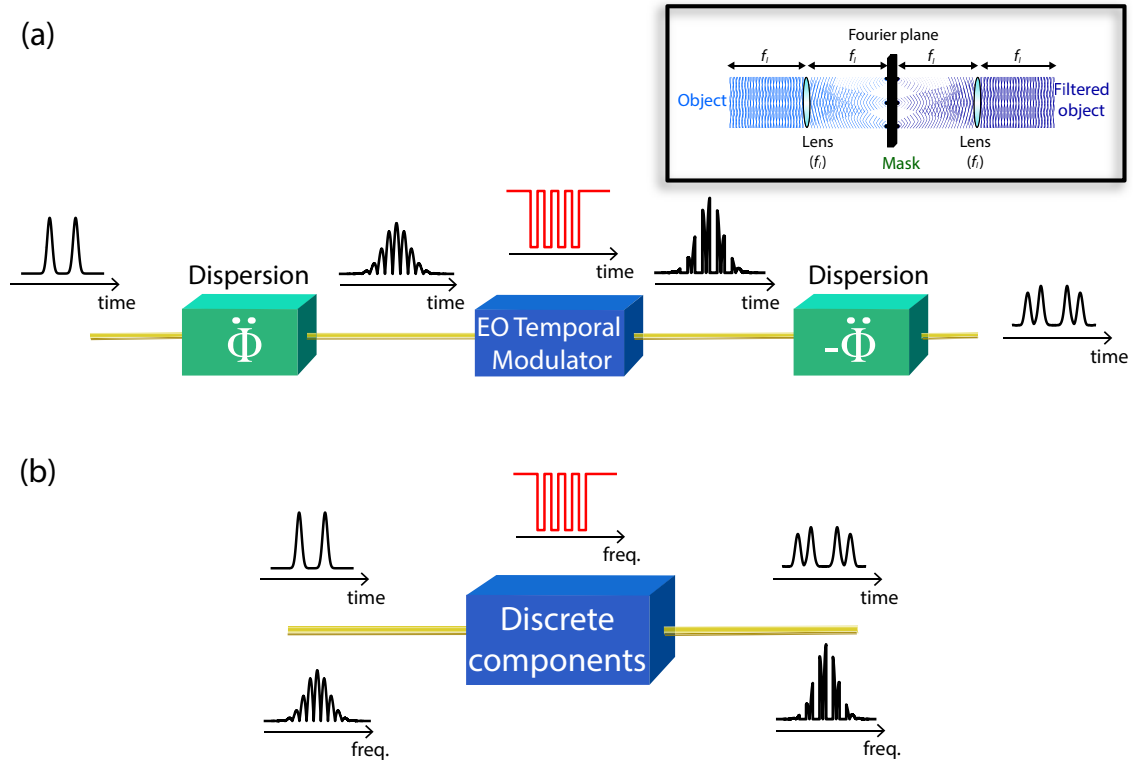


**Figure 1.4 – Procedures for implementing time-domain optical linear filters: (a) inspired in spatial-domain filters, such as the one in the inset, and implemented for time-domain processing following the space-time duality, and (b) based on discrete components, e.g., ring resonators or fiber gratings. The system in (a) is time-variant, but when assuming synchronization between the modulating electrical signal and the modulated optical input, it can be considered as an optical filter.**

mathematical equivalence between the problems of paraxial diffraction and narrow-band dispersion. Thus, a number of signal-processing tools previously developed in spatial optics have been exploited for processing information in the time domain, including the time-lens concept, temporal imaging, self-imaging systems, real-time Fourier transformation and filtering [56–64]. An example of the latter is depicted in Fig. 1.4(a).

On the other hand, discrete components have been widely used to implement optical filters that act directly on the spectral content of the input signal (Fig. 1.4(b)). Among the typically used components, we can mention ring resonators [47–50], interferometers [51, 52] or periodic structures such fiber or waveguide gratings [11, 53–55]. Bragg gratings in fibers are specially interesting components due to their advantages such as low losses, polarization insensitivity, full compatibility with fiber optical systems and the potential for low cost [53, 54].

In the following Sections, we delve deeper into the mathematical fundamentals of the two aforementioned methods for designing and implementing linear optical signal processors. Thus, we first

present the basis of the space-time duality. Then, we introduce the principle of operation of fiber grating structures, namely fiber Bragg gratings (FBG) and long period gratings (LPG). In this Thesis, we focus on FBG structures for the development of ultrafast all-optical linear signal processors' design techniques. It is worth mentioning that the design techniques introduced for these components could be also applied to other periodic structures, such as LPGs or thin-film filters.

### 1.3.1 Space-time duality

Pioneering optical signal processing systems were developed in the spatial domain [13]. The principles of Fourier optics made it possible to describe the propagation of light waves based on harmonic analysis, which led to the development of the first space-domain optical filters and imaging systems. Thus, a myriad of signal processing functionalities were achieved in the spatial domain, such as amplitude or frequency modulators [12], Fourier transformers, imaging (magnification/compression) systems [13], or classical holography [65–67], among others.

The principle of Fourier optics establishes that any arbitrary wave in free space can be analyzed as a superposition of plane waves with different complex amplitudes and propagation directions. The complex amplitude of a plane wave is defined as  $\hat{e}_p(x, y, z) = A \exp\{-j(k_x x + k_y y + k_z z)\}$ , with wavevector  $\vec{k} = (k_x, k_y, k_z)$ , wavelength  $\lambda_0$  (i.e., the light has an angular frequency  $\omega_0 = 2\pi c_0/\lambda_0$ , with  $c_0$  being the speed of light in vacuum), wavenumber  $k = (k_x^2 + k_y^2 + k_z^2)^{1/2} = 2\pi/\lambda_0$  and complex envelope  $A$ . The vector  $\vec{k}$  makes angles  $\theta_x = \sin^{-1}(k_x/k)$  and  $\theta_y = \sin^{-1}(k_y/k)$  with the  $y - z$  and  $x - z$  planes, respectively, as illustrated in the Fig. 1.5. The complex amplitude in the  $z = 0$  plane  $e_p(x, y, 0) = A \exp\{-j2\pi(\nu_x x + \nu_y y)\}$  is a spatial harmonic function with spatial frequencies  $\nu_x = k_x/(2\pi)$  and  $\nu_y = k_y/(2\pi)$  (cycles/m). The angles of the wavevector are therefore related to the spatial frequencies of the harmonic function by [12]

$$\begin{aligned}\theta_x &= \sin^{-1}(\lambda_0 \nu_x) \\ \theta_y &= \sin^{-1}(\lambda_0 \nu_y).\end{aligned}\tag{1.3}$$

In Fourier optics theory (spatial-domain), two hypotheses are typically assumed: (i) the propagating wave is monochromatic, which means that it has a well defined wavelength  $\lambda_0$  or frequency  $\omega_0$ , and (ii) it propagates within the paraxial approximation, that is, its wavefront normals make

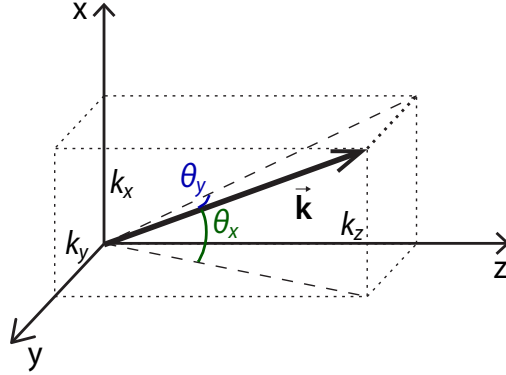


Figure 1.5 – Schematic illustrating the angles of propagation of a traveling plane wave with wavevector  $\vec{k}$ .

small angles with the propagation axis. In the paraxial approximation, Eq. 1.3 can be approximated as  $\theta_x \approx \lambda_0 \nu_x$  and  $\theta_y \approx \lambda_0 \nu_y$ . Under these hypotheses, the propagation of light in free space can be described by the spatial “impulse response”

$$\hat{h}_z(x, y) \propto \exp \left\{ -j \frac{\pi}{\lambda_0 z} (x^2 + y^2) \right\}, \quad (1.4)$$

where  $x$  and  $y$  are the Cartesian coordinates in the plane transverse to the propagation direction.

There exists a well-known analogy between the equations that describe the paraxial diffraction of beams in space and the dispersion of narrow-band pulses in dielectrics [56, 68].

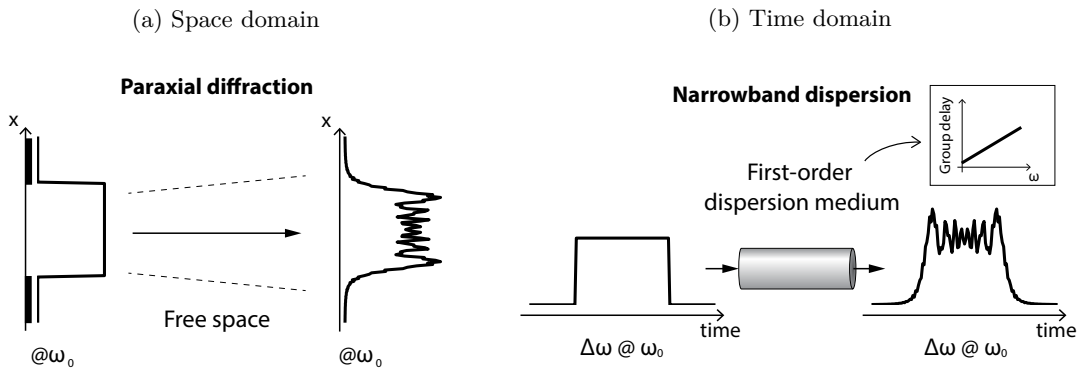


Figure 1.6 – Schematic diagram of the duality between spatial paraxial diffraction and first-order temporal dispersion: (a) Propagation of a plane wave through a rectangular aperture in free space. For simplicity, the problem has been reduced to the  $x$ -axis in the illustration. The same behavior would be observed in the  $y$ -axis. (b) Propagation of a temporal rectangular pulse through a first-order dispersion medium.

In the time domain, two different hypotheses are considered: (i) the spatial profile of the wave is approximated as an infinite plane wave (or the spatial variables are simply not considered), and

(ii) propagation of narrow-band pulses is assumed. The latter implies that the temporal-frequency spectrum is limited to a suitable range, making it possible to describe the propagation of any spectral component by a Taylor-series expansion of the propagation constant  $\beta(\omega)$  [56], with  $\omega$  being the angular frequency variable. A dispersive medium can be modeled as an LTI system with transfer function  $H(\omega) = |H(\omega)| \exp\{j \Phi(\omega)\}$ , with  $\Phi(\omega) = \beta(\omega) \cdot L$  and  $L$  being the fiber length. For the analogy with the spatial domain, let us consider just the two first terms of the Taylor expansion of  $\beta(\omega)$ , leading to  $H(\omega)$  having a flat amplitude and a quadratic phase response (i.e., linear group delay) over a spectral bandwidth  $\Delta\omega$  centered at a pulsation frequency  $\omega_0$ ;

$$\begin{aligned} \Phi(\omega) &\approx \left. \frac{d\beta(\omega)}{d\omega} \right|_{\omega=\omega_0} \cdot (\omega - \omega_0) L + \frac{1}{2} \left. \frac{d^2\beta(\omega)}{d\omega^2} \right|_{\omega=\omega_0} \cdot (\omega - \omega_0)^2 L \\ &= \dot{\beta} (\omega - \omega_0)L + \frac{1}{2}\ddot{\beta} (\omega - \omega_0)^2 L = \dot{\Phi} (\omega - \omega_0) + \frac{1}{2}\ddot{\Phi} (\omega - \omega_0)^2. \end{aligned} \quad (1.5)$$

The linear term of  $\Phi(\omega)$  represents a temporal delay and can be neglected without loss of generality. The second-order dispersion coefficient,  $\ddot{\Phi}$ , is constant within the considered spectral bandwidth. Considering that the bandwidth of the input optical pulses is narrower than  $\Delta\omega$ , the impulse response of the resulting dispersive medium,  $h(t') = \hat{h}(t') \cdot \exp\{j\omega_0 t'\}$ , has a complex envelope  $\hat{h}(t')$  with the same mathematical structure as Eq. 1.4:

$$\hat{h}(t') \propto \exp \left\{ j \frac{1}{2\ddot{\Phi}} t'^2 \right\}, \quad (1.6)$$

where  $t'$  represents the time variable with the group delay at  $\omega_0$  taken as a reference, i.e.,  $t' = t - \dot{\beta}L$ .

The observation of this mathematical duality led to the definition of the concept of *time lens* [56, 60]. The time-lens concept enabled the implementation of time-domain analogs of imaging systems, providing interesting applications as temporal magnification, compression, or time reversal of temporal optical pulses [60]. The effect of a thin spatial lens can be described by a quadratic phase transformation in the form,

$$t_{sl}(x, y) = \exp\{-j kn_l \Delta_l\} \exp \left\{ -j \frac{k}{2f_l} (x^2 + y^2) \right\}, \quad (1.7)$$

at  $\omega_0$ , where  $\Delta_l$  is the maximum thickness of the lens,  $n_l$  is its effective refractive index,  $f_l$  is the focal length and  $k$  is the wavenumber [12, 56]. The first term in Eq. 1.7 is a constant phase shift and therefore, it can be ignored for this discussion. Consequently, a lens produces a quadratic phase

modulation in space. In order to find the time-domain counterpart of the space lens, it is needed to produce a quadratic phase modulation on the local time variable  $t'$ . Therefore, the time lens' transmittance function can be written as

$$t_{tl}(t') \propto \exp \left\{ -j \frac{\omega_0}{2f_{tl}} t'^2 \right\}, \quad (1.8)$$

where  $f_{tl}$  is the “focal time” of the time lens. Hence, the time lens can be easily implemented with an EO phase modulator driven by a quadratic voltage (see Fig. 1.7). Reference [56] provides the expressions for  $f_l$  and  $f_{tl}$  in terms of the lens curvature surface and modulation parameters, respectively. A time lens works properly under the assumption of synchronization between the input temporal waveform and the quadratic modulating (electrical) voltage. The spatial-domain analogy of this assumption can be seen as the fact that the spatial information signal needs to be spatially aligned with the lens.

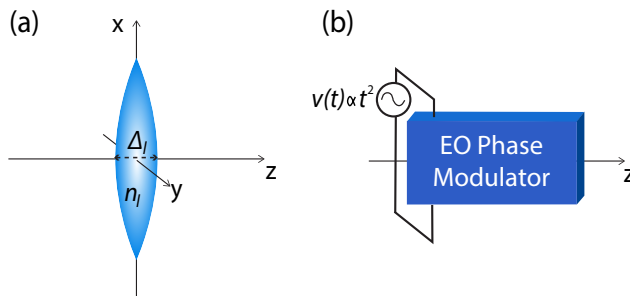


**Figure 1.7 – (a) Conventional space lens; (b) Time lens implemented with a phase modulator driven by a quadratic voltage.**

Thereby, it is possible to exploit spatial-domain techniques in the temporal domain using space-time duality. This approach has enabled more sophisticated and powerful methods to realize time-domain signal processing and characterization [57, 58, 61, 63, 64].

### 1.3.2 Fiber grating structures

Fiber gratings are periodic perturbations of the refractive index along the core of an optical fiber, typically generated by exposition of this optical fiber to a spatially varying pattern of ultraviolet (UV) light [53, 69]. Since their discovery in 1978, fiber gratings have been extensively studied for their application as linear passive filters, with interesting advantages over other filtering technologies, such low losses, polarization insensitivity, full compatibility with fiber-optics systems and relatively

low cost [53, 54, 69]. Still, the main advantage of fiber gratings is their flexibility to implement nearly any desired linear optical filtering functionality, only constrained by practical fabrication limitations. Mathematically, the perturbation of the effective refractive index of the guided mode of interest along the fiber length  $z$  is described as

$$n_{FG}(z) = n_{av} + \Delta n(z) \cdot \cos \left\{ \int_0^z \frac{2\pi}{\Lambda(z')} dz' \right\}, \quad (1.9)$$

where  $n_{av}$  is the “dc” index change spatially averaged over a grating period,  $\Delta n(z)$  is the envelope of the induced refractive index change, also defined as the apodization profile, and  $\Lambda(z)$  is the period variation, or chirp, along the grating length. The grating is confined over a length  $L$ , i.e.,  $n_{FG}(z)$  is defined for  $z \in [0, L]$ . Figure 1.8 shows a schematic of a fiber grating where the above-mentioned grating parameters are represented.

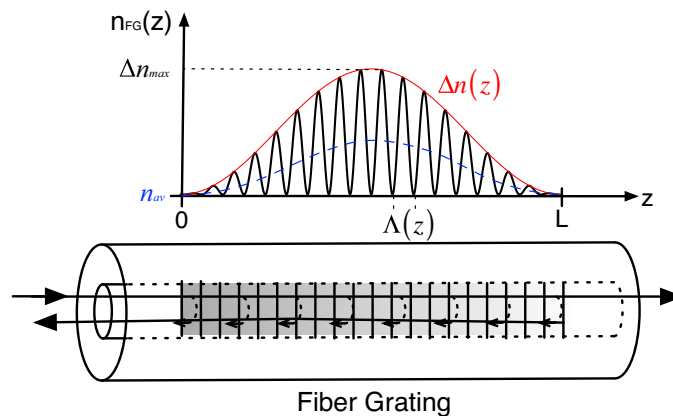


**Figure 1.8** – Schematic of the sinusoidal perturbation at the core of an optical fiber, creating a fiber grating. The lower figure depicts light coupling to a counter-propagating mode.

In order to achieve the target grating spectral response, nearly all the grating’s physical parameters can be varied: induced index change  $n_{av}$  and  $\Delta n(z)$ , length  $L$ , period chirp  $\Lambda(z)$ , and whether the grating supports counterpropagating or copropagating coupling at a desired wavelength [54]. Much research effort has been devoted to develop design tools that provide a direct relationship between the refractive index perturbation and the resulting grating spectral response. Thus, analysis [53, 54, 70–72] and synthesis tools [73–76] have been developed and they possess nowadays a high level of technical maturity. Analysis tools provide the spectral response  $H(\omega)$  of a grating with a particular refractive index profile  $n_{FG}(z)$ , and they are used to study how variations in the parameters of the grating (e.g.,  $\Delta n(z)$  and/or  $\Lambda(z)$ ) affect the resulting spectral response. On the

other hand, synthesis tools provide the required  $n_{FG}(z)$  to achieve a target  $H(\omega)$ , and they are widely employed in design procedures for obtaining the required grating parameters aimed at a desired filtering functionality.

An important limitation of fiber grating solutions as signal processing units is the lack of reconfigurability. Fortunately, there are a broad range of applications for which a particular fixed spectral response is required, e.g., differentiators, integrators, signal processors as Hilbert transformers, or rectangular or parabolic pulse shapers [11, 77–92], to name just a few. In those cases, a simple, highly efficient and easily reproducible component would be preferred over nonlinear or EO schemes. Moreover, nowadays much effort is put into integrating these periodic structures on photonics integrated chips (PICs) [55, 93–98].

The most widely extended theory to model and describe the functionality of fiber gratings is the coupled-mode theory (CMT) [71, 72]. This theory considers the fiber grating as a device able to couple optical power between two electromagnetic modes (with propagation constants,  $\beta_1$  and  $\beta_2$ ) when the grating period verifies the phase-matching condition [54]

$$\beta_1 - \beta_2 = m \frac{2\pi}{\Lambda}; \quad m = 1, 2, 3, \dots \quad (1.10)$$

where  $m$  is the Bragg-order and  $\Lambda$  is the nominal grating period. Depending of the value of  $\Lambda$ , fiber gratings can be broadly classified into two types: fiber Bragg (short period) gratings and long period gratings. In the next Sections, a brief review of the fundamentals of these two kinds of gratings is presented.

### 1.3.2.1 Fiber Bragg gratings (FBG)

FBGs, also called reflection and short-period gratings, typically have a sub-micron period and couple light from the forward-propagating fundamental core-mode to the counter-propagating (backward) core-mode of the optical fiber, i.e,  $\beta_2 = -\beta_1$  (Fig. 1.9). This coupling dominates at a specific wavelength  $\lambda_0$ , defined by the Bragg phase-matching condition (Eq. 1.10 considering  $m = 1$ ). An FBG operates as a band-pass filter in reflection and, consequently, as a band-stop filter in transmission (see Fig. 1.9).

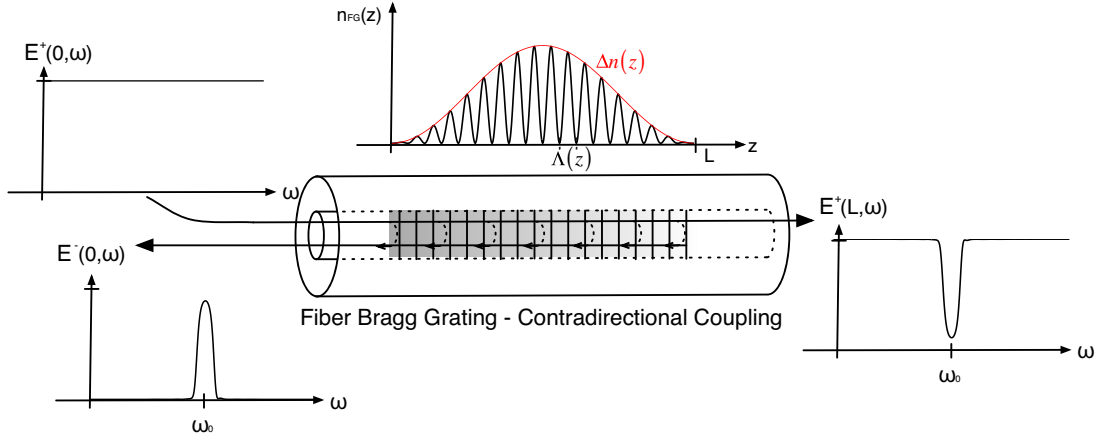


Figure 1.9 – Schematic diagram of a fiber Bragg grating (FBG), indicating two operation possibilities: the reflection mode and the transmission mode.  $\omega_0$  is the Bragg angular frequency,  $\omega_0 = 2\pi c_0/\lambda_0$ .

FBGs can be characterized in reflection and transmission by their spectral transfer functions  $H_R(\omega)$  and  $H_T(\omega)$ , or the corresponding temporal impulse responses  $h_R(t)$  and  $h_T(t)$ , respectively:

$$H_R(\omega) = \frac{E^-(0, \omega)}{E^+(0, \omega)}; \quad h_R(t) = \mathcal{F}^{-1}[H_R(\omega)]; \quad (1.11)$$

$$H_T(\omega) = \frac{E^+(L, \omega)}{E^+(0, \omega)}; \quad h_T(t) = \mathcal{F}^{-1}[H_T(\omega)], \quad (1.12)$$

where  $\mathcal{F}$  denotes Fourier transformation and  $\omega$  is the angular frequency variable. The propagating waves  $E(z, \omega)$  at the input ( $z = 0$ ) and output ( $z = L$ ) of the FBG have the subindex + for waves propagating in the direction of longitudinal variable  $z$ , and the subindex – for waves propagating in the opposite direction. These input and output signals are represented in Fig. 1.9.

FBGs are typically used in reflection mode. The major advantage of this configuration is that the grating can be designed to implement any desired arbitrary filtering functionality, within practical limitations imposed by the fabrication process. The main practical constraints are (i) the limited spatial resolution of the apodization profile, in the sub-millimeter range, and (ii) the maximum refractive index modulation  $\Delta n_{max}$ , typically restricted to values under  $\sim 10^{-3}$ . Those limitations impose a stringent operation bandwidth limitation of a few hundreds of GHz (typically it is assumed a limitation of  $\sim 200$  GHz, corresponding to temporal resolutions of at least several picoseconds). Reflective FBGs also require additional elements to separate the output from the input, such as an optical circulator or an optical coupler [99]. The use of FBGs operating in transmission pro-

vides interesting advantages: transmissive FBGs avoid the requirement of an additional element to separate the output signal from the input, reducing the complexity and cost of the processor unit. Also, they are more robust against fabrication errors due to the weak interaction between the transmitted optical signal and the grating. Hence, imperfections in the grating do not become impressed upon the signal field [100]. However, FBGs in transmission have an important drawback for their application as processing units of complex-valued transfer functions. The amplitude of the grating's spectral response in transmission  $H_T(\omega)$  uniquely determines its phase by means of a Hilbert transformation, that is, the transmission spectral response is a minimum-phase (MP) function [101] (factoring out the delay and dispersion caused by the propagation length in the fiber). Therefore, there is no freedom in choosing the complex spectral response to be implemented using this configuration.

### 1.3.2.2 Long period gratings (LPG)

LPGs, also called transmission gratings, have a period typically in the range of hundreds of  $\mu\text{m}$ , and induce coupling between the propagating fundamental core-mode and higher-order core or cladding modes. In LPGs, phase matching occurs at discrete wavelengths associated with the excitation of specific higher-order modes [54]. The period of the LPG is selected so that most of the power from the fundamental mode is coupled to a particular high-order mode at the frequency of interest, following Eq. 1.10. Figure 1.10 illustrates the wavelength-dependent attenuation resonances of a LPG, in this example the period of the LPG has been chosen to couple most of the power from the fundamental mode to the mode  $\text{LP}_{05}$  at  $\omega_0$ .

LPGs just work in transmission (no coupling occurs to a counter-propagating mode) offering two possibilities: the core-to-cladding ( $c-cl$ ) coupling mode or the core-to-core ( $c-c$ ) coupling mode operation. In the remainder of this Thesis, we assume LPGs implemented in a single mode fiber (SMF), i.e., only the fundamental mode propagates through the core. In this case, the core-to-core configuration is characterized by a multi-band rejection spectral response, while the core-to-cladding mode has a multi-band pass response. Similarly to FBGs, the analogous spectral transfer functions and temporal impulse responses for the two LPGs operation modes are obtained as:

$$H_{c-cl}(\omega) = \frac{E_{cl}^+(L, \omega)}{E^+(0, \omega)}; \quad h_{c-cl}(t) = \mathcal{F}^{-1}[H_{c-cl}(\omega)]; \quad (1.13)$$

$$H_{c-c}(\omega) = \frac{E_{co}^+(L, \omega)}{E^+(0, \omega)}; \quad h_{c-c}(t) = \mathcal{F}^{-1}[H_{c-c}(\omega)], \quad (1.14)$$

where the input and output propagating waves are shown in Fig. 1.10. For coupling between the core (fundamental) mode and the cladding mode of interest, the solution of the coupled-mode equations reveals that LPGs can have a significantly broader bandwidth than FBG in its coupling between the fundamental counter-propagating modes. The reason is that, whereas the bandwidth of a FBG is inversely proportional to the effective refractive index of the fundamental mode, the bandwidth of a resonance of an LPG is inversely proportional to the difference between the effective refractive indices of the two involved modes (the analytic demonstration can be found in Ref. [54]). This fact enables the large bandwidth typical for these fiber filters, scaling the filtering operation well into the THz-bandwidth regime.

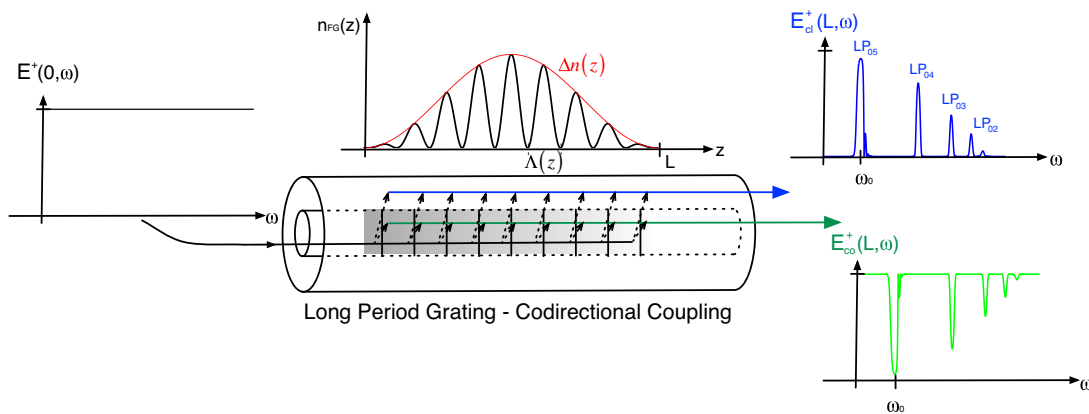


**Figure 1.10** – Schematic diagram of a long-period fiber grating (LPG), indicating two operation possibilities, the core-to-core mode and the core-to-cladding mode. In the figure, coupling to a higher-order cladding mode ( $LP_{05}$ ) is assumed.

LPGs have recently attracted a great deal of interest for linear optical pulse shaping and processing applications [79, 80, 89, 92, 102–105], since they allow faster operation speeds (bandwidths) than conventional FBG-based optical waveform generation and processing schemes. Fiber LPGs are typically based on coupling between the core mode and a cladding mode, i.e., core-to-cladding operation. In order to transfer the cross-coupling signal in the fiber cladding-mode to the fiber core-mode it is necessary either to concatenate a core-mode blocker and a short, strong uniform LPG [102], or to splice a suitably misaligned fiber in such a way that the cladding mode directly couples into its core [106]. Moreover, as compared with FBG devices, LPGs suffer from serious limitations,

particularly instabilities and high sensitivity to environmental fluctuations, and a significantly larger footprint for implementation in integrated formats.

## 1.4 Optical pulse shaping

A relevant application of optical signal processing is *pulse shaping*. Optical pulse shaping involves synthesizing the desired shape of the complex (amplitude and phase) temporal envelope of an optical electromagnetic pulse, and it plays a fundamental role in communication, computation or control systems [107–117]. Pulse shaping techniques are required to generate advanced pulse waveforms that optimize the overall performance of a telecommunication system, e.g., with the aim of (i) extending the transmission reach of the communication link, (ii) achieving optical multiplexing at highest spectral efficiency or (iii) limiting nonlinear distortions [107–110, 117].

Arbitrary temporal pulse shaping of ultrashort optical pulses, with resolutions in the picosecond regime and higher, is of great interest for a broad range of applications, such as high-speed coding/decoding, all-optical switching, or wavelength conversion, among many others [107–117]. Several of the signal processing techniques investigated in this dissertation are aimed at achieving picosecond-resolution pulse shaping functions. In this Section, a revision of approaches existing to date for optical pulse shaping is performed.

### 1.4.1 Nonlinear optical pulse shaping

Realizing optical pulse shaping using nonlinear optics effects has attracted much interest, due to the broad operation bandwidths that can be potentially obtained and the all-optical nature of the processing operation. It has been recently demonstrated that various pulse profiles can be achieved from the propagation of ultrashort strong pulses in nonlinear media with normal dispersion [18].

Pulses with parabolic intensity profiles with a linear frequency chirp (i.e., a parabolic phase modulation), known as *similaritons*, have been generated from the propagation of ultrashort pulses in media with varying dispersion [43, 44]. Moreover, the linear chirp achieved during the parabolic amplification make it possible to compress the obtained pulses through their propagation in a suitable dispersive medium. Thus, shaped pulses with much shorter temporal duration than the

initial seed pulse can be obtained. Also, the combination of a pulse prechirping and nonlinear propagation in a normally dispersive medium has been introduced as a method for passive nonlinear pulse shaping, which have proven useful for generating advanced field distributions, including flat-top and triangular profiles with a linear chirp [43, 45]. The initial power value and chirp of the input Gaussian-like pulse determines the reshaping process in the nonlinear propagation.

In spite of the fact that these nonlinear approaches are promising solutions to achieve all-optical, ultrafast pulse shaping operations, nonlinear optical pulse shaping is still restricted to few, well prescribed intensity-only shapes and under stringent control of the signals involved in the process, only achieved nowadays in a laboratory. Moreover, the shaped pulses obtained by these means have finite life distance (i.e., they conserve the target shape during a limited distance) that depends sensibly on the initial conditions (pulse shape, energy, and chirp profile). These circumstances, together with the general handicaps of nonlinear optical signal processing methods already mentioned in Section 1.2, have strongly limited the practical use of nonlinear optical pulse shaping techniques.

### 1.4.2 Linear optical pulse shaping

Linear photonic techniques are generally much more attractive than nonlinear solutions for realizing optical pulse shaping in the context of telecommunication and information processing applications. In this Section, a review of most relevant linear optical pulse shaping techniques is performed.

A straightforward technique for shaping of optical waveforms involves the use of high-speed electronics to directly drive an external EO modulator. The modulating signal is an electronic waveform with the target shape that carves the information in an input monochromatic optical carrier [118, 119]. The speed limitation of electronics typically restricts the frequency content of the generated optical waveforms below a few tens of GHz.

Pulse shaping methods based on spatial-domain Fourier optics filters are well known and have been widely applied. These methods, also referred to as “spectral shaping”, routinely offer temporal resolutions better than 100 fs. In the original technique, the temporal information is converted into a one-dimensional spatial domain waveform through a diffraction grating, as illustrated in Fig. 1.11 [120, 121]. This conversion is achieved by the spatial spreading of the different spectral

components of the temporal information signal. The resulting waveform is shaped by a simple spatial-domain linear filtering process based on the concatenation of two Fourier-transform systems in a configuration called  $4-f_l$  system, with  $f_l$  being the focal length of the involved thin lenses. In the central plane of the system, the so-called Fourier plane, an amplitude or phase mask is placed, which acts as the optical filter implementing modulation on the different spatial frequency components of the input beam. The resulting shaped wave is converted back to the time-domain via a second diffraction grating. In state-of-the-art schemes, conventional picosecond and femtosecond pulse shaping techniques have been implemented by replacing the amplitude or phase mask by advanced devices, such as liquid crystal spatial light modulators (SLM) [120–122], acousto-optic modulators [120], or EO phase arrays [122], which impart user-specified spectral amplitude and phase modulations on the pulse in a programmable fashion. The main drawback of this scheme is the requirement of bulky optical components, which require strict tolerances in their alignment and have limited integration with waveguide devices. Also, the need for coupling the shaped waveforms back into an SMF introduces loss and further limits the temporal extent of the generated pulse shapes [123].

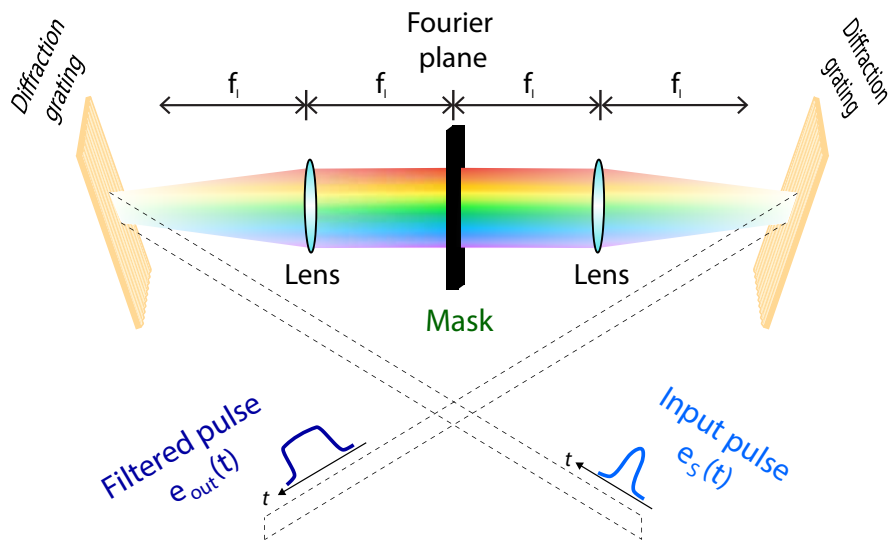


**Figure 1.11** – Schematic of a spatial-domain filter for time-domain optical pulse shaping. The optical pulses are pre- and post- converted to the spatial-domain by means of diffraction gratings.

To overcome this practical complexity problem, an important body of research has focused on the search for alternative implementations of spectral shaping using optical fiber or integrated-waveguide platforms. To give a first relevant example, an integrated version of the original Fourier optics pulse shaping concept has been implemented using arrayed waveguide gratings, which have been used to spatially distribute the temporal frequency components of an input waveform. The

amplitude and phase profile of the spatially-dispersed pulse is subsequently manipulated with an array of modulators and combined again using a second arrayed waveguide grating [124, 125]. These pulse shapers are compact, integrated devices, but they are typically limited to time resolutions above 10 ps.

A similar approach has been recently developed, but using an optical frequency comb (OFC) as the input signal [126]. Each frequency line of the OFC is separately modulated using IQ modulators and then, the spectral slices are combined to produce a target waveform. This technique is able to generate broad bandwidth signals (scalable to THz frequencies) from narrow spectral slices with bandwidths accessible by current electronics. However, the complexity, power consumption and cost of the required electronic circuits quickly scale up with the bandwidth of the output signal.

With the understanding of the space-time duality, the equivalent of pulse-shapers based on spatial-domain optical filtering has been implemented using in-line fiber-optic components. In particular, the spatial  $4-f_l$  system can be substituted by two all-fiber dispersive elements with opposite dispersion and a single EO modulator in between the dispersive elements (see Fig. 1.4(a)). This configuration is just an approximation of the truly temporal counterpart of a spatial  $4-f_l$  system: making use of the far-field diffraction and considering that waveguides can produce either positive or negative group-velocity dispersion, the middle two regions of dispersion and both of the time lenses can be eliminated, dramatically simplifying the system. This implementation based on pure fiber optics offers the advantages of smaller size, lower loss, better stability and higher potential for integration [123]. Different schemes have been proposed based on this configuration, using either an EO intensity modulator [127, 128] or a phase modulator [129–131], all of them with a resolution reaching the sub-picosecond range.

All the previously mentioned approaches are electronically programmable: either the target shape or its spectral response is generated through an electrical bit pattern generator or arbitrary waveform generator. Simpler, more compact optical pulse shapers have been explored using fiber-optic or integrated-waveguide linear optical filters with customized spectral responses. A relevant example is that of optical lattice filters [132–134]. They are a good all-purpose solution due to their ability to generate complicated spectral transfer functions by cascading identical units cells. In a widely used configuration, shown in Fig. 1.12, each unit cell employs a combination of a ring resonator and a Mach-Zehnder interferometer, and it contributes a separately controllable pole and

zero pair [134]. However, the phase-shifter employed as part of the interferometer in each unit cell makes it difficult to achieve operation bandwidths above a few tens of GHz.

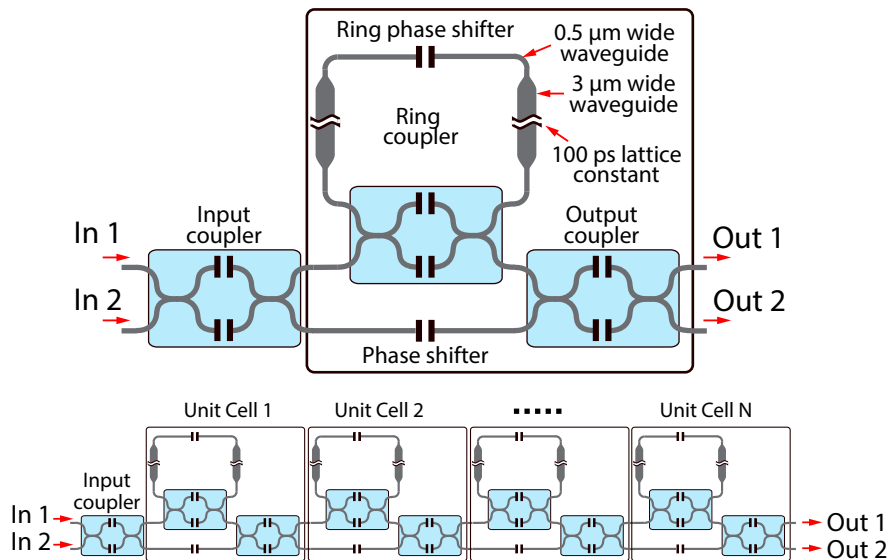


Figure 1.12 – Schematic design of a single unit-cell lattice filter, at the top of the figure, and example of an  $N$ -unit cell filter, at the bottom. Figure reproduced from Ref. [134].

Alternative pulse shaping techniques have been also demonstrated using the concept of temporal coherence synthesization. They are based on the synthesis of the desired output pulse shape by coherently combining a set of input pulse replicas with different time delays, as illustrated in Fig. 1.13 [52]; or similarly, using coherent overlapping of different (first and high-order) derivatives of the input optical pulse with specific relative weights [135]. Programmability can be achieved by properly programming the time-delays (first approach) or relative weights using amplitude and/or phase optical modulators (second approach). A sub-picosecond resolution, silicon-based pulse-shaper based on temporal coherence synthesization has been recently proposed in [136]. This approach uses cascaded co-directional couplers to manipulate both amplitude and phase of the input pulse to be shaped.

Finally, optical pulse shaping operation has been also investigated using fiber gratings. FBGs operating in the weak-coupling condition (first-order Born approximation) have been employed as pulse shapers [70, 86, 109, 112, 137, 138]. If the grating is sufficiently weak, the corresponding reflection impulse response  $h_R(t)$  is directly related to the spatial profile of the index-modulation depth  $\Delta n(z)$ . This simple approach permits the synthesis of nearly any desired optical waveform with resolutions in the picosecond regime. As relevant examples of this design approach, we can

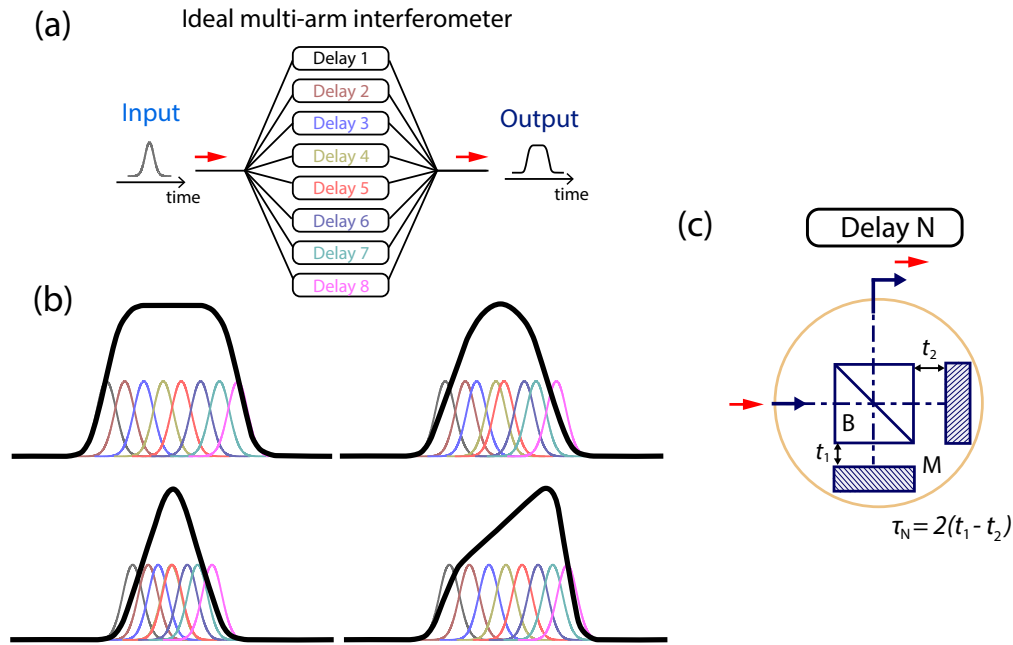


Figure 1.13 – (a) Conceptual diagram of the pulse shaping technique based on the concept of temporal coherence synthesization; (b) Examples of synthesized temporal waveforms: flat-top, parabolic, triangular and trapezoidal pulse; (c) Schematic of a single stage of the multi-stage interferometric setup for pulse shaping based on this concept. B: 50:50 beam splitter; M: Mirror. Figure reproduced from Ref. [52]

mention the implementation of flat-top [137, 138], parabolic [112] and saw-tooth (triangular) [109] pulse shapers based on specially apodized FBGs.

Another approach for FBG-based pulse shaping based on the Born approximation is based on a space-to-frequency-to-time mapping [139]. It enables the synthesis of arbitrary waveforms in the picosecond/nanosecond regime, although with a lower energy efficiency. This method involves using a specially designed apodized linearly chirped FBG (LC-FBG), in the regime of weak coupling condition. If the FBG chirp induced dispersion is sufficiently large, the amplitude of the grating impulse response is proportional to the amplitude of the spectral response of the filter, which is in turn proportional to  $\Delta n(z)$  (under the Born approximation). In this case, the desired temporal (or spectral) waveform only needs to be spatially “recorded” in the apodization mask used to write the grating. The application of this approach is limited to amplitude-only pulse shaping, and the time duration of the output pulses is limited by the length of the grating that can be written, typically in the nanosecond regime (corresponding to a physical fiber-grating length shorter than  $\sim 10$  cm).

More advanced solutions for the use of FBGs as pulse shapers involve the application of general grating-synthesis algorithms [74–76] to determine the amplitude and phase profiles of the refractive-

index modulation that are necessary to obtain a given temporal response. These methods allow one to design high-reflectivity FBGs to achieve the desired pulse-shaping operation, leading to increased energy efficiency. Employing these gratings design techniques, FBGs have been designed to implement several optical pulse shapers [83, 140–147].

In regards to pulse shapers based on LPGs, some interesting LPG-based optical code generation designs were first reported in [104] but they were limited to the synthesis of temporally symmetric and binary intensity-only (OOK) optical codes, (sub-) picosecond flat-top shapes and first- and high-order Hermite-Gaussian pulse waveforms from Gaussian-like optical pulses. A THz-bandwidth optical pulse shaping theory has been recently developed using fiber LPG devices [105, 106, 148], that has enabled the demonstration of complex-envelope optical code sequences and other interesting pulse shapes (e.g., rectangular or triangular) with temporal resolutions that are not limited by the spatial resolution of the grating fabrication technologies.

Nowadays, the trend is towards the realization of pulse shaping technologies in integrated formats. For this purpose, compact, highly flexible grating systems appear as practical and promising approaches for real-world applications. This represents a very interesting perspective for the future development of fully integrated optical circuits for communications, information processing and computing [149].

## Chapter 2

# Motivation and organization of the Thesis

### 2.1 General motivation

As introduced in Chapter 1, there is a high interest in decreasing the complexity of the circuits for processing information of complex-envelope temporal optical signals, aimed at reducing costs and power consumption. Moreover, the design and implementation of all-optical signal processors able to operate at ultrafast speeds (ideally, with processing bandwidths into the THz regime) is critical to reduce electro-optical (EO) conversions and increase the capacity of current networks and computing systems [150].

The problem of simultaneously controlling the amplitude and phase of an electromagnetic signal has long been solved in the spatial domain. Holography in the spatial domain is a well-known imaging process that was first introduced by D. Gabor in 1949 [65]. In this process, the entire information (i.e., amplitude and phase) of a desired complex optical waveform can be recorded, generated and/or processed by the employment of a photosensitive medium that responds only to the intensity of light [66, 67]. Holography has been used not only for three dimensional (3D) imaging processing, but also for the implementation of complex (amplitude and phase) optical filters in the spatial domain, i.e., the so-called Vander-Lugt filters [151], among other interesting applications. The basics of space domain holography will be reviewed in Chapter 3.

In this Thesis, we propose the concept of *time-domain holography*, developed as the exact time-domain counterpart of classical (spatial-domain) holography. The time-domain equivalent of the recording process in holography involves photo-detection of the interference between the temporal complex-envelope waveform under analysis (information signal) and a reference optical local oscillator, typically a continuous wave light at a wavelength properly shifted from the spectral content of the information signal. This procedure is already employed for complex optical signal characterization and it is referred to as heterodyne detection [152]. In a conventional heterodyne detection scheme, the amplitude (or intensity) and phase temporal profiles of the optical information signal are numerically recovered from the recorded interferogram using an algorithm based on Fourier transforms. Also, if the detected signal is to be used for additional processing, the in-phase and quadrature components need to be handled independently. The time-domain holography scheme introduced here goes one important step further by using the detected electrical interferogram (the *temporal hologram*) for generation and processing of an exact replica of the original complex information signal directly in the optical domain. Thus, time domain holography can be seen as a signal processing methodology that enables the *simultaneous* control of the amplitude and phase of a temporal optical waveform using EO or all-optical components sensitive to intensity-only variations, namely, temporal detection and/or amplitude modulation optical devices. The resulting procedure greatly simplifies present approaches aimed to similar generation and processing tasks, e.g. in the optical coherent transmitter and receiver. Indeed, the currently required circuitry can be significantly reduced, as the IQ components of the coherent optical information signal will be processed simultaneously, avoiding the independent detection, processing, and re-combination with proper synchronization.

Further investigation on this concept leads us to the proposal of the frequency-domain counterpart of time-domain holography, that is, the *spectral-domain holography*. The term “spectral holography” has been already used in the literature to define systems in which a spatial-domain filter is used to process a complex-envelope (amplitude and phase) time-domain optical signal. Once the spectral information of the input signal is converted to the spatial-domain, the method performs *frequency-to-space mapping* (with a  $4f_l$  system) within a holographic apparatus. In this Thesis, the concept of spectral-domain holography involves creating a *spectral interferogram* that allows one to control both the amplitude and phase spectral content of a temporal optical signal by just manipulating the signal’s amplitude spectrum. This methodology enables the implementation

of new kinds of optical filters and signal processors using different technologies. In particular, in this Thesis we focus on two main technologies: first, we present picosecond-resolution, reconfigurable optical processors and shapers based on Fourier optics EO filters. These processors make use of a *frequency-to-time mapping*, and they can be seen as the “time-domain” counterpart of previously presented spectral holography. Also, we go beyond Fourier optics-based filters and we investigate the implementation of ultrafast arbitrary (minimum-phase (MP) and non-MP) signal processors based on MP all-optical filters. These processors prove a promising solution to overcome the speed limitation of current electronic systems.

The concept at the core of this Thesis, namely time/spectral-domain holography, can be interpreted as a new milestone within the context of the space-time duality [56]. The mathematical dual formalism between spatial holography and temporal optical heterodyning (or frequency mixing) is introduced in this Thesis, and subsequently utilized in a number of applications inspired by holographic concepts. Further exploration of the presented duality might contribute to bring new understanding in the two domains.

## 2.2 Original contributions

First of all, the concept of time-domain holography is introduced and analytically formalized as the dual process of spatial-domain holography [153]. Time-domain holography will be employed for implementing functionalities at the transmitter and receiver of optical communications links. In particular, the stage of generation of complex (amplitude and phase) optical waveforms will be significantly simplified by the employment of holographic concepts. The proposed configuration is based on a simple amplitude modulator and a band-pass filter, what substitutes current IQ modulators or more complex configurations (e.g., quad-parallel Mach-Zehnder modulator [7]) requiring stringent synchronization of the complex-envelope signal’s real and imaginary parts. Besides, a new configuration to implement an impairment compensation system based on temporal phase conjugation (TPC) will be also presented and experimentally demonstrated [154]. The proposed configuration employs the same components than the previous generation system, avoiding the detection and subsequent processing of the signal’s phase information in the electrical domain. TPC is useful for compensation of even order dispersion and some nonlinear effects such as self phase modulation or intra-Raman scattering. For the previously mentioned applications, time-domain

holography is carried out using EO circuits. In this Thesis, we also introduce an all-optical approach to implement time-domain holography, based on nonlinear cross phase modulation (XPM) [155]. This configuration will be applied to perform wavelength conversion of complex-envelope ultrafast signals, improving the performance of previous XPM-based wavelength converters, which are limited to the conversion of intensity-only or signals, and it avoids the stringent phase-matching requirement of four-wave-mixing-based approaches.

By considering the Fourier transform property of duality between time domain and frequency domain [46], we will introduce the concept of spectral-domain holography (referring to time-domain optical signals). This concept mainly involves creating a “spectral interferogram” to implement optical processors that control both amplitude and phase spectral responses of a temporal input signal by just manipulating its amplitude spectral response. This approach is used to develop the time-domain counterpart of Vander-Lugt filters [156], which allows the implementation of tunable and reconfigurable coherent optical pulse processors, using a similar configuration than those presently available for the development of optical processors with amplitude-only spectral responses. Also, this spectral-domain holography approach is especially interesting for the design of arbitrary optical signal processors based on MP optical filters (i.e. filters whose phase spectral response cannot be engineered independently of the amplitude response, since amplitude and phase are related by a Hilbert transform). Particular attention will be paid to the case of fiber Bragg gratings (FBGs) operating in transmission. We will first develop a design technique to overcome the bandwidth limitation of FBGs, enabling the achievement of operation bandwidths one order of magnitude higher than the ones typically achieved in reflection. To prove the validity of the newly introduced design technique, we will analyze the design of two MP signal processors with operation bandwidths in the THz regime, namely arbitrary-order optical differentiators and a flat-top pulse shaper [84]. The latter will be also experimentally demonstrated [157]. Then, by means of spectral-domain holography, we will implement signal processing operations described by non-MP transfer functions on this configuration (transmissive FBGs) [85]. As a proof of concept, an ultrafast (ultra-wide band) all-optical non-MP processor, i.e., a Hilbert transformer, will be implemented based on a transmissive FBG [158].

## 2.3 Thesis organization

This Thesis is organized as follows:

**Chapter 1** discusses the importance of signal processing in the present technological world and highlights the advantages that the use of fiber optics systems have provided in current telecommunications networks, particularly in terms of information transmission rate. Also, it introduces the limitations that optical communications are facing nowadays, due to the bottleneck imposed by the processing speed of electronics and the scaling of circuitry complexity and power consumption. The theory behind the basis of nonlinear and linear optical processing systems is briefly introduced. Special attention is devoted to the theory of space-time duality, which is employed to develop the novel concepts presented in this Thesis. Then, a brief introduction to fiber grating devices, and in particular FBGs and long period gratings (LPGs) is included, summarizing their main advantages and drawbacks as linear optical filters. Finally, the state-of-the-art of pulse shaping methods is described, as this is a relevant application of optical signal processing continuously revisited along this dissertation.

**Chapter 2** exposes the general motivation of the work presented in the Thesis, which mainly focuses on the search for solutions to the problems presented in Chapter 1. Also, the original contributions of the Thesis are briefly commented.

**Chapter 3** provides a comprehensive introduction to spatial-domain holography, where the analytic description of the method and its fundamental properties are discussed. Also, techniques for the implementation of optical filters with complex-valued transfer functions based on spatial-domain holography, i.e., the so-called Vander-Lugt filters, are studied. The concepts reviewed in this Chapter will serve as the basis for the original ideas presented in the remainder of the Thesis.

**Chapter 4** introduces the concept of time-domain holography as an exact counterpart of classical spatial-domain holography. Two approaches are presented and analytically studied for the practical implementation of time-domain holography, namely an EO approach and an all-optical approach. Then, three relevant applications of practical interest are numerically and experimentally demonstrated by means of time-domain holography, namely, (i) complex-signal generation and detection, (ii) temporal phase conjugation and (iii) wavelength conversion of

complex-waveforms. Those applications are implemented using either the EO approach (for the two former applications) or the all-optical approach (for the latter application).

**Chapter 5** introduces the concept of spectral-domain holography and its use for implementation of optical filters/processors with arbitrary complex-valued transfer functions using two different technologies. One of them is an EO approach, which can be considered as the time-domain counterpart of Vander-Lugh filters. The second one is an all-optical approach based on MP optical filters (e.g., transmissive FBGs), where spectral domain holography is employed to implement any arbitrary non-MP processing operation.

**Chapter 6** summarizes the work presented in this Thesis and proposes potential prospects for future work.

## Chapter 3

# Review of classical space-domain holography

### 3.1 Introduction to space-domain holography

Classical (spatial domain) holography is a well-known lensless imaging process that was first introduced by D. Gabor in 1949 [65]. The fundamental problem addressed by holography is that of recording, and later reconstructing, both the amplitude and phase of an optical wave arriving from a coherently illuminated object. All recording media respond only to light intensity. It is therefore required that the phase information is converted to intensity variations for recording purposes. Holography accomplishes this task through the use of *interferometry*.

A great deal of research was carried out following the original proposal of Gabor in [65]. In particular, the dramatic improvements accomplished in the 1960s vastly extended the applicability and practicability of holography. One of the key breakthroughs was proposed by Leith and Upatnieks [67]. They presented a methodology that solved the main practical problem of Gabor's original recording geometry, namely the fact that the target output image appeared overlapped with other auxiliary waves, hindering its visibility. Leith and Upatnieks proposed a recording geometry able to angularly separate the different output components, in such a way that they could be clearly distinguished and isolated from each other. This method will be described in detail later in the Chapter. In general, the important outcomes achieved in the last decades have led to an outstanding

development of holography and have expanded its applicability to a myriad of fields, including 3D imaging, optical signal processing, data storage or microscopy [159–161], among others. A review of the historical evolution of holography can be found in several excellent references [162–164].

### 3.2 Mathematical formalism of space-domain holography

The holographic process comprises two steps, the recording and the subsequent retrieval of the amplitude and phase of an optical information signal. Let us assume the information signal is an unknown monochromatic wave with complex amplitude  $e_{SG}(x, y) = |e_S(x, y)| \exp\{j \phi_S(x, y)\}$ , where  $x$  and  $y$  are the Cartesian coordinates in the plane transverse to the propagation direction. In the recording process, a mutually coherent known reference wave  $e_{LO,1}(x, y) = |e_{LO,1}(x, y)| \exp\{j \phi_{LO,1}(x, y)\}$  is added to  $e_{SG}(x, y)$ , making them interfere. The intensity of the sum of the two complex fields can be written

$$\begin{aligned} i_H(x, y) &= |e_{SG}(x, y) + e_{LO,1}(x, y)|^2 \\ &= |e_{SG}(x, y)|^2 + |e_{LO,1}(x, y)|^2 \\ &\quad + 2|e_S(x, y)||e_{LO,1}(x, y)| \cos(\phi_S(x, y) - \phi_{LO,1}(x, y)). \end{aligned} \quad (3.1)$$

The first two terms of the right hand side (RHS) of Eq. 3.1 depend only on the intensities of the individual waves. However, the third term is dependent on both their amplitudes and their relative phases. The reference wave is generally chosen to be a uniform plane wave propagating along the  $z$  axis,  $e_{LO,1}(x, y) = i_{LO,1}^{1/2}$ . The intensity pattern  $i_H(x, y)$  can be then recorded in a photosensitive medium, e.g., a photographic film or plate. For simplicity, let us consider a linear mapping of the intensity variations into the amplitude transmittance  $t_A$  of the photosensitive medium. Obviously, intensity variations exceeding the linear region of the curve of  $t_A$  vs. exposure (i.e., the energy incident per unit area on the photographic film) would lead to aberrations at the output of the imaging process. Thus, the amplitude transmittance  $t_A$  is

$$t_A(x, y) = \beta' \left( |e_{SG}(x, y)|^2 + i_{LO,1} + i_{LO,1}^{1/2} e_{SG}(x, y) + i_{LO,1}^{1/2} e_{SG}^*(x, y) \right), \quad (3.2)$$

where  $\beta'$  is the slope of the curve of  $t_A(x, y)$  vs exposure at the bias point and exposure time. The recording of the pattern of interference between the information wave  $e_{SG}(x, y)$  and the reference wave  $e_{LO,1}(x, y)$  is defined as a *hologram*.

The second step of holography entails the reconstruction of the complex information signal  $e_{SG}(x, y)$ . To this purpose, the developed transparency must be illuminated by a coherent *reconstruction* wave  $e_{LO,2}(x, y)$ . The resulting wave transmitted by the transparency is expressed as

$$\begin{aligned} e_{out}(x, y) &= e_{LO,2}(x, y)t_A(x, y) \\ &= \beta' e_{LO,2}(x, y)|e_{SG}(x, y)|^2 + \beta' e_{LO,2}(x, y)i_{LO,1} \\ &\quad + \beta' e_{LO,2}(x, y)i_{LO,1}^{1/2}e_{SG}(x, y) + \beta' e_{LO,2}(x, y)i_{LO,1}^{1/2}e_{SG}^*(x, y). \end{aligned} \quad (3.3)$$

If the reconstruction wave is chosen to be a plane wave similar to the reference wave employed in the recording process, Eq. 3.3 can be rewritten as

$$\begin{aligned} e_{out}(x, y) &= \beta' i_{LO,2}^{1/2}|e_{SG}(x, y)|^2 + \beta' i_{LO,2}^{1/2}i_{LO,1} \\ &\quad + \beta' i_{LO,2}^{1/2}i_{LO,1}^{1/2}e_{SG}(x, y) + \beta' i_{LO,2}^{1/2}i_{LO,1}^{1/2}e_{SG}^*(x, y). \end{aligned} \quad (3.4)$$

The first term in the RHS of Eq. 3.4 is proportional just to the intensity of the information signal and therefore, it is of no interest in our analysis. This term, usually known as the *ambiguity term*, can be neglected if the power of the reference signal  $e_{LO,1}(x, y)$  is much higher than the power of the information wave. Thus, the first term is then much smaller than the others since it is the only one that does not involve  $i_{LO,1}$ , as observed in Eq. 3.4. The second term is a plane wave traveling down the optical axis. The third and four terms are proportional to the information wave and its conjugate, respectively. At the observation point, the component proportional to the original information wave originates a virtual image of the object, while the component proportional to the conjugate of the information signal leads to the formation of a real image [13].

In Gabor's original apparatus, the different output components appeared overlapped on the  $z$  axis. Hence, when the virtual image was brought to focus, an observer saw a defocused real image and vice versa, accompanied at least by a coherent background due to the output plane wave.

To properly observe the reconstructed objects, it is necessary that the various wave components of the transmitted light do not overlap in space. Leith and Upatnieks proposed an off-axis holographic apparatus that solved the problem of Gabor's recording geometry [67]. It consists of applying different propagation angles to the information and the reference wave in the recording process, as depicted in Fig. 3.1.

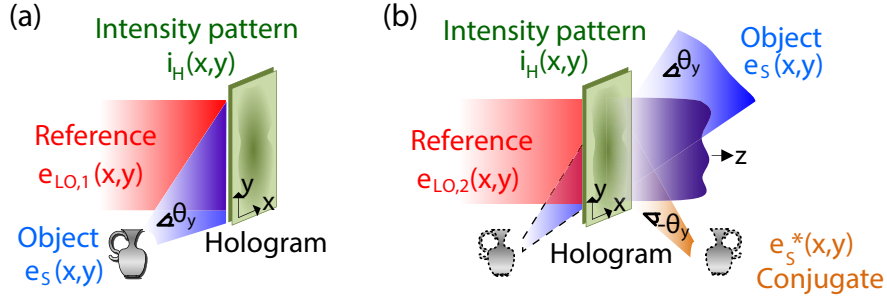


**Figure 3.1** – (a) Signal recording step and (b) signal retrieval step in classical holography. The figure represents the geometry proposed by Leith and Upatnieks, from which the information signal and its conjugate appear angularly separated from the reference and ambiguity components.

Assuming that the information wave propagates along a direction with angle of  $\theta_y$  with respect to the reference wave, its complex amplitude can be expressed as

$$e_S(x, y) = |e_S(x, y)| \exp \left\{ j(\phi_S(x, y) - k \sin \theta_y y) \right\}, \quad (3.5)$$

where  $k$  is the propagation number  $k = 2\pi/\lambda_0$ ,  $\lambda_0$  being the light's wavelength. As reviewed in Section 1.3.1, the angle of propagation of a lightwave is related to its spatial frequency. Therefore, the central (or *carrier*) spatial frequency of  $e_S(x, y)$  is

$$\nu_{Sy} = \frac{\sin(\theta_y)}{\lambda_0}. \quad (3.6)$$

The intensity pattern at the recording plane is

$$\begin{aligned} i_H(x, y) = & |e_S(x, y)|^2 + i_{LO,1} \\ & + i_{LO,1}^{1/2} e_S(x, y) \exp \left\{ -j k \sin \theta_y y \right\} + i_{LO,1}^{1/2} e_S^*(x, y) \exp \left\{ j k \sin \theta_y y \right\}. \end{aligned} \quad (3.7)$$

In this case, the third term in the RHS of Eq. 3.7 is a replica of the information signal arriving from a direction at an angle  $\theta_y$ , while the fourth term is proportional to the conjugated of the

information signal, propagating with an angle  $-\theta_y$ , as shown in Fig. 3.1(b). If the central spatial frequency of  $e_S(x, y)$  is sufficiently high, the third and fourth terms of Eq. 3.7 do not overlap with the other two terms and therefore, they can be unambiguously recovered from the recorded interference pattern  $i_H(x, y)$ .

In order to figure out which is the minimum spatial frequency of  $e_S(x, y)$  required so that the different output components do not overlap, it is necessary to study the spatial frequency spectrum of  $i_H(x, y)$ . Applying the Fourier transform to Eq. 3.7, we obtain

$$I_H(\nu_x, \nu_y) = E_S(\nu_x, \nu_y) \otimes E_S^*(-\nu_x, -\nu_y) + i_{LO,1} \delta(\nu_x, \nu_y) + i_{LO,1}^{1/2} E_S(\nu_x, \nu_y - \nu_{Sy}) + i_{LO,1}^{1/2} E_S^*(-\nu_x, -\nu_y - \nu_{Sy}), \quad (3.8)$$

where  $\otimes$  indicates the convolution operation,  $\delta(\nu_x, \nu_y)$  represents the Dirac delta function,  $I_H(\nu_x, \nu_y) = \mathcal{F}\{i_H(x, y)\}$ ,  $E_S(\nu_x, \nu_y) = \mathcal{F}\{e_S(x, y)\}$ , and  $E_{LO,1}(\nu_x, \nu_y) = \mathcal{F}\{e_{LO,1}(x, y)\}$ , where  $\mathcal{F}$  denotes Fourier transformation. We observe that the angular/spatial bandwidth of the third and fourth terms in the RHS of Eq. 3.8 are identical to the bandwidth of the information signal, denoted as  $B$  cycles/m (Fig. 3.2). The second term is a single tone at the  $(\nu_x, \nu_y)$  plane. The spectrum of the ambiguity term is the convolution between two signals of bandwidth  $B$ , so its spectral content has a maximum extent of  $2B$ . Hence, in order to avoid any overlapping between the components of the intensity pattern, the minimum spatial frequency of  $e_S(x, y)$  should be (see Fig. 3.2(b))

$$\nu_{Sy} \geq 3B/2. \quad (3.9)$$

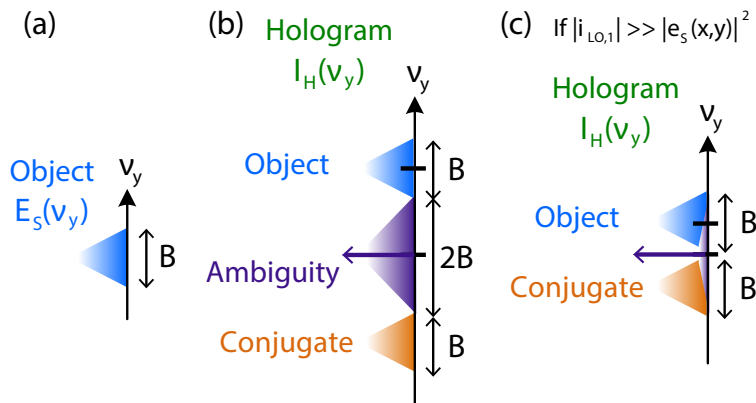


**Figure 3.2** – Spectral content of (a) information signal  $e_S(x, y)$ , (b) hologram, and (c) hologram considering that  $i_{LO} \gg |e_S(x, y)|^2$ .

As discussed previously, if the reference wave  $e_{LO,1}(x,y)$  is much stronger than  $e_S(x,y)$ , the first term in the RHS of Eq. 3.7 can be neglected. Then, the minimum spatial frequency of the information signal can be reduced to (see Fig. 3.2(c))

$$\nu_{Sy} \geq B/2. \quad (3.10)$$

### 3.3 Computer-generated holograms

It is possible to create a hologram by modeling the interference process in a digital computer and then transferring the obtained interference pattern to a transparency by means of a plotting or printing device, see Fig. 3.3. The hologram obtained by this means is generally known as a computer-generated hologram (CGH). This concept was introduced some years after the development of off-axis holography [165, 166], and provides the possibility to generate and process images without the need for the real object.

The success in generating CGHs depends on the ability to mathematically describe the image of the object to be displayed (two-dimensional or three dimensional) with sufficient resolution. This problem reduces to find the minimum number of samples required to properly create a target real or virtual image from the numerical model. The number of samples is dependent on the bandwidth of the target signal. Its calculus is out of the scope of this Thesis, and further details can be found in [13].

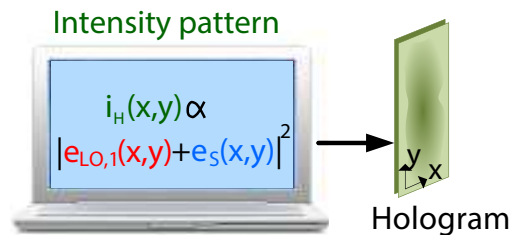


**Figure 3.3** – The hologram can be created by computationally modeling the interference pattern between an object and a reference plane wave, and transferring the result to a transparency.

As the CGH is artificially designed, one can create an intensity pattern that includes information from the target complex (amplitude and phase) wave and a reference wave, but without including

the plane wave and the ambiguity term components of Eq. 3.7, i.e.,

$$i_{CGH}(x, y) = i_{LO,1}^{1/2} e_S(x, y) \exp \left\{ -j k \sin \theta_y y \right\} + i_{LO,1}^{1/2} e_S^*(x, y) \exp \left\{ j k \sin \theta_y y \right\}. \quad (3.11)$$

As such, the condition for the required spatial frequency of  $e_S(x, y)$  can be selected to match Eq. 3.10 without the intensity constraint of  $e_S(x, y)$  with respect to the intensity of the reference wave. Therefore, the resulting hologram lacks a constant background and it is therefore possible to increase the dynamic range of the information signal for the same transparency.

### 3.4 Vander-Lugt filters

Holography finds applications in much broader fields than that of recording and displaying three-dimensional images. Holographic optical elements can perform the functions of mirrors, lenses, gratings, or combinations of them, and they are currently used in a myriad of technical devices. One particularly interesting application of holography is its use to implement complex field optical filters in the spatial domain, using intensity-only spatial masks.

The traditional filtering process, briefly reviewed in Section 1.4.2, is illustrated in Fig. 3.4. A converging lens can perform two-dimensional Fourier transforms with extraordinary simplicity in a coherent optical system, taking advantage of the basic laws of propagation and diffraction of light [12, 13]. Let us assume an input waveform containing the information to be Fourier-transformed. This optical wave, with complex waveform  $e_{in}(x, y)$ , may be generated from the illumination of a device with a transmittance proportional to the function of interest (e.g., a photographic transparency or a spatial light modulator) by a monochromatic light. The input waveform can be analyzed as a superposition of harmonic functions (i.e., plane waves) of different spatial frequencies  $(\nu_x, \nu_y)$ . The spatial frequencies are related to the angle of propagation of the waves by the Eqs. 1.3. A lens transform each plane wave into a paraboloidal wave focused to a single point in the lens focal plane, located at a distance equal to its focal length  $f_l$ . Thus, a plane wave traveling at the angles  $(\theta_x, \theta_y)$  is mapped into a point  $(x, y) = (\theta_x f_l, \theta_y f_l) = (\lambda_0 f_l \nu_x, \lambda_0 f_l \nu_y)$ , where the paraxial approximation has been considered and  $\lambda_0$  is the wavelength of the incident light. The complete mathematical derivation of this result can be found, e.g., in Refs. [12, 13]. It can be easily demonstrated that, if the optical information waveform is placed at a distance  $d$  before the lens, the complex waveform

at the focal plane can be calculated as

$$\begin{aligned}
e_{FP}(x', y') &= \left[ (e_{in}(x, y) \otimes \hat{h}_d(x, y)) \cdot t_{sl}(x, y) \right] \otimes \hat{h}_{f_l}(x, y) \\
&= \frac{A}{j \lambda_0 f_l} \exp \left\{ j \frac{k}{2f_l} \left( 1 - \frac{d}{f} \right) (x'^2 + y'^2) \right\} \\
&\quad \times \int_{-\infty}^{\infty} \int_{-\infty}^{\infty} e_{in}(x, y) \exp \left\{ -j \frac{2\pi}{\lambda_0 f_l} (x'x + y'y) \right\} dx dy, \tag{3.12}
\end{aligned}$$

where the impulse response of free space propagation  $\hat{h}_z(x, y)$  and the transmissivity of the lens  $t_{sl}(x, y)$  have been defined in Section 1.3.1, and  $(x', y')$  are the transverse Cartesian coordinates in the Fourier plane. In the case  $d = f_l$ , the quadratic phase term is canceled out and at the complex amplitude of the signal at the Fourier plane is

$$\begin{aligned}
e_{FP}(x', y') &\propto \int_{-\infty}^{\infty} \int_{-\infty}^{\infty} e_{in}(x, y) \exp \left\{ -j \frac{2\pi}{\lambda_0 f_l} (x'x + y'y) \right\} dx dy, \\
&= \mathcal{F} \left\{ e_{in}(x, y) \right\} \Big|_{\nu_x = \frac{x'}{\lambda_0 f_l}, \nu_y = \frac{y'}{\lambda_0 f_l}} = E_{in} \left( \frac{x'}{\lambda_0 f_l}, \frac{y'}{\lambda_0 f_l} \right). \tag{3.13}
\end{aligned}$$

This system is known as *Fourier-transforming*. Then, the wave at the Fourier plane travels through an amplitude and/or phase mask with transmittance  $t_H(x', y')$ , modulating the waveform. Finally, the modulated wave  $(E_{out}(x''/(\lambda_0 f_l), y''/(\lambda_0 f_l)) = E_{in}(x'/(\lambda_0 f_l), y'/(\lambda_0 f_l)) \cdot t_H(x', y'))$  passes through a second Fourier-transforming system ( $(x'', y'')$  being the Cartesian coordinates at the output plane). This second Fourier transformation process can be seen as an inverse Fourier transformation where the coordinate plane at the output is inverted. Therefore, the complete process can be seen as a convolution between the input signal and the inverse Fourier transform of the transmittance of the mask, i.e.,  $e_{out}(-x'', -y'') = e_{in}(x, y) \otimes \mathcal{F}^{-1} \{ t_H(x', y') \}$ .

However, a mask with a complex-value transmittance (i.e., containing amplitude and phase components) is difficult to fabricate using conventional printing techniques. Thus, coherent spatial optical filters were originally limited to those that have very simple transfer functions.

In 1963, A. B. Vander Lugt proposed and experimentally demonstrated a holographic-based configuration able to effectively control both the amplitude and phase of the filter's transfer function [151], using an amplitude-only mask. This configuration is known as Vander-Lugt filter and it can be applied as long as the corresponding impulse response is a real-valued function (note that in this

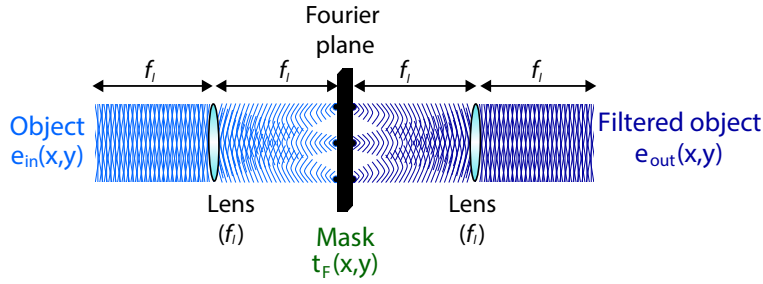


**Figure 3.4 – Spatial filtering process.** The first lens generates the Fourier transform of the object wave; in the Fourier plane (at twice the focal length  $f_l$  of the lens), an amplitude or phase mask modulates the traveling wave; finally a second lens in the same configuration at the previous one generates the Fourier transform of the modulated wave. The total system performs the operation of convolution. For simplicity, the coordinates in all the planes have been labeled as  $(x, y)$ .

case, the spatial impulse response-like waveform can be generated using a traditional amplitude-only mask).

For consistency, the same nomenclature employed in the description of the spatial domain optical filter will be used in the following derivation. The first step of the Vander-Lugt filtering process consists in creating a hologram that contains the amplitude and phase information of the target complex-valued transfer function  $H_F(\nu_x, \nu_y)$ . To this purpose, an input wave proportional to the filter's impulse response  $h_F(x, y) = \mathcal{F}^{-1}\{H_F(\nu_x, \nu_y)\}$  is launched through a Fourier-transforming system. At the Fourier plane, the propagating wave is proportional to the filter transfer function. At this point, this wave is holographically recorded by interfering with a reference plane wave  $e_{LO,1}(x, y)$ . The transmittance imprinted in the photosensitive plate is

$$t_F(x', y') \propto i_{LO,1} + i_{LO,1}^{1/2} H_F\left(\frac{x'}{\lambda_0 f_l}, \frac{y'}{\lambda_0 f_l}\right) \exp\{-j k \sin \theta_y y'\} \\ + i_{LO,1}^{1/2} H_F^*\left(\frac{x'}{\lambda_0 f_l}, \frac{y'}{\lambda_0 f_l}\right) \exp\{j k \sin \theta_y y'\}, \quad (3.14)$$

where we have assumed that  $i_{LO,1} \gg |H_F(x/(\lambda_0 f_l), y/(\lambda_0 f_l))|^2$ . The recording process of the filter transfer function is illustrated in Fig. 3.5(a).

Once the hologram has been recorded, any input information wave  $e_S(x, y)$  can be filtered with the complex-valued transfer function  $H_F(\nu_x, \nu_y)$  by simply applying the two-lens filtering procedure described above, as depicted in Fig. 3.5(b). As expected from the holographic configuration, the output wave will propagate with an angle equal to the angle between the reference wave and the wave with the transfer function information,  $\theta_y$ . The overall system performs the operation of convolution between  $e_S(x, y)$  and  $h_F(x, y)$ , which is the basis of spatial filtering.

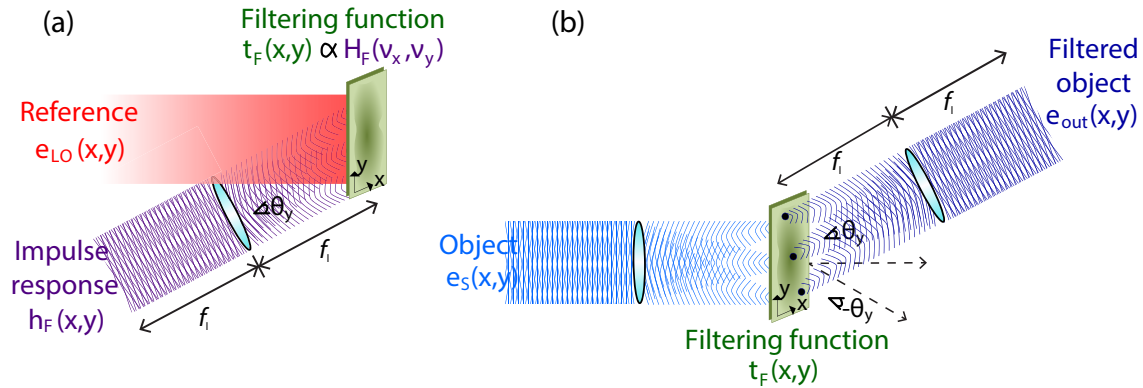


**Figure 3.5 – Vander-Lugt filter:** (a) Recording of the hologram, which contains information on the amplitude and phase of the complex-valued filter transfer function and (b) signal filtering process based on the concatenation of two Fourier-transforming systems and placing the hologram in the Fourier plane.

It is worth noting that in case the conjugate wave (propagating at an angle  $-\theta_y$ ) is inverse Fourier transformed, the operation of correlation is performed, instead of the convolution. The operation of correlation is useful in image-processing operations, including pattern recognition [167].

### 3.5 Conclusions

Classical holography (in the spatial domain) has been one of the more recognized inventions in the 20<sup>th</sup> century, and D. Gabor was awarded the Nobel prize in Physics for its discovery. With the maturity of holographic techniques, they have been widely employed in a broad range of areas. In this Chapter, the mathematical formalism of spatial domain holography has been briefly reviewed, with special interest in the configuration presented by Leith and Upatnieks. This configuration solved the main problem of Gabor’s original recording geometry, by angularly separating the different components resulting from this imaging system using different carrier angular frequencies for each of them. The concept of CGH has been also reviewed, which is an alternative to the traditional recording process. This procedure enables the generation of a target image by designing the required hologram in a computer. Finally, a well-know holography-based technique to implement signal processors has been discussed, namely the Vander-Lugt filter. Vander-Lugt filters enable the implementation of processing functionalities with complex-valued transfer functions using an amplitude-only mask. The concepts and mathematical formalism presented in this Chapter will serve as the basis of the ideas proposed in the remainder of the Thesis.

## Chapter 4

# Time-domain signal processing based on holographic concepts

### 4.1 Introduction to time-domain holography

Inspired by the space-time duality [56], the formal time-domain counterpart of spatial domain holography (outlined in Chapter 3) is presented. The concept of time-domain holography may provide appealing applications in a broad range of fields, since it allows the treatment of complex-envelope optical temporal information by use of simple amplitude-only (or phase-only) modulation and photodetection devices; significantly simplifying the generation and processing of complex-envelope optical signals. Such capability has become increasingly important in several fields, particularly in coherent high-speed optical telecommunications and ultrafast information-processing systems [6, 8, 152, 168, 169]. In these systems, the desired information is typically encoded in both amplitude and phase temporal variations. Additionally, the impairments undergone by data signals in an optical communication link or a signal-processing device affect both the amplitude and phase temporal signal profiles. In general, controlling the amplitude and phase temporal profiles in a simultaneous fashion is a difficult task and requires complicated setups as well as synchronization efforts, which are critical and very challenging when dealing with signals operating at ultra-high (Gbps) data rates.

It is important to note that generation of temporal interferograms containing amplitude and phase temporal information is well known and routinely used to extract phase information from intensity measurements. This process is known as heterodyne detection. In heterodyne detection schemes, the phase profile of a complex-envelope optical wave is retrieved using numerical Fourier-based algorithms. Alternatively, if the detected signal is to be processed, their in-phase and quadrature components need to be handled independently in the electrical domain, additionally requiring stringent synchronization. Time-domain holography goes one important step further by realizing that the detected interferogram can be readily used a temporal modulation function to generate any desired complex-envelope optical time-domain waveform, with fully customized amplitude and phase profiles. Hence, the amplitude and phase information of the target signal can be optically processed in a simultaneous fashion, using simplified schemes based on intensity-only sensitive components, and avoiding the need for synchronization tasks.

In this Chapter, we present the mathematical formalism of time-domain holography, inspired by the formalism reviewed in Chapter 3 for classical (spatial-domain) holography. Then, we discuss two different approaches to physically implement this new concept; namely, an electro-optic (EO) approach and an all-optical approach. The EO approach is based on the use of an opto-electronic (OE) photodetector for the recording step, and an EO intensity modulator plus a band-pass filter (BPF) for the signal reconstruction step. The all-optical approach is based on the nonlinear cross-phase modulation (XPM) effect. In the latter case, an approximation needs to be done so that the phase modulation process behaves as an amplitude modulation. Finally, several proof-of-concept applications will be experimentally demonstrated to prove the potential of time-domain holography for the generation, detection and processing of complex-envelope optical signals using significantly simplified schemes as compared with previous approaches. In particular, we prove: (i) generation and detection of optical data signals under complex-valued modulation formats, (ii) temporal phase conjugation and (iii) wavelength conversion of complex-envelope signals.

## 4.2 Mathematical formalism of time-domain holography

Here, a scheme similar to the one presented in Section 3.2 will be followed. However, in this Section and in the remainder of this Thesis, only temporal domain optical signals are considered, i.e., signals whose information is encoded in the temporal variation of electromagnetic waves. Time-

domain holography is presented then as a time-domain imaging system that can be divided in two steps. Although in the time domain, the name of these steps may not define properly the actual processes, for consistency they will be referred to as the “recording process” and the “reconstruction process” [153].

Let us define a complex-envelope optical information signal  $e_S(t)$ , which is a pure time-domain variation, as  $e_S(t) = \hat{e}_S(t) \exp\{j\omega_S t\}$ , where  $\hat{e}_S(t) = |\hat{e}_S(t)| \exp\{j\phi_S(t)\}$  is the complex amplitude envelope, and  $\omega_S$  denotes the optical carrier frequency. In the recording step, this signal interferes with a mutually coherent reference signal, which is selected to be a continuous wave (CW)  $e_{LO,1}(t) = i_{LO,1}^{1/2} \exp\{j\omega_{LO,1}t + \phi_{LO,1}\}$ , where  $i_{LO}$  is the constant optical intensity of the CW reference,  $\omega_{LO,1}$  is the reference optical carrier frequency and  $\phi_{LO,1}$  is an arbitrary constant phase. The interference between the information and reference signals is observed at the output of an optical coupler (OC), and the resulting time-domain intensity pattern  $i_H(t)$  is

$$\begin{aligned} i_H(t) &= |e_S(t) + j e_{LO,1}(t)|^2 \\ &= |\hat{e}_S(t)|^2 + i_{LO,1} + 2|\hat{e}_S(t)| i_{LO,1}^{1/2} \sin(\omega_i t + \phi_S(t) - \phi_{LO,1}), \end{aligned} \quad (4.1)$$

where  $j = (-1)^{1/2}$  is associated with the  $\pi/2$  phase difference induced by the OC, and  $\omega_i$  is an intermediate frequency  $\omega_i = \omega_S - \omega_{LO,1}$ . This recorded temporal interferogram can be interpreted as the time-domain equivalent of a spatial hologram (Eq. 3.1) and consequently, it will be referred here as the *temporal hologram*.

The frequency spectrum of this temporal hologram is

$$\begin{aligned} I_H(\omega) &= E_{s0}(\omega) \otimes E_{s0}^*(-\omega) + i_{LO,1} \delta(\omega) \\ &\quad + 2\pi i_{LO,1}^{1/2} E_{s0}(\omega - \omega_i) \exp\{-j(\phi_{LO,1} + \pi/2)\} \\ &\quad + 2\pi i_{LO,1}^{1/2} E_{s0}^*(-\omega - \omega_i) \exp\{j(\phi_{LO,1} + \pi/2)\}, \end{aligned} \quad (4.2)$$

where  $\otimes$  represents convolution,  $*$  represents complex conjugation,  $\omega$  is the angular frequency and  $E_{s0}(\omega) = \mathcal{F}\{\hat{e}_S(t)\}$ . Thus, if the information signal  $\hat{e}_S(t)$  has an angular frequency bandwidth of  $2\pi B$  rad/s, the first term in the right hand side (RHS) of Eq. 4.2 (the so-called autocorrelation or ambiguity term) has a bandwidth of  $\sim 2(2\pi B)$  rad/s (the second component of the RHS is an ideal delta, with zero spectral support around  $\omega = 0$ ). To avoid spectral overlapping between

this first term and the sine term of Eq. 4.1, the intermediate frequency should be fixed so that  $\omega_i \geq 3(2\pi B)/2$ . As a result, the bandwidth of the temporal hologram is at least four times higher than that of the optical signal under analysis, in consistency with the spatial-domain case for the configuration proposed by Leith and Upatnieks [67], see Fig. 3.2. Inspired by spatial-domain holography concepts, it is worth noting that in Eq. 4.1, the first term in the RHS may be neglected if the reference intensity is sufficiently strong, i.e. whenever  $i_{LO,1} \gg |\hat{e}_S(t)|^2$ . If this condition is accomplished, the intermediate frequency may be selected to be  $\omega_i \geq (2\pi B)/2$ , leading to a two fold decrease of the bandwidth specifications.

The next step in the time-domain holography process is the reconstruction of the original complex information. To this purpose, a second optical CW reference signal,  $e_{LO,2} = i_{LO,2}^{1/2} \exp\{j\omega_{LO,2}t\}$ , is employed as a carrier in a simple modulation process, typically an amplitude modulation, which is driven by a signal proportional to the temporal hologram  $i_H(t)$  in Eq. 4.1. In exact analogy with its spatial-domain counterpart (Fig. 3.1(b)), the generated optical signal has a frequency spectrum composed by the four terms in Eq. 4.2, but spectrally shifted by the reference optical frequency,  $\omega_{LO,2}$ :

$$\begin{aligned} E_{out}(\omega) \propto & E_{s0}(\omega - \omega_{LO,2}) \otimes + E_{s0}^*(-\omega - \omega_{LO,2}) + i_{LO,1}\delta(\omega - \omega_{LO,2}) \\ & + 2\pi i_{LO,1}^{1/2} E_{s0}(\omega - \omega_{out,S}) \exp\{-j(\phi_{LO,1} + \pi/2)\} \\ & + 2\pi i_{LO,1}^{1/2} E_{s0}^*(-\omega - \omega_{out,-S}) \exp\{j(\phi_{LO,1} + \pi/2)\}, \end{aligned} \quad (4.3)$$

where the central frequencies of the terms proportional to the original information signal and to its conjugate have been redefined as  $\omega_{out,S} = \omega_S - \omega_{LO,1} + \omega_{LO,2}$  and  $\omega_{out,-S} = -\omega_S + \omega_{LO,1} + \omega_{LO,2}$ , respectively.

In line with our discussions above, the first term in the RHS of Eq. 4.3 may be neglected whenever  $i_{LO,1} \gg |\hat{e}_S(t)|^2$ . Finally, the complex-field (amplitude and phase) information optical signal can be recovered from the modulated waveform by simply filtering in the corresponding spectral component, using a suitable optical BPF centered at  $\omega_{out,S}$ . The employed filter should ideally exhibit a flat-top spectral amplitude response and a linear spectral phase profile over the bandwidth of the information signal. The band-pass filtering procedure is the time-domain equivalent of the image selection process by angular diffraction in spatial holography.

The frequency of the CW source used to reconstruct the complex waveform ultimately determines the central optical frequency of the information term to be filtered in. In general, this procedure easily enables to locate the generated optical waveform around the wavelength of interest, effectively implementing a complex-envelope signal's wavelength conversion process. Wavelength conversion is emerging as a fundamental functionality in WDM networks, allowing transparent interoperability, contention resolution, wavelength routing, and, in general, better utilization of the network resources under dynamic traffic patterns [14, 22–30, 170–180]. In the case the reconstructing reference signal is selected to be a CW at the same frequency of the CW employed in the recording process, i.e., if  $\omega_{LO,2} = \omega_{LO,1}$ , the reconstructed information signal will be centered at the same frequency of the original signal (at  $\omega_S$ ), achieving wavelength-preserving operation.

Notice also that the modulating signal is composed by the target signal and its temporal conjugate. Thus, if the band-pass filtering procedure is implemented to select the spectral component corresponding to the conjugated signal, one could directly achieve the temporal phase conjugation (TPC) of the original optical waveform. TPC is an interesting tool for a variety of signal processing functionalities in diverse areas such as laser technologies, optical data processing, or impairments compensation (such as dispersion or nonlinear effects) for coherent-light transmission in fiber-optic telecommunication links [39–42]. These two interesting applications of time-domain holography will be described in detail and experimentally demonstrated below in this Chapter.

In this Section, the basis of time-domain holography has been introduced, but no physical implementation has been presented. Next, we propose two different methods to implement time-domain holography: (i) an electro-optical approach and (ii) an all-optical approach.

### 4.3 Electro-optical approach

A straightforward procedure to physically implement time-domain holography is based on the use of EO components. A scheme of this EO approach is depicted in Fig. 4.1. For the recording step, the interference pattern  $i_H(t)$  between the original information signal and the reference signal  $e_{LO,1}(t)$  can be recorded using, e.g., a high-speed photodetector (PD). The temporal hologram  $i_H(t)$  is then an electrical signal that contains the complete information (in amplitude and phase) of the complex envelope of  $e_S(t)$ .

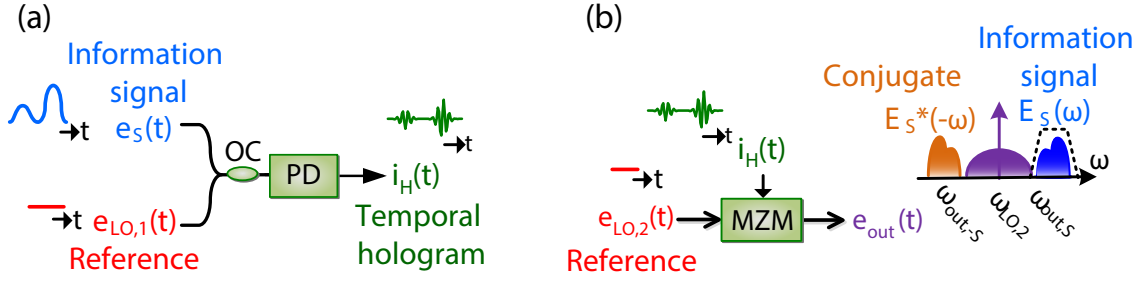


Figure 4.1 – Implementation of the concept of time-domain holography as the temporal counterpart of spatial-domain holography. (a) Generation of the temporal hologram; (b) Retrieval of the complex information signal. For the sake of simplicity, the optical temporal signals are represented by their amplitude envelope. OC, optical coupler; PD, photodetector; MZM, Mach-Zehnder modulator.

This method for complex-envelope optical signal detection based on PDs is extensively employed nowadays, known as *heterodyne detection*. Typically, current heterodyne detectors rely on two PDs, following a configuration known as balanced photodetection [152]. The signals  $e_S(t)$  and  $e_{LO,1}(t)$  are added in phase and counter phase in each PD, and the resulting electrical waveforms are conveniently subtracted. Only the third term in the RHS of Eq. 4.1 remains, removing the autocorrelation term (i.e., the so-called ambiguity term in Chapter 3). In this case, the bandwidth requirements of the detection process are reduced by two fold, i.e., the photodetection bandwidth should be at least twice that of the information signal, or, in other words, the intermediate frequency should be fixed to satisfy  $\omega_i \geq 2\pi B/2$ .

The use of a reference signal with an intensity much higher than the intensity of the information signal can be readily exploited to relax by half the bandwidth requirements in the typical optical heterodyne phase detection scheme using a *single PD*. If the above condition ( $i_{LO,1} \gg |\hat{e}_S(t)|^2$ ) is satisfied, the photodetection bandwidth should be only twice broader than the bandwidth of the information signal (instead of four times). As already mentioned, this bandwidth requirement is similar to that of balanced dual photodetection schemes, but in this case we use only one PD. Nevertheless, balance photodetection is expected to provide higher performance in terms of signal-to-noise ratio [181, 182], since it makes use of the power at the two outputs of the OC placed before the balanced PD. Additionally, the two first terms of Eq. 4.3 are completely canceled out in the electrical domain, offering a cleaner response for decreased reference signal power requirements.

On the other hand, the signal reconstruction step can be practically carried out using a single Mach-Zehnder modulator (MZM). A MZM is an amplitude modulator implemented by interferometrically combining two waves with different phase change. The phase change is achieved via

the the Pockels effect<sup>1</sup> [19, 183, 184], where the refractive index of the medium (a crystal) changes proportionally to the applied electric field, resulting in a change of the phase of the wave passing through the crystal. The splitting and combination of waves is done by use of two directional OCs in a Mach-Zehnder interferometer configuration [12]. The MZM modulates the CW signal  $e_{LO,2}(t)$  and the modulating signal is proportional to  $i_H(t)$ , as shown in Fig. 4.1(b). A graphic example of the spectrum of the optical signal at the MZM output is represented in Fig. 4.1(b). The bias point of the MZM must be chosen so that the bias voltage plus the DC value of the electrical signal (whose modulated spectral response is described by the second term in the RHS of Eq. 4.3) corresponds to the MZM's minimum transmission point, eliminating the strong discrete tone at  $\omega_{LO,2}$ . Finally, the spectral band proportional to the target information signal  $e_S(t)$  is filtered in by a BPF. It is important to note that no synchronization tasks are needed to generate the complex information signal, contrary to the case in which an IQ modulator is used, which requires precise synchronization between the in-phase and quadrature components. The price to pay for achieving full control of complex-envelope information signals using e.g., intensity-only modulation is the fact that the required processing bandwidth is at least two fold the bandwidth of the target optical signal.

The scheme employed for the holographic reconstruction step in temporal holography (i.e., an intensity-modulator followed by a BPF) is similar to the scheme used to perform single-side band modulation with carrier suppression (SSB-CS) [46]. However, both applications should not be confused: in SSB modulation, the target signal carries information encoded only in amplitude. The spectrum of this signal is then symmetrical. Thus, a BPF is employed to filter in half of the total signal's spectral content, allowing a more efficient utilization of the spectrum. Time-domain holography deals with a different problem; the target signal has information encoded in amplitude and phase, and the spectrum is duplicated to be able to employ an amplitude-only modulation process for the generation of the target signal.

### 4.3.1 Computer-generated temporal holograms

The temporal hologram may be also created numerically through a process that can be interpreted as the time-domain counterpart of CGH [165, 166], and therefore, we refer it to as a computer-generated temporal hologram (CGTH). The recording step of holography is computationally mod-

---

<sup>1</sup>The Pockels effect is a nonlinear effect governed by  $\chi^2$ , see Eq. 1.1, which typically occurs in non-centrosymmetric media.

eled by numerically emulating the photodetected signal in Eq. 4.1, taking into consideration the desired complex-envelope optical information signal,  $e_S(t)$ , to be subsequently generated. As in the spatial domain (Section 3.3), the two first components of Eq. 4.1 can be directly omitted, which translates into the above-described two-fold photodetection/modulation bandwidth decrease. The numerically computed temporal hologram can be practically generated by means of an electrical arbitrary waveform generator (AWG), as shown in Fig. 4.2(b).

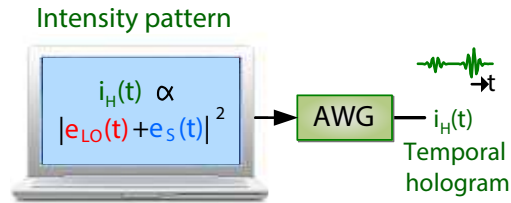


Figure 4.2 – The temporal hologram can be created by computationally modeling the interference pattern between the information signal and a reference CW signal, and generating this interference pattern via an arbitrary waveform generator (AWG).

## 4.4 All-optical approach

The EO approach represents a straightforward method for implementing time-domain holography, as it employs devices that are sensitive to temporal intensity-only variations. Although that procedure significantly reduces the circuitry complexity and avoids the need for precise synchronization between the in-phase and quadrature components of a complex-envelope signal in any generation or detection scheme, still the use of electronics imposes a stringent limitation in the operation bandwidth of the system.

To overcome this bandwidth limitation, we have developed a novel scheme to perform time-domain holography in the all-optical domain [155]. The scheme relies on a phase-only modulation process, instead of amplitude modulation, which is carried out all-optically by means of an XPM process in a highly nonlinear fiber (HNLF). Note that, to date, XPM has been employed to perform phase-only or intensity-only<sup>2</sup> all-optical modulation.

Similarly to the described procedure in Section 4.2, the recording step of all-optical holography involves the generation of a linear interference between the optical input signal to be processed,  $e_S(t)$ , and the coherent CW light beam,  $e_{LO,1}(t)$ , by means of an OC. The temporal hologram, i.e.,

<sup>2</sup>Intensity modulation is achieved by using XPM inside an interferometer, similarly to the electro-optical MZM.

the intensity of the interference pattern, is described by the expression in Eq. 4.1. However, in this case, no PD is employed to generate this intensity signal. Instead, the interference signal acts as the pump in the following XPM stage, and its power is defined as

$$P_{pump}(t) = i_H(t) \cdot A_{eff}, \quad (4.4)$$

where  $A_{eff}$  is the effective area of the waveguide through which the propagation mode is traveling (a HNLF in the proposed configuration).

According to holography's theory, amplitude modulation of a reference signal is required to generate the desired complex-envelope signal from the information encoded in the hologram. However, under certain conditions, phase modulation can also be applicable, as we detail in what follows. The reconstructing reference signal is a low-power CW light beam,  $e_{LO,2}(t)$ , with carrier frequency  $\omega_{LO,2}$ . Both the pump and reference signals then propagate through a HNLF, and the expression of the reference after undergoing XPM is [19]

$$e_{out}(t) = e_{LO,2}(t) \cdot \exp \left\{ j 2\gamma P_{pump}(t) L \right\}, \quad (4.5)$$

where  $\gamma$  and  $L$  are the nonlinear coefficient and the length of the HNLF, respectively. Substituting Eq. 4.4 into Eq. 4.5 and expanding the terms of  $i_H(t)$ , the signal at the output of the HNLF is

$$e_{out}(t) = e_{LO,2}(t) \cdot \exp \left\{ j 2\gamma L A_{eff} i_{LO,1}^{1/2} |\hat{e}_S(t)| \sin(\omega_i t + \phi_S(t)) \right\}. \quad (4.6)$$

In Eq. 4.6, three assumptions have been done: (i) the constant term of  $i_H(t)$  has been omitted, as it just adds a constant phase to  $e_{out}(t)$ ; (ii) the autocorrelation (ambiguity) term has been neglected, considering that the condition  $i_{LO,1} \gg |\hat{e}_S(t)|^2$  is accomplished, and (iii) as the reference signal  $e_{LO,1}(t)$  is a coherent CW light, its phase  $\phi_{LO,1}$  has been omitted for simplicity.

If the phase modulating term  $2\gamma L A_{eff} i_{LO,1}^{1/2} |\hat{e}_S(t)| \ll \pi$ , the process is within the limit of *narrowband phase modulation*<sup>3</sup> [46], and Eq. 4.6 can be further simplified to

$$e_{out}(t) = i_{LO,2}^{1/2} \exp\{j\omega_{LO,2}t\} \cdot \left( 1 + j 2\gamma L A_{eff} i_{LO,1}^{1/2} |\hat{e}_S(t)| \sin(\omega_i t + \phi_S(t)) \right). \quad (4.7)$$

---

<sup>3</sup>Note that the following approximation can be used:  $e^{j\varepsilon} \approx (1 + j\varepsilon)$  if  $\varepsilon \ll \pi$ .

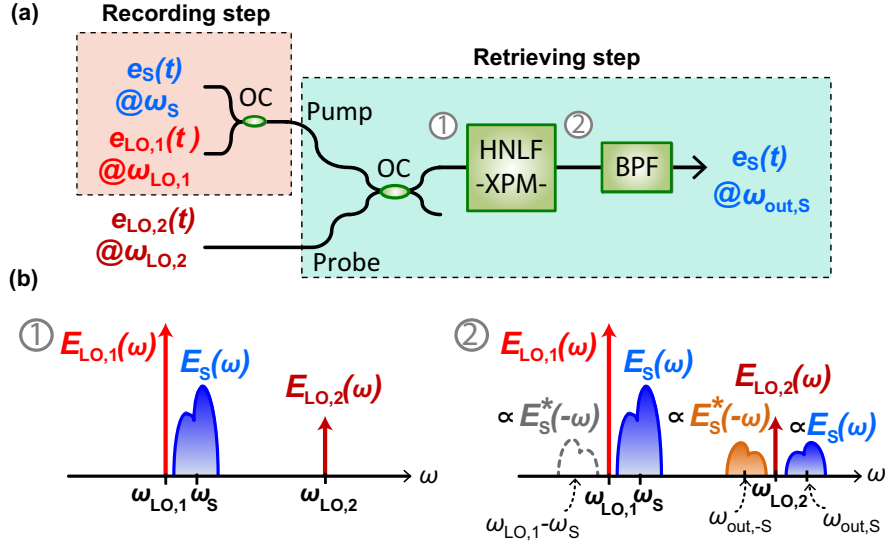


Figure 4.3 – (a) Scheme for performing time-domain holography based on XPM. In this case, both the recording and the retrieving processes are concatenated; (b) Spectra before and after the highly nonlinear fiber (HNLF): Blue components represent the information signal, the yellow component represents the conjugated signal and the dashed grey component represents the conjugated signal resulting from four wave mixing (FWM) between the pump’s components.

Equation 4.7 shows that  $e_{out}(t)$  has three components in the spectral domain: (i) a pure tone at  $\omega_{LO,2}$ , (ii) a copy of the original information signal  $e_S(t)$  centered at  $\omega_{out,S} = \omega_{LO,2} + \omega_S - \omega_{LO,1}$ , and (iii) a copy of the temporal conjugate of  $e_S(t)$  ( $e_S^*(t)$ ) centered at  $\omega_{out,-S} = \omega_{LO,2} - \omega_S + \omega_{LO,1}$  (Fig. 4.3). These components are well separated in the spectral domain if  $\omega_i (= \omega_S - \omega_{LO,1}) \geq 2\pi B/2$ . Finally, a BPF is required to select either the wavelength converted signal (at  $\omega_{out,S}$ ) or its temporal conjugate (at  $\omega_{out,-S}$ ).

Figure 4.3(b) illustrates the spectra at the input of the HNLF and at its output, where a component proportional to  $e_S(t)$  and to its conjugate have been generated around  $e_{LO,2}(t)$  through XPM. An additional copy of  $e_S^*(t)$  (depicted in grey in Fig. 4.3(b.2)) is expected to be induced around  $e_{LO,1}(t)$  by degenerate four wave mixing (FWM) between this strong CW pump and the input signal.

Note that an exact copy of  $e_S(t)$  and  $e_S^*(t)$  appear at the frequencies  $\omega_{out,S}$  and  $\omega_{out,-S}$  only if the condition  $2\gamma L A_{eff} i_{LO,1}^{1/2} |\hat{e}_S(t)| \ll \pi$  is fulfilled. In this case, the phase modulation affects the reference signal  $e_{LO,2}(t)$  in the same manner as an intensity modulation process, causing a spectral broadening around  $\omega_{LO,2}$  proportional to the spectrum of  $P_{pump}(t)$ . In the described scenario, i.e., with three signals propagating through a HNLF, a FWM process may occur as long as the phase matching condition is accomplished. If this was the case, an exact copy of the information signal and

its conjugate would also appear at the frequencies  $\omega_{out,S}$  and  $\omega_{out,-S}$ . In this case, the occurrence of FWM in the HNLF can add up power at the spectral regions of interest, which add coherently with the results of the XPM process.

## 4.5 Applications of time-domain holography

Classical holography finds applications in a broad range of fields, including the highly spread application of recording and displaying three-dimensional images, but also in optical signal processing, data storage, microscopy, or security, among others [13]. Considering the vast range of applications of classical holography, we foresee a similarly vast number of interesting uses for its time-domain counterpart. Time-domain holography allows the treatment of complex optical temporal information by use of amplitude-only or phase-only-based modulation and photodetection devices. Thus, any application requiring the managing of complex-envelope signals can be significantly simplified with respect to traditional approaches.

In this Section, we propose some interesting applications of the newly introduced concept. In particular, we show the generation [153] and processing, i.e., TPC [158], of complex-envelope optical signals based on the EO approach. Also, wavelength conversion of complex-envelope signals is presented using the all-optical approach [155]. The validity of all the proposed ideas is proven through experimental demonstrations.

### 4.5.1 Generation and detection of complex-envelope optical signals

The generation and detection of optical waveforms (e.g. data streams) with arbitrary complex (amplitude and phase) temporal profiles is a topic of increased interest, e.g. due to the introduction of advanced complex modulation formats in optical telecommunication networks [152]. Solutions to date require the use of EO modulators and OE detectors able to simultaneously detect or control the amplitude and phase of complex-envelope optical waveforms. These devices are typically implemented using interferometric schemes with suitable, precise phase adjustments, and as such, they are generally costly and difficult to control [126, 152].

Here, we apply time-domain holography concepts to the generation of arbitrary, user-defined complex-envelope temporal signals by intensity-only modulation of CW light [153]. In particular, for a proof of concept, two distinct optical complex-envelope signals are targeted. First, a stream of 16 arbitrarily chirped optical Gaussian pulses is generated to prove that the proposed technique has the capability to generate optical waveforms with purely arbitrary, user-defined temporal phase profiles. Secondly, as a more practically relevant example, a telecom 1024-symbol 3-Gbps optical data stream under a 16-state Quadrature Amplitude Modulation (16-QAM) format is experimentally generated.

The generation of the target complex-envelope waveforms is based on the concept of CGTH (Section 4.3.1). The experimental setup is shown in Fig. 4.4. A CW laser generates a reference signal centered at  $f_{LO,2} = \omega_{LO,2}/2\pi = 193.381$  THz ( $\lambda_{LO,2} = f_{LO,2}/c_0 = 1550.27$  nm, where  $c_0$  is the speed of light in vacuum), which is split by a 10/90 OC for further use in the generation (90% of the power) and the subsequent detection processes (10% of the power).  $f_{LO,2}$  is selected to be the same carrier frequency as the one employed in the computer-based generation process,  $f_{LO,1}$ . The CW light acts as a carrier for a 10-GHz dual-drive MZM (5.1-V biased, corresponding to its minimum transmission point). The modulator is driven by an electrical waveform  $i_H(t)$  (temporal hologram), which is numerically designed based on CGTH. The time-domain hologram  $i_H(t)$  is then practically generated using an electronic AWG, namely the AWG-7122C from Tektronix with an analog 3dB-bandwidth of 9.6 GHz (sampling rate of 24 GSps). The MZM optical output has a complex envelope proportional to  $i_H(t)$  and is centered at  $f_{LO,2}$ . Hence, the lobe corresponding to the spectrum of  $e_S(t)$ , which is shifted by  $f_i = \omega_i/2\pi = 4.5$  GHz with respect to  $f_{LO,2}$ , is centered at  $f_S = \omega_S/2\pi = 193.385$  THz ( $\lambda_S = f_S/c_0 = 1550.24$  nm). Obviously, the optical central frequency of the generated signal can be easily tuned by correspondingly tuning the oscillator frequency  $f_{LO,2}$ . After an amplification stage, the resulting modulation signal is band-pass filtered using a tunable optical filter (Santec OTF-350) centered at  $f_S$ , and the complex desired data stream is finally generated.

To validate this claim, the intensity and phase temporal profiles of the resulting optical signal are measured by the time-domain holography-based recording step. The recording process is carried out using a single 10-GHz PD attached to a real-time oscilloscope, namely, the DSO90254A Infiniium from Agilent, with a sampling rate of 28 GSps. The losses in the upper arm of Fig. 4.4 intrinsically introduce a sufficiently high power difference to satisfy the above stated condition  $i_{LO,1} \gg |\hat{e}_S(t)|^2$ , leading to the anticipated two-fold increased bandwidth efficiency. In all tested

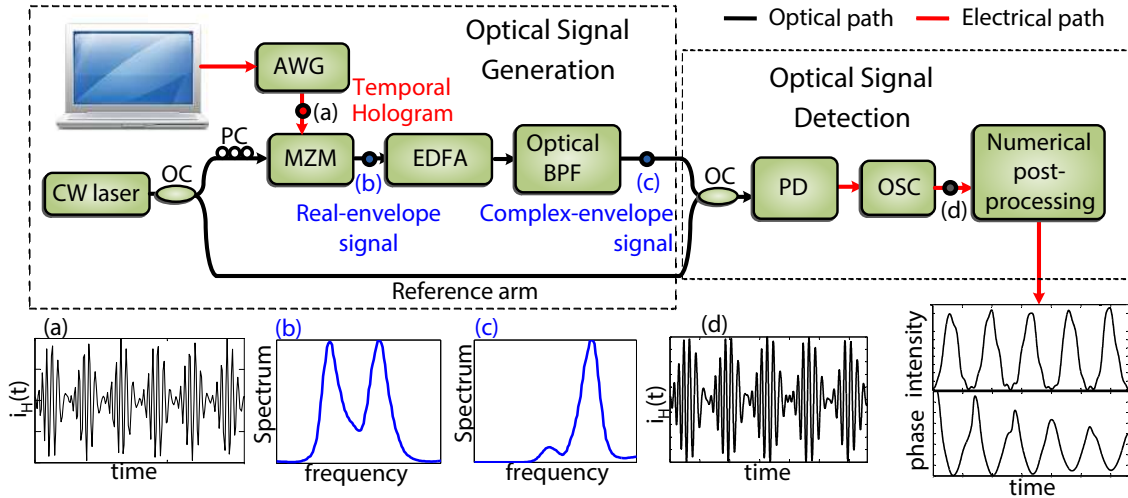


Figure 4.4 – Setup used to generate optical complex-envelope optical signals based on the concept of CGTH, i.e, using a single MZM and a BPF. The figure also shows the signal in time (black) and frequency (blue) along the setup. The optical path is represented by black lines, whereas the electrical path is represented by red lines. AWG, arbitrary waveform generator; CW, continuous wave; MZM, Mach-Zehnder modulator; EDFA, Erbium-doped fiber amplifier; BPF, band pass filter; PD, photodetector; OSC, real-time oscilloscope.

cases, the photodetected temporal interferogram is nearly identical to the numerically designed temporal hologram, validating the above-described numerical design procedure and overall time-domain holography theory. Finally, the intensity and phase temporal profiles of the signal under test are numerically recovered from the recorded temporal interferogram using a conventional Fourier transform – based algorithm [185], enabling further validation through a direct comparison with the target data. Note that the frequency bandwidth of the modulating time-domain waveform (temporal hologram), which in turn determines the bandwidth of the generated complex-envelope optical waveform, is limited by either the operation bandwidth of the MZM or the processing speed of the employed AWG.

#### 4.5.1.1 Arbitrary chirped Gaussian pulses

The complex envelope of the target optical stream of 16 chirped Gaussian pulses is given by

$$\hat{e}_S(t) = A \cdot \sum_{m=1}^{16} \exp \left\{ - \frac{(1 - j C_m) (t - m T_S)^2}{2 T_0^2} \right\}, \quad (4.8)$$

where  $A$  is the pulses' constant peak amplitude,  $T_0$  ( $= 260$  ps) defines the time width of each Gaussian waveform,  $C_m$  is the chirp parameter and  $T_S$  ( $= 1.3$  ns) is the sequence period. The

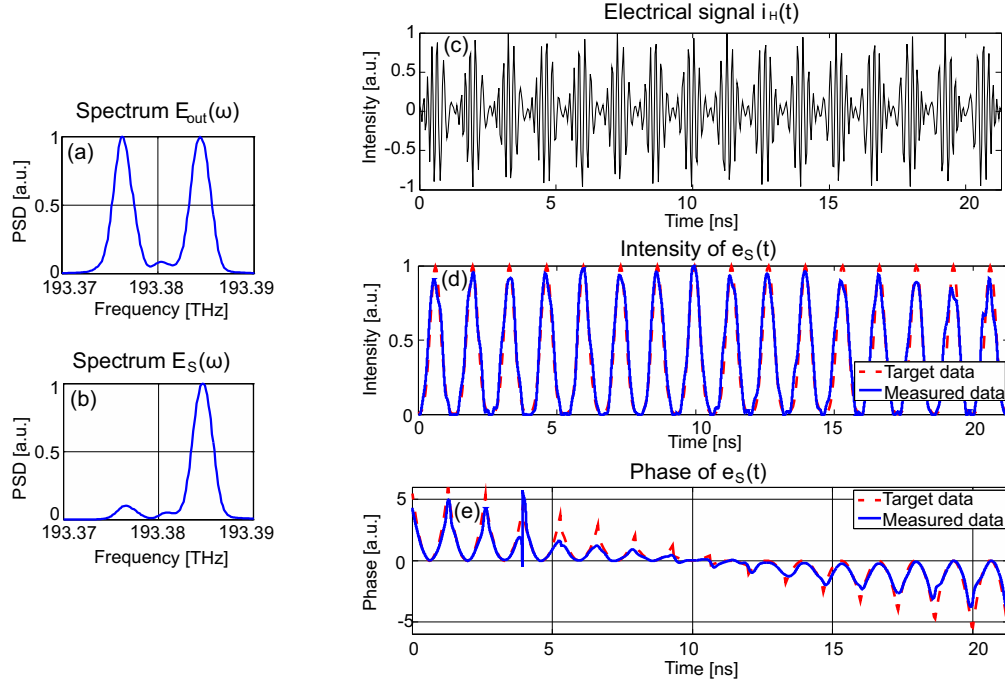


**Figure 4.5** – 16-symbol sequence of arbitrary chirped Gaussian pulses. (a) Power spectral density (PSD) of the optical signal after the intensity modulation; (b) PSD of the optical signal after the band pass filtering; (c) Electrical signal  $i_H(t)$  generated by the AWG; (d) Intensity of the generated waveform (solid blue line) and target intensity (dashed red line); (e) Phase of the generated complex-envelope waveform (solid blue line), obtained by applying off-line digital signal processing to the electrical interferogram measured in the detection process, and target phase profile (dashed red line).

stream is designed such that each pulse in the data stream exhibits a different chirp value. In particular,  $C_m$  ranges from  $C_1 = 2$  to  $C_{16} = -2$ . The computationally designed temporal hologram  $i_H(t)$  has a 3dB bandwidth of  $\sim 6$  GHz and is plotted in Fig. 4.5(c). The spectra of the optical modulated signals after the MZM and after the optical BPF are represented in Fig. 4.5(a) and (b), respectively. The latter corresponds to the spectrum of the target optical complex-envelope pulse stream  $\propto e_S(t)$ , centered at the desired optical frequency  $f_S$ . Figures 4.5(d) and 4.5(e) show the measured intensity and phase temporal profiles of the generated optical signal, together with the target data. The figure shows an excellent agreement between the measured (blue curve) and the target complex-envelope waveform (dashed red curve), in both amplitude and phase profiles.

### 4.5.1.2 16-QAM modulated data stream

The second example proves the generation of a telecom 1024-symbol 3-Gbps 16-QAM modulated data stream. Its complex envelope is defined as

$$\begin{aligned}\hat{e}_S(t) &= \sum_{m=1}^{1024} \left[ r_m \cdot \exp \left\{ -\frac{1}{2} \frac{(t - mT_S)^2}{T_0^2} + j \cdot \phi_m \right\} \right], \\ r_m &= \sqrt{i_m^2 + q_m^2}, \quad \phi_m = \arctan \left( \frac{q_m}{i_m} \right),\end{aligned}\tag{4.9}$$

where  $i_m$  and  $q_m$  are the in-phase and quadrature components of the signal, respectively,  $T_0$  (= 150 ps) defines the time-width of each Gaussian pulse in the data sequence and  $T_S$  (= 1.3 ns) is the inter-symbol period. The computationally designed temporal hologram  $i_H(t)$  has a 3dB-bandwidth of 6.8 GHz and is plotted in Fig. 4.6(a). The desired data stream is generated using the intensity-only modulation scheme illustrated in Fig. 4.4. Figures 4.6(b) and (c) present the measured temporal intensity and phase profiles of the generated data stream over 16 consecutive symbols, showing an excellent agreement with the target data. Clearly, the desired data stream, with 4 discrete levels of amplitude and 8 discrete levels of phase, is successfully generated: Figure 4.6(d) shows the constellation (or symbol diagram) obtained from the generated 1024-symbol data stream.

To quantify the amount of error introduced by the generation scheme, we have calculated the error vector magnitude (EVM) in the case of the 16-QAM signal, measured with respect to the maximum power,  $\text{EVM}_m$  [186]. The EVM provides a measurement of the deviation of a symbol in the constellation in relation with its ideal position, and it is calculated as

$$\text{EVM}_m = \sqrt{\frac{\frac{1}{M} \sum_{m=1}^M \left( (i_m - i'_m)^2 + (q_m - q'_m)^2 \right)}{(i_{max}^2 + q_{max}^2)}},\tag{4.10}$$

where  $M$  is the number of received symbols,  $i_m$  and  $q_m$  represent the ideal in-phase and quadrature components;  $i'_m$  and  $q'_m$  are the measured components and  $i_{max}$  and  $q_{max}$  are the components of the symbol of maximum power. The obtained value of EVM is equal to 15.5%. Note that the constellation shown in Fig. 4.6(d) has been calculated by using the value of amplitude and phase at the center of each symbol from the analog electrical signal measured in an oscilloscope, i.e.,

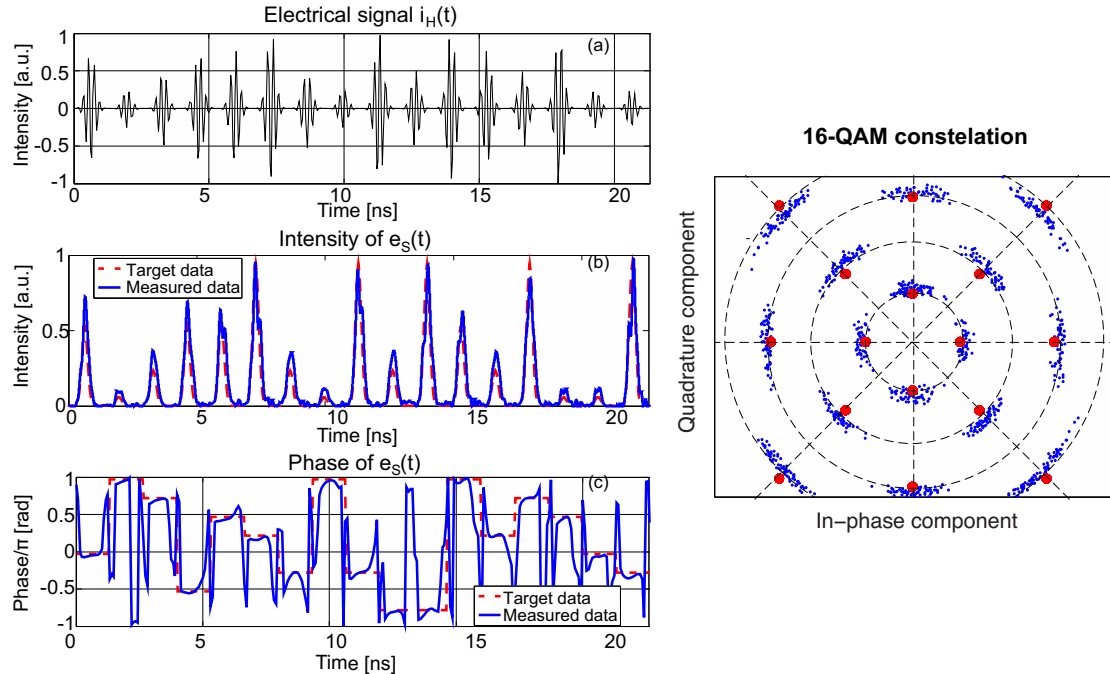


**Figure 4.6 – 1024-symbol 16-QAM optical data stream.** (a) A portion of the numerically designed temporal hologram, shown over 16 consecutive symbols, as generated by the electrical AWG; (b) Intensity and (c) phase profiles of the generated complex-envelope optical signal (solid blue line) and target data stream (dashed red line) over the signal portion (16 symbols) shown in (a); (d) Constellation of the generated data stream (blue points) and ideal constellation of a 16-QAM signal.

no front-end correction or additional optimization algorithms have been employed. Hence, the estimated EVM clearly indicates that the induced distortion in the generation process is relatively small, considering that, for 16-QAM modulated signals, it is generally accepted that the transmitted information is detectable if the  $EVM_m$  remains lower than 18% [186]. It is worthy mentioning that the measured error is induced not only by the generation process but also by the holographic detection process (i.e., based on a single PD).

The results presented above convincingly prove the concepts introduced in this Chapter. Further optimization of the employed experimental setups would enable to minimize some of the observed deviations in the generated optical complex-envelope waveforms. A main source of deviations in our specific experimental setup concerns the broad transition band of the used BPF, preventing a complete and accurate filtering out of the unwanted spectral content from the modulated optical signal. On the other hand, the plotted results of the output phase also present some deviations due to the noise in the photodetection procedure.

### 4.5.2 Temporal phase conjugation

Optical time-domain phase conjugation (TPC) involves conjugating the optical information in the time domain, which translates into a conjugation and a spectral inversion of the original optical information in the frequency domain. TPC has been widely investigated for mid-span spectral inversion (MSSI), allowing the compensation of even-order chromatic dispersion and several kinds of nonlinear impairments (such as self-phase modulation or intra-Raman scattering) on optical data signals propagating along long-haul, high-speed optical fiber communication systems [41, 187]. More generally, optical TPC is an interesting tool for a variety of signal processing functionalities, e.g., for direct recovery of the IQ components of an incoming complex-envelope optical waveform.

A straightforward scheme to perform TPC employs the detection of the amplitude and phase of the complex-envelope signal to be conjugated by means of a balanced OE-PD. Then, the resulting signal is conjugated in the electrical domain and converted again into the optical domain by the employment of e.g., an EO-IQ modulator [4]. As discussed above, EO-OE schemes require duplicated circuitry for the IQ components of the signals, which have to be precisely synchronized.

To overcome these limitations, several techniques have been proposed and experimentally demonstrated to carry out TPC directly in the all-optical domain. Most of them rely on parametric nonlinear effects, such as FWM in optical fiber [39–41], or in semiconductor optical amplifiers (SOAs) [42]. TPC can be directly achieved through degenerate or quasi-degenerate FWM, which results in an idler signal that is the temporal conjugate of the probe signal. One of the main drawbacks of this parametric technique is the fact that the wavelength of the phase-conjugate light is generally shifted from the original light. Whereas mechanisms have been demonstrated for wavelength-preserving TPC based on a FWM process [41, 188, 189], they typically involve the use of two well-controlled orthogonal pump beams, significantly hindering the practical realization and applicability of the scheme. Furthermore, the efficiency of a FWM process is limited to the accomplishment of the phase-matching condition between the pumps and the probe, which requires a very precise control of the dispersion characteristics of the used nonlinear medium [19].

TPC based on time domain holography greatly simplifies the straightforward method based on phase-sensitive OE detection and EO modulation, requiring only the use of intensity-only light detection and modulation devices combined with a BPF. Moreover, this method provides a high degree

of flexibility to center the conjugated output at the desired wavelength, including the possibility of wavelength-preserving operation, and it also avoids the need for any processing in the electronic domain (particularly, phase detection and conjugation). This method for TPC can be interpreted as an exact time-domain dual procedure of the spatial holographic technique for generation of the real image of an object (see Section 3.2).

The proposed setup for TPC is shown in Fig. 4.7 [158]. It comprises the concatenation of the detection and the reconstruction steps of holography. The spectrum of the signal at the output of the MZM is defined by the expression in Eq. 4.3 (Fig. 4.7(2)). Thus, the scheme enables centering the generated TPC at the desired frequency by simply properly fixing the frequency of the reference signal  $e_{LO,2}(t)$ . In particular, wavelength preserving TPC can be achieved when  $f_{LO,2} = 2f_s - f_{LO,1}$ . Note that there is no need for signals' synchronization in this scheme. In this case, a BPF centered at  $f_s$  allows selecting the conjugated component,

$$e_{BPF}(t) \propto i_{LO,1}^{1/2} |\hat{e}_S(t)| \exp \{ j 2\pi f_s t - j \phi_S(t) \}. \quad (4.11)$$

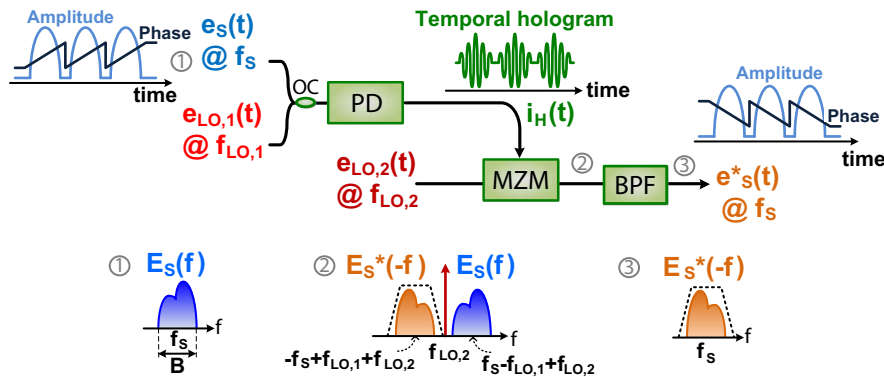
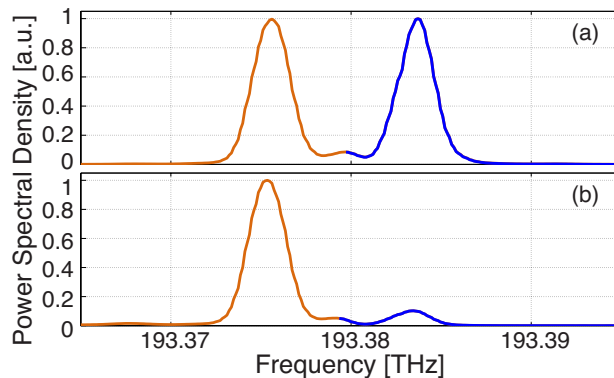


Figure 4.7 – Scheme to perform TPC based on time-domain holography. The scheme comprises the concatenation of the detection and reconstruction steps of holography, in this case using two different reference signals in each step.

In the following Sections, the proposed TPC methodology is experimentally validated by performing conjugation of two different optical waveforms. For consistency, they have been chosen to be the same set of waveforms employed in Section 4.5.1, illustrating the potential of the proposed methodology to conjugate optical signals with arbitrary phase profiles of practical interest. In particular, we first report TPC of a set of arbitrarily-chirped Gaussian-like pulses. Secondly, a telecommunication optical information signal under a 16-QAM modulation is also successfully conjugated. The used experimental setup follows the general scheme shown in Fig. 4.7.

### 4.5.2.1 Arbitrary chirped Gaussian pulses

The experimental demonstration of the proposed scheme for TPC requires a previous step, i.e., the generation of the complex-envelope temporal waveforms to be processed, in this case a set of 16 arbitrary Gaussian pulses. This step is carried out following the procedure described in Section 4.5.1.1. The complex envelope of the input optical stream is defined by Eq. 4.8. In this case,  $T_0 = 133$  ps and  $T_S = 666$  ps. The input waveform has a 3dB-bandwidth of 2 GHz (bandwidth at 1% of the maximum is 5.1 GHz). The spectrum of the signal is centered at  $f_S = 193.408$  THz (i.e, at  $\lambda_S = 1550.05$  nm). The interference between the input signal and a reference signal  $e_{LO,1}(t)$  centered at  $f_{LO,1} = 193.401$  THz ( $\lambda_{LO,1} = 1550.1$  nm) is detected using a 40-GHz PD. The electrical signal, i.e., the temporal hologram, directly drives a 40 GHz MZM that modulates the reference signal  $e_{LO,2}(t)$  centered at  $f_{LO,2} = 193.415$  THz ( $\lambda_{LO,2} = 1549.01$  nm). The MZM is biased in such a way that the electrical DC component plus the bias voltage are coincident with the minimum transmission point of the modulator. Therefore, the optical component that is expected to appear between the two spectral lobes in Fig. 4.8(a) is almost negligible, simplifying the filtering process. A tunable BPF (Santec OTF-350) centered at  $f_{LO,2} - f_i = 193.408$  THz after the modulator finally filters in (selects) the time-conjugate spectral component (see Fig. 4.8(b)), which in this example is centered at the same frequency as the original information signal  $f_S$  (wavelength-preserving operation).



**Figure 4.8** – Power spectral density of (a) the real optical signal after the modulation process; (b) the complex-envelope optical signal after the BPF. The spectrum of the input signal  $e_S(t)$  is nearly coincident with (b).

To verify that we have conjugated the input signal, we detect the output signal using coherent detection; in particular, the signal recording step of time-domain holography. For this purpose, the signal to be characterized  $e_{BPF}(t) = e_{out}(t) \otimes h_{BPF}(t)$ , where  $h_{BPF}(t)$  is the impulse response

of the employed BPF, is beaten with  $e_{LO,2}(t)$  in a PD. From the detected electrical signal, we extract the temporal amplitude and phase of the conjugated waveform using an off-line numerical algorithm, implemented using digital signal processing. As discussed above, this algorithm is based on the traditional numerical scheme for phase reconstruction in heterodyne detection [12]. The obtained results are plotted in Fig. 4.9. We can observe an excellent agreement in the recovery of the intensity of the conjugated signal, while the obtained phase has the exact opposite sign with respect to the input pulses' phase, confirming that the conjugation process has been successfully achieved (Fig. 4.9(c)-(d)). The peaks that appear in between the optical pulses in the second half of Figs. 4.9(c) and (d) are  $2\pi$  phase jumps that have been numerically removed from the graph. The appearance of those peaks is attributed to the fact that the intensity at those instants is reduced to almost null.

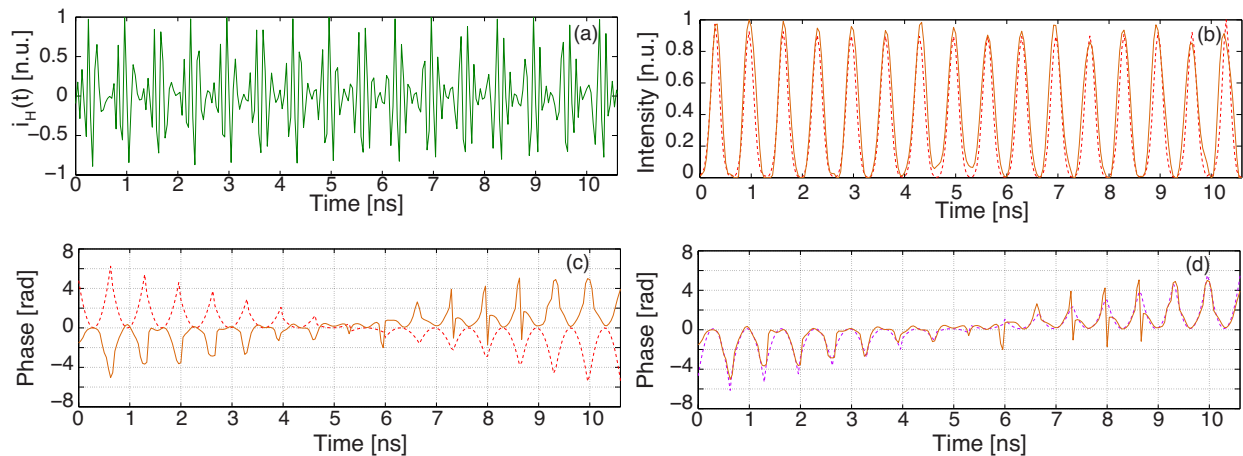


**Figure 4.9 – TPC of a 16-symbol sequence of arbitrary chirped Gaussian pulses. (a) Temporal hologram of the input signal after the detection process; (b) Detected intensity of the conjugated signal after modulation and band-pass filtering (solid orange line), compared with the intensity profile of the input signal (dashed red line); (c) Detected phase of the conjugated signal after modulation and band-pass filtering (solid orange line) and phase of the input signal (dashed red line), and (d) Comparison between the detected output phase (solid orange line) and the phase of the ideally conjugated input (dashed purple line).**

#### 4.5.2.2 16-QAM modulated data stream

The second example involves conjugation of a 1024-symbol 16-QAM signal, previously generated using the approach described in Section 4.5.1.2. Each symbol consists of a Gaussian-like pulse with a full-width at half maximum (FWHM) of 260 ps ( $\text{FWHM} = 2T_0\sqrt{\ln 2}$ ), i.e. the 3dB-bandwidth of the input signal is  $\sim 1.7$  GHz (full-bandwidth at 1% of the maximum is 4.3 GHz). The complex envelope of the input data sequence is defined in Eq. 4.9, where  $T_S = 1.3$  ns (repetition rate of

0.75 GHz). The same procedure as in the first example was employed, and the temporal output intensity and phase are shown in Fig. 4.10(b)-(d). For comparison purposes, the detected phase has been compared with the phase of the ideally conjugated waveform in Fig. 4.10(d), confirming that the conjugation has been successfully achieved in this case as well. Also, we have calculated the constellation of the output waveform (Fig. 4.10(e)), where relatively low amplitude and phase noise is observed on the conjugated signal, mostly for the symbols of lower intensity.

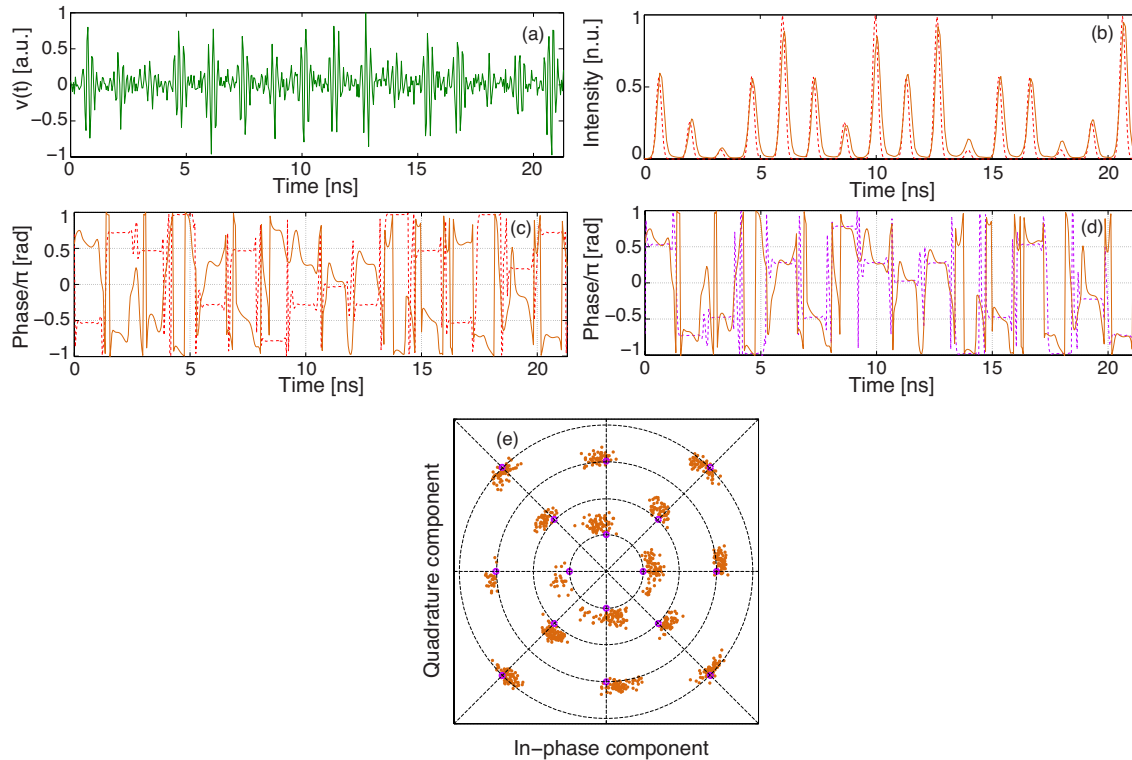


**Figure 4.10** – TPC of a 1024-symbol 16-QAM optical data stream. (a) Temporal hologram of the input signal; (b) Detected intensity of the conjugated signal; (c) Detected phase of the conjugated signal (orange line); (d) Comparison between the detected phase (orange line) and phase of the ideally conjugated input (dashed purple line), and (e) Output constellation (purple circles represent the symbol's ideal positions).

To quantify the amount of error introduced by the conjugator scheme, we have calculated the  $EVM_m$  in this case (16-QAM signal), following Eq. 4.10. The obtained value is  $EVM_m = 10\%$ . As in the case of the 16QAM signal generation (Section 4.5.1.2), the constellation shown in Fig. 4.10(e) has been calculated by using the value of amplitude and phase at the center of each symbol from the analog electrical signal measured in an oscilloscope, i.e., without employing front-end correction or any additional optimization algorithm. Also, the measured error is induced not only by the conjugation process but also by the holographic detection process (i.e., based on a single PD). Still, the estimated EVM remains lower than 18% [186], indicating a reduced distortion induced

by the conjugator. In this case, the obtained symbols have generally less phase error than in the case presented in Section 4.5.1.2, but higher amplitude error in the symbols of lowest intensity. These differences are attributed to the fact that different equipment was used in the experiment realization. Therefore, further improvement is expected if optimized components are employed (see Section 6.2).

The limitation in the processing speed of the reported proof-of-concept experimental results is due to intrinsic bandwidth constraints of the scheme used for generation of the input optical waveforms [153]; in particular, the available AWG (AWG7122C) limits the complex-envelope signal bandwidth in our experiments to  $\sim 5$  GHz. However, current OE detectors and EO intensity modulators can process data bandwidths exceeding 40 GHz, potentially enabling direct conjugation of optical waveforms with bandwidths of at least  $\sim 20$  GHz. Furthermore, significantly broader operation bandwidths could be achieved by implementing the intensity detection and modulation processes in the all-optical domain, e.g. through the use of XPM [155], as detailed in the following Section.

### 4.5.3 Wavelength conversion of complex-envelope optical signals

All-optical wavelength conversion is a fundamental process in high-speed WDM systems, ensuring full flexibility in the network, preventing wavelength blocking, and allowing high-speed operation while avoiding inefficient OE-EO conversion [14, 22–30, 170–180]. With the renewed interest in coherent technologies [4, 29, 30] for increasing the spectral efficiency of optical telecommunications systems, wavelength conversion of complex (amplitude and phase) information signals is especially desired.

A number of all-optical wavelength conversion techniques have appeared in the last few decades. Most of them rely on parametric nonlinear effects, such as FWM [25–30, 174]. However, FWM-based schemes present several drawbacks that limit their practical application, which include (i) the need to satisfy a stringent phase-matching condition, which either limits the wavelength conversion tunability or requires using dispersion-engineered media [19, 28, 30]; (ii) the need to use very high power for the involved signals (typically,  $> 10$  dBm average powers) and (iii) the fact that the wavelength converted signal is phase conjugated in time with respect to the original one when using the higher efficiency configurations, e.g. one [25, 28–30] or two [26, 27] CW pumps (in general,

phase conjugation depends on the configuration of the pumps and signal). Whereas all-optical TPC of data signals is also desired for a range of operations in fiber-optics communication links [41, 190], in order to achieve wavelength conversion of the original signal, a second conjugation process, typically another FWM stage, is required. Alternatively, wavelength conversion schemes have been proposed based on XPM. As introduced in Section 1.2, XPM is generally easier to excite than FWM since it is not conditioned to a phase matching between the probe and the pump. In these schemes, wavelength conversion is achieved from the intensity modulation of a probe CW light with a high power pump signal (the information signal) through a stage of XPM into an interferometric configuration, e.g., such as a Sagnac interferometer [14, 22, 23]; or through the sideband filtering of the output [24, 176, 191]. However, these configurations are limited to wavelength conversion of amplitude-only data signals.

Here, we propose and experimentally prove wavelength conversion of complex-envelope optical signals based on time-domain holography [155]. Wavelength conversion can be seen as a modulation process where the complex envelope of the information signal modulates a different carrier signal. In the presented scheme, the temporal holograms are generated by phase-only modulation, namely XPM, in a HNLF. Although the proposed configuration is similar to that of FWM-based schemes [26, 27], it avoids the need to satisfy the phase matching condition and also significantly relaxes the power requirements. In our experimental tests, we achieve down and up conversion of a train of chirped Gaussian-like pulses with similar efficiency ( $\sim -20$  dB [25–30]) but using much lower power levels than previous FWM-based configurations, e.g.,  $\sim 0.4$  dBm and  $\sim 3$  dBm signal and probe powers, respectively.

To validate the proposed scheme, first two numerical simulations are carried out. In the first example, we assume a HNLF with a dispersion curve that ensures that phase matching condition is not satisfied. Thus, this example illustrates the capability of XPM-only for realizing the wavelength conversion process of complex-envelope optical signals. In the second example, the parameters of the HNLF available in our laboratory at the time of these experiments are employed. In both cases, the input signal  $e_S(t)$  is a train of 2 ps-FWHM Gaussian-like pulses with a repetition rate of 10 GHz, dispersed by 1-km single-mode fiber (SMF) section. The dispersed pulses are centered at  $f_S = 193.79$  THz (i.e., at  $\lambda_S = 1547$  nm) and have an average power of 0.4 dBm. The FWHM of the pulses after the dispersion is 30 ps and the full bandwidth (at 1% of the maximum amplitude) of  $e_S(t)$  is  $B \sim 800$  GHz (6 nm). The reference signal of the recording step  $e_{LO,1}(t)$  has a central

frequency of  $f_{LO,1} = 193.41$  THz ( $\lambda_{LO,1} = 1550$  nm) and an average power of 13 dBm. The reference signal of the recovering step  $e_{LO,2}(t)$  is centered at  $f_{LO,2} = 195.57$  THz ( $\lambda_{LO,1} = 1533$  nm) and has an average power of only 3 dBm. All these parameters well accomplish the conditions established in Section 4.4, i.e.,  $i_{LO,1} \gg |\hat{e}_S(t)|^2$  and  $2\gamma LA_{eff} i_{LO,1}^{1/2} |\hat{e}_S(t)| \ll \pi$ . Based on these settings, the wavelength converted signal is expected at  $\lambda_{out,S} = 1530$  nm.

The specifications for the HNLF in the first example are  $\gamma = 11.3$  W<sup>-1</sup>km<sup>-1</sup>,  $L = 1015$  m, the zero dispersion wavelength (ZDW) is 1540 nm and the dispersion slope  $S_0$  (at 1540 nm) = 0.092 ps/nm<sup>2</sup>/km. To check if the phase matching condition is accomplished in this case, we first derive the equations for the phase mismatch. The spectral locations of the different involved signals are illustrated in Fig. 4.11, where we define the parameters  $\Delta\omega_p$  and  $\Delta\omega_s$  to be employed in the derivation of the phase mismatch.

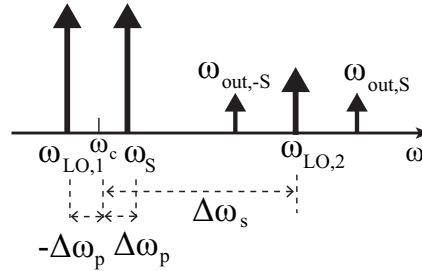


**Figure 4.11** – Scheme of the central frequency of the signals involved in the wavelength conversion process and nomenclature given to the spectral separation between signals to develop the equations of phase-matching condition (Eqs. 4.12 and 4.13).

Thus, the effective phase mismatch of the resulting wavelength-converted signal and conjugate are defined as  $k_{4,1}$  and  $k_{4,2}$ , respectively [19], which are derived as

$$\begin{aligned} k_{4,1} &= \Delta\kappa_{4,1} + \gamma P_{LO,1} = \beta_{T,1} - \beta_{T,2} + \beta_{T,3} - \beta_{T,4} + \gamma P_{LO,1} \\ &= \ddot{\beta}[-2\Delta\omega_p^2 - 2\Delta\omega_s\Delta\omega_p] + \ddot{\beta}[-\Delta\omega_p^3 - 2\Delta\omega_s\Delta\omega_p^2 - \Delta\omega_s^2\Delta\omega_p] + \gamma P_{LO,1}; \end{aligned} \quad (4.12)$$

$$\begin{aligned} k_{4,2} &= \Delta\kappa_{4,2} + \gamma P_{LO,1} = \beta_{T,1} - \beta_{T,2} - \beta_{T,3} + \beta_{T,4} + \gamma P_{LO,1} \\ &= \ddot{\beta}[2\Delta\omega_p^2 - 2\Delta\omega_s\Delta\omega_p] + \ddot{\beta}[-\Delta\omega_p^3 + 2\Delta\omega_s\Delta\omega_p^2 - \Delta\omega_s^2\Delta\omega_p] + \gamma P_{LO,1}. \end{aligned} \quad (4.13)$$

In Eqs. 4.12 and 4.13,  $\Delta\kappa_{4,w}$ , with  $w \in [1,2]$ , is the phase mismatch due to the material dispersion of the employed fiber;  $\beta_{T,v}$ , with  $v \in [1,4]$  is the total dispersion value of the fiber at the

frequencies of the four waves involved in the process (i.e., the three input signals plus the target output at  $\omega_{out,S}$  in Eq. 4.12 or  $\omega_{out,-S}$  in Eq. 4.13). Those dispersion values are obtained from decomposing the fiber dispersion curve  $\beta(\omega)$  using the Taylor series expansion around  $\omega_c$  (see Fig. 4.11).  $\overset{4}{\beta}$  and  $\overset{\cdot\cdot}{\beta}$  are the resulting values of the second and third order dispersion of the fiber<sup>4</sup>, respectively. The last term of  $k_{4,w}$  is the phase mismatch due to SPM of the strong reference signal  $e_{LO,1}(t)$ , being  $P_{LO,1}$  its peak power value. The evaluation of Eqs. 4.12 and 4.13 using the values presented above leads to  $k_{4,1} = 438 \text{ m}^{-1}$  and  $k_{4,2} = 2.19 \times 10^6 \text{ m}^{-1}$ , where the dispersion terms  $\overset{4}{\beta}$  and  $\overset{\cdot\cdot}{\beta}$  have the values  $\overset{4}{\beta} = -4.28 \times 10^{-2} \text{ ps}^2$  and  $\overset{\cdot\cdot}{\beta} = 2.39 \times 10^{-3} \text{ ps}^3$ .

The high values of  $k_{4,1}$  and  $k_{4,2}$  clearly indicate that the phase matching condition is not accomplished, impeding the build-up of FWM. In this example, the ZDW has been located at the central wavelength between the probe and the pump. Thus, even with a strong dispersion slope, the group delay values at the wavelengths of probe and pump are very similar, reducing the effects of walk-off, which is a main cause of distortion in XPM processes. Our predictions are confirmed through simulations based on the nonlinear Schrödinger equation, which is numerically solved by the split-step Fourier method [19]. The spectrum at the output of the HNLF is plotted in Fig. 4.12(a). The different amplitude between the spectral components proportional to  $E_S(\lambda)$  (at 1530 nm) and  $E_S^*(-\lambda)$  (at 1536) is attributed to the walk-off induced at 1536 nm, given the ZDW of the fiber. The spectral component centered at 1530 nm is then filtered in, and the corresponding temporal waveform is shown in Fig. 4.12(b), together with the original  $e_S(t)$ . To verify that the output signal has preserved its original phase, we also include in Fig. 4.12(b) the resulting waveform from propagation through a medium with the exact opposite dispersion to that of 1-km SMF, and it is confirmed that the dispersion-induced pulse spectral phase has been well compensated for. The difference between the complex envelope of the output signal with respect to the input is also attributed to the high value of  $S_0$ , which imposes different group delays to the different frequency components of  $e_S(t)$  in the propagation along the HNLF.

In the second example the characteristics of the three input signals are the same as in the previous case. The specifications for the HNLF are  $\gamma = 11.3 \text{ W}^{-1}\text{km}^{-1}$ ,  $L = 1015 \text{ m}$ , the ZDW is 1545 nm and  $S_0$  (at 1545 nm) =  $0.017 \text{ ps/nm}^2/\text{km}$ . In this case, the solution of Eqs. 4.12 and 4.13, leads to  $k_{4,1} = -3.3 \text{ m}^{-1}$  and  $k_{4,2} = -1.8 \text{ m}^{-1}$ , for what the second and third order dispersion evaluated at the frequency  $\omega_c$  result in  $\overset{4}{\beta} = -7.53 \times 10^{-5} \text{ ps}^2$  and  $\overset{\cdot\cdot}{\beta} = 2.75 \times 10^{-5} \text{ ps}^3$ . These values

---


$$\overset{4}{\beta} = \left. \frac{d^2\beta(\omega)}{d\omega^2} \right|_{\omega=\omega_c}; \overset{\cdot\cdot}{\beta} = \left. \frac{d^3\beta(\omega)}{d\omega^3} \right|_{\omega=\omega_c}$$

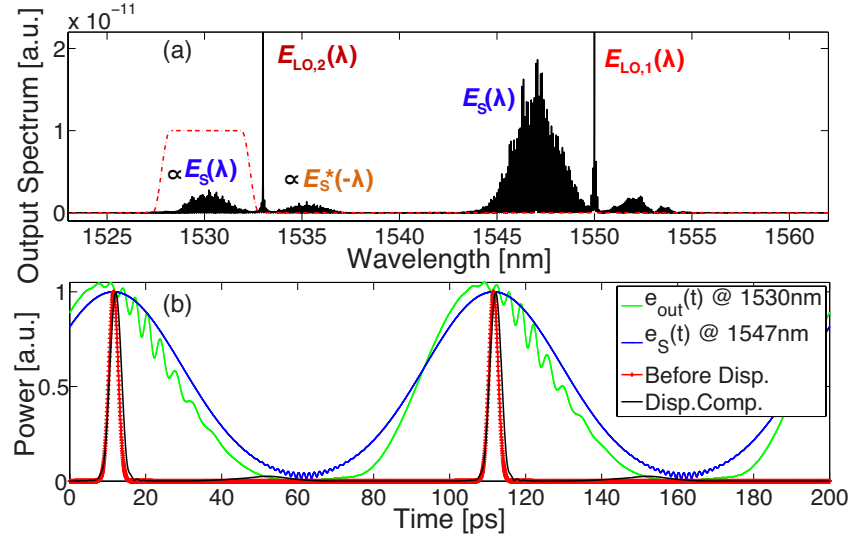


**Figure 4.12** – Results from the numerical simulation of the proposed scheme (no phase-matching) (a) Spectrum at the output of the HNLF; dashed red line represents the applied numerical BPF (b) Resulting temporal waveform after the BPF (green line); transform-limited input before propagation through the SMF (red line); input chirped signal to be conjugated (blue line); wavelength-converted output after compensating the dispersion from the SMF (black line).

of phase mismatch suggest that parametric gain due to FWM might still occur in the system. As discussed in Section 4.4, two idlers proportional to  $e_S(t)$  and  $e_S^*(t)$  would appear at the frequencies  $f_{out,S}$  and  $f_{out,-S}$  as a consequence of a mixing between the pumps  $e_S(t)$  and  $e_{LO,1}(t)$  and the probe signal  $e_{LO,2}(t)$ . These idlers are proportional to the frequency components generated from XPM around  $f_{LO,2}$ , and consequently they are added coherently. The obtained spectrum at the output of the HNLF and the resulting temporal output waveform (before and after dispersion compensation) in comparison with the input signal are plotted in Fig. 4.13.

Still, it is worth noticing that in the proposed scheme, only one sufficiently strong CW signal,  $e_{LO,1}(t)$ , is required as part of the pump, which is additionally undepleted [192]; in particular, before the HNLF

$$i_{LO,1} \gg |\hat{e}_S(t)|^2, \quad i_{LO,2} \quad |e_{out}(t)|^2 = 0. \quad (4.14)$$

This fact suggests that the mixing between the three input signals present at the input of the HNLF would be weak at the output frequencies of interest.

Next, the experimental proof-of-concept of the proposed XPM-based wavelength conversion scheme is presented. The experiment setup is shown in Fig. 4.14. We process a train of chirped

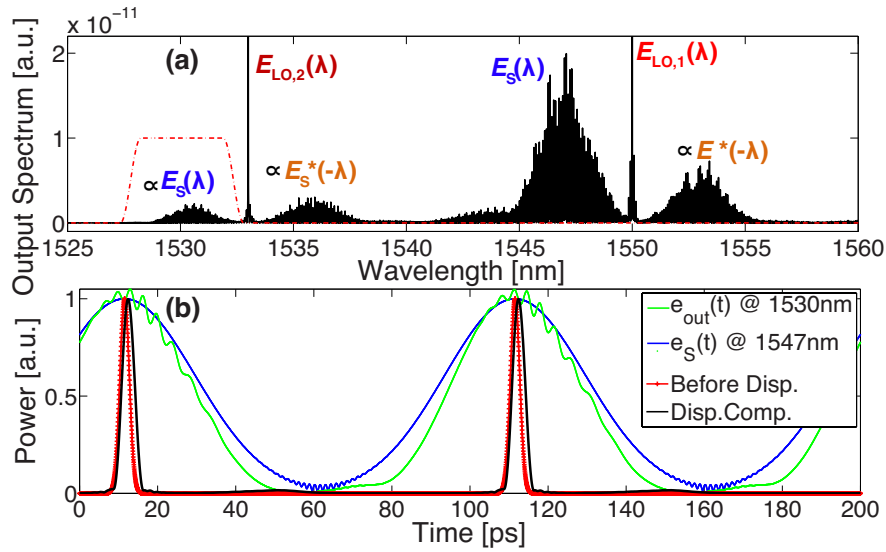


Figure 4.13 – Results from the numerical simulation of the proposed scheme (a) Spectrum at the output of the HNLf; dashed red line represents the applied numerical BPF. (b) Resulting temporal waveform after the BPF (green line); transform-limited input before propagation through the SMF (red line); input chirped signal to be conjugated (blue line); wavelength-converted output after compensating the dispersion from the SMF (black line).

Gaussian-like pulses similar to the one assumed in the above numerical simulations. The specifications of the employed HNLf are identical to those of the second example presented. A configuration with phase matching between signals has been employed due to the limitations imposed by the equipment available in our laboratory.

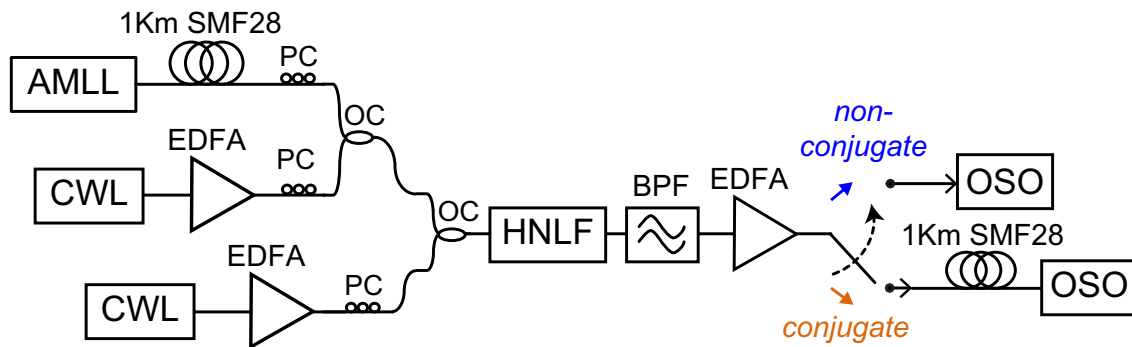
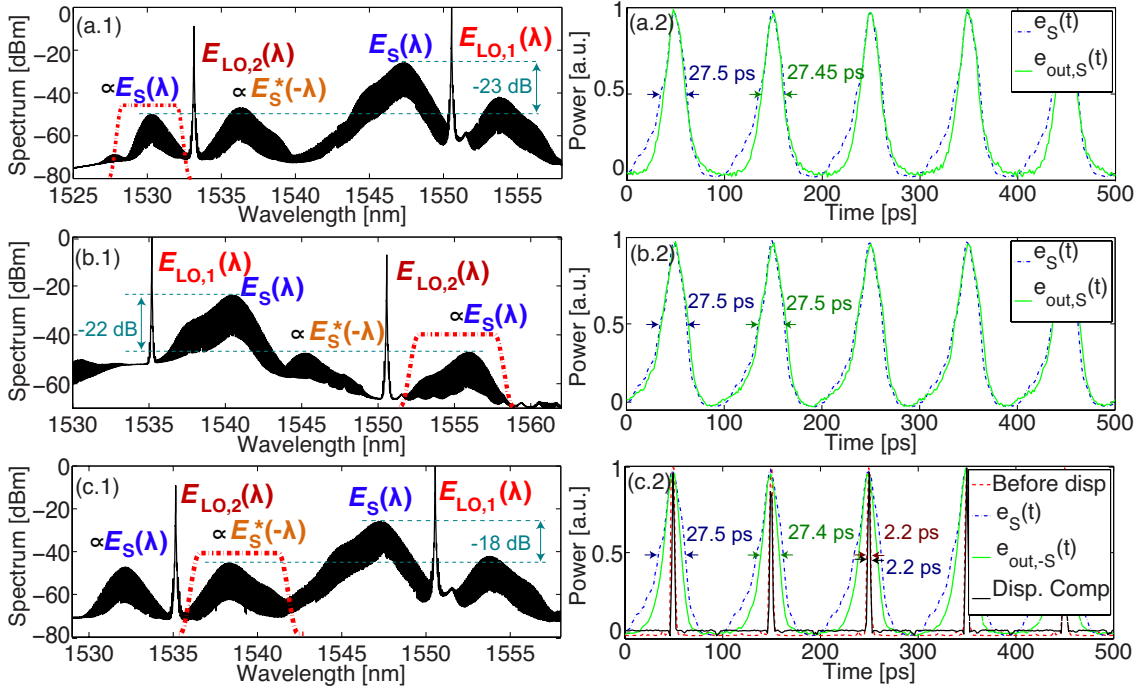


Figure 4.14 – Experimental setup of the XPM-based wavelength converted scheme for complex-envelope optical signals. AMLL: Active mode-locked laser; PC: Polarization controller; CWL: Continuous-wave laser; EDFA: Erbium-doped fiber amplifier. OSO: Optical sampling oscilloscope.

First, the information signal  $e_S(t)$  is generated from a 10-GHz repetition-rate active mode-locked laser (AMLL). The generated pulses have a FWHM of 2.2 ps. To add a quadratic spectral phase to the pulses, the signal propagates through 1 km of SMF, as shown in Fig. 4.14. The resulting chirped pulses have a FWHM of 27.5 ps. The average power values of the three signals involved in

the process, i.e.,  $e_S(t)$ ,  $e_{LO,1}(t)$  and  $e_{LO,2}(t)$  just before the HNLFF are coincident with the values used for the numerical simulation, that is, 0.4 dBm, 13 dBm and 3 dBm, respectively. Figure 4.15 shows the results of the experimental demonstration in three different cases: (a) 17-nm down-conversion of  $e_S(t)$ , (b) 17-nm up-conversion of  $e_S(t)$  and (c) 10-nm down-conversion of  $e_S^*(t)$ . The first column of Fig. 4.15 shows the spectrum at the output of the HNLFF and the second column shows the corresponding temporal waveforms after filtering in the desired spectral component by a tunable BPF (Santec OTF-350). A 500-GHz optical sampling oscilloscope (Exfo PSO-101) is used to measure the resulting temporal waveforms.



**Figure 4.15** – (a) Down-conversion of  $e_S(t)$ ; (b) Up-conversion of  $e_S(t)$ ; (c) Down-conversion of  $e_S^*(t)$ ; a-c (1) Spectrum after HNLFF; a,b (2) Temporal signal after BPF (green line) vs input signal (dashed blue line); c (2) includes output from AMLL (red line) and signal after dispersion compensation (black line).

The conversion efficiency of the scheme, defined as the ratio of the wavelength converted power at the output end of the HNLFF to the input signal power, varies from -17 dB to -23 dB when the wavelength conversion varies from 7 nm to 17 nm, as shown in Fig. 4.16. From Fig. 4.16 we observe that the conversion efficiency for both down-conversion and up-conversion is very similar; this is in sharp contrast to the expected behavior of parametric effects such a FWM, where the down-conversion process is more efficient than the up-conversion due to increased phase mismatch for the up-conversion case [25]. This suggests that the induced FWM process should be notably weaker than the XPM at the output frequencies, which is consistent with the significant low power of two

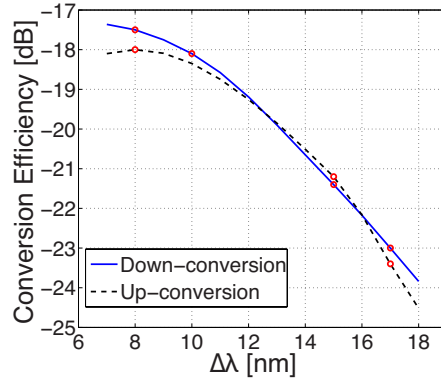


**Figure 4.16** – Conversion efficiency of the XPM-based wavelength converter scheme as a function of the wavelength shift  $\Delta\lambda$ , for the cases of down-conversion (solid blue line) and up-conversion (dashed black line).

of the three input signals involved in the mixing process. It is worth mentioning that the obtained conversion efficiency depends on the power of the reference signal  $e_{LO,2}(t)$ , as observed from Eq. 4.7. In this particular proof-of-concept experiment, the power of  $e_{LO,2}(t)$  is kept one order of magnitude lower than typical values of pump power in FWM-only based wavelength converters, still achieving similar values of conversion efficiency [25–30]. In all the three reported cases, it is observed that the pulse spectral and temporal shapes of the wavelength-converted signal coincide with those of the original input, confirming that the quadratic phase induced by dispersion is preserved. Furthermore, in the case of phase conjugation (Fig. 4.15(c)), we show the waveform of the conjugated signal after propagating again through the 1-km SMF, black line in Fig. 4.15(c.2), and the results clearly prove that the originally induced dispersion has been well compensated for. All experimental results show an excellent agreement with the simulation results presented above.

## 4.6 Conclusions

In this Chapter, we have formally introduced the concept of time-domain holography. This concept allows the generation, processing and detection of the amplitude and phase temporal profiles of a target complex-envelope optical signal in a simultaneous fashion, by use of intensity-only or phase-only sensitive processes. In particular, two approaches have been presented to implement time-domain holography. First, we presented an EO approach, in which the recording step is carried out by use of a single PD and the retrieval step is implemented via an MZM and a BPF. We have also proposed a configuration to generate CGTH, where the interference pattern is modeled computationally and

the temporal hologram is generated using an AWG. The second proposed approach is an all-optical approach, which enables the control of the amplitude and phase of a complex-envelope signal at a data rate not limited by electronics. All-optical time-domain holography can be implemented via a nonlinear XPM process, e.g., in a HNLF.

These approaches have been employed to experimentally demonstrate three appealing applications of time-domain holography. The first presented application has been the generation of optical waveforms with arbitrary, user-defined complex (amplitude and phase) modulation patterns, i.e., a sequence of arbitrarily chirped Gaussian pulses, and a 3-Gbps 16-QAM modulated data pattern, by using an extremely simple setup involving intensity-only modulation of a CW light source and band-pass filtering. The second application has been wavelength-preserving TPC of those same optical waveforms. Our proposal significantly reduces the complexity and cost of previous OE-EO approaches, as it avoids the detection, subsequent electronic processing of the phase of the optical signal prior to the conjugation process, the conjugation in the electrical domain and the final generation of the optical conjugated waveform using an IQ modulation process. Finally, the last presented application has been the all-optical wavelength conversion of a complex-envelope waveform (i.e. a train of chirped Gaussian pulses) based on XPM. This scheme enables good conversion efficiency for a broad wavelength range, without the need to accomplish the stringent phase matching condition of previous FWM-based schemes, while relaxing in at least one order of magnitude the power requirements for the pump and probe signals and also providing a symmetrical conversion efficiency for down- and up-conversion.

## Chapter 5

# Spectral-domain signal processing based on holographic concepts

### 5.1 Introduction to spectral domain holography

There is a well-known property in Fourier transform's theory that establishes a duality between the time and the frequency domains,

$$\begin{aligned} \text{If } x(t) &\longleftrightarrow X(\omega) \\ X(t) &\longleftrightarrow 2\pi x(-\omega), \end{aligned} \tag{5.1}$$

where the arrows separate the time-domain (at the left hand side (LHS)) and the frequency-domain (at the right hand side (RHS)) representation of a signal, related by the Fourier transform. In this Chapter, this duality is used to develop a new concept, *spectral-domain holography*, presented as the frequency-domain equivalent of time-domain holography (introduced in Chapter 4).

It is worth mentioning that the term “spectral holography” has been already used in the literature to define processes in which a spatial-domain Vander-Lugt filter (Section 3.4) is used to perform complex (amplitude and phase) filtering to a time-domain optical signal. In those schemes, two diffraction gratings are used to convert the spectral content of the temporal signal to angularly spread waves in the spatial domain [193–195]. The main drawbacks of these schemes for processing

temporal information are: the requirement of bulky optical components, which require strict tolerances in their alignment and have limited integration with waveguide devices, and the need for coupling the shaped waveforms back into an optical fiber, which introduces high losses [123]. In this Thesis, the concept of spectral-domain holography involves creating a *temporal-spectral interferogram* that allows one to control both the amplitude and phase spectral content of a temporal optical signal by just manipulating the signal’s amplitude spectrum. Still, the same terminology (“spectral holography”) is used for consistency within the presented work.

The proposed technique is of particular interest for the implementation of optical linear signal processors with arbitrary complex-valued transfer functions based on optical components or systems with a fundamental restriction in the processing operations that can implement, e.g., limited to real-valued-only or minimum phase (MP) spectral responses. It is important to mention that the processors presented here are not LTI. Still, they will be able to be defined by an impulse response and the corresponding transfer function under certain restrictions: (i) the signal to be processed is a single pulse or a signal defined over a prescribed temporal window, and (ii) in the cases in which an optical amplitude modulator is used as part of the processing system, synchronization between the input optical signal and the electrical modulating signal is assumed.

In this Chapter, we will derive the equations that describe spectral-domain holography, as the frequency-domain dual process of time-domain holography. Then, we employ this formalism to implement pulse processors based on two different technology solutions. First, we apply spectral-domain holography to the implementation of electro-optical (EO) processors based on time domain spectral shaping (TDSS) techniques. TDSS can be interpreted as the time-domain equivalent of a Fourier-based spatial-domain optical filter (described in Section 1.4.2), and it is a very promising fiber-optic technique for realization of electronically reconfigurable pulse shaping operations with resolutions in the sub-picosecond regime [115, 128, 131, 196, 197]. Spectral domain holography proves a solution to overcome the limitation in the operation capabilities of this optical system, typically restricted to the control of the temporal intensity profile of the input optical waveform, with no control of its temporal phase profile. Then, we apply spectral-domain holography to the realization of arbitrary signal processors based on MP optical filters. MP filters have a spectral response in which the spectral phase profile is uniquely related to the amplitude spectral response, since the real and imaginary parts of the spectral response are inter-dependent in terms of the Kramers-Kronig relationship [16]. This condition severely limits the functionalities susceptible to

be implemented using these filters. Technologies having such a fundamental restriction include fiber/waveguide Bragg gratings (F/W-BGs) operating in transmission [99], long period gratings (LPGs) in their core-to-core configuration (under certain, commonly satisfied conditions<sup>1</sup>) [198], or thin-film optical filters used in transmission. We will show how spectral domain holography can be employed to extend the capabilities of MP filters to implement any desired, arbitrary (including non-MP) signal processing operations.

## 5.2 Mathematical formalism of spectral domain holography

In this Section, we present the mathematical formalism that describes the spectral-domain holography process, with focus on its application for designing optical processing systems with arbitrary (complex-valued) transfer functions. Once again, the two steps involved in the holography process will be referred to as “recording” and a “retrieval” steps for consistency with the conventional terminology in spatial domain holography. Note that the following is a mathematical derivation of the dual concept of time-domain holography in the frequency domain, without considering its physical implementation. The practical application of spectral holography will be contemplated in Sections 5.3 and 5.4).

As starting point, we assume an optical signal processor to be implemented defined by the transfer function  $H_F(\omega')$ , where  $\omega' = \omega - \omega_0$ , with  $\omega$  being the angular frequency and  $\omega_0$  being the central frequency. This processor can be also defined by the corresponding impulse response,  $h_F(t) = \hat{h}_F(t) \cdot \exp\{j\omega_0 t\}$ , whose complex envelope is obtained as  $\hat{h}_F(t) = \mathcal{F}^{-1}\{H_F(\omega')\}$ . A feasible processor requires that its transfer function is limited over a finite spectral window  $\Delta\omega_F$ , and its impulse response is causal, i.e., the impulse response is zero at negatives values of the time variable. We also assume that  $\hat{h}_F(t)$  is limited over a finite temporal window  $\Delta t_F$  and centered at  $t = t_C$ . A spectral hologram can be generated following the frequency-domain dual process of the temporal holographic recording step, where the target transfer function interferes with a reference signal. In this case, the reference signal must have an instantaneous temporal envelope,  $\hat{h}_{Ref}(t) = A \cdot \delta(t - t_D)$  (at  $\omega_0$ ), with  $\delta(t)$  being the Dirac delta function, corresponding to a uniform energy spectrum over the bandwidth of interest, and  $t_D$  is the time instant at which the reference signal is defined. Thus,

---

<sup>1</sup>LPGs have an MP spectral response in their core-to-core configuration when they are implemented in a single mode fiber (only the fundamental mode propagates through the core) and in under-coupling conditions, that is, the product  $\kappa L < \pi/2$ , where  $\kappa$  is the grating coupling coefficient and  $L$  is its length.

the spectral hologram is calculated as the square of the spectral interference between the signal and reference,

$$\begin{aligned} P_{Hol}(\omega') &= |H_F(\omega') + H_{Ref}(\omega')|^2 \\ &= |H_F(\omega')|^2 + A^2 + 2A|H_F(\omega')| \cos\left(t_p\omega' + \angle H_F(\omega')\right), \end{aligned} \quad (5.2)$$

where  $t_p = t_D - t_C$ . The temporal profile of the resulting spectral hologram is

$$\hat{p}_{Hol}(t) = \hat{h}_F(t) \otimes \hat{h}_F^*(-t) + A^2\delta(t) + A\hat{h}_F(t - t_p) + A\hat{h}_F^*(-t - t_p). \quad (5.3)$$

Note that the first term of the RHS of Eq. 5.3 has a total duration of  $2\Delta t_F$ . Therefore, to avoid any temporal overlapping between the different components of the output signal,  $t_p$  must be set to be  $t_p > 3\Delta t_F/2$ . It is possible to reduce in two fold the temporal duration of the spectral hologram if the constant  $A$  is set to be  $A \gg |\hat{h}_F(t)|$ , since in this case the first term in the RHS of Eq. 5.3 can be neglected. This procedure can be seen as the counterpart of the procedure carried out in Section 4.2 to reduce the bandwidth requirements of temporal holograms.

The symmetric function  $\hat{p}_{Hol}(t)$  can be used as a filter's impulse response, whose corresponding transfer function  $P_{Hol}(\omega')$  is real-valued, but in turn contains information of the amplitude and phase of the target arbitrary spectral response  $H_F(\omega')$ . Let us consider the propagation of an input optical signal  $e_{in}(t) = \hat{e}_{in}(t) \exp\{j\omega_0 t\}$  ( $\hat{e}_{in}(t)$  being the complex-envelope) through a system with an impulse response equal to  $p_{Hol}(t)$ . The output signal has a complex envelope given by

$$\begin{aligned} \hat{e}_{out}(t) &\propto \hat{e}_{in}(t) \otimes \hat{p}_{Hol}(t) \\ &= \hat{e}_{in}(t) \otimes (\hat{h}_F(t) \otimes \hat{h}_F^*(-t)) + \hat{e}_{in}(t) \otimes A^2\delta(t) \\ &\quad + \hat{e}_{in}(t) \otimes A\hat{h}_F(t - t_p) + \hat{e}_{in}(t) \otimes A\hat{h}_F^*(-t - t_p). \end{aligned} \quad (5.4)$$

This output signal is composed of four different terms, one of them being proportional to the desired processed signal, i.e.,  $\propto \hat{e}_{in}(t) \otimes A\hat{h}_F(t - t_p)$ . To be able to retrieve this target component, it is necessary that the different terms in Eq. 5.4 do not overlap in time. Note that in this case, the temporal window available for the processing operation will also depend on the temporal width of the input signal to be processed, see Fig. 5.1. Thus, assuming that the input signal  $e_{in}(t)$  has

a temporal width of  $\Delta t_S$  and that the different components of  $e_{out}(t)$  do not overlap, the total temporal duration of  $e_{out}(t)$  must be  $> 4\Delta t_F + 3\Delta t_S$ , as depicted in Fig. 5.1(a). To this purpose, the temporal delay  $t_p$  must be chosen to be  $t_p > (3\Delta t_F + 2\Delta t_S)/2$ . This imposes a severe limitation in the effective operation temporal window of the target processor.

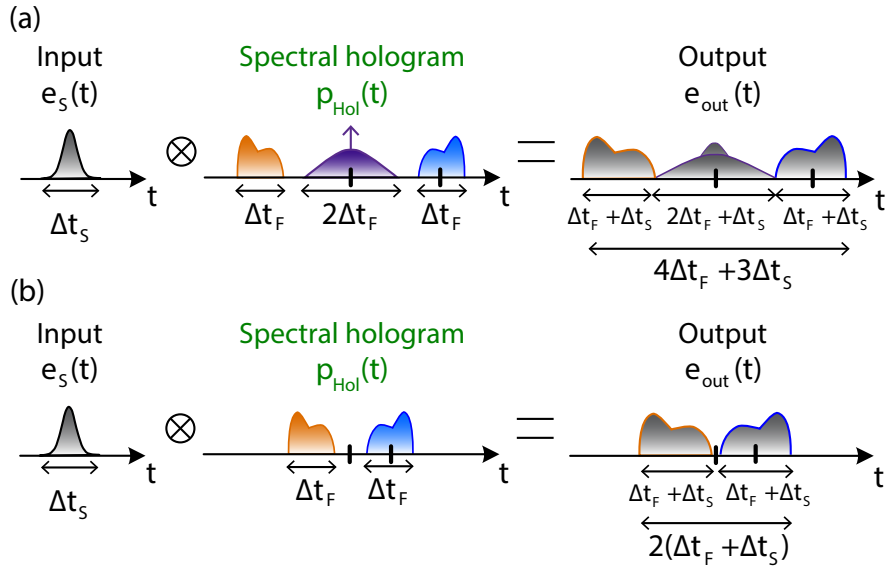


**Figure 5.1** – (a) Temporal width of the output signal resulting from convolving the input signal to be processed with the impulse response of the spectral hologram; (b) Temporal width of the output signal if the terms proportional to the intensity of the target impulse response and reference signal are not considered in the generation of the spectral hologram.

If the condition  $A \gg |\hat{h}_F(t)|$  is satisfied, the first term in the RHS of Eq. 5.4 can be neglected, relaxing the temporal window requirement in  $2\Delta t_F$ . Still, the temporal duration of the output signal would be  $> 2\Delta t_F + 3\Delta t_S$ , due to the presence of a copy of the input signal at the output ( $\propto \hat{e}_{in}(t) \otimes A^2\delta(t)$ ). In case the spectral hologram is computationally designed (instead of being obtained from the physical implementation of the interferometry process), the two components proportional to intensity-only variations of  $\hat{h}_F(t)$  or  $\hat{h}_{Ref}(t)$  (first and second terms) in the RHS of Eq. 5.3 can be omitted, significantly relaxing the temporal aperture of the output signal. In this case, the spectral hologram has the following temporal profile,

$$\hat{p}_{Hol}(t) = A\hat{h}_F(t - t_p) + A\hat{h}_F^*(-t - t_p). \quad (5.5)$$

Then, as depicted in Fig. 5.1(b), the total time window of  $p_{Hol}(t)$  is reduced to  $2\Delta t_F + 2\Delta t_S$ . The output signal will be then composed of two terms, and the temporal overlapping between them is avoided by imposing  $t_p > (\Delta t_F + \Delta t_S)/2$ .

Finally, the target output component ( $\propto \hat{e}_{in}(t) \otimes A\hat{h}_F(t - t_p)$ ) can be isolated from the rest of the output signal by using a time gating process. This can be implemented through a simple temporal EO modulation process, of straightforward application for an output signal with a duration of hundred of picoseconds [12]; or through a nonlinear optical switching process, e.g. using a Kerr shutter, for output signals' duration in the picosecond or sub-picosecond regime [199].

In the following Sections, the concept of spectral-domain holography will be employed for the design of optical signal processors with arbitrary (complex-valued) impulse responses for their implementation in two different component technologies, namely, TDSS-based methods and FBGs operating in transmission. Thus, we will demonstrate how the typical limitation of the former, i.e., restricted to real-valued transfer functions; and the latter, i.e., limited to MP spectral responses, can be overcome by the use of this newly presented concept.

### 5.3 Electro-optical approach: time-domain Vander-Lugt filters

The traditional scheme to implement optical filters in the spatial domain, reviewed in Section 3.4, performs a spectral shaping process by (i) Fourier transforming an incident wave using a lens-based system; (ii) shaping the resulting Fourier transformed wave by means of a modulation process using an amplitude and/or phase mask or a spatial light modulator (SLM), and (iii) inverse Fourier transforming the resulting wave using a second lens-based system (Fig. 3.4) [12, 120–122]. Prior to the development of modern SLMs, Vander-Lugth filters were proposed as a holography-based solution to implement complex-valued filtering in the spatial domain using amplitude-only or phase-only masks.

The spectral shaping technique for performing spatial domain filtering has inspired a very promising method for implementing fiber-based electronically reconfigurable temporal pulse processors with resolutions in the sub-picosecond regime, following the space-time duality [56], see Fig. 5.2. This method is referred to as TDSS, and it employs: (i) an all-fiber dispersive medium, instead of spatial diffraction, to temporally separate the input pulse spectral components, (ii) a single modulator device, typically an EO modulator, to carry out the desired filtering process along the time domain, instead of the spatial mask or SLM of the space-domain case, and (iii) a second dispersive

medium with opposite dispersion with respect to the first one to recombine the previously separated spectral components of the modulated signal.

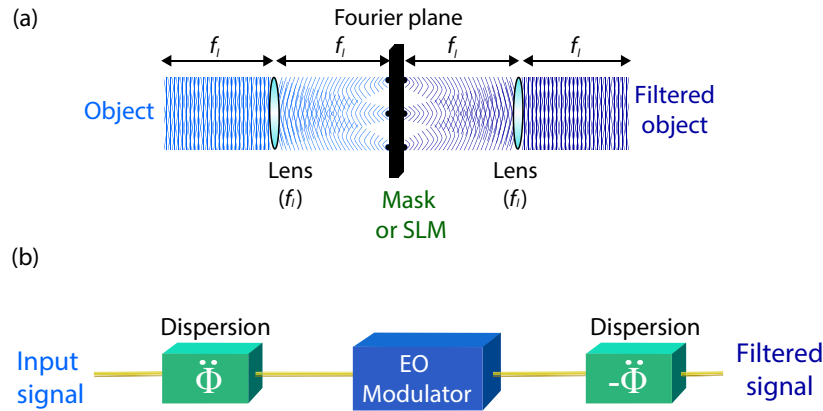


**Figure 5.2** – (a) Spatial domain spectral shaping setup, and (b) time-domain spectral shaping (TDSS) setup.  $f_l$  is the focal length of the lenses.

TDSS schemes based on an amplitude-only [115, 128, 196] or a phase-only [131, 197] modulation process have been proposed. The main limitation of traditional schemes implementing TDSS is that they are only capable of controlling the temporal intensity profile of the output waveform, and they have been typically limited to the synthesis of purely symmetric temporal shapes [115, 128, 131]. A novel technique to shape the pulse intensity profile into arbitrary, including non-symmetric, temporal profiles using phase-only EO modulation has been theoretically demonstrated; in this technique the radio frequency (RF) modulating signal is specially designed using an optimization algorithm [197]. Still, this method does not provide any control of the temporal phase profile of the synthesized waveforms. Also, a method for implementing complex-valued pulse shaping has been theoretically proposed [196]. This method requires however that the modulating signal is nonuniformly sampled with a very high temporal resolution, significantly hindering the practical implementation of the proposal. To date, no experimental demonstration has been reported of a complex-valued pulse shaper based on a TDSS scheme using a single amplitude-only or phase-only modulator. In fact, if an arbitrary (non-symmetric) complex-valued pulse shaper is to be implemented using previous designs, an IQ modulator, or the concatenation of precisely synchronized amplitude and phase modulators, would need to be used for realization of a complex-valued filter's transfer function. However, this configuration would significantly increase the complexity and cost of the system.

It is possible to implement a signal processor with a complex-valued transfer function still using a similar setup to those previously used for TDSS techniques (Fig. 5.3), i.e., composed of a single

amplitude EO modulator in between two opposite-dispersion media. This can be achieved through the use of a spectral hologram as the driving signal in the EO modulation process. As described above, a spectral hologram is a signal with a real-valued spectral response that contains complex information of the target filter's transfer function. The overall scheme can be interpreted as the time-domain counterpart of Vander-Lugt filters [151], reviewed in Section 3.4. In our proposed configuration, the spectral hologram is computationally designed following the derivation in Section 5.2, and then physically generated using an arbitrary waveform generator (AWG), i.e., similarly to the computer-based design process to generate temporal holograms (Section 4.3.1) [153].

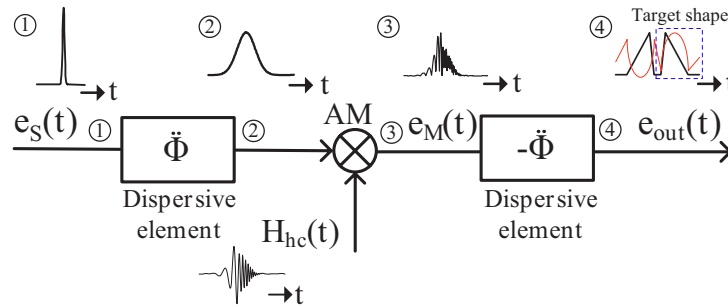


**Figure 5.3 – Schematic of operation of the TDSS system. Vander-Lugt filters are based on this configuration, but using a spectral hologram as the modulating signal. AM: amplitude modulation.**

In general, this system using a temporal modulation process is a time variant system. However, the response of this system can be approximated as LTI when assuming certain restrictions related to the timing synchronization and the temporal duration of the input pulse. In particular, it is necessary to assume that (i) the optical input pulse is synchronized with the electrical modulating signal and (ii) the temporal width of the dispersed pulse is shorter than the modulating signal. Under these restrictions, the system response can be characterized by a temporal impulse response and the corresponding spectral transfer function. These requirements can be seen as the time-domain equivalents of the need for imposing a spatial alignment between the input wave and the optical components and the aperture limitation when using a spatial-domain optical filter.

It is important to notice the fundamental difference between the schemes for performing spectral shaping in the spatial and the time domains (illustrated in Fig. 5.2). In the spatial domain approach (Section 3.4), the lens-based Fourier transforming system placed before and after the modulating mask is able to generate the exact Fourier transform (in amplitude and phase) of an input waveform. Also, in the spatial-spectral hologram recording process (Fig. 3.5(a)), an additional Fourier transforming system is used, which also computes the exact Fourier transform of the filter

impulse response. In the time domain approach, however, dispersive media (operating within the Fraunhofer condition) are used to separate and recombine the spectral components of the input temporal signal. In this case, the Fourier transforming process is achieved only in amplitude, since the resulting phase contains an additional quadratic term [200]. This circumstance must be taken into consideration for the design of the spectral hologram  $P_{Hol}(\omega')$  (with temporal profile defined in Eq. 5.5), which requires additional important considerations for the design strategy presented in the previous Section 5.2.

In the following derivation of the spectral hologram, capital letters are employed for signals proportional to spectral profiles, and lowercase letters for signals proportional to temporal profiles, regardless of their domain of definition ( $t$  for time domain and  $\omega$  for frequency domain).

Let us assume that the input signal is a transform-limited Gaussian pulse, defined as  $e_S(t) = \hat{e}_S(t) \exp\{j\omega_0 t\}$ , where  $\hat{e}_S(t) = \exp\{-t^2/2T_0^2\}$ ,  $T_0$  is the half width at  $1/e$  maximum and  $\omega_0$  is the carrier optical frequency. The envelope of the target filter's temporal impulse response is  $\hat{h}_F(t)$  (at  $\omega_0$ ). The input signal  $e_S(t)$  is first dispersed in a medium with transfer function

$$H_{\ddot{\Phi}}(\omega') = \exp\left\{-j\frac{\ddot{\Phi}\omega'^2}{2}\right\}, \quad (5.6)$$

where  $\ddot{\Phi} = \ddot{\beta}L$  is the chromatic dispersion, with  $\ddot{\beta}$  and  $L$  being the second order chromatic dispersion coefficient and the length of the medium, respectively. The dispersed signal is amplitude modulated by an RF signal  $H_{hc}(t)$ , which is a spectral hologram built from the function  $h_F(t)$ . The Fourier transform of the signal at the output of the modulator is

$$E_M(\omega') \propto [E_S(\omega') \cdot H_{\ddot{\Phi}}(\omega')] \otimes h_{hc}(\omega), \quad (5.7)$$

where  $E_S(\omega') = \mathcal{F}\{\hat{e}_S(t)\}$ , and  $h_{hc}(\omega) = \mathcal{F}\{H_{hc}(t)\}$ . Following the derivation in Section 5.2, the modulating waveform would be defined as

$$H_h(t) \propto H_F(t) \exp\{-j\omega_p t\} + H_F^*(-t) \exp\{j\omega_p t\}, \quad (5.8)$$

which has been named as  $H_h(t)$  instead of  $H_{hc}(t)$  since an additional step has to be made on top of the described algorithm, as detailed in what follows. The parameter  $\omega_p$  is chosen to avoid any spectral overlapping between the two terms in the RHS of Eq. 5.8; namely  $\omega_p > \Delta\omega_F/2$ , where

$\Delta\omega_F$  is the bandwidth of  $h_F(\omega) = \mathcal{F}\{H_F(t)\}$ . The parameter  $\omega_p$  should be associated with the delay  $t_p$  in Section 5.2. Both terms ( $\omega_p$  and  $t_p$ ) represent a shift between the target “impulse response” and the reference signal that is used to generate the spectral hologram. The change of domain of definition (frequency  $\rightarrow$  time) in the spectral hologram for implementation of Vander-Lugt filters is intrinsic to its setup. To provide an intuitive insight, it can be considered that the dispersion medium brings the spectrum shape to the time domain to perform the target spectral shaping via a temporal modulation process. Note that capital letters are used in Eq. 5.8 to point out the fact that the signals  $H_F(t)$  and  $H_h(t)$  have a temporal complex envelope with a shape proportional to the corresponding spectral transfer functions.

When the dispersed input signal is amplitude modulated with  $H_h(t)$  (meaning that in Eq. 5.7:  $h_{hc}(\omega) = \mathcal{F}\{H_h(t)\}$ ) and subsequently propagated through a medium with chromatic dispersion  $-\ddot{\Phi}$ , the resulting output signal is proportional to  $\hat{e}_S(t) \otimes h_{hc}(t) \exp\{-j t^2/2\ddot{\Phi}\}$ , which exhibits an additional quadratic temporal phase term that prevents to obtain the target output phase profile. The reason of this additional chirp is the fact that a dispersive medium is not performing an exact Fourier transformation (in amplitude and phase). In order to cancel out this undesired phase term, a quadratic spectral phase term proportional to  $H_{-\ddot{\Phi}}(\omega)$  needs to be added to the spectrum of  $H_h(t)$ , i.e.,  $h_h(\omega)$ . However, the modulating signal (the spectral hologram) must still be a real-valued function. For this purpose, we use the following design strategy: the added phase terms to the two corresponding spectral sidebands of  $H_h(t)$  must have opposite sign, in such a way that the total spectral phase added is an odd symmetric function. Recall that a temporal signal with even magnitude and odd phase has a real-valued spectral response [46]. This operation results in a modulation signal with the following spectral response,

$$h_{hc}(\omega) \propto h_F(\omega - \omega_p) \exp\left\{j \frac{\ddot{\Phi}\omega^2}{2}\right\} + h_F^*(-\omega - \omega_p) \exp\left\{-j \frac{\ddot{\Phi}\omega^2}{2}\right\}, \quad (5.9)$$

where  $h_{hc}(\omega) = \mathcal{F}\{H_{hc}(t)\}$ . Substituting Eq. 5.9 into Eq. 5.7, and assuming that the spectrum of  $H_{hc}(t)$  is confined to a small spectral range such that  $T_0\omega_m \ll 1$ , where  $\omega_m$  is the maximum frequency of  $H_{hc}(t)$ , the modulated optical signal spectrum,  $E_M(\omega')$ , can be approximated as

$$E_M(\omega') \propto E_S(\omega') H_{\ddot{\Phi}}(\omega') \left[ H_F(\omega') \exp\{j \ddot{\Phi}\omega_p\omega'\} + H_F^*(\omega') \exp\{-j \ddot{\Phi}\omega_p\omega'\} \otimes \exp\{-j \ddot{\Phi}\omega'^2/4\} \right] \quad (5.10)$$

The interested reader can find the mathematical derivation of this result in Section A.2 of Appendix A. Finally, the modulated optical signal propagates through a second dispersive medium with a dispersion value of  $-\ddot{\Phi}$ , as shown in Fig. 5.3. At the output, the complex envelope of the resulting temporal waveform can be written as

$$\hat{e}_{out}(t) \propto \hat{e}_S(t) \otimes h_F(t - \ddot{\Phi}\omega_p) + \hat{e}_S(t) \otimes (h_F^*(-t - \ddot{\Phi}\omega_p) \exp(-j t^2/\ddot{\Phi})). \quad (5.11)$$

Equation 5.11 shows that the output signal consists of two different terms, one of them being proportional to the desired temporal waveform (first term in the RHS of the Equation). The two terms are temporally shifted with respect to each other; therefore, the operation time window  $\Delta T_{out}$  of the scheme is reduced at least by half with respect to the case where a symmetrical intensity-only system's impulse response is targeted. In this latest case, the temporal aperture is determined by the product of the modulating signal bandwidth ( $\omega_m \propto 1/\delta t_{hc}$ , where  $\delta t_{hc}$  is the modulation temporal resolution), and the employed dispersion value  $|\ddot{\Phi}|$  [131]. The temporal resolution of the output optical shape,  $\delta t_{out}$ , is just limited by the input pulse time-width ( $\propto T_0$ ), assuming that the input pulse frequency bandwidth is narrower than the pass band of the dispersive medium  $\Delta\omega_D$ , similarly to the case where intensity-only shapes are targeted [128, 131, 197]. Therefore, the time-bandwidth product (TBP) of the Vander-Lugt filter (TBP =  $\Delta T_{out}/\delta t_{out}$ ), which is typically used as a figure of merit of pulse shaping systems, is directly proportional to the product  $\omega_m \cdot \ddot{\Phi} \cdot \Delta\omega_D$ . Thus, it is possible to increase the TBP by increasing the bandwidth of the modulating signal or increasing the dispersion value. As observed from the mathematical derivation (see Appendix A), there is not a condition imposed on the value of  $\ddot{\Phi}$  with respect to the temporal duration of  $e_S(t)$ , i.e., there is no need to work within the Fraunhofer condition<sup>2</sup> [201]. However, it is still important to ensure that the temporal duration of the dispersed input signal is longer than the duration of the modulating signal  $H_{hc}(t)$ . Finally, the desired portion of the output temporal signal may be filtered in by a time-gating process if needed.

---

<sup>2</sup>The time-domain analog of the spatial Fraunhofer condition is  $|\ddot{\Phi}| \gg \Delta t_0^2/(2\pi)$ , where  $\Delta t_0$  is the total temporal duration of the input pulse [200].

### 5.3.1 Application of time-domain Vander-Lugt filters as pulse shapers

Time-domain Vander-Lugt filters have been introduced as reconfigurable EO pulse processors that generate an output signal with a complex envelope proportional to the convolution between an input optical signal and the Fourier transform of a “cleverly designed” RF signal (Eq. 5.11). Convolution is the basis of any linear, time invariant signal processing function and as such, Vander-Lugt filters have a myriad of applications within the context of optical signal processing. As introduced in Section 5.1, time-domain Vander-Lugt filter can be considered as LTI system assuming synchronization between the optical input pulse and the electrical modulating signal. This assumption can be seen as the time-domain dual of assuming a spatial alignment between the waveform to be processed, the holographic mask and the  $4f_l$  lens system in the classical (spatial-domain) case<sup>3</sup>. In this Section we employ time-domain Vander-Lugt filters for fiber-based, truly arbitrary optical pulse shaping. The required setup has the same circuitry complexity as previously proposed TDSS schemes, while their shaping restrictions are overcome by the design of a prechirped spectral hologram [156].

Figure 5.4 shows the setup employed for experimental demonstration of optical pulse shaping based on time-domain Vander-Lugt filters. In particular, this figure includes the setup required for performing a time-domain Vander-Lugt filter and subsequently characterizing the synthesized output waveforms. The capabilities of the proposed scheme are successfully demonstrated by synthesizing two different temporal waveforms of practical interest, namely, an asymmetric triangular-shaped pulse with parabolic phase, and a 4-symbol 16-QAM pulse code sequence.

The input signal  $e_S(t)$  is generated by a passive mode-locked laser (PMLL). It consists of a train of 2 ps-FWHM Gaussian-like optical pulses with a repetition rate of 10 MHz, centered at  $\lambda_0 = 2\pi c_0/\omega_0 = 1545$  nm. This signal is dispersed using a reflective linearly-chirped FBG (LC-FBG) providing a dispersion equivalent to 120 km of SMF, i.e.,  $\ddot{\Phi} \propto -2600$  ps<sup>2</sup> over the entire optical telecommunication C band (1535-1565 nm). The dispersed output is modulated using a Mach-Zehnder modulator (MZM). The MZM is biased in the minimum transmission point so that it operates as an amplitude modulator [128].

The modulating signal, i.e., the spectral hologram  $H_{hc}(t)$ , is generated using an AWG; namely the AWG-7122C from Tektronix with a 3dB analog bandwidth of 9.6 GHz and a sampling rate of

---

<sup>3</sup>Note that certain restrictions are also applied on the width of the optical input signal to be processed, see Sections 5.1 and 5.3.

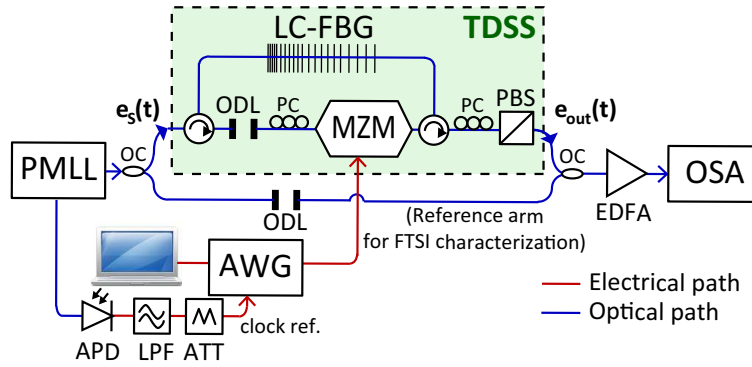


**Figure 5.4** – Setup employed for the experimental demonstration of pulse shapers based on time-domain Vander-Lugt filters. The setup includes the time-domain Vander-Lugt filter in the upper arm of an interferometry configuration (inside the green rectangle); the interferometry configuration is employed for characterization of the output shaped signal via Fourier transform spectral interferometry (FTSI). PMLL: passive mode-locked laser; OC: optical coupler; ODL: optical delay line; PC: polarization controller; PBS: polarization beam splitter; LC-FBG: linearly-chirped fiber Bragg grating, EDFA: Erbium-doped fiber amplifier; APD: avalanche photodiode; LPF: low pass filter; ATT: attenuator.

20 GSps. The secondary output of the PMLL is used to synchronize the laser with the output of the AWG. This low power laser output is first photodetected using an avalanche photodiode, in order to have a sufficiently powerful electrical signal after the photodetection. The electrical signal is filtered using a low pass filter (LPF) with a 3dB bandwidth of 14 MHz, which only keeps the first harmonic of the RF signal at 10 MHz (the LPF's insertion loss at the frequency of the second harmonic, i.e., at 20 MHz, is 31.35 dB). Therefore, the output of the filter is a sinusoidal RF signal with a frequency of 10 MHz, which is used by the AWG as a reference clock signal (the used AWG only accepts a sinusoidal function as reference clock). The optical modulated signal is then reflected from the opposite extreme of the LC-FBG, being thus affected by a dispersion value of  $-\Phi$ . After that, the desired output from the FBG is discriminated from the residual transmitted input by using a polarization controller (PC) and a polarization beam splitter (PBS).

To characterize the system's output, a Fourier transform spectral interferometry (FTSI) scheme is employed [202]. The setup for implementing the Vander-Lugt filter is placed in one arm of a Mach-Zehnder interferometer (depicted within the green rectangle in Fig. 5.4). The second arm, i.e., the so-called reference arm, is set to provide a delay of about 100 ps difference with respect to the delay introduced by the first arm. The spectrum of the signals at both arms plus the spectrum of the interference are measured using a high resolution optical spectrum analyzer (OSA), namely the AP2043B from Apex with a resolution of 0.04 pm.

Figure 5.5(a) shows the designed spectral hologram  $H_{hc}(t)$  to generate the first target waveform, namely an asymmetric triangular shape with parabolic phase (details of the specifications are given below). The amplitude and phase profiles of the resulting temporal waveform are plotted in Fig. 5.5(b) and (c), respectively. As expected from the theoretical derivation, the output temporal signal consists of two separated components (see Eq. 5.11). In this case, the spectral-domain hologram is designed to properly re-shape the RHS of the resulting output signal (highlighted in Fig. 5.5(b) and (c)), in both amplitude and phase.

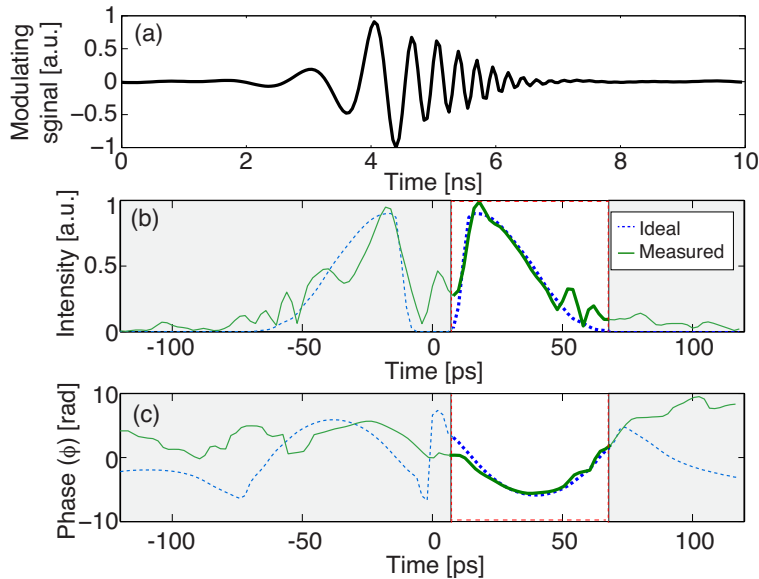


**Figure 5.5 – Asymmetric triangular pulse with parabolic phase:** (a) spectral hologram  $H_{hc}(t)$ ; (b) temporal intensity of the output signal; and (c) temporal phase of the output signal: target (dotted blue line) and measured (solid green line) output. The spectral hologram was designed so that the right-hand side of the temporal output (highlighted and marked with a dashed red line) matches the target profile.

The target triangular shape has a total duration (measured at 1% of its power peak) of 60 ps. The leading edge of the asymmetrical triangular shape has a total duration of 10 ps. The quadratic phase has a chirp value (defined as the second derivative of the phase with respect to the time variable) of  $0.008 \text{ ps}^2$ . From Fig. 5.5 (b) and (c), we observe a good matching between the numerically simulated (‘ideal’) amplitude and phase temporal profiles and those retrieved from FTSI measurements. The small peak in between the two copies of the triangular shape (at the center of Fig. 5.5(b)) is a residual DC component from an imperfect biasing of the MZM.

The second example shows the generation of a 4-symbol circular 16-QAM pulse code sequence. Figure 5.6(a) presents the designed temporal hologram. The amplitude and phase of the obtained temporal waveform are plotted in Fig. 5.6(b) and (c), respectively; in this case only the RHS of

the resulting waveform is presented. The total length of the 4-symbol code is  $\sim 72$  ps, and the full width at half maximum (FWHM) of each symbol is  $\sim 6$  ps. Again, a fairly good matching between the target signal and the measured signal can be observed.

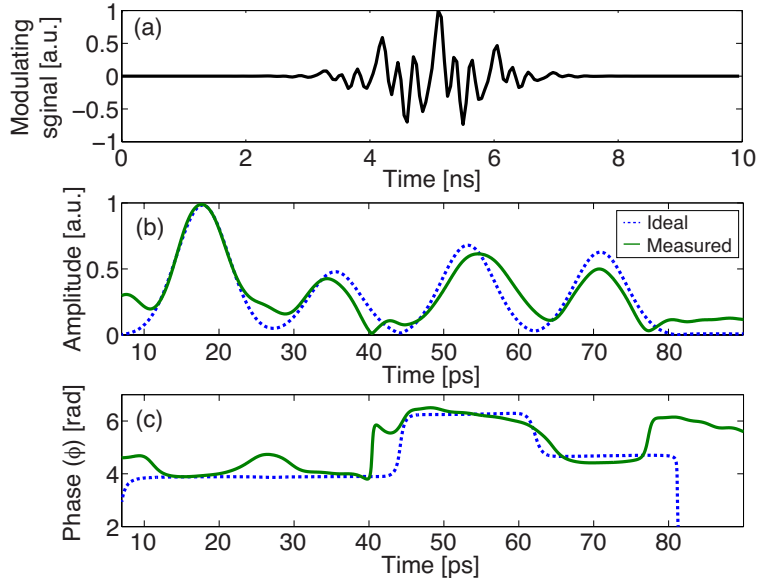


**Figure 5.6** – 4-symbol 16-QAM code: (a) spectral hologram  $H_{nc}(t)$ ; (b) temporal amplitude of the output signal, just right-hand side is shown; (c) temporal phase of the output signal: target (dotted blue line) and measured (solid green line) output.

In both reported experiments, considering the AWG bandwidth limitation (9.6 GHz) and employed dispersion ( $\sim 2600$  ps<sup>2</sup>), the maximum duration of our target output signals is limited to  $< \omega_m \ddot{\Phi}/2 = 125$  ps. The reduction in the experimental aperture with respect to the estimated maximum value is due to the fact that the temporal hologram was designed to have a bandwidth notably lower than the maximum allowed by the AWG, in order to enhance the quality of the modulation process and optical output. On the other hand, the temporal resolution of the output temporal waveforms,  $\delta t_{out}$ , and input optical pulses have been measured as the inverse of the full width at 1% of the maximum of the corresponding signal spectrum, considering that both the output and input pulses are nearly transform limited. In the two reported examples, we estimate an output temporal resolution of  $\delta t_{out} \sim 6.7$  ps, very close to the temporal resolution of the input pulse,  $e_S(t)$ , which is  $\sim 5.8$  ps. The slightly reduction in the resolution of the output signals with respect to the resolution of the input is due to the fact that the spectral holograms have been designed to have a temporal width shorter than the total temporal width (e.g., at 1% of its maximum) of the dispersed Gaussian pulse.

## 5.4 Spectral-domain holography for the design of arbitrary optical filters based on minimum-phase structures

Fiber Bragg gratings and long period gratings are periodic perturbations of the refractive index in the core of an optical fiber (defined in Eq. 1.9 and illustrated in Fig. 1.8). They have arisen as a critical component technology for a broad range of applications, specially in optical communications and sensor systems. In particular, in the last decade, this technology has attracted researchers' attention to effectively implement a wide variety of optical signal processors and optical pulse shapers based on linear filtering [11, 77–92, 102–105, 203, 204]. Advantages of fiber gratings include their all-fiber geometry, low insertion loss, compact format and potential low cost. Furthermore, the most distinctive feature of fiber gratings is the extraordinary flexibility they offer to achieve almost any desired band-pass spectral filtering characteristics (in amplitude or/and phase) when working in reflection, in the case of FBGs, or in a core-to-cladding configuration, in the case of LPGs.

For some applications, the use of FBGs in transmission may turn out to be more advantageous than in reflection. When the grating is operating in transmission, the complexity and cost of the system are reduced as it is not necessary to use a coupler or a circulator to retrieve the reflected signal. This feature is particularly interesting for implementation of gratings in integrated-waveguide platforms, where efficient optical circulators are not still available. In addition, the phase response in transmission is often more robust to imperfections in the grating structure than the phase response in reflection [100] (as reviewed in Section 1.3.2.1). Similarly, there are several reasons for preferring the use of the LPG in their core-to-core configuration. First of all, it is not needed to use an additional LPG [102] or a misaligned splicing [106] to couple the output signal back to the core. Besides, the phase response of LPGs is less sensitive to environmental perturbations in the core-to-core configuration than in the core-to-cladding configuration, due to a minor exposure of the mode at the core (reviewed in Section 1.3.2.2).

In this Section we will focus on signal processors based on FBGs. In spite of the fact that LPGs intrinsically provide operation bandwidths much broader than FBGs, i.e., well in the THz regime (recall that FBGs are typically limited to operation bandwidths of  $\sim 200$  GHz) [79, 80, 105], they suffer from serious limitations, particularly instabilities and high sensitivity to environmental fluctuations, which notably hinder their use as signal processors. Also, their significantly larger

footprint make their implementation in integrated formats very challenging. Still, it is anticipated that the design method employed here for processors based on FBGs in transmission could be potentially applied to LPGs in their core-to-core configuration (in under-coupling conditions) [198].

A couple of decades ago, there was a strong interest in the use of FBGs operating in transmission due to their aforementioned advantages. In particular, several approaches for implementing dispersion compensators were proposed [100, 205–207]. Dispersion compensation is an example of optical filter in which the amplitude and phase spectral response must be independently specified over a limited operation bandwidth. As introduced in Section 1.3.2.1 and demonstrated in Ref. [101], transmissive FBGs have a linear spectral response that is necessarily MP, i.e., the phase spectral response of the grating transmission is uniquely related to its amplitude spectral response through a Hilbert transform relationship. In this case, dispersion compensation operation was achieved by using the highly dispersive (but narrow) spectral regions near the band edge of a uniform [205] or apodized [100, 206, 207] FBG. Even though, the extremely restrictive MP condition of transmissive FBGs made researchers disregard this configuration.

Recently, there has been a renewed interest in FBGs operating in transmission [91, 146, 147]. Hence, several optical signal processors such as optical differentiators, integrators or flat-top pulse shapers have been recently proposed based on transmissive FBGs [91, 146, 147]. However, all the presented processors were restricted to (i) have an MP spectral response and (ii) operate within an operation bandwidth  $\leq 200$  GHz.

In this Section, we describe and numerically demonstrate a general and practical approach to design THz-bandwidth all-optical linear signal processing devices based on especially-apodized LC-FBGs working in transmission. The proposed methodology can be directly used to implement any optical signal-processing device based on an MP linear optical filter, offering operation bandwidths well into the THz regime (corresponding to sub-picosecond time features). Then, we extend the applicability of ultra-broadband transmissive FBGs to non-MP processing functions by the use of spectral-domain holography. Hence, spectral-domain holography arises as an interesting solution to overcome the limitation in the functionalities susceptible to be implemented using transmissive FBGs: any complex-valued spectral response with independent amplitude and phase profiles can be encoded in amplitude-only variations of a second spectral response, i.e., the spectral hologram. The presented methodologies are experimentally demonstrated through the design and implemen-

tation of THz-bandwidth, MP and non-MP functionalities in transmissive FBGs; in particular, we demonstrate an optical differentiator, a flat-top pulse shaper (MP functionalities) and a photonic Hilbert transformer (non-MP functionality).

#### 5.4.1 Increasing the operation bandwidth of fiber Bragg gratings

The proposed approach to increase the operation bandwidth of an FBG operating in transmission exploits the degree of freedom that is available in fixing the FBG reflection spectral phase response [99]. Thus, by inducing a suitable quadratic spectral phase profile in reflection, corresponding to a linear period chirp along the grating length, it is possible to increase the FBG's operation bandwidth without increasing the spectral resolution of the apodization profile. This quadratic phase in reflection does not affect the transmissive phase response due to its MP condition, as detailed in what follows.

The problem under analysis concerns the design of a linear optical filter providing a prescribed MP spectral transfer function,  $H_{ideal}(\omega')$ , over an ultra-broad bandwidth. Recall that  $\omega' = \omega - \omega_0$ , where  $\omega_0$  is the spectral response's central frequency. In the following derivation, we use the same notation as the one used in the Section 1.3.2; therefore,  $H_T(\omega')$  and  $H_R(\omega')$  determine the FBG transmissive and reflective spectral responses, respectively. As the processor to be designed is based on an FBG working in transmission,  $H_T(\omega')$  must be proportional to  $H_{ideal}(\omega')$  over the target operation bandwidth. In an MP filter (e.g. FBG in transmission), the filter's spectral phase response is necessarily determined by the desired spectral amplitude response since the real and imaginary parts of the spectral response are related by means of the Kramers-Kronig relationship. In addition, in an FBG, the transmissivity ( $T = |H_T(\omega')|^2$ ) and reflectivity ( $R = |H_R(\omega')|^2$ ) are necessarily related by  $T = 1 - R$ . Thus, the specifications of  $|H_T(\omega')|$  uniquely impose the functions  $\angle\{H_T(\omega')\}$  and  $|H_R(\omega')|$ . Therefore, from the specifications of the desired transmission amplitude spectral response,  $|H_T(\omega')|$ , the design problem reduces to synthesizing an FBG providing the reflection amplitude spectral response,  $|H_R(\omega')|$ , *with no additional constraints on the FBG reflection spectral phase response*,  $\angle\{H_R(\omega')\}$ . Hence, the FBG reflection spectral phase can be suitably fixed to achieve the simplest grating design according to the target specifications. Among different alternatives, minimum-phase, maximum-phase, linear phase, quadratic phase, cubic phase profiles (and so on) can be used [99].

In previous designs of all-optical signal processing devices based on transmissive FBGs, the selected reflection spectral phase has been linear [90] or maximum-phase [146]. Here, we make use of a reflection quadratic spectral phase for the synthesis of a transmission FBG, i.e. reflection linear group-delay which translates into a linear grating-period variation (or linear grating-period chirp) along the device length [53]. As the reflected frequency components along the grating are related to its period, the bandwidth of the spectral response in reflection, i.e. the corresponding rejected bandwidth in transmission, can then be significantly higher than in the uniform grating-period case. Our numerical simulations show that the reflective quadratic spectral phase enables the synthesis of arbitrary amplitude spectral responses over bandwidths well in the THz range using feasible and remarkably simple FBG apodization profiles.

In particular, the FBG reflection spectral response that must be synthesized can be mathematically expressed by

$$H_R(\omega') = W(\omega') \sqrt{R_{max} \left(1 - |H_T(\omega')|^2\right)} \exp \left\{ j \frac{1}{2} D \omega'^2 + \tau_{shift} \omega' \right\}, \quad (5.12)$$

where  $H_T(\omega')$  is proportional to  $H_{ideal}(\omega')$  over the target operation bandwidth;  $R_{max}$  is the maximum peak reflectivity;  $D$  is the dispersion parameter ( $s^2$ ) or equivalently, the group-delay slope;  $W(\omega')$  represents a windowing function, which is introduced considering that the reflective response of an FBG must be a limited band-pass filtering function; and  $\tau_{shift}$  is a time delay, which translates into the linear spectral phase factor in Eq. 5.12, introduced to make the device causal. The dispersion parameter  $D$  will determine the minimum grating length  $L$ , according to the relationship

$$D = \frac{2Ln_{av}/c_0}{2\pi B}, \quad (5.13)$$

where  $n_{av}$  is the average refractive index of the grating (see Eq. 1.9);  $c_0$  is the speed of light in vacuum; and  $B$  is the full-width reflection bandwidth of the device (Hz). From the target reflective spectral response specifications defined by Eq. 5.12, the proposed method obtains the grating perturbation using a layer-peeling FBG synthesis algorithm [74] based on coupled-mode theory (CMT) combined with a transfer-matrix method (TMM). The interested reader can find a detailed description of the CMT-TMM algorithm in Section B.2.1 of Appendix B. The use of this exact FBG synthesis approach is essential to obtain the correct grating profile since the weak-coupling space-to-frequency mapping conditions that are typically assumed in previous designs based on LC-FBGs

[208] are not usually fulfilled. This is associated with the fact that generally, the target spectral response ought to be strong-coupling ( $R_{max} \sim 1$ ).

It is worth mentioning that our numerical studies have confirmed that the resulting grating apodization specifications (spatial resolution and maximum peak index modulation) can be easily relaxed by suitably increasing the specified value of the dispersion parameter ( $D$ ). The higher the dispersion parameter, the longer the resulting grating device: there is higher group delay over the same bandwidth, what implies longer length. This also leads to lower maximum peak refractive index modulation as the reflection of light is distributed over this longer length.

## 5.4.2 Applications of ultra-broadband transmissive FBGs as MP processors

In this Section, we show examples of MP all-optical pulse processors and shapers with up to several THz operation bandwidth using feasible transmissive FBGs incorporating a properly designed grating period chirp. In particular, we present the design of two relevant MP optical processors, namely, arbitrary order optical differentiators and a flat-top pulse shaper. Moreover, the flat-top pulse shaper has been also successfully fabricated and characterized, and experimental results are presented here as well.

### 5.4.2.1 Arbitrary order optical differentiators

A temporal optical differentiator is a signal processing device that provides at its output the derivative of the temporal complex envelope of an input optical signal. The ideal spectral transfer function of an arbitrary order differentiator can be expressed as

$$H_{diff}(\omega') \propto (j \cdot \omega')^N, \quad (5.14)$$

where  $N$  is the differentiator order. A number of different approaches for first- and high-order optical differentiators have been proposed based on FBGs operating in reflection, each of them trying to improve their operation bandwidth or spectral resolution within practical limitations of the employed technology [81, 87, 91, 208, 209]. Optical differentiators have been employed for the generation of first- and high-order Hermite-Gaussian optical pulses [210]. Hermite-Gaussian polynomials form a complete set of orthogonal temporal functions, a property that can be readily exploited

in advanced coding for network access applications. Moreover, based on this property, a platform has been proposed for programmable arbitrary optical pulse shaping involving the combination of weighted first- and high-order derivatives of an input Gaussian-like pulse [135].

We have designed a first-order all-optical differentiator ( $N = 1$ ) with a processing bandwidth of  $B = 2$  THz (full-width at 1% of the maximum spectral amplitude), using the approach described in Section 5.4.1 [84]. In the design process, Eq. 5.12 is employed, where  $H_T(\omega') = H_{diff}(\omega')$ , the dispersion parameter  $D$  was set to  $80 \text{ ps}^2$ ,  $\tau_{shift} = 1.356 \text{ ns}$ , and  $R_{max}$  was set to 99.9999%. In this case, no windowing is required,  $W(\omega') = 1$ , as the reflective transfer function is inherently a band-pass function.

A CMT-TMM synthesis tool [74] was employed to obtain the grating profile of the desired FBG-based optical differentiator from the specifications in Eq. 5.12, which is plotted in Fig. 5.7(a). The synthesized grating device is readily feasible with current fabrication technology, with (i) an effective length of 10.37 cm (as expected from Eq. 5.13), (ii) a chirp value of  $-0.52 \text{ nm/cm}$ , (iii) an amplitude-only apodization function with a peak refractive index modulation  $\Delta n_{max} = 0.72 \times 10^{-3}$ , and (iv) an average spatial resolution of the ripples in the apodization profile of  $\sim 0.3 \text{ mm}$ . Therefore, the fabrication parameters were significantly relaxed as compared with previous designs based on uniform-period transmissive FBGs [91], while the achievable processing speed was increased in one order of magnitude. To give a quantitative comparative analysis on the improvements of our design, we have numerically simulated the same specified spectral response  $H_T(\omega')$ , but selecting a linear phase for the reflection spectral response, i.e.  $D = 0$ . The synthesized FBG, which is in this case has uniform period, requires a  $\Delta n_{max} = 9.4 \times 10^{-3}$ , more than one order of magnitude higher than using a quadratic reflective spectral response. Moreover a challenging spatial apodization profile with a resolution  $\leq 0.05 \text{ mm}$  and multiple discrete phase shifts is required to achieve the same target processing bandwidth [84]. These results are in line with the ones presented in Ref. [91] for an optical differentiator based on a uniform period transmissive FBG.

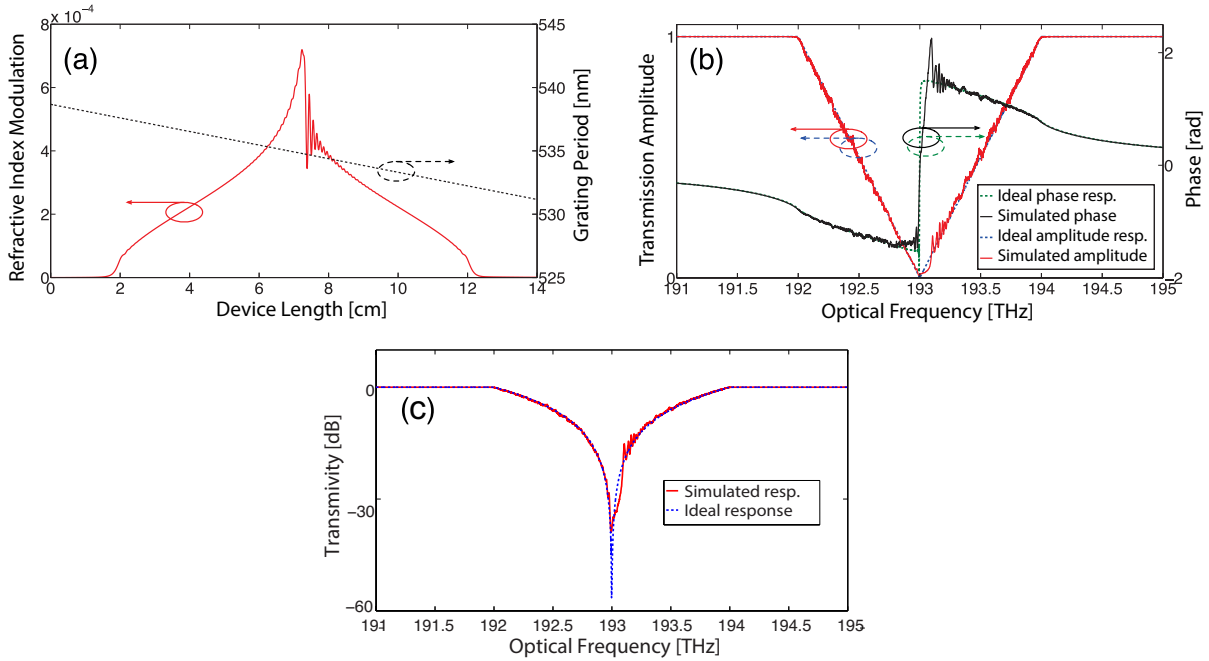
As this example has not been experimentally demonstrated, we have numerically analyzed its robustness against realistic variations in the amplitude and phase grating profiles with respect to the designed nominal values, as induced during a typical fabrication process [211]. Those deviations

have been modeled and included in the resulting grating profile shown in Fig. 5.7(a) as,

$$\begin{aligned} n_{FG}(z) &= n_{av} + \Delta n \left( 1 + \delta n(z) \right) \cos \left( \frac{2\pi}{\Lambda} z + \phi(z) + \theta(z) \right); \\ \phi(z + \Delta) - \phi(z) &= \int_z^{z+\Delta} \delta\phi(\zeta) \cdot d\zeta, \end{aligned} \quad (5.15)$$

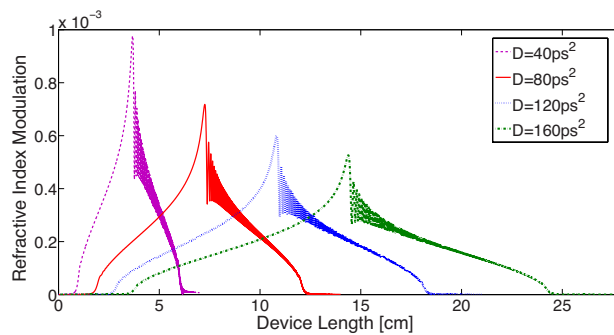
where  $n_{av}$  is the average effective index and, among the deterministic grating parameters,  $\Delta n$  accounts for the obtained local grating strength (apodization),  $\Lambda$  is the reference period and  $\theta(z)$  determines the obtained phase variation and local period in the synthesis process. The random properties of the grating are described by the amplitude and phase stochastic processes  $\delta n(z)$  and  $\delta\phi(z)$ , respectively. The amplitude fluctuations in the refractive index have been modeled by a zero-average, stationary Gaussian variable  $\delta n(z)$  whose standard deviation has been set equal to 2% of the maximum refractive index change. The random phase component is also described by a zero-average, stationary Gaussian function  $\delta\phi(z)$  with a standard deviation equal to 0.1% of its grating period, which drives the phase term  $\phi(z)$ . These values are similar to typical values found in practice [211]. The grating profile obtained from the synthesized LC-FBG, with the added stochastic amplitude and phase variations, has been numerically analyzed using a CMT-TMM-based analysis algorithm [54] (a description of this algorithm can be found in Section B.1.1 of Appendix B). Figure 5.7(b) shows the resulting transmission amplitude and phase spectral responses (after compensating constant and linear phase terms). The target linear spectral amplitude variation over the desired bandwidth is achieved with high accuracy. The  $\pi$ -phase shift required at the central frequency  $f_0 = \omega_0/2\pi$  is intrinsically generated due to the MP condition of the transmission spectral response. As observed in the plot, the anticipated fabrication errors slightly modify the original expected response, and in particular, they mainly have an impact on the random ripples observed over the ideal linear-amplitude spectral response. The higher deviation occurs around the central frequency, as observed in Fig. 5.7(c). Nevertheless, this deviation barely affects the device's behavior as an optical temporal differentiator, it just limits the duration of the pulses that can be processed (narrow bandwidth), as numerically demonstrated in the following temporal characterization.

Figure 5.8 shows the synthesized grating apodization profiles for different chosen values of the dispersion parameter. The dispersion parameter can be easily tuned by accordingly changing the slope of the linear grating-period variation (for a fixed operation bandwidth). Figure 5.8 clearly illustrates that the dispersion parameter is a fundamental design parameter which can be properly



**Figure 5.7 – First-order optical differentiator based on an FBG in transmission: (a) Apodization (red solid line) and period (black dashed line) profiles considering realistic spatial resolution (limited to 0.3 mm) and linearly chirped phase mask; (b) Specified transmission spectral response, amplitude (dotted blue line) and phase (dotted green line) compared to fabrication-constrained transmission spectral response, amplitude (solid black line) and phase (solid red line); (c) Ideal transmissivity in dB (dotted blue line) and fabrication-constrained transmissivity in dB (solid red line).**

selected to ensure that the resulting grating apodization specifications match the fabrication constraints. In particular, a higher dispersion value translates into a more relaxed spatial resolution and a lower refractive index modulation peak, but requiring a longer device.



**Figure 5.8 – First-order optical differentiator based on an FBG in transmission: Grating apodization profiles and device lengths obtained for different values of the dispersion parameter.**

The temporal characterization of the designed optical differentiator is presented in Fig. 5.9(a), where a 1 ps-FWHM input Gaussian pulse centered at  $\omega_0$  is considered. In the figure, the ideal expected output signal and the output from an FBG with typical fabrication constraints are com-

pared, showing an excellent match between the two curves. Besides, the accuracy and robustness of the designed differentiator have been estimated through the cross-correlation coefficient ( $C_C$ ) [212]. The  $C_C$  coefficient provides a precise estimate of the level of similarity of the processed waveform with respect to that expected for an ideal processor, and it is calculated as

$$C_C[\%] = \frac{\int_{-\infty}^{+\infty} \hat{e}_{out}(t) \cdot \hat{e}_{ideal}(t) \cdot dt}{\sqrt{\int_{-\infty}^{+\infty} \hat{e}_{out}^2(t) dt \cdot \int_{-\infty}^{+\infty} \hat{e}_{ideal}^2(t) dt}} \times 100\%, \quad (5.16)$$

where  $\hat{e}_{out}(t)$  and  $\hat{e}_{ideal}(t)$  represent the actual (experimentally measured) and the ideal amplitude envelopes of the temporal output waveforms. In particular, Fig. 5.9(b) shows that the obtained  $C_C$  is higher than 90% when the input of the optical differentiator is a Gaussian pulse with a 3-dB spectral bandwidth ranging between 6 GHz and 2.53 THz. Note that the maximum value of bandwidth is higher than  $B = 2$  THz, pointing out that the tails of the Gaussian-like spectrum of the pulse being outside the linear spectral region of the differentiator slightly affects the temporal shape of the output pulse. This result allows us to make an estimation of the TBP of the device, which is the product of the maximum time window of the processor and its maximum operating bandwidth. The maximum bandwidth is related with the temporal resolution of the filter, and the maximum time window is related to the spectral resolution. Therefore, an estimation of the TBP can be calculated as the ratio between the maximum and the minimum temporal FWHM of an input Gaussian pulse for which the  $C_C$  of the output is higher than a predefined value (corresponding to the ratio between the maximum and minimum 3dB-bandwidth of an input Gaussian pulse for which the  $C_C$  of the output holds higher than the predefined value). Even if the TBP is a commonly employed metric to measure the performance of optical filters, in the literature there is no agreement on the value of  $C_C$  to be used for its calculus. In general, its choice is based on the observation of the quality of the output pulses and it is left to the designer's criterion. In this Thesis, we estimate the TBP considering  $C_C > 90\%$ . Hence, the obtained TBP for the designed differentiator is  $\sim 420$ . Further simulations reveal that the values of  $C_C$  are approximately the same for all the implemented differentiators presented in Fig. 5.8 (variations within 0.01%). Secondly, to give numerical data about the influence of the fabrication inaccuracies,  $C_C$  has been also calculated from the spectral response obtained after taking into account the aforementioned fabrication errors, results plotted in red in Fig. 5.9(b). As observed in the figure, the range of input pulse-widths that gives a  $C_C$  coefficient higher than 90% is practically the same as the one without considering the anticipated errors.

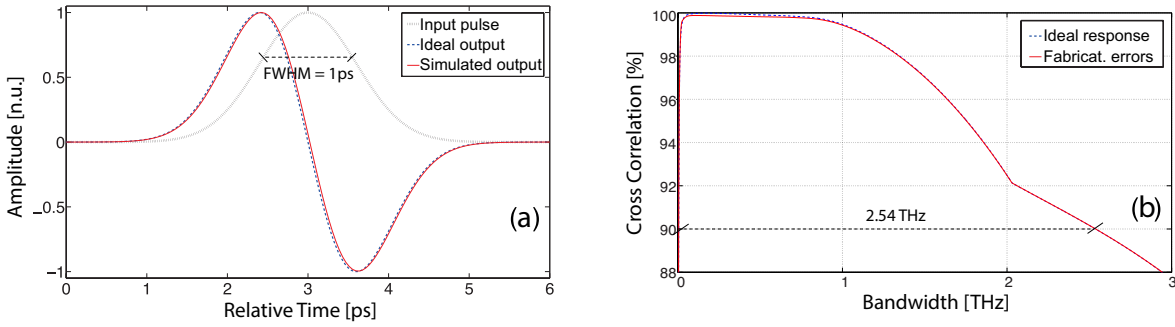


**Figure 5.9 – First-order optical differentiator based on an FBG in transmission:** (a) Input Gaussian-like pulse (dotted black line) and comparison between the ideal output (dashed blue line) and the numerically obtained output from a differentiator assuming fabrication constrains (red solid line); (b) Cross-correlation coefficient between the ideal and the numerically obtained temporal output waveform as a function of the 3 dB-bandwidth of an input Gaussian pulse for the original design (blue dashed line) and the perturbed design considering potential fabrication errors (red solid line).

The design of 2 THz higher order (up to  $N = 4$ ) optical differentiators was also proposed based on the same design methodology, shown in Fig. 5.10 [213]. All the design parameters were set to similar values to those ones from the previous example. Only the specified transmission dip varies from  $20 \cdot \log(|H_T(\omega' = 0)|) = -60$  dB from the first order to  $-90$  dB for the fourth order. These values are related to the required  $R_{max}$  for each order: as the differentiator order increases, the value of  $|H_R(\omega' = 0)|$  needs to be higher to guarantee quasi-zero transmission at  $\omega' = 0$ . Numerical simulations are used to evaluate the output temporal waveforms when a Gaussian-like 850 fs-FWHM input pulse is launched at the input of the FBG. Figure 5.10(b) shows the first-to-fourth order derivatives of the input pulse, exhibiting an excellent agreement with the expected output waveforms from the ideal differentiators.

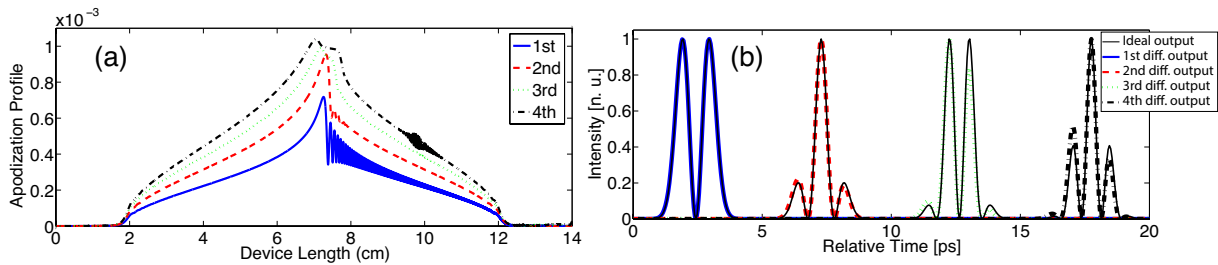


**Figure 5.10 –  $N^{th}$ -order optical differentiators (up to  $N = 4$ ) based on FBGs in transmission:** (a) Apodization profiles considering realistic spatial resolution (limited to 0.5 mm); (b) Time-domain intensity outputs from practical FBG-based differentiators.

### 5.4.2.2 Ultra-fast flat-top (rectangular) pulse shapers

A flat-top (rectangular) pulse shaper provides at its output an optical pulse with a rectangular-like envelope. To define the transfer function of the flat-top pulse shaper, it is necessary to specify the input pulse as well. The required spectral response is

$$H_{ft}(\omega') = \frac{E_{out}(\omega')}{E_{in}(\omega')} \propto \frac{\text{sinc}(\omega' \cdot \tau_{FWHM}/2\pi)}{E_{in}(\omega')}, \quad (5.17)$$

where the sinc function is defined as  $\text{sinc}(\pi\omega')/(\pi\omega')$ , and  $\tau_{FWHM}$  is the FWHM duration of the desired output flat-top pulse. Assuming a sufficiently short Gaussian input pulse, it is possible to approximate its transfer function as  $H_{ft}(\omega') \simeq \text{sinc}(\omega' \cdot \tau_{FWHM}/2\pi)$ . Flat-top (rectangular) pulses are of high interest for a wide range of applications. They are fundamental control signal in nonlinear optical switching, most prominently in the context of temporal demultiplexing of optical time-division multiplexing (OTDM) systems [107, 214]. The approximately constant intensity of flat-top pulses defines a clean switching time window avoiding the problem of pulse breakup, which is a main reason of degradation in the performance of optical temporal switches [113]. Another application of rectangular pulses is wavelength conversion by optical time gating, where they are employed as pump pulses. The duration of the gate opening time depends on the pump pulse width and the wavelength tunability depends on their pump pulse power [114]. Additionally, flat-top pulses are desired for orthogonal frequency division multiplexing (OFDM) applications, where the system data is encoded onto subcarriers with a rectangular shaped impulse response [117].

Next, we present an experimental demonstration of a 2-ps rectangular pulse shaper based on an FBG in transmission [157]. For fabrication of the LC-FBG, a 14.5 cm-long phase mask was used, with a period of 1064.05 nm (i.e. grating Bragg wavelength of 1544.87 nm) and a chirp of 2.5 nm/cm. These parameters fixed the dispersion induced in the grating to  $D = 33.77 \text{ ps}^2$ . The target output temporal waveform was set to be a 2-ps flat-top optical pulse, and therefore,  $\tau_{FWHM} = 2 \text{ ps}$ . In this case, a raised cosine function was employed as the window function  $W(\omega')$ . The full-bandwidth of  $W(\omega')$  (measured at 1% of the maximum reflectivity) was 4.95 THz. The output pulse spectrum was then fixed to extend over a full width of  $\sim 5 \text{ THz}$ , thus including a few sidelobes of the sinc function.  $R_{max}$  was set to 99.99% (transmission dip of -40 dB) to guarantee almost zero transmission at the zeroes of the sinc-like transmissivity.

Applying the CMT-TMM synthesis tool to the prescribed reflection spectral response  $H_R(\omega')$ , the apodization and period profiles were obtained, which are shown in blue in Fig. 5.11(a) and (b), respectively. The synthesized device has an effective length of 11 cm with a peak refractive index of  $\Delta n_{max} = 1.2 \times 10^{-3}$ . Due to the expected limitation in the fabrication resolution, the apodization profile was subsequently smoothed to have a conservative spatial resolution of 1 mm. The smoothed grating-apodization profile used for the LC-FBG fabrication, as well as the linear period grating profile provided by the employed phase mask, are shown in red in Fig. 5.11(a) and (b), respectively. Notice that no additional phase variations are needed on top of the linear grating period chirp.

Based on the calculated refractive index profiles, the LC-FBG was fabricated via UV illumination of hydrogen-loaded specialty single-mode fiber (UVS-INT from Coractive) by a frequency-doubled argon-ion laser operating at 244 nm through the described linearly-chirped phase mask. The designed refractive index apodization was implemented by dithering the phase mask during the fiber scan in order to control the visibility of the interference pattern while keeping the average refractive index constant. The FBG fabrication took place at Prof. Sophie LaRochelle's laboratory, in University of Laval. Figures 5.11(d) and (e) show the resulting transmissivity and transmission phase compared with the specified ideal ones.

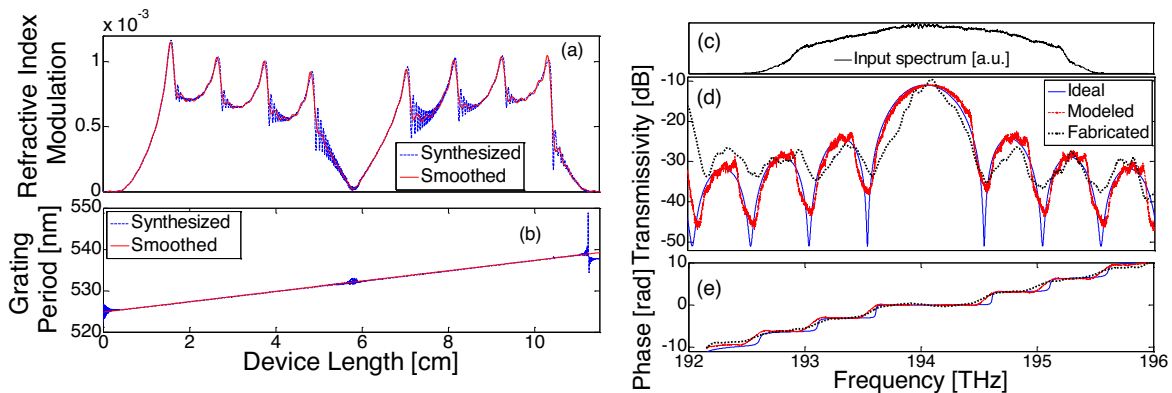


**Figure 5.11 – Flat-top pulse shaper based on an FBG in transmission: Obtained grating apodization profile (a) and period (b) from synthesis (blue line) and smooth profiles adapted to fabrication constraints, i.e., spatial resolution  $\geq 1$  mm (red line); (c) Input signal spectrum; (d) transmissivity and (e) transmission phase response: ideal (blue line), simulated considering fabrication constraints (red line) and measured from fabricated device (dotted black line).**

For full time-domain characterization, an FTSI scheme was implemented [202]. The employed input optical source is composed by an optical parametric oscillator (OPO) followed by a 16-nm

rectangular-shape band pass filter (BPF), so that the input signal matches the operation bandwidth of the device. The input pulse spectrum is plotted in Fig. 5.11(c). The input and output temporal waveforms are plotted in Fig. 5.12. The device is optimized for an input Gaussian-like pulse with a FWHM of 400 fs, depicted in blue in Fig. 5.12. The experimental input pulse (OPO + BPF), calculated by assuming a flat phase along the measured spectrum in 5.11(c), is shown in green. A comparison between the measured data (red line) and the target data (black line) shows a good agreement between the ideal and the experimentally obtained pulses, verifying the capability of the fabricated grating for the target ultrafast pulse-shaping application. The FWHM of the measured output pulse's amplitude is 2.1 ps. The 5-THz operation bandwidth provides a rising/decaying time (measured between the 10% and the 90% of the the maximum amplitude) of 0.5 ps. Figure 5.12 also includes some numerical results for comparative purposes. The expected output from the designed sinc-like spectral response is plotted with a black line when considering the ideal input pulse; and with a purple line when considering the experimental input pulse. This analysis allows us to conclude that the slight amplitude reduction at the center of the output flat-top waveform is partly due to deviations in the input pulse with respect to its nominal Gaussian shape. The measured output also suffers from this effect, but additionally, it does not fully recover the initial amplitude at the trailing edge. This fact may be mainly attributed to numerical artifacts associated to the FTSI phase-recovery algorithm. Deviations in the fabricated grating parameters (apodization profile and period variation) with respect to the targeted ones may be also responsible for some of the observed deviations in the output pulse waveform.

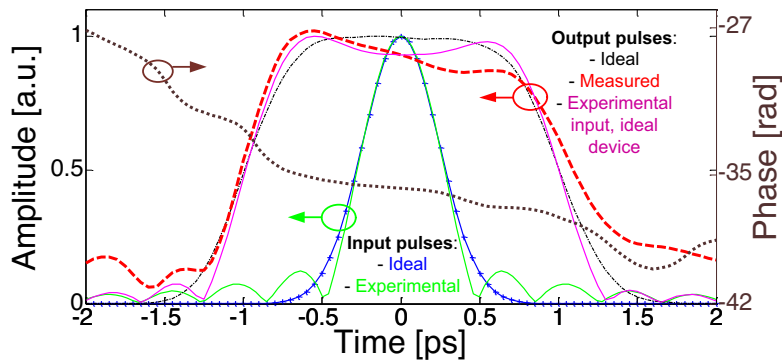


**Figure 5.12 – Flat-top pulse shaper based on an FBG in transmission: Temporal signals from FTSI; ideal input pulse (crossed blue line); experimental input pulse (dotted green line); ideal output pulse (dotted-dashed black line); measured flat-top output pulse (dashed red line); output pulse obtained numerically from the experimental input pulse and the ideal grating response (solid purple line); phase of the measured output pulse (dotted line).**

Note that many other MP optical pulse shapers of practical interest, e.g., parabolic, triangular, or Nyquist-pulse shapers, with resolutions in the sub-picosecond regime, could be implemented on a transmissive FBG using the described design approach.

### 5.4.3 Spectral-domain holography for the design of non-MP optical filters on transmissive FBGs

As explained in Section 5.4.1, if a THz-bandwidth MP optical signal processor is to be implemented using an FBG operating in transmission, only the desired spectral magnitude response needs to be specified to the algorithm described above (using Eq. 5.12). However, if the desired system is non-MP, i.e., its amplitude and phase spectral responses need to be independently engineered, and its operation can be limited over a well-defined, finite time window, it is possible to use spectral-domain holography to implement this non-MP system using a transmissive FBG. Hence, a spectral hologram can be designed, containing the complex information of the target spectral transfer function encoded in amplitude-only variations. In this Section, we detail how the inherent minimum phase of a FGB's transmission response affects this spectral hologram.

A non-MP optical system can be fully described by its transfer function  $H_{NMP}(\omega')$  (frequency domain) or its impulse response  $\propto \hat{h}_{NMP}(t)$  (time domain). For the design of the spectral hologram, we consider a reference signal with complex envelope  $\hat{h}_{Ref}(t) = A \cdot \delta(t - t_D)$  (at  $\omega_0$ ). As described in Section 5.2, the spectral response of the spectral hologram is,

$$\begin{aligned} P_{Hol}(\omega') &= |H_{NMP}(\omega') + H_{Ref}(\omega')|^2 \\ &= |H_{NMP}(\omega')|^2 + A^2 + 2A|H_{NMP}(\omega')| \cos(t_p\omega' + \angle H_{NMP}(\omega')), \end{aligned} \quad (5.18)$$

and its temporal profile is

$$\hat{p}_{Hol}(t) = \hat{h}_{NMP}(t) \otimes \hat{h}_{NMP}^*(-t) + A^2\delta(t) + A\hat{h}_{NMP}(t - t_p) + A\hat{h}_{NMP}^*(-t - t_p). \quad (5.19)$$

In the spectral hologram's design process, the first term in the RHS of Eqs. 5.18 and 5.19 can be omitted to increase the time window of the optical processor, leading to

$$P_{Hol}(\omega') = A^2 + AH_{NMP}(\omega') \exp\{j t_p\omega'\} + AH_{NMP}^*(\omega') \exp\{-j t_p\omega'\}. \quad (5.20)$$

$$\hat{p}_{Hol}(t) = A^2\delta(t) + A\hat{h}_{NMP}(t - t_p) + A\hat{h}_{NMP}^*(-t - t_p). \quad (5.21)$$

If  $A$  is chosen to be sufficiently high, namely  $A > \max\{|H_{NMP}(\omega')|\}$ , Eq. 5.20 corresponds to a spectral response that involves amplitude-only variations. If  $P_{Hol}(\omega')$  is to be implemented using an FBG operating in transmission, the magnitude of the MP spectral response can be  $H_{MP}(\omega') = P_{Hol}(\omega')$ , while the phase will be given by the expression

$$\angle\{H_{MP}(\omega')\} = \frac{\omega'}{\pi} \left[ P.V. \int_{-\infty}^{\infty} \frac{\ln(P_{Hol}(\omega'))}{\Omega^2 - \omega'^2} d\Omega \right], \quad (5.22)$$

where  $P.V.$  stands for the principal value of the Cauchy integral and  $\Omega$  is an integration variable [101]. It has been observed that the minimum phase acts on the total system's temporal impulse response  $\hat{h}_{MP}(t) = \mathcal{F}^{-1}\{H_{MP}(\omega') = |H_{MP}(\omega')| \cdot \exp\{j \angle(H_{MP}(\omega'))\}\}$  by eliminating the component  $A\hat{h}_{NMP}^*(-t - t_p)$  in Eq. 5.21. Hence, the resulting MP system has an impulse response with complex envelope

$$\hat{h}_{MP}(t) \propto A\delta(t) + \hat{h}_{NMP}(t - t_p); \quad (5.23)$$

and, consequently, a transfer function,

$$H_{MP}(\omega') = A + H_{NMP}(\omega') \exp\{-j t_p \omega'\}. \quad (5.24)$$

This result concurs with a well-known property that establishes that any causal temporal function with a dominant peak around or close to the origin will be either an MP function or close to one [16, 215]. This property has proven useful to recover spectral phase profiles from frequency amplitude interferograms, alternatively to conventional Fourier analysis-based phase recovery algorithms [215, 216]. Indeed, the impulse response of the resulting MP system is composed of a dominant peak close to the origin followed by a causal, non-MP temporal function  $\hat{h}_{NMP}(t)$ .

The system response with transfer function  $H_{MP}(\omega')$  can be then synthesized by means of an FBG operating in transmission. Hence,  $H_T(\omega')$  must approach  $H_{MP}(\omega')$  over the device's operation bandwidth. To completely define  $H_{MP}(\omega')$ , the amplitudes of  $A$  and  $\hat{h}_{NMP}(t)$  have to be settled considering the grating physical constraints. For clarity purposes, let us consider that  $\hat{h}_{NMP}(t)$  is

normalized ( $\max\{|\hat{h}_{NMP}(t)| = 1\}$ ) and redefine Eq. 5.23 and consequently, Eq. 5.24, as

$$\hat{h}_{MP}(t) \propto K_1 \delta(t) + K_2 \cdot \hat{h}_{NMP}(t - t_p), \quad (5.25)$$

$$H_{MP}(\omega') \propto K_1 + K_2 \cdot H_{NMP}(\omega') \exp\{-j t_p \omega'\}, \quad (5.26)$$

where the constants  $K_1$  and  $K_2$  are the weights given to each of the two component terms, which determine the signal energy distribution at the system output.

The fact that the system  $H_{MP}(\omega')$  is MP can be verified by analyzing the evolution of the phasors of  $H_{NMP}(\omega')$  and  $H_{MP}(\omega')$ , illustrated in Fig. 5.13. The phase of  $H_{NMP}(\omega')$  is represented by the angle of the phasor, which is rotating in the complex plane. As this phasor completes a turn around zero, a  $2\pi$  indetermination is added to the phase of  $H_{NMP}(\omega')$ . Therefore the relationship between the amplitude and phase spectral response of the system is not univocal. However, after applying the transformation in Eq. 5.23 and properly choosing the values of  $K_1$  and  $K_2$ , the phase of the resulting spectral transfer function is no longer undetermined, since it is restricted to the range from  $-\pi/2$  and  $\pi/2$ . This translation in the complex plane leads to a spectral response with a univocal relation between its amplitude and phase, satisfying the MP condition [216].

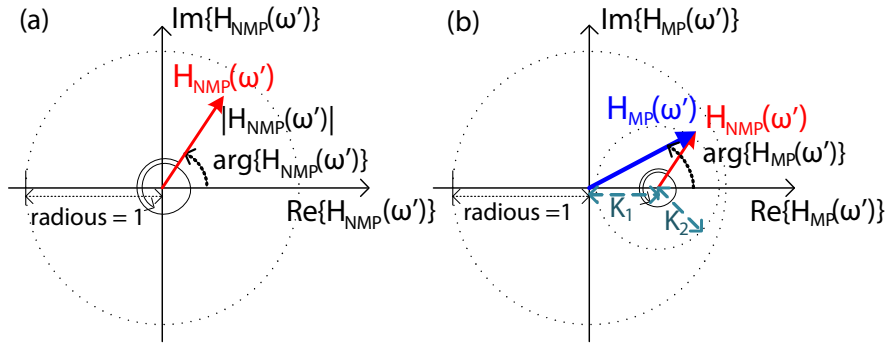


**Figure 5.13** – (a) Phasor diagram of  $H_{NMP}(\omega')$ ; (b) Phasor diagram of  $H_{MP}(\omega')$ , illustrating how its phase varies only between  $-\pi/2$  and  $\pi/2$ .

In order to calculate the value of  $K_1$  and  $K_2$ , two considerations must be taken into account. On the one hand, since an FBG is a passive device, the maximum transmissivity  $T_{max} = 1$ , and consequently

$$|H_T(\omega')| \leq \sqrt{T_{max}} \Rightarrow K_1 + K_2 \leq 1. \quad (5.27)$$

On the other hand, the maximum reflectivity  $R_{max}$  achieved by the device imposes a limitation on the minimum of  $|H_T(\omega')|$

$$|H_T(\omega')| \geq \sqrt{1 - R_{max}} \quad \Rightarrow \quad K_1 - K_2 \geq \sqrt{1 - R_{max}}. \quad (5.28)$$

This inequality becomes strict if  $R_{max} = 1$  to avoid singular points in  $H_{MP}(\omega')$ . As a 100% reflectivity peak cannot be usually achieved in practice,  $K_1$  and  $K_2$  are obtained by solving the equation system defined by Eqs. 5.27 and 5.28 with the equality signs, thus optimizing the amount of energy that is transferred into the non-MP portion of the output signal. Nearly 50% of the output signal energy could be transferred into the non-MP portion as the maximum reflectivity approaches 100%.

Due to the necessary MP condition of a transmissive FBG, the required spectral phase response is intrinsically provided by the grating structure once its spectral magnitude response is properly fixed. Thus, first the grating magnitude spectral response in transmission must be fixed,  $|H_{MP}(\omega')| \rightarrow |H_T(\omega')|$ , which in turn determines the FBG magnitude spectral response in reflection,  $|H_R(\omega')|$ . As discussed above (Section 5.4.1), there is a degree of freedom in the spectral phase in reflection,  $\angle\{H_R(\omega')\}$ , which allows us to choose the one that simplifies the grating apodization profile according to the desired system specifications. A quadratic phase term enables the achievement of an operation bandwidth in the THz regime. In this case, the complete reflection transfer function to be synthesized can be expressed as in Eq. 5.12. Finally, introducing this equation into a CMT-TMM-based FBG synthesis tool [74], the apodization profile and period for the required grating can be obtained.

Let us consider an optical input pulse  $e_{in}(t) = \hat{e}_{in}(t) \cdot \exp\{j\omega_0 t\}$ , where  $\hat{e}_{in}(t)$  is the pulse's temporal complex envelope and  $\omega_0$  is the optical carrier angular frequency (coincident with the grating central Bragg frequency). If  $e_{in}(t)$  is processed by an FBG implementing the impulse response given in Eq. 5.25, the output  $e_{out}(t)$  from the FBG has a complex envelope

$$\begin{aligned} \hat{e}_{out}(t) &= \hat{e}_{in}(t) \otimes \hat{h}_{MP}(t) = K_1 \cdot \hat{e}_{in}(t) + K_2 \cdot \hat{e}_{in}(t) \otimes \hat{h}_{NMP}(t - t_p) \\ &= K_1 \cdot \hat{e}_{in}(t) + K_2 \cdot \hat{e}_{NMP}(t - t_p), \end{aligned} \quad (5.29)$$

where  $\otimes$  refers to convolution and the properties of the Dirac delta function have been used. The signal  $\hat{e}_{out}(t)$  is composed by two terms, the first one is a scaled version of the input signal, and the second one  $\hat{e}_{NMP}(t)$  is proportional to the output of the non-MP processor, i.e., the desired processed waveform. In order to be able to recover the desired processed waveform, these two components must be properly separated in time. Therefore, the time delay  $t_p$  between the delta function and  $h_{NMP}(t)$  in Eq. 5.25 must be suitably designed, which essentially imposes a limitation on the input and output signal temporal duration. This design restriction will translate into a constraint in the maximum TBP of the processor. Depending on the target application, the desired processed waveform may need to be extracted through an additional temporal modulation process. This situation should be identified with the output of time-domain Vander-Lugt filters (Section 5.3), i.e., the system's output is composed of several delayed terms that can be isolated from each other through a temporal gating process. This step may not be always required: since in this case the input signal is transferred without distortion through the device, this interesting feature could be eventually exploited for in-line processors requiring further use of this input signal.

#### 5.4.4 Applications of ultra-broadband transmissive FBGs as non-MP processors

In this Section, we present the design and experimental demonstration of a THz-bandwidth non-MP pulse processor, namely a photonic Hilbert transformer (PHT), based on an FBG in transmission. In this case, we combine the two newly proposed methods for the design of arbitrary (non-MP) ultra-broadband signal processors based on FBGs, presented in Sections 5.4.1 and 5.4.3.

##### 5.4.4.1 Ultrafast photonic Hilbert transformers

A PHT is a pulse processor that provides the Hilbert transform of an incident optical pulse. The transfer function of an arbitrary order PHT is defined as

$$H_{PHT}(\omega') \propto \begin{cases} e^{-jP\pi/2} & \text{if } \omega > \omega_0, \\ 0 & \text{if } \omega = \omega_0, \\ e^{jP\pi/2} & \text{if } \omega < \omega_0, \end{cases} \quad (5.30)$$

where  $P$  is the fractional order. In the particular case of  $P = 1$ , the PHT is integer. PHTs are important components for a wide range of applications in the fields of computing and communi-

cations, such as for single-sideband (SSB) modulation, characterization of broadband microwave signals or image processing [217]. Moreover, as pulse shapers, PHTs are particularly useful for generation of phase-shifted monocycle or doublet pulses, of high interest for ultra-wide band (UWB) communications [218, 219]. A monocycle pulse is characterized by two lobes with opposite phase, and can be directly obtained from integer Hilbert transformation of a Gaussian-like input pulse. On the other hand, a doublet pulse is the first derivative of a monocycle pulse, and can be synthesized from the combination of an optical differentiator and a PHT. Besides, the order of the PHT allows one to control the amplitude ratio between the two resulting pulse lobes, enabling further pulse tunability. FBG-based reflective PHTs have been previously proposed and experimentally demonstrated [78, 88, 203, 220], and in those previous cases, the maximum practically achievable operation bandwidth has been limited to  $< 100$  GHz.

To demonstrate the potential of the spectral-holography-based proposed method for encoding an arbitrary phase shift in an MP spectral response, we target the realization of two PHTs; an integer PHT, i.e.,  $P = 1$  and a fractional one,  $P = 0.81$ . In both cases we use the design strategy in Eq. 5.12 for the target FBG reflection spectral response. We impose  $H_T(\omega') = H_{MP}(\omega')$  in Eq. 5.26, with  $H_{NMP}(\omega') = H_{PHT}(\omega')$ . In our analysis, we consider  $t_p \sim 17$  ps,  $D = 34.24$  ps<sup>2</sup>, corresponding to a grating chirp of  $C = 1.25$  nm/cm,  $\tau_{shift}$  is set to 0.21 ns, and  $W(\omega')$  is chosen to be a raised cosine function with a full-width bandwidth (measured at 1% of the maximum amplitude) of 3.4 THz and a roll-off factor of 0.03. A raised cosine is used as windowing function because it maintains the desired spectrum over the bandwidth of interest while having smooth transition bands. We impose different maximum reflectivities  $R_{max}$  for the two devices. This is intended to evaluate the influence of grating strength or peak reflectivity in the PHT device performance, see discussions below. Thus, the integer PHT has  $K_1 = 0.88$  and  $K_2 = 0.11$ , corresponding to a peak reflectivity  $R_{max} = 0.4$ . The fractional PHT has  $K_1 = 0.97$  and  $K_2 = 0.02$ , corresponding to  $R_{max} = 0.12$ . The power spectral response (reflectivity) and group delay in reflection of the integer PHT are plotted in Fig. 5.14, dashed black curves. The power spectral response follows the anticipated interferogram-like profile with nearly uniform envelope, corresponding to the constant amplitude spectral response of the all-pass PHT filter; the phase shift in the middle of the sinusoidal interferogram profile corresponds to the target discrete shift in the phase spectral response of the PHT filter, see Eq. 5.30. This desired spectral response can be practically achieved using two superimposed, unapodized, LC-FBGs in a Fabry-Perot configuration [221], i.e., where the gratings are suitably spatially shifted

with respect to each other. In particular, Table 5.1 shows the grating parameters used to achieve the spectral-response specifications given above:

**Table 5.1 – Grating’s specifications for the integer and fractional PHTs**

PHT Type	Length	$\Delta n_{max}$	Shift	Chirp
Integer	7 cm	$2.4 \times 10^{-4}$	1.7 mm	1.25 nm/cm
Fractional	7 cm	$2.8 \times 10^{-5}$	1.8 mm	1.25 nm/cm

In Table 5.1,  $\Delta n_{max}$  represents the maximum peak-to-peak refractive index modulation and the column labeled as *Shift* provides the spatial shift induced between the two gratings in the fabrication process. These values of shift impose  $t_p \sim 16.76$  ps for the integer PHT and  $t_p \sim 18$  ps for the fractional PHT. Besides, one of the gratings that compose the Fabry-Perot structure must have a phase transition of  $\pi$  rad and  $0.81\pi$  rad, respectively, at the center of its length. The comparison between the target spectrum for the integer PHT and the reflective spectral response of the FBG-based Fabry-Perot structure is plotted in Fig. 5.14. In this case, the expected spectral response from the designed superimposed FBGs has been numerically obtained using a multi-layer (ML) method based on TMM, due to the fact that CMT is not effective for the analysis of superimposed grating structures. The interested reader can find a description of the ML-TMM algorithm in Section B.1.2 of Appendix B.

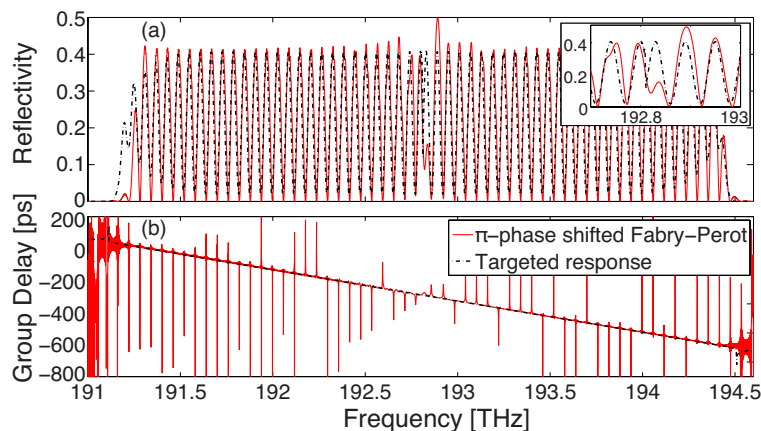


**Figure 5.14 – PHT based on an FBG in transmission: (a) Reflectivity and (b) Group delay. The dashed black line represents the specified spectral response and the red line represents the spectral response of an FBG-based  $\pi$ -phase shifted Fabry-Perot structure.**

The gratings were fabricated in Prof. LaRochelle’s laboratory at University of Laval. The fabrication was carried out in two steps via UV illumination of hydrogen-loaded specialty SMF (UVS-INT from Coractive) by a frequency-doubled argon-ion laser operating at 244 nm. First, the UV beam swept a linearly-chirped phase mask with the required phase shift at the middle of its

length. The desired refractive index modulation was implemented by controlling the exposure time using an average power of 35 mW. Then, a second linearly-chirped phase mask without phase shift was scanned by the UV beam with the same average power and sweep time to achieve the same refractive index modulation as the first grating.

The transmission spectral transfer function of the fabricated gratings was measured by an optical frequency-domain reflectometer (Optical vector analyzer (OVA) from Luna Tech.) with a spectral resolution of 48 pm. The measured transmissive power spectra for the integer and fractional PHTs are shown in Fig. 5.15(a) and (c), respectively. We observe a close approach to the ideally expected interferogram-like responses, which are also shown in the figures. In particular, both the expected and the measured spectra have a similar quasi-periodic spectral response with coincident transmission peaks over the whole operation bandwidth (3 THz). Besides, the expected phase shift in the interferogram response is observed around the device's central frequency ( $f_0 = \omega_0/2\pi = 192.85$  THz). The MP responses associated to each of these power spectra are plotted in Fig. 5.15(b) and (d), after removing the linear phase term.

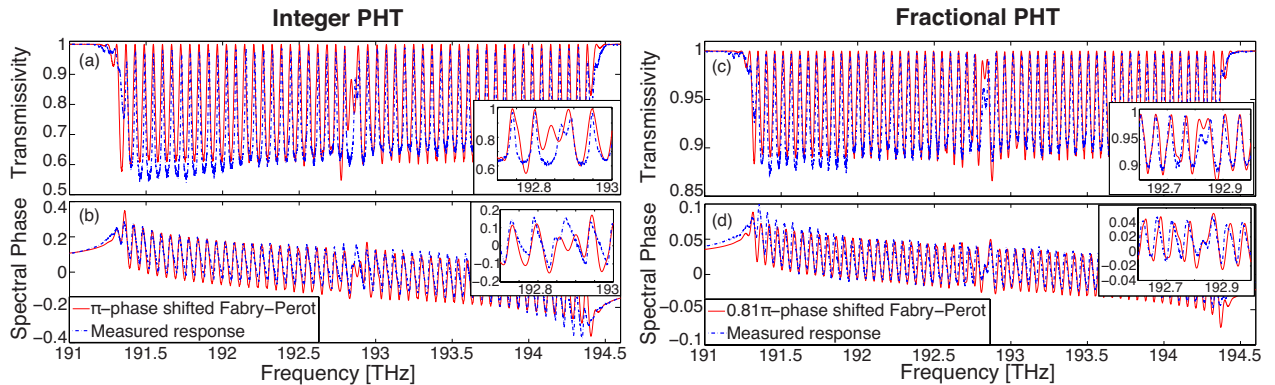


**Figure 5.15 – PHT based on an FBG in transmission:** (a) Simulated transmissivity of the integer PHT to be fabricated (red line) and measured transmissivity of the fabricated device (dashed blue line); (b) Simulated minimum phase (red line) and measured phase in transmission (dashed blue line); (c) Simulated transmissivity for the fractional ( $P = 0.81$ ) PHT to be fabricated (red line) and measured transmissivity of the fabricated device (dashed blue line); (d) Simulated minimum phase (red line) and measured phase in transmission (dashed blue line).

Next, we carried out the full time-domain characterization of the fabricated devices by means of an FTSI [202] scheme. The employed input optical source consists of an OPO followed by a tunable Gaussian-like BPF. By adjusting the bandwidth of the tunable filter, pulses with different durations/bandwidths can be applied to the PHT. Figure 5.16 (solid blue curves) provides the temporal output profiles measured by the FTSI method for input pulse widths of 0.88 ps (1), 1.18 ps (2) and 2 ps (3) at FWHM for the cases (a) integer PHT and (b) 0.81-order PHT. The dotted-

dashed pink lines in Fig. 5.16 are for the numerically simulated outputs from the spectrum of the measured inputs (OPO + Gaussian-like filter) and an ideal integer PHT. As we observe from the figure, there is a good agreement between the obtained temporal waveforms and the output of the ideal PHTs. In the integer PHT cases, there is a pronounced tail in the leading edge of the output pulse. Such a tail is also observed in the numerically simulated temporal output using the measured spectral response of the fabricated FBG (results in Fig. 5.15) and an ideal Gaussian input. As such, we attribute the observed leading-edge tails to the non-uniform, irregular envelope of the interferogram-like pattern of the device transmissive spectral response.

On the other hand, the 0.81-order fractional PHT offers an improved performance, as observed in its time-domain characterization results (Fig. 5.16(b)), where the leading-edge trails are much less pronounced than for the integer PHT.

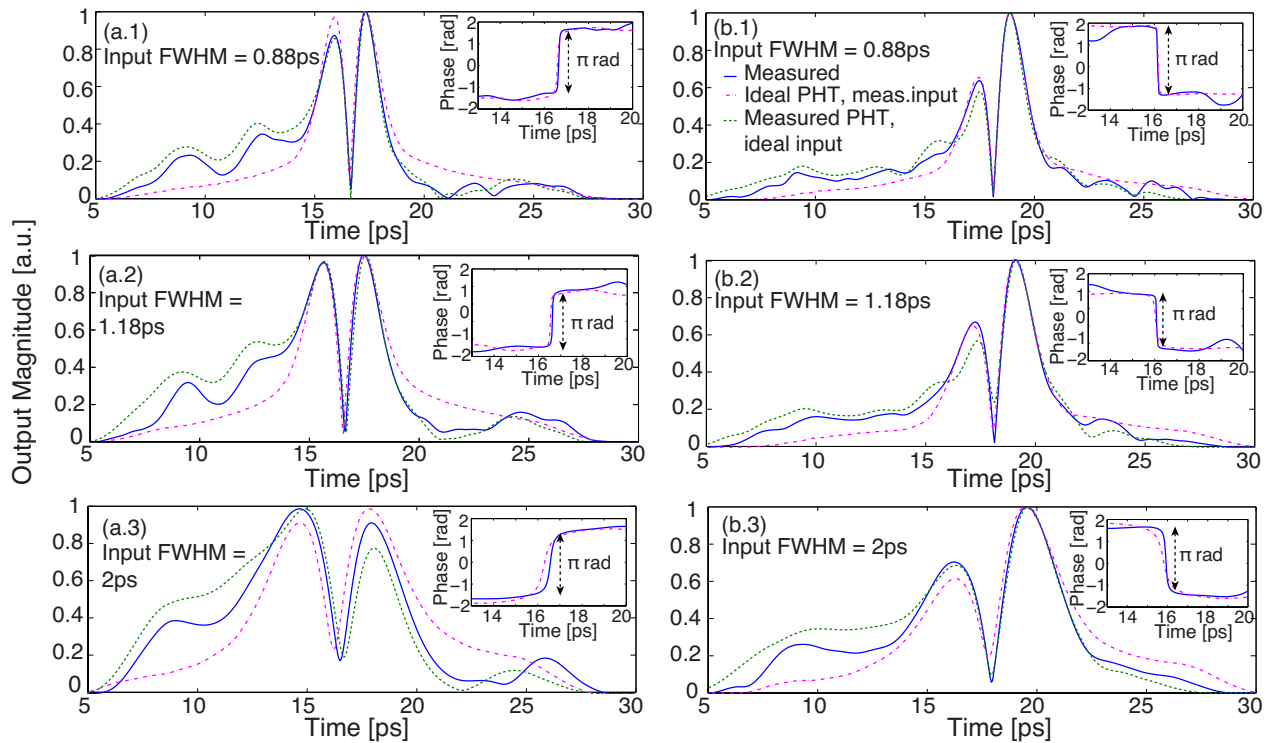


**Figure 5.16 – PHT based on an FBG in transmission: Measured Hilbert-transformed output component of the fabricated integer (a) and fractional (b) PHTs (blue line) for the measured Gaussian-like input pulses with a FWHM of (1) 0.88 ps; (2) 1.18 ps and (3) 2 ps. The corresponding simulated output of an ideal integer PHT and a 0.81-order fractional PHT (dotted-dashed pink line) are also represented for comparative purposes. The insets show the corresponding (simulated and measured) temporal output phases. The dashed green lines show the simulated output from the fabricated FBG (using the measured spectral responses in Fig. 5.15) assuming an ideal Gaussian input.**

To analytically evaluate the performance of the two fabricated PHT devices, we calculate the TBP. To this purpose, the values of the maximum and minimum FWHM of the input pulse that this device is able to process (i.e.  $\text{FWHM}_{max}$  and  $\text{FWHM}_{min}$ , respectively) with a prescribed accuracy are obtained by calculating the  $C_C$  between the temporal Hilbert transformed pulses at the output of (i) the fabricated gratings and (ii) an ideal PHT, as a function of the temporal FWHM of an input Gaussian pulse. In this case, the values of FWHM for what the output pulse has a  $C_C > 90\%$  with respect to the ideal output are selected. The results plotted in Fig. 5.17(a) show that the integer PHT is able to successfully process pulses with a FWHM time-width ranging between 0.18 ps and 1.42 ps, corresponding to a TBP of 7.8. The performance evaluation of the fractional device shows a TBP  $\sim 17.9$  (Fig. 5.17(b)). As expected from the temporal characterization, the TBP of the fractional PHT is notably higher than that of the integer PHT. Whereas both devices exhibit a similar maximum operation bandwidth ( $\sim 2.5$  THz), the fractional PHT allows processing longer pulses with higher precision; we attribute this to the use of a lower grating strength (refractive index modulation peak), which translates into a transmissivity with more uniform spectral envelope, while also approaching more precisely the target interferogram pattern around the phase transition (at  $\omega_0$ ).

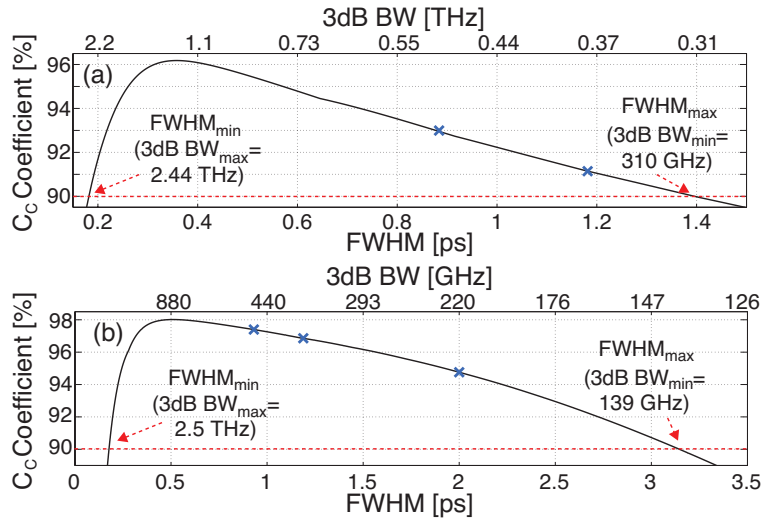


**Figure 5.17 – PHT based on an FBG in transmission: Cross-correlation coefficient between the output of the measured PHT and an ideal PHT vs. the temporal FWHM (or 3dB bandwidth) of an input Gaussian pulse; (a) integer PHT; and (b) fractional PHT. The position of the input pulses in the temporal characterization is marked by a blue cross.**

Obviously, a trade-off of this design is that a smaller grating strength translates into a lower peak reflectivity and therefore, lower device energy efficiency. One alternative to overcome this problem is to apply a CMT layer peeling algorithm to the specified spectral response (Eq. 5.12)

and grow an FBG with the resulting apodization profile (as detailed in Section 5.4.3). However, this solution may require a higher precision in the fabrication process. The values of FWHM of the input pulses employed in the temporal characterization process are marked in the curves of Fig. 5.17 by blue crosses. Note that the input pulse in Fig. 5.16(a.3) is outside the range of operation of the integer PHT, according to the above-defined criterion ( $C_C > 90\%$ ).

To further evaluate the validity of the fabricated structure as a PHT, we numerically isolate the measured Hilbert transformed pulses and calculate its Fourier transform. Figure 5.18(a) shows the result in the case of the integer PHT when the input pulse has a FWHM of 1.18 ps. We can observe an amplitude spectral response similar to the one of the input pulse and a  $\pi$ -phase transition, as expected at the output of an integer PHT (see Eq. 5.30). Figure 5.18(b) shows the Fourier transform of the isolated measured Hilbert transformed pulse for the case of the fractional PHT when the input pulse has a FWHM of 2 ps, validating once again the correct functionality of the fabricated device as a 0.81-order PHT. The ripples observed in the spectral phase in Fig. 5.14 are due to the dissimilar envelope of the interferometric-like transmissive response of the FBG. It is worth noting that they do not affect the proper functionality of the devices as PHT, as previously confirmed by the temporal characterization and the values of  $C_C$  coefficient obtained.

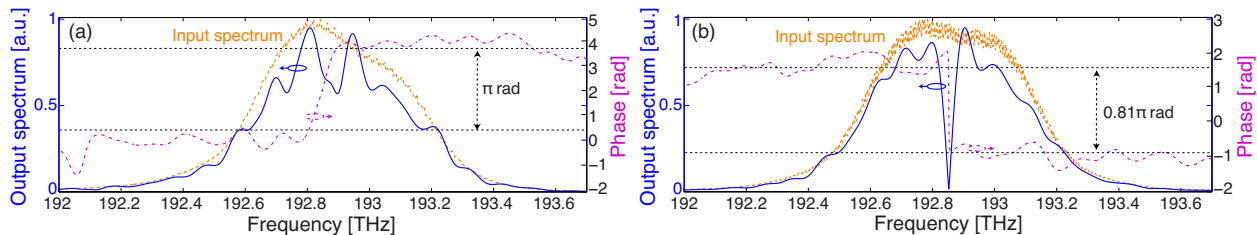


**Figure 5.18 – PHT based on an FBG in transmission: Amplitude (blue line) and phase (dashed purple line) of the spectrum of the isolated Hilbert transformed pulse at the output of the integer PHT. Orange line shows the input pulse: (a) Integer PHT; and (b) 0.81-order fractional PHT.**

## 5.5 Conclusions

In this Section, we have introduced the concept of spectral-domain holography, as the frequency-domain counterpart of time-domain holography. Spectral-domain holography consists in the generation of a real-valued spectral response that contains information on the amplitude and phase profiles of the target arbitrary (complex-valued) spectral response. As such, spectral-domain holography proves to be an interesting technique to design optical signal processors implemented using circuits

or components with a fundamental limitation in the functionalities (spectral responses) that can perform (e.g., structures that can implement real-only impulse responses or minimum-phase transfer functions). In particular, we have employed spectral domain holography in two different pulse processing configurations. First, we have used this concept for the design of an arbitrary complex-valued picosecond-resolution optical pulse shaping scheme using an in-fiber, reconfigurable setup with identical circuitry complexity than those previously used for real-valued-only time-domain pulse shaping. Also, spectral domain holography has been applied for the generation of arbitrary (non-MP) optical signal processors based on FBGs operating in transmission. Transmissive FBGs offer a simpler, more robust configuration that additionally enables operation bandwidths in the THz regime (by using a design methodology also introduced in this Thesis), but they have been typically limited to MP-only functionalities.

The use of spectral-domain holography in a TDSS configuration can be seen as the time-domain counterpart of Vander-Lugt filters. In this Chapter, we have derived an analytic expression for the required modulation signal, which can be directly calculated from the target impulse response, avoiding the use of complex and time-consuming optimization algorithms [197]. To validate this newly proposed approach, we have successfully generated (i) an asymmetrical triangular pulse with a raising time of 10 ps and decaying time of 50 ps and a controlled quadratic phase, and (ii) a 4-symbol 16-QAM pulse code sequence in which each symbol has a FWHM of  $\sim 6$  ps.

On the other hand, we have described a general approach for designing ultra-fast (THz-bandwidth) all-optical (all-fiber) signal processing devices based on apodized LC-FBGs operating in transmission. This approach has been successfully demonstrated through the realization of (i) two MP signal processing functionalities, namely arbitrary-order optical differentiators and a picosecond flat-top pulse shaper, and (ii) a non-MP processor, a PHT, where spectral-domain holography has been employed as a key part of the design methodology. The general design approach presented in this Chapter could be applied to a variety of optical filtering technologies with similar inherent restrictions to those of a transmissive FBG, possibly including thin-film optical filters, fiber/waveguide long-period gratings, and other resonator-based filter structures [54, 222].

# Chapter 6

## Conclusions

### 6.1 Conclusions of the Thesis

In this Thesis, we have introduced two novel concepts in the frame of optical communications and information processing systems, namely the formal time-domain and spectral-domain counterparts of spatial-domain (classical) holography. The two concepts are aimed at improving current technologies for two key sub-systems in any optical network: the coherent transmitter/receiver and ultrafast optical signal processing units. On the one hand, time-domain holography can be useful to simplify functionalities in the transmitter and receiver of any coherent optical communication system, not only in the generation and measurement stages, but also to potentially enable new, simplified schemes for impairment compensation in optical telecommunication links. On the other hand, spectral-domain holographic techniques can also allow the development of new design techniques for ultrafast temporal optical signal processors (in the sub-picosecond and femtosecond regime). In fact, the introduction of ultra-fast communication systems based on optical signal processing is considered to be one of the most promising ways to handle the rapidly increasing global communication traffic.

The extraordinary applicability of classical holography is due to its capacity to simultaneously control the amplitude and phase of an arbitrary complex-envelope optical waveform by use of simpler, more widely available intensity-only control techniques. The interferometry-based recording and reconstruction steps of this lensless imaging system have been reviewed in Chapter 3. Gabor's

original apparatus has been presented, highlighting the main problem of its recording configuration, namely the fact that the output target image appeared overlapped with other auxiliary waveforms generated in the process. To overcome this problem, an alternative configuration has been described, which was introduced by Leith and Upatnieks few years after Gabor's original proposal. In this new configuration, the light scattered from an object (information wave) and the reference wave propagate with different angles of propagation; or equivalently, they have different carrier spatial-frequencies. Thus, in the recording process, the different output waves can be angularly separated just by applying a sufficiently separated carrier spatial frequencies of both incident waves. In Chapter 3, we also reviewed the concept of Vander-Lugt filters. Vander-Lugt filters are a technology solution to enable the implementation of complex-valued optical filters using a configuration similar to previous Fourier-optics-based  $4f_l$  spatial optical filters, employing amplitude-only spatial filtering masks. For this purpose, the transparency placed at the Fourier plane consists of an intensity-only varying pattern that has been holographically recorded through the interference between the target complex-valued transfer function and a reference signal. All the concepts reviewed in Chapter 3 constitute the basis of the original ideas introduced in this Thesis.

In Chapter 4 the concept of *time-domain holography* is introduced as the time-domain counterpart of classical holography. The strong potential of time-domain holography is its capacity for simultaneously controlling the complex information of a temporal electromagnetic waveform by using components sensitive to intensity-only or phase-only variations, i.e., without requiring additional synchronization of the amplitude and phase, or equivalently the in-phase and quadrature components, of the original complex-envelope optical signal. The price to pay for achieving full control of complex information signals using e.g., intensity-only sensitive devices is the fact that the required processing bandwidth is at least two fold the bandwidth of the target complex-envelope signal. Two practical configurations have been proposed, namely an electro-optical (EO) approach and an all-optical approach. Both configurations have been experimentally demonstrated by implementing interesting applications of time-domain holography in the frame of optical communications. In particular, the EO approach has been employed to generate and subsequently reconstruct the amplitude and phase temporal profiles of two user-defined complex modulation patterns, i.e., a sequence of arbitrarily chirped Gaussian pulses and a 3-Gbps 16-QAM modulated data pattern; using an extremely simple setup involving intensity-only modulation of a continuous wave (CW) light source and band-pass filtering. Also, this EO recording and generation holographic method has

been modified to implement a simple, general technique for wavelength-preserving temporal phase conjugation of optical waveforms. The proposed scheme significantly simplifies previous OE-EO approaches by (i) using intensity-only photodetection and modulation components, combined with a simple band pass filter (BPF), reducing the complexity and the cost and (ii) avoiding the detection and subsequent processing of the phase of the optical signal prior to the conjugation process, minimizing errors and simplifying the procedure. Finally, an all-optical approach has been demonstrated for implementing a wavelength conversion process of complex-envelope optical signals based on nonlinear cross phase modulation (XPM). This proposed scheme allows achieving temporal conjugation of the original signal as well. The use of XPM is particularly interesting for wavelength conversion schemes as it enables good conversion efficiency for a broad wavelength range, without the need for accomplishing the stringent phase matching condition of previous four wave mixing (FWM)-based implementations (previous XPM-based wavelength converters were limited to the conversion of intensity-only information signals). Moreover, the obtained conversion efficiency is symmetrical for down- and up-conversion. If the conditions for occurrence of FWM are satisfied, the generated idlers add coherently with the results from XPM, increasing the output power at the frequencies of interest. An additional advantage is that, compared with standard FWM-based implementations, the proposed scheme relaxes the power requirements for the information signal and the output-wavelength CW in more than one order of magnitude for a similar conversion efficiency.

The second novel concept introduced in this Thesis (Chapter 5) is *spectral-domain holography*, derived as the frequency-domain counterpart of the previously presented time-domain holography concept. Spectral-domain holography is an advantageous technique to enhance the capabilities of current technologies for ultra-fast optical signal processing. Spectral-domain holography enables the design of amplitude-only transfer functions containing the information of a second target complex-valued transfer function. In this case, the time window of the target complex-valued functionality is reduced in at least two-fold with respect to the case where a functionality defined by an amplitude-only transfer function is targeted. This technique has been applied to the development of *time-domain Vander-Lugt filters*. Similarly to the classical (spacial domain) Vander-Lugt filters, time-domain Vander-Lugt filters are based on a time-domain spectral shaping configuration, where the temporal modulating signal is generated holographically. This methodology has been applied for realization of electronically reconfigurable complex-valued and asymmetric pulse shapers with resolution in the picosecond regime, using a setup similar to the one previously employed for gen-

eration of real-only temporal pulse shapes. In particular, the capabilities of the proposed scheme have been successfully demonstrated by synthesizing two different temporal waveforms of practical interest, namely, an asymmetric triangular-shaped pulse with parabolic phase, and a 4-symbol 16-QAM coded sequence.

The versatility of spectral-domain holography is also applied to a substantially different technology, namely, to the design of signal processors based on fiber Bragg gratings (FBGs). In Chapter 5, we have presented a novel, general approach for designing ultra-fast (THz-bandwidth) all-optical (all-fiber) signal processing devices based on apodized linearly chirped (LC)-FBGs operating in transmission. This methodology can be used, in principle, as long as the signal-processing device is based on an MP linear optical filter. The use of an FBG in transmission translates into important practical advantages, such as avoiding the use of additional mechanisms to retrieve the reflected signal and the associated losses, and an improved robustness against the expected grating fabrication errors. By taking advantage of the degree of freedom in the FBG reflection spectral phase, we have numerically demonstrated that the use of a quadratic phase in reflection (i.e. constant group-velocity dispersion) allows one to achieve processing bandwidths easily of a few THz using readily feasible and greatly simplified grating apodization profiles. The insertion of a quadratic phase in reflection is actually achieved through the use of an LC-FBG with a proper linear grating-period variation. Indeed, we have shown that the FBG dispersion (or equivalent grating-period variation slope) is a fundamental design parameter, which must be properly chosen to ensure that the resulting grating-apodization specifications are within the fabrication constraints. This new design approach has been successfully demonstrated through the numerical design of 2-THz arbitrary order (up to fourth order) optical differentiators and through the experimental demonstration of a 2 ps flat-top (rectangular) pulse shaper. In spite of the fact that there are a myriad of interesting optical processors described by an MP transfer function, the extremely restrictive MP condition has severely limited the functionalities susceptible to be implemented using this configuration. To overcome this limitation, we have applied spectral-domain holography to develop a new, general approach that enables the design of non-MP linear optical pulse processors based on MP optical filters. In this case, spectral-domain holography allows us to encode the required processor's spectral phase in amplitude variations. The proposed approach has been proven through the successful design of a 3-THz real-time photonic Hilbert transformer (PHT) based on a transmission FBG,

showing an unprecedented operation bandwidth for a non-MP pulse processing device implemented in an FBG.

As a general conclusion, considering the broad range of applications of classical holography, we can foresee a similarly vast number of interesting uses for its time/spectral-domain counterpart. Due to the broad set of applications where this newly introduced concept can be applied (some of them have been experimentally demonstrated in this Thesis), this project may inspire the development of new, more efficient optical systems in the areas of communication and information processing. Advantages of these new subsystems include (i) a significant simplification of the currently required setups to achieve the same sort of functionalities, (ii) the possibility of developing all-optical processors with operation speeds difficult to achieve so far through technology widely used nowadays and (iii) the significant relaxation of practical difficulties in the device fabrication processes. All the proposed schemes arise as stable and reliable solutions for readily practical applications and they may be also well positioned for short time-to-market and a vast knowledge base. Overall, we expect that the research outcome of our proposed project will have an extremely important scientific, social and economical impact in such diverse fields as communication, computing and information processing.

## 6.2 Future perspectives

Next, we briefly discuss several potential lines of future research considered as of higher relevance by the author:

1. In Chapter 4, we have proposed an implementation of time-domain holography for the generation of complex modulation formats which is based on a single Mach-Zehnder modulator and a BPF. However, the limitation in the operation bandwidth imposed by the employed arbitrary waveform generator (analog bandwidth of 9.6 GHz), and the wide transition band of the employed tunable BPF (in GHz range) led to a very weak output complex-envelope signal. In particular, the two spectral lobes of the generated temporal hologram were separated  $< 4.5$  GHz. Thus, in order to have sufficient suppression of the spectral lobe corresponding to the conjugated temporal component, it was necessary to attenuate part of the target spectral lobe. As described in Chapter 4, there is an analogy between the presented configuration

and the scheme for single sideband amplitude modulation with carrier suppression (SSB-CS). Therefore, it should be possible to employ a setup in which the BPF is substituted by a PHT-based configuration (as the one presented in Ref. [223]), in order to improve the performance of the proposed scheme in terms of energy efficiency.

2. The design procedure developed for the implementation of MP optical filters based on FBGs in transmission should enable the synthesis of a myriad of important ultra-fast linear optical signal processing and shaping devices in compact and robust all-fiber formats. Among them, we can mention:

(a) First and high-order all-optical integrators [90, 224–228]: they are of high interest for the implementation of optical unit memories [229], photonic bit counters [230], or reconfigurable unit-step time-domain functions, e.g., flat-top pulse shapers. In the last example, reconfigurability of the flat-top temporal width can be achieved by using two opposite phase control pulses to be integrated [224, 227].

(b) Parabolic pulse shaping: parabolic pulses are widely employed to achieve ultra-flat self phase modulation (SPM)-induced spectral broadening in super continuum generation experiments [111, 117]. They are also interesting as pump signals in nonlinear signal processing methods, such as for implementation of nonlinear pulse retiming or time-lens processes [112, 116].

(c) Triangular pulse shaping: Triangular pulses are required for the implementation of tunable delay lines, time-domain add-drop multiplexing, wavelength conversion, doubling of optical signals, time-to-frequency mapping of multiplexed signals, among other applications [109, 111].

(d) Nyquist pulse shape shaping: Nyquist pulses are of high interest for orthogonal time division multiplexing systems [110, 231].

3. In Chapter 5, the introduced design technique for Vander-Lugt filters has been employed for the implementation of reconfigurable optical pulse shapers. However, that approach could be easily modified to implement other signal processing functionalities. For example, if the spectral-domain hologram is designed so that the quadratic phase component that compensates the induced dispersion is added to the term proportional to the conjugate of the target impulse response, the overall system acts as a correlator between the input signal and the

electrical modulating signal. Also, if the designed hologram has constant amplitude and the odd-symmetric quadratic phase, the system would act as a spectral phase conjugator (SPC). SPC systems are of high interest for the compensation of even and odd-order chromatic dispersion and several nonlinear effects, including SPM and self-steepening [187].

4. The general design approach presented in Chapter 5 for implementation of non-MP optical signal processors based on FBG operating in transmission could be applied to a variety of optical filtering technologies with similar inherent restrictions to those of a transmissive FBG, possibly including thin-film optical filters, fiber/waveguide long period gratings (LPGs) in their core-to-core configuration, and other resonator-based filter structures. In particular, it would be of high interest the implementation of a non-MP optical processor, e.g., a PHT, in the core of a LPG, and study if the addition of a linearly chirp would enable the achievement of a broader operation bandwidth than the one typically achieved by non-chirped LPGs.



# References

- [1] Affiliates., “Cisco Visual Networking Index: Forecast and Methodology, 2014-2019,” *White paper*, pp. 1–14 (2015).
- [2] URL <https://www.ncta.com/positions/internet-of-things>.
- [3] R. G. H. van Uden, R. Amezcua Correa, E. Antonio López, F. M. Huijskens, C. Xia, G. Li, A. Schulzgen, H. de Waardt, A. M. J. Koonen, and O. C. M., “Ultra-high-density spatial division multiplexing with a few-mode multicore fibre,” *Nature Photonics*, **8** (11), 865–870 (2014).
- [4] K. Kikuchi *Coherent optical communications: Historical perspective and future directions*, 6, Springer-Verlag Berlin Heidelberg (2010).
- [5] S. Yan, D. Wang, Y. Gao, C. Lu, A. P. T. Lau, L. Liu, and X. Xu (2012) “Generation of square or hexagonal 16-QAM signals using a single-dual drive IQ modulator driven by binary signals,” in *Optical Fiber Communications (OFC)*, OW3H.3.
- [6] D. S. Makovejs, S. Millar, V. Mikhailov, G. Gavioli, R. I. Killey, S. J. Savory, and P. Bayvel, “Novel method of generating QAM-16 signals at 21.3 Gbaud and transmission over 480 km,” *IEEE Photonics Technology Letters*, **22** (1), 36–38 (2010).
- [7] A. Chiba, T. Sakamoto, T. Kawanishi, K. Higuma, M. Sudo, and J. Ichikawa, “16-level quadrature amplitude modulation by monolithic quad-parallel mach-zehnder optical modulator,” *Electronics Letters*, **46** (3), 227–228 (2010).
- [8] A. Chiba, T. Sakamoto, T. Kawanishi, K. Higuma, M. Sudo, and J. Ichikawa, “75-km SMF transmission of optical 16 QAM signal generated by a monolithic quad-parallel Mach-Zehnder optical modulator,” *IEEE Photonics Technology Letters*, **23** (14), 977–979 (2011).
- [9] A. E. Willner, S. Khaleghi, M. R. Chitgarha, and O. F. Yilmaz, “All-optical signal processing,” *Journal of Lightwave Technology*, **32** (4), 660–680 (2014).
- [10] B. Sklar *Digital Communications: Fundamentals and Applications*, Prentice Hall, Upper Saddle River, NJ, 2nd edn. (2001).
- [11] J. Azaña, “Ultrafast analog all-optical signal processors based on fiber-grating devices,” *IEEE Photonics Journal*, **2**, 359–386 (2010).
- [12] B. E. A. Saleh and M. C. Teich *Fundamentals of Photonics*, John Wiley and Sons, New York (1991).
- [13] J. W. Goodman *Introduction to Fourier optics*, McGraw-Hill, New York (1996).

- [14] B. E. Olsson, P. Ohlen, L. Rau, and D. J. Blumenthal, "A simple and robust 40-Gb/s wavelength converter using fiber cross-phase modulation and optical filtering," *IEEE Photonics Technology Letters*, **12**, 846–848 (2000).
- [15] J. H. Lee, T. Tanemura, K. Kikuchi, T. Nagashima, T. Hasegawa, S. Ohara, and N. Sugimoto, "Use of 1-m Bi<sub>2</sub>O<sub>3</sub> nonlinear fiber for 160-Gbit/s optical time-division demultiplexing based on polarization rotation and a wavelength shift induced by cross-phase modulation," *Optics Letters*, **30** (11), 1267–1269 (2005).
- [16] A. V. Oppenheim and R. W. Schaffer *Discrete-Time Signal Processing*, Prentice-Hall, New Jersey, 2nd edn. (1989).
- [17] W. Sibbett, A. A. Lagatsky, and C. T. A. Brown, "The development and application of femtosecond laser systems," *Optics Express*, **20** (7), 6989–7001 (2012).
- [18] S. Boscolo and C. Finot, "Nonlinear pulse shaping in fibres for pulse generation and optical processing," *International Journal of Optics*, **2012**, 1–14 (2012).
- [19] G. P. Agrawal *Nonlinear fiber optics*, Academy press, San Diego, California, 3rd edn. (2001).
- [20] G. P. Agrawal *Applications of nonlinear fiber optics*, Academy press, New York, 2nd edn. (2008).
- [21] OFS, "Standard highly nonlinear fiber," . URL <http://fiber-optic-catalog.ofsoptics.com/item/optic>
- [22] J. Yu, X. Zheng, C. Peucheret, A. T. Clausen, H. N. Poulsen, and P. Jeppesen, "40-Gb/s all-optical wavelength conversion based on a nonlinear optical loop mirror," *Journal of Lightwave Technology*, **18**, 1001–1006 (2000).
- [23] C. H. Kwok, S. H. Lee, K. K. Chow, C. Shu, C. Lin, and A. Bjarklev, "Widely tunable wavelength conversion with extinction ratio enhancement using PCF-based NOLM," *IEEE Photonics Technology Letters*, **17**, 2655–2657 (2005).
- [24] M. Galili, L. K. Oxenlowe, L. K. H. C. H. Mulvad, A. T. Clausen, and P. Jeppesen, "Optical wavelength conversion by cross-phase modulation of data signals up to 640 Gb/s," *IEEE Journal of Selected Topics in Quantum Electronics*, **14**, 573–579 (2008).
- [25] A. D'Ottavi, P. Spano, G. Hunzinker, R. Paiella, R. Dall'Ara, G. Guekos, and K. J. Vahala, "Wavelength conversion at 10 Gb/s by four-wave mixing over a 30-nm interval," *IEEE Photonics Technology Letters*, **10**, 952–954 (1998).
- [26] J. Ma, J. Yu, C. Yu, Z. Jia, X. Sang, Z. Zhou, T. Wang, and G. K. Chang, "Wavelength conversion based on four-wave mixing in high-nonlinear dispersion shifted fiber using a dual-pump configuration," *Journal of Lightwave Technology*, **24**, 2851–2858 (2006).
- [27] M. F. Huang, J. Yu, and G. K. Chang, "Polarization insensitive wavelength conversion for 4x112 Gbit/s polarization multiplexing RZ-QPSK signals," *Optics Express*, **16**, 21 161–21 169 (2008).
- [28] L. Xu, N. Ophir, M. Menard, R. K. W. Lau, A. C. Turner-Foster, M. A. Foster, M. Lipson, A. L. Gaeta, and K. Bergman, "Simultaneous wavelength conversion of ASK and DPSK signals based on four-wave-mixing in dispersion engineered silicon waveguides," *Optics Express*, **19**, 12 172–12 179 (2011).

- [29] G. W. Lu, T. Sakamoto, and T. Kawanishi, "Wavelength conversion of optical 64 QAM through FWM in HNLF and its performance by constellation monitoring," *Optics Express*, **22**, 15–22 (2013).
- [30] R. Adams, M. Spasojevic, M. Chagnon, M. Malekiha, J. Li, D. V. Plant, and L. R. Chen, "Wavelength conversion of 28 Gbaud 16-QAM signals based on four-wave mixing in a silicon nanowire," *Optics Express*, **22**, 4083–4090 (2014).
- [31] T. Sakamoto, H. C. Lim, and K. Kikuchi, "All-optical polarization-insensitive time-division demultiplexer using a nonlinear optical loop mirror with a pair of short polarization-maintaining fibers," *IEEE Photonics Technology Letters*, **14** (12), 1737–1740 (2002).
- [32] T. Sakamoto, S. Koji, K. Taira, N. S. Moon, and K. Kikuchi, "Polarization-insensitive all-optical time-division demultiplexing using a fiber four-wave mixer with a peak-holding optical phase-locked loop," *IEEE Photonics Technology Letters*, **16** (2), 563 – 565 (2004).
- [33] P. V. Mamyshev (1998) "All-optical data regeneration based on self-phase modulation effect," in *European Conference of Optical Communications*.
- [34] T. H. Her, G. Raybon, and C. Headley, "Optimization of pulse regeneration at 40 Gb/s based on spectral filtering of self-phase modulation in fiber," *IEEE Photonics Technology Letters*, **16**, 200–202 (2004).
- [35] C. Kouloumentas, M. Bougioukos, A. Maziotis, and H. Avramopoulos, "DPSK regeneration at 40 Gb/s and beyond using a fiber-Sagnac interferometer," *IEEE Photonics Technology Letters*, **22** (16), 1187–1189 (2010).
- [36] Y. Inoue and T. Mukai, "Experimental study on noise characteristics of a gain-saturated fiber optical parametric amplifier," *Journal of Lightwave Technology*, **20** (6), 969–974 (2002).
- [37] M. Westlund, P. A. Andrekson, H. Sunnerud, J. Hansryd, and J. Li, "High-performance optical-fiber-nonlinearity-based optical waveform monitoring," *Journal of Lightwave Technology*, **23** (6), 2012–2022 (2005).
- [38] T. T. Ng, J. L. Blows, M. Rochette, J. A. Bolger, I. Littler, and B. J. Eggleton, "In-band OSNR and chromatic dispersion monitoring using a fibre optical parametric amplifier," *Optics Express*, **13** (14), 5542–5552 (2005).
- [39] G. S. He, "Optical phase conjugation: principles, techniques, and applications," *Prog. Quantum Electronics*, **26** (3), 131–191 (2002).
- [40] S. Watanabe and M. Shirasaki, "Exact compensation for both chromatic dispersion and Kerr effect in a transmission fiber using optical phase conjugation," *Journal of Lightwave Technology*, **14**, 243–248 (1996).
- [41] A. Corchia, C. Antonini, A. D'Ottavi, A. Mecozzi, F. Martelli, P. Spano, G. Guekos, and R. Dall'Ara, "Mid-span spectral inversion without frequency shift for fiber dispersion compensation: a system demonstration," *IEEE Photonics Technology Letters*, **11** (2), 275–277 (1999).
- [42] C. L. Janer and M. J. Connelly, "Optical phase conjugation technique using four-wave mixing in semiconductor optical amplifier," *Electronics Letters*, **47** (12), 12–13 (2011).

- [43] J. M. Dudley, C. Finot, G. Millot, and D. J. Richardson, “Self-similarity in ultrafast nonlinear optics,” *Nature Physics*, **3** (9), 597–603 (2007).
- [44] T. Hirooka and M. Nakazawa, “Parabolic pulse generation by use of a dispersion-decreasing fiber with normal group-velocity dispersion,” *Optics Letters*, **29** (5), 498–500 (2004).
- [45] S. Boscolo, A. I. Latkin, and S. K. Turitsyn, “Passive nonlinear pulse shaping in normally dispersive fiber systems,” *IEEE Journal of Quantum Electronics*, **44** (12), 1196–1203 (2008).
- [46] A. V. Oppenheim and A. S. Willsky *Signals and Systems*, Prentice-Hall, 2nd edn. (1997).
- [47] J. Azaña and L. R. Chen, “Multiwavelength optical signal processing using multistage ring resonators,” *IEEE Photonics Technology Letters*, **14** (5), 654–656 (2002).
- [48] L. Zhuang, M. R. Khan, A. Beeker, W. and Leinse, R. Heideman, and C. Roeloffzen, “Novel microwave photonic fractional Hilbert transformer using a ring resonator-based optical all-pass filter,” *Optics Express*, **20** (24), 26 499–26 510 (2012).
- [49] W. S. Fegadolli, L. Feng, M. Mujeeb-U-Rahman, J. E. B. Oliveira, V. R. Almeida, and A. Scherer, “Experimental demonstration of a reconfigurable silicon thermo-optical device based on spectral tuning of ring resonators for optical signal processing,” *Optics Express*, **22** (3), 3425–3431 (2014).
- [50] T. Yang, J. Dong, L. Lu, L. Zhou, A. Zheng, X. Zhang, and J. Chen, “All-optical differential equation solver with constant-coefficient tunable based on a single microring resonator,” *Scientific Reports*, **4**, 5581 (2014).
- [51] K. Takano, N. Hanzawa, S. Tanji, and K. Nakagawa (2007) “Experimental demonstration of optically phase-shifted SSB modulation with fiber-based optical Hilbert transformers,” in *Optical Fiber Communication (OFC)*, JThA48.
- [52] Y. Park, M. H. Ashgari, T. J. Ahn, and J. Azaña, “Transform-limited picosecond pulse shaping based on temporal coherence synthesization,” *Optics Express*, **15** (15), 9584–9599 (2007).
- [53] R. Kashyap *Fiber Bragg gratings*, Academy press (1999).
- [54] T. Erdogan, “Fiber grating spectra,” *Journal of Lightwave Technology*, **15** (8), 1277–1294 (1997).
- [55] M. J. Strain and M. Sorel, “Integrated III-V Bragg gratings for arbitrary control over chirp and coupling coefficient,” *IEEE Photonics Technology Letters*, **20** (22), 1863–1865 (2008).
- [56] B. H. Kolner, “Space-time duality and the theory of temporal imaging,” *IEEE Journal of Quantum Electronics*, **30** (8), 1951–1963 (1994).
- [57] J. van Howe and C. Xu, “Ultrafast optical signal processing based upon space-time dualities,” *Journal of Lightwave Technology*, **24**, 2649–2661 (2006).
- [58] T. Jannson and J. Jannson, “Temporal self-imaging effect in single-mode fibers,” *Journal of the Optical Society of America*, **71**, 1373–1376 (1981).
- [59] D. Mendlovic, O. Melamed, and H. M. Ozaktas, “Compact optical temporal processors,” *Applied Optics*, **34** (20), 4113–4118 (1995).

- [60] A. W. Lohmann and D. Mendlovic, “Temporal filtering with time lenses,” *Applied Optics*, **31**, 6212–6219 (1992).
- [61] J. Azaña, L. R. Chen, M. A. Muriel, and P. W. E. Smith, “Experimental demonstration of real-time Fourier transformation using linearly chirped fiber Bragg gratings,” *Electronics Letters*, **35**, 2223–2224 (1999).
- [62] D. F. Geraghty, R. Salem, M. A. Foster, and A. L. Gaeta, “A simplified optical correlator and its applications to packet-header recognition,” *IEEE Photonics Technology Letters*, **20** (7), 487–489 (2008).
- [63] B. Jalali, D. R. Solli, and S. Gupta, “Silicon photonics: Silicon’s time lens,” *Nature Photonics*, **3**, 8–10 (2009).
- [64] M. Fridman, A. Farsi, Y. Okawachi, and A. L. Gaeta, “Demonstration of temporal cloaking,” *Nature*, **481** (7379), 62–65 (2012).
- [65] D. Gabor, “A new microscope principle,” *Nature*, **161**, 777–778 (1949).
- [66] D. Gabor, G. W. Stroke, D. Brumm, A. Funkhouser, and A. Labeyrie, “Reconstruction of phase objects by holography,” *Nature*, **208**, 1159–1162 (1965).
- [67] E. N. Leith and J. Upatnieks, “Reconstructed wavefronts and communication theory,” *Journal of the Optical Society of America*, **52**, 1123–1128 (1962).
- [68] A. Papoulis, “Pulse compression, fiber communications, and diffraction: a unified approach,” *Journal of the Optical Society of America A*, **11** (1), 3–13 (1994).
- [69] K. O. Hill and G. Meltz, “Fiber Bragg grating technology: fundamentals and overview,” *Journal of Lightwave Technology*, **15** (8), 1263–1275 (1997).
- [70] H. Kogelnik, “Filter response of nonuniform almost-periodic structures,” *Bell System Technical Journal*, **55**, 109–126 (1976).
- [71] S. E. Miller, “Coupled wave theory and waveguide applications,” *Bell System Technical Journal*, **33**, 661–719 (1954).
- [72] A. Yariv, “Coupled-mode theory for guided-wave optics,” *IEEE Journal of Quantum Electronics*, **9**, 919–933 (1973).
- [73] E. Peral, J. Capmany, and J. Marti, “Iterative solution to the Gel’Fand-Levitan-Marchenko coupled equations and application to synthesis of fiber gratings,” *IEEE Journal of Quantum Electronics*, **32**, 2078–2084 (1996).
- [74] R. Feced, M. N. Zervas, and M. A. Muriel, “An efficient inverse scattering algorithm for the design of non uniform fiber Bragg gratings,” *IEEE Journal of Quantum Electronics*, **35**, 1105–1115 (1999).
- [75] L. Poladian, “Simple grating synthesis algorithm,” *Optics Letters*, **25**, 787–789 (2000).
- [76] J. Skaar, L. Wang, and T. Erdogan, “On the synthesis of fiber Bragg gratings by layer peeling,” *IEEE Journal of Quantum Electronics*, **37**, 165–173 (2001).

- [77] M. H. Asghari and J. Azaña, “On the design of efficient and accurate arbitrary-order temporal optical Integrators using fiber Bragg gratings,” *Journal of Lightwave Technology*, **27** (17), 3888–3895 (2009).
- [78] M. H. Asghari and J. Azaña, “All-optical Hilbert transformer based on a single phase-shifted fiber Bragg grating: Design and analysis,” *Optics Letters*, **34** (3), 334–336 (2009).
- [79] R. Ashrafi, M. Li, and J. Azaña, “Coupling-strength-independent long-period grating designs for THz-bandwidth optical differentiators,” *IEEE Photonics Journal*, **5**, 7100 311 (2013).
- [80] R. Ashrafi and J. Azaña, “Terahertz bandwidth all-optical Hilbert transformers based on long-period gratings,” *Optics Letters*, **37**, 2604–2606 (2012).
- [81] N. K. Berger, B. Levit, B. Fischer, M. Kulishov, D. V. Plant, and J. Azaña, “Temporal differentiation of optical signals using a phase-shifted fiber Bragg grating,” *Optics Express*, **15** (2), 371–381 (2007).
- [82] G. Curatu, S. LaRochelle, C. Pare, and P. A. Belanger, “Antisymmetric pulse generation using phase-shifted fibre Bragg grating,” *Electronics Letters*, **38**, 307–309 (2002).
- [83] X. Fang, D. N. Wang, and S. Li, “Fiber Bragg grating for spectral phase optical code-division multiple-access encoding and decoding,” *Journal of the Optical Society of America B*, **20**, 1603–1610 (2003).
- [84] M. R. Fernández-Ruiz, A. Carballar, and J. Azaña, “Design of ultrafast all-optical signal-processing devices based on fiber Bragg gratings in transmission,” *Journal of Lightwave Technology*, **31** (10), 1593–1600 (2013).
- [85] M. R. Fernández-Ruiz, A. Carballar, and J. Azaña, “Arbitrary time-limited optical pulse processors based on transmission fiber Bragg gratings,” *IEEE Photonics Technology Letters*, **26** (17), 1754–1757 (2014).
- [86] D. Gatti, T. T. Fernández, S. Longhi, and P. Laporta, “Temporal differentiators based on highly-structured fibre Bragg gratings,” *Electronics Letters*, **46**, 943–945 (2010).
- [87] M. Li, D. Janner, J. Yao, and V. Pruneri, “Arbitrary-order all-fiber temporal differentiator based on a fiber Bragg grating: design and experimental demonstration,” *Optics Express*, **17** (22), 19 798–19 807 (2009).
- [88] M. Li and J. Yao, “Experimental demonstration of a wideband photonic temporal Hilbert transformer based on a single fiber Bragg grating,” *IEEE Photonics Technology Letters*, **22** (21), 1559–1561 (2010).
- [89] Y. Park, M. Kulishov, R. Slavík, and J. Azaña, “Picosecond and sub-picosecond flat-top pulse generation using uniform long-period fiber gratings,” *Optics Express*, **14**, 12 670–12 678 (2006).
- [90] M. A. Preciado and M. A. Muriel, “Ultrafast all-optical integrator based on a fiber Bragg grating: proposal and design,” *Optics Letters*, **33** (12), 1348–1350 (2008).
- [91] M. A. Preciado and M. A. Muriel, “Desing of an ultrafast all-optical differentiator based on fiber Bragg grating in transmission,” *Optics Letters*, **33** (21), 2458–2460 (2008).

- [92] R. Slavík, Y. Park, M. Kulishov, and J. Azaña, “Terahertz-bandwidth high-order temporal differentiators based on phase-shifted long-period fiber gratings,” *Optics Letters*, **34**, 3116–3118 (2009).
- [93] L. M. Rivas, M. J. Strain, D. Duchesne, A. Carballar, M. Sorel, R. Morandotti, and J. Azaña, “Picosecond linear optical pulse shapers based on integrated waveguide Bragg gratings,” *Optics Letters*, **33**, 2425–2427 (2008).
- [94] M. J. Strain and M. Sorel, “Desing and fabrication of integrated chirped Bragg gratings for on-chip dispersion control,” *IEEE Journal of Quantum Electronics*, **46** (5), 774–782 (2010).
- [95] M. Burla, L. Romero Cortés, M. Li, X. Wang, L. Chrostowsky, and J. Azaña, “Integrated waveguide Bragg gratings for microwave photonics signal processing,” *Optics Express*, **21** (21), 25 120–25 147 (2013).
- [96] W. Zhang, W. Li, and J. Yao, “Optical differentiator based on integrated sidewall phase-shifted Bragg grating,” *IEEE Photonics Technology Letters*, **26** (23), 2383 – 2386 (2014).
- [97] M. Burla, M. Li, L. Romero Cortés, X. Wang, M. R. Fernández-Ruiz, L. Chrostowsky, and J. Azaña, “Terahertz-bandwidth photonic fractional Hilbert transformer based on a phase-shifted waveguide Bragg grating on silicon,” *Optics Letters*, **39** (21), 6241–6244 (2014).
- [98] A. D. Simard, M. J. Strain, L. Meriggi, M. Sorel, and S. LaRochelle, “Bandpass integrated Bragg gratings in silicon-on-insulator with well-controlled amplitude and phase responses,” *Optics Letters*, **40** (5), 736–739 (2015).
- [99] J. Skaar, “Synthesis of fiber Bragg gratings for use in transmission,” *Journal of the Optical Society of America A*, **18** (3), 557–564 (2001).
- [100] K. Hinton, “Dispersion compensation using apodized Bragg fiber gratings in transmission,” *Journal of Lightwave Technology*, **16** (12), 2336–2347 (1998).
- [101] L. Poladian, “Group-delay reconstruction for fiber Bragg gratings in reflection and transmission,” *Optics Letters*, **22** (20), 1571–1573 (1997).
- [102] R. Slavík, M. Kulishov, Y. Park, and J. Azaña, “Long-period fiber-grating-based filter configuration enabling arbitrary linear filtering characteristics,” *Optics Letters*, **34**, 1045–1047 (2009).
- [103] M. Kulishov, D. Krcmarik, and R. Slavík, “Design of terahertz-bandwidth arbitrary-order temporal differentiators based on long-period fiber gratings,” *Optics Letters*, **32**, 2978–2980 (2007).
- [104] S. J. Kim, T. J. Eom, B. H. Lee, and C. S. Park, “Optical temporal encoding/decoding of short pulses using cascaded long-period fiber gratings,” *Optics Express*, **11**, 3034–3040 (2003).
- [105] R. Ashrafi, M. Li, S. LaRochelle, and J. Azaña, “Superluminal space-to-time mapping in grating-assisted co-directional couplers,” *Optics Express*, **21**, 6249–6256 (2013).
- [106] R. Ashrafi, M. Li, N. Belhadj, M. Dastmalchi, S. LaRochelle, and J. Azaña, “Experimental demonstration of superluminal space-to-time mapping in long period gratings,” *Optics Letters*, **38**, 1419–1421 (2013).

- [107] J. H. Lee, L. K. Oxenlowe, M. Ibsen, K. S. Berg, A. T. Clausen, D. J. Richardson, and P. Jeppesen, “All-optical TDM data demultiplexing at 80 Gb/s with significant timing jitter tolerance using a fiber Bragg grating based rectangular pulse switching technology,” *Journal of Lightwave Technology*, **21** (11), 2518 – 2523 (2003).
- [108] P. R. Prucnal *Optical Code Division Multiple Access: Fundamentals and Applications*, CRC Press: Taylor and Francis Group (2006).
- [109] F. Parmigiani, M. Ibsen, T. T. Ng, L. Provost, P. Petropoulos, and D. J. Richardson, “An efficient wavelength converter exploiting a grating-based saw-tooth pulse shaper,” *IEEE Photonics Technology Letters*, **20** (17), 1461–1463 (2008).
- [110] M. Nakazawa, T. Hirooka, P. Ruan, and P. Guan, “Ultra-high-speed orthogonal TDM transmission with an optical Nyquist pulse train,” *Optics Express*, **20** (2), 1129–1140 (2012).
- [111] S. O. Iakushev, O. V. Shulika, I. A. Sukhoivanov, V. I. Fesenko, M. V. Andres, and H. Sayinc, “Formation of ultrashort triangular pulses in optical fibers,” *Optics Express*, **22** (23), 29 119–29 134 (2014).
- [112] F. Parmigiani, P. Petropoulos, M. Ibsen, and D. J. Richardson, “Pulse retiming based on XPM using parabolic pulses formed in a fiber Bragg grating,” *IEEE Photonics Technology Letters*, **18** (7), 829–832 (2006).
- [113] A. M. Weiner, Y. Silberberg, H. Fouckhardt, D. E. Leaird, M. A. Saifi, M. J. Andrejco, and P. W. Smith, “Use of femtosecond square pulses to avoid pulse breakup in all-optical switching,” *IEEE Journal of Quantum Electronics*, **25** (12), 2648–2655 (1989).
- [114] A. K. Dutta, N. K. Dutta, and M. Fujiwara *WDM Technologies: Optical Networks*, Elsevier Academic Press (2004).
- [115] P. C. Chou, H. A. Haus, and J. G. Brennan, “Reconfigurable time-domain spectral shaping of an optical pulse stretched by a fiber Bragg grating,” *Optics Letters*, **25** (8), 524–526 (2000).
- [116] T. T. Ng, F. Parmigiani, M. Ibsen, Z. Zhang, P. Petropoulos, and D. J. Richardson, “Compensation of linear distortions by using XPM with parabolic pulses as a time lens,” *IEEE Photonics Technology Letters*, **20** (13), 1097 – 1099 (2008).
- [117] S. Wabnitz and B. J. Eggleton *All-optical signal processing: data communications and storage applications*, Springer (2015).
- [118] G. L. Li and P. K. L. Yu, “Optical intensity modulators for digital and analog applications,” *Journal of Lightwave Technology*, **19**, 2010–2030 (2003).
- [119] N. Dagli, “Wide-bandwidth lasers and modulators for RF photonics,” *IEEE Transactions on Microwave Theory and Techniques*, **47**, 1151–1171 (1999).
- [120] A. M. Weiner, “Ultrafast optical pulse shaping: A tutorial review,” *Optics Communications*, **284**, 3669–3692 (2011).
- [121] A. M. Weiner, “Femtosecond pulse shaping using spatial light modulators,” *Review of Scientific Instruments*, **71** (5), 1929–1960 (2000).
- [122] S. T. Cundiff and A. M. Weiner, “Optical arbitrary waveform generation,” *Nature Photonics*, **4** (11), 760–766 (2010).

- [123] R. E. Saperstein, A. D. Panasenko, R. Roktiski, and Y. Fainman, "Time-domain waveform processing by chromatic dispersion for temporal shaping of optical pulses," *Journal of the Optical Society of America B*, **22** (11), 2427–2436 (2005).
- [124] T. Kurokawa, H. Tsuda, K. Okamoto, K. Naguma, H. Takenouchi, Y. Inoue, and M. Ishii, "Time-space conversion optical signal processing using arrayed-waveguide grating," *Electronics Letters*, **33** (22), 1890–1891 (1997).
- [125] B. Muralidharan, V. Balakrishnan, and A. M. Weiner, "Design of double-passed arrayed-waveguide gratings for the generation of flat-topped femtosecond pulse trains," *Journal of Lightwave Technology*, **24** (1), 586–597 (2006).
- [126] N. K. Fontaine, D. J. Geisler, R. P. Scott, T. He, J. P. Heritage, and S. J. B. Yoo, "Demonstration of high-fidelity dynamic optical arbitrary waveform generation," *Optics Express*, **18**, 22 988–22 995 (2010).
- [127] M. Li, Y. Han, S. Pan, and J. Yao, "Experimental demonstration of symmetrical waveform generation based on amplitude-only modulation in a fiber-based temporal pulse shaping system," *IEEE Photonics Technology Letters*, **23** (11), 715–717 (2001).
- [128] H. Chi and J. Yao, "Symmetrical waveform generation based on temporal pulse shaping using an amplitude-only modulator," *Electronics Letters*, **43** (7), 415–417 (2007).
- [129] J. Azaña, N. K. Berger, B. Levit, and B. Fischer, "Reconfigurable generation of high-repetition-rate optical pulse sequences based on time-domain phase-only filtering," *Optics Letters*, **30** (23), 3228–3230 (2005).
- [130] X. Wang and N. Wada, "Spectral phase encoding of ultra-short optical pulse in time domain for OCDMA application," *Optics Express*, **15** (12), 7319–7326 (2007).
- [131] S. Thomas, A. Malacarne, F. Fresi, L. Poti, A. Bogoni, and J. Azaña, "Programmable fiber-based picosecond optical pulse shaper using time-domain binary phase-only linear filtering," *Optics Letters*, **34** (4), 545–547 (2009).
- [132] E. J. Norberg, R. S. Guzzon, S. C. Nicholes, J. S. Parker, and L. A. Coldren, "Programmable photonic lattice filters in InGaAsP-InP," *IEEE Photonics Technology Letters*, **22** (2), 109–111 (2010).
- [133] P. Dong, N. N. Feng, D. Feng, W. Qian, H. Liang, D. C. Lee, B. J. Luff, T. Banwell, A. Agarwal, P. Toliver, R. Menendez, T. K. Woodward, and M. Ashgari, "GHz-bandwidth optical filters based on high-order silicon ring resonators," *Optics Express*, **18**, 23 784–23 789 (2010).
- [134] B. Guan, S. S. Djordjevic, N. K. Fontaine, L. Zhou, S. Ibrahim, R. P. Scott, D. J. Geisler, Z. Ding, and S. J. B. Yoo, "CMOS compatible reconfigurable silicon photonic lattice filters using cascaded unit cells for RF-photonic processing," *IEEE Journal of Selected Topics in Quantum Electronics*, **20** (4), 8202 110 (2014).
- [135] M. H. Asghari and J. Azaña, "Proposal and analysis of a reconfigurable pulse shaping technique based on multi-arm optical differentiator," *Optics Communications*, **281**, 4581–4588 (2008).

- [136] H. P. Bazargani, M. Burla, and J. Azaña, “Experimental demonstration of sub-picosecond optical pulse shaping in silicon based on discrete space-to-time mapping,” *Optics Letters*, **40** (23), 5423–5426 (2015).
- [137] P. Petropoulos, M. Ibsen, and D. J. Richardson, “Rectangular pulse generation based on pulse reshaping using a superstructured fiber Bragg grating,” *Journal of Lightwave Technology*, **19** (5), 746–752 (2001).
- [138] F. Parmigiani, P. Petropoulos, M. Ibsen, and D. J. Richardson, “All-optical pulse reshaping and retiming systems incorporating pulse shaping fiber Bragg gratings,” *Journal of Lightwave Technology*, **24** (1), 357–364 (2006).
- [139] J. Azaña and L. R. Chen, “Synthesis of temporal optical waveforms by fiber Bragg gratings: a new approach based on space-to-time-to-frequency mapping,” *Journal of the Optical Society of America B*, **19** (1), 2758–2769 (2003).
- [140] A. Grunnet-Jepsen, A. E. Johnson, E. S. Maniloff, T. W. Mossberg, M. J. Munroe, and J. N. Sweetser, “Demonstration of all-fiber sparse lightwave CDMA based on temporal phase encoding,” *IEEE Photonics Technology Letters*, **11**, 1283–1285 (1999).
- [141] P. C. Teh, P. Petropoulos, M. Ibsen, and D. J. Richardson, “A comparative study of the performance of seven- and 63-chip optical code-division multiple-access encoders and decoders based on superstructured fiber Bragg gratings,” *Journal of Lightwave Technology*, **19** (9), 1352–1365 (2001).
- [142] P. C. Teh, M. Ibsen, J. H. Lee, P. Petropoulos, and D. J. Richardson, “Demonstration of a four-channel WDM/OCDMA system using 255-chip 320-Gchip/s quaternary phase coding gratings,” *IEEE Photonics Technology Letters*, **14**, 227–229 (2002).
- [143] S. Ayotte, M. Rochette, J. Magne, L. A. Rusch, and S. LaRochelle, “Experimental verification and capacity prediction of FE-OCDMA using superimposed FBG,” *Journal of Lightwave Technology*, **23** (2), 724–731 (2005).
- [144] M. R. Mokhtar, M. Ibsen, P. C. Teh, and D. J. Richardson (2012) “Simple dynamically reconfigurable OCDMA encoder/decoder based on uniform fiber Bragg grating,” in *Optical Fiber Communications (OFC)*.
- [145] L. R. Chen *Optical code-division multiple access enabled by fiber Bragg grating technology, in Optical CDMA: Fundamentals and Applications*, Boca Raton: CRC Press, Taylor and Francis Group (2006).
- [146] M. A. Preciado and M. A. Muriel, “Flat-top pulse generation based on a fiber Bragg grating in transmission,” *Optics Letters*, **34** (6), 752–754 (2009).
- [147] M. A. Preciado, X. Shu, and K. Sugden, “Proposal and design of phase-modulated fiber gratings in transmission for pulse shaping,” *Optics Letters*, **38** (1), 70–72 (2013).
- [148] R. Ashrafi, M. Li, and J. Azaña, “Tsymbol/s optical coding Based on Long Period Gratings,” *IEEE Photonics Technology Letters*, **25**, 910–913 (2013).
- [149] G. Lifante *Integrated photonics: fundamentals*, John Wiley and Sons, Sussex, England (2003).
- [150] H. Ishikawa *Ultrafast all-optical signal processing devices*, Wiley, United Kingdom (2008).

- [151] A. B. Vander Lugt, "Signal detection by complex spatial filtering," *IEEE Transactions Information Theory*, **10**, 139–145 (1964).
- [152] E. Ip, A. P. T. Lau, D. J. F. Barros, and J. M. Kahn, "Coherent detection in optical fiber systems," *Optics Express*, **16**, 753–791 (2008).
- [153] M. R. Fernández-Ruiz, M. Li, and J. Azaña, "Time-domain holograms for generation and processing of temporal complex information by intensity-only modulation processes," *Optics Express*, **21** (8), 10 314–10 323 (2013).
- [154] M. R. Fernández-Ruiz and J. Azaña, "Temporal phase conjugation based on time-domain holography," *Optics Letters*, **40** (1), 127–130 (2015).
- [155] M. R. Fernández-Ruiz, L. Lei, M. Rochette, and J. Azaña, "All-optical wavelength conversion based on time-domain holography," *Optics Express*, **23** (17), 22 847–22 856 (2015).
- [156] M. R. Fernández-Ruiz, H. J., and J. Azaña (2016) "Fiber-optics Reconfigurable Arbitrary (Complex) Picosecond Pulse Shaping/Coding by Time-domain Amplitude-only Spectrum Modulation," in *Optical Fiber Communication (OFC)*, Anaheim, California, USA, Th3H.2.
- [157] M. R. Fernández-Ruiz, M. Li, M. Dastmalchi, A. Carballar, S. LaRochelle, and J. Azaña, "Picosecond optical signal processing based on transmissive fiber Bragg gratings," *Optics Letters*, **38** (7), 1247–1249 (2013).
- [158] M. R. Fernández-Ruiz, L. Wang, A. Carballar, M. Burla, J. Azaña, and S. LaRochelle, "THz-bandwidth photonic Hilbert transformers based on fiber Bragg gratings in transmission," *Optics Letters*, **40** (1), 41–44 (2015).
- [159] M. Kato and T. Suzuki, "Fourier-transform holograms by Fresnel zone-plate achromatic-fringe interferometer," *Journal of the Optical Society of America*, **59**, 303–306 (1969).
- [160] J. F. Heanue, M. Bashaw, and L. Hesselink, "Volume holographic storage and retrieval of digital data," *Science*, **265**, 749–752 (1994).
- [161] T. Zhang and I. Yamaguchi, "Three-dimensional microscopy with phase-shifting digital holography," *Optics Letters*, **23**, 1221–1223 (1998).
- [162] R. J. Collier, C. B. Burckhardt, and L. H. Lin *Optical holography*, Academy press, New York (1971).
- [163] P. Hariharan *Optical holography: principles, techniques and applications*, Cambridge University Press, Cambridge, UK (1984).
- [164] H. M. Smith *Principles of holography*, John Wiley and Sons, New York, 2nd edn. (1975).
- [165] B. R. Brown and A. W. Lohmann, "Complex spatial filtering with binary masks," *Applied Optics*, **5**, 967–969 (1966).
- [166] J. P. Waters, "Holographic image synthesis utilizing theoretical methods," *Applied Physics Letters*, **9**, 405–407 (1968).
- [167] F. Dubois, C. Minetti, O. Monnom, C. Yourassowsky, J. C. Legros, and P. Kischel, "Pattern recognition with a digital holographic microscope working in partially coherent illumination," *Applied Optics*, **41** (20), 4108–4119 (2002).

- [168] D. J. Geisler, N. K. Fontaine, R. P. Scott, T. He, L. Paraschis, O. Gerstel, J. P. Heritage, and S. J. B. Yoo, "Bandwidth scalable, coherent transmitter based on the parallel synthesis of multiple spectral slices using optical arbitrary waveform generation," *Optics Express*, **19**, 8242–8253 (2011).
- [169] S. Yan, X. Weng, Y. Gao, C. Lu, A. P. T. Lau, L. Liu, and X. Xu, "Generation of square or hexagonal 16-QAM signals using a single-dual drive IQ modulator driven by binary signals," *Optics Express*, **20**, 9023–29 034 (2012).
- [170] K. Inoue and H. Toba, "Wavelength conversion experiment using fiber four-wave mixing," *IEEE Photonics Technology Letters*, **4** (1), 69–72 (1992).
- [171] M. C. Tatham, G. Sherlock, and L. D. Westbrook, "20-nm optical wavelength conversion using nondegenerate four-wave mixing," *IEEE Photonics Technology Letters*, **5** (11), 1303–1306 (1993).
- [172] T. Durhuus, B. Mikkelsen, C. Joergensen, S. L. Danielsen, and K. E. Stubkjaer, "All-optical wavelength conversion by semiconductor optical amplifiers," *Journal of Lightwave Technology*, **14** (6), 942–954 (1996).
- [173] J. P. Donnelly, H. Q. Le, E. A. Swanson, S. H. Groves, A. Darwish, and I. E. P., "Nondegenerate four-wave mixing wavelength conversion in low-loss passive InGaAsP-InP quantum-well waveguides," *IEEE Photonics Technology Letters*, **8** (5), 623–625 (1996).
- [174] S. L. Danielsen, P. B. Hansen, and K. E. Stubkjaer, "Wavelength conversion in optical packet switching," *Journal of Lightwave Technology*, **16**, 2095–2108 (1998).
- [175] K. E. Stubkjaer, A. Kloch, P. B. Hansen, H. N. Poulsen, S. Wolfson, K. S. Jepsen, A. T. Clausen, E. Limal, and A. Buxens, "Wavelength converter technology," *IEICE Transactions on Communications*, **2** (2), 390–400 (E82-B).
- [176] V. G. Ta'eed, L. Fu, M. Pelusi, M. Rochette, I. C. M. Littler, D. J. Moss, and J. Eggleton, "Error free all optical wavelength conversion in highly nonlinear As-Se chalcogenide glass fiber," *Optics Express*, **14** (22), 10 271–10 276 (2006).
- [177] A. Pasquazi, R. Ahmad, M. Rochette, M. Lamont, B. E. Little, S. T. Chu, R. Morandotti, and D. J. Moss, "All-optical wavelength conversion in an integrated ring resonator," *Optics Express*, **18** (4), 3859–3864 (2010).
- [178] Y. Gong, J. Huang, K. Li, N. Copner, M. J. J., L. Wang, T. Duan, W. Zhang, and W. H. Loh, "Spoof four-wave mixing for all-optical wavelength conversion," *Optics Express*, **20** (21), 24 030–24 037 (2012).
- [179] B. Fillion, W. C. Ng, A. T. Nguyen, L. A. Rusch, and S. LaRochelle, "Wideband wavelength conversion of 16 Gbaud 16-QAM and 5 Gbaud 64-QAM signals in a semiconductor optical amplifier," *Optics Express*, **21** (17), 19 825–19 833 (2013).
- [180] C. Li, C. Gui, X. Xiao, Q. Yang, S. Yu, and J. Wang, "On-chip all-optical wavelength conversion of multicarrier, multilevel modulation (OFDM m-QAM) signals using a silicon waveguide," *Optics Letters*, **39** (15), 4583–4586 (2014).

- [181] G. L. Abbas, V. W. S. Chan, and T. K. Yee, "A dual-detector optical heterodyne receiver for local oscillator noise suppression," *Journal of Lightwave Technology*, **LT-3** (5), 1110–1121 (1985).
- [182] R. Stierlin, R. Battig, P. D. Henchoz, and H. P. Weber, "Excess-noise suppression in a fibre-optic balanced heterodyne detection system," *Optical and Quantum Electronics*, **18** (6), 445–454 (1986).
- [183] B. Chmielak, M. Waldow, C. Matheisen, C. Ripperda, J. Bolten, T. Wahlbrink, M. Nagel, F. Merget, and H. Kurz, "Pockels effect based fully integrated, strained silicon electro-optic modulator," *Optics Express*, **19** (18), 17 212–17 219 (2011).
- [184] B. Chmielak, C. Matheisen, C. Ripperda, J. Bolten, T. Wahlbrink, M. Waldow, and H. Kurz, "Investigation of local strain distribution and linear electro-optic effect in strained silicon waveguides," *Optics Express*, **21** (21), 25 324–25 332 (2013).
- [185] I. A. Walmsley and C. Dorrer, "Characterization of ultrashort electromagnetic pulses," *Advances in Optics and Photonics*, **1**, 308–437 (2009).
- [186] R. Schmogrow, B. Nebendahl, M. Winter, A. Josten, D. Hillerkuss, S. Koenig, J. Meyer, M. Dreschmann, M. Huebner, C. Koos, J. Becker, W. Freude, and J. Leuthold, "Error vector magnitude as a performance measure for advanced modulation formats," *IEEE Photonics Technology Letters*, **24** (1), 61–63 (2012).
- [187] M. Tsang and D. Psaltis, "Dispersion and nonlinearity compensation by spectral phase conjugation," *Optics Letters*, **28**, 1558–1560 (2003).
- [188] K. Inoue, "Spectral inversion with no wavelength shift based on four-wave mixing with orthogonal pump beams," *Optics Letters*, **22** (23), 1772–1774 (1997).
- [189] H. C. Lim, F. Futami, and K. Kikuchi, "Polarization-independent, wavelength-shift-free optical phase conjugator using a nonlinear fiber Sagnac interferometer," *IEEE Photonics Technology Letters*, **11** (5), 578–560 (1999).
- [190] S. Ayotte, H. Rong, S. Xu, O. Cohen, and M. J. Paniccia, "Multichannel dispersion compensation using silicon waveguide-based optical phase conjugator," *Optics Letters*, **32**, 2393–2395 (2007).
- [191] V. G. Ta'eed, L. Fu, M. Rochette, I. C. M. Littler, D. J. Moss, and B. J. Eggleton (2006) "XPM wavelength conversion in highly nonlinear singlemode As<sub>2</sub>Se<sub>3</sub> fiber," in *Conference on Lasers and Electro-optics*, CMW4, pp. 1–2.
- [192] Y. Chen, "Four-wave mixing in optical fibers: exact solution," *Journal of the Optical Society of America B*, **6**, 1986–1993 (1989).
- [193] A. M. Weiner, D. E. Leaird, D. H. Reitze, and E. G. Paek, "Spectral holography of shaped femtosecond pulses," *Optics Letters*, **17** (3), 224–226 (1992).
- [194] A. M. Weiner, D. E. Leaird, D. H. Reitze, and E. G. Paek, "Femtosecond spectral holography," *IEEE Journal of Quantum Electronics*, **28** (10), 2251–2261 (1992).
- [195] M. P. Shih, "Spectral holography for imaging through scattering media," *Applied Optics*, **38** (5), 743–750 (1999).

- [196] Y. Dai and J. Yao, “Arbitrary pulse shaping based on intensity-only modulation in the frequency domain,” *Optics Letters*, **22** (4), 390–392 (2008).
- [197] S. Thomas, A. Malacarne, F. Fresi, L. Poti, and J. Azaña, “Fiber-based programmable picosecond optical pulse shaper,” *Journal of Lightwave Technology*, **28** (12), 1832–1843 (2010).
- [198] B. Zou and K. S. Chiang, “Phase retrieval from transmission spectrum for long-period gratings,” *Journal of Lightwave Technology*, **31** (13), 2223–2229 (2013).
- [199] M. Asobe, H. Kobayashi, H. Itoh, and T. Kanamori, “Laser-diode-driven ultrafast all-optical switching by using highly nonlinear chalcogenide glass fiber,” *Optics Letters*, **18** (13), 1056–1058 (1993).
- [200] M. A. Muriel, J. Azaña, and A. Carballar, “Real-time Fourier transformer based on fiber gratings,” *Optics Letters*, **24** (1), 1–3 (1999).
- [201] J. Azaña, “Design specifications of time-domain spectral shaping optical system based on dispersion and temporal modulation,” *Electronics Letters*, **39** (21), 1530–1532 (2003).
- [202] Y. Park, F. Li, and J. Azaña, “Characterization and optimization of optical pulse differentiation using spectral interferometry,” *IEEE Photonics Technology Letters*, **18** (17), 1798–1800 (2006).
- [203] M. Li and J. Yao, “All-fiber temporal photonic fractional Hilbert transformer based on a directly designed fiber Bragg grating,” *Optics Letters*, **35** (2), 223–225 (2010).
- [204] C. Wu and M. G. Raymer, “Efficient picosecond pulse shaping by programmable Bragg gratings,” *IEEE Journal of Quantum Electronics*, **42** (9), 873–884 (2006).
- [205] F. Ouellette, “Limits of chirped pulse-compression with an unchirped Bragg grating filter,” *Applied Optics*, **29**, 4826–4829 (1990).
- [206] B. J. Eggleton, T. Stephen, P. A. Krug, G. Dhosi, Z. Brodzeli, and F. Ouellette, “Dispersion compensation using a fibre grating in transmission,” *Electronics Letters*, **32**, 1610–1611 (1996).
- [207] N. M. Litchinitser, B. J. Eggleton, and D. B. Patterson, “Fiber Bragg gratings for dispersion compensation in transmission: theoretical model and design criteria for nearly ideal pulse recompression,” *Journal of Lightwave Technology*, **15**, 1303–1313 (1997).
- [208] L. M. Rivas, K. Singh, A. Carballar, and J. Azaña, “Arbitrary-order ultrabroadband all-optical differentiators based on fiber Bragg gratings,” *IEEE Photonics Technology Letters*, **19** (16), 1209–1211 (2007).
- [209] M. Kulishov and J. Azaña, “Design of high-order all-optical temporal differentiators based on multiple-phase-shifted fiber Bragg gratings,” *Optics Express*, **15** (10), 6152–6166 (2007).
- [210] Y. Park, R. Slavík, and J. Azaña (2007) “Ultrafast all-optical differentiators for generation of orthogonal (sub-) picosecond Hermite-Gaussian waveforms,” in *Optical Fiber Communication (OFC)*, OTh12.
- [211] R. Feded and M. N. Zervas, “Effects of random phase and amplitude errors in optical fiber Bragg gratings,” *Journal of Lightwave Technology*, **18** (1), 90–101 (2000).
- [212] A. Papoulis *The Fourier integral and its applications*, McGraw-Hill, New York (1962).

- [213] M. R. Fernández-Ruiz, J. Azaña, and A. Carballar (2012) “Ultrafast all-optical Nth-order differentiators based on transmission fiber Bragg gratings,” in *IEEE Photonics Conference (IPC)*, WCC3, pp. 656–657.
- [214] L. K. Oxenlowe, R. Slavík, M. Galili, H. C. H. Mulvad, A. T. Clausen, Y. Park, J. Azaña, and P. Jeppesen, “640 Gbit/s timing jitter tolerant data processing using a long-period fiber grating-based flat-top pulse shaper,” *IEEE Journal of Selected Topics in Quantum Electronics*, **14**, 566–572 (2008).
- [215] A. Ozcan, M. J. F. Digonnet, and G. S. Kino, “Characterization of fiber Bragg gratings using spectral interferometry based on minimum-phase functions,” *Journal of Lightwave Technology*, **24** (4), 1739–1757 (2006).
- [216] A. Carballar and C. Janer, “Complete fiber Bragg grating characterization using an alternative method based on spectral interferometry and minimum-phase reconstruction algorithms,” *Journal of Lightwave Technology*, **30** (16), 2574–2582 (2012).
- [217] H. Emami, N. Sarkbosh, L. A. Bui, and A. Mitchell, “Wideband RF photonic in-phase and quadrature-phase generation,” *Optics Letters*, **33** (2), 98–100 (2008).
- [218] Q. Wang and J. Yao, “Switchable optical UWB monocycle and doublet generation using a reconfigurable photonic microwave delay-line filter,” *Optics Express*, **15** (22), 14 667–14 672 (2007).
- [219] C. Wang, F. Zeng, and J. Yao, “All-fiber ultrawideband pulse generation based on spectral shaping and dispersion-induced frequency-to-time conversion,” *IEEE Photonics Technology Letters*, **19** (3), 137–139 (2007).
- [220] C. Cuadrado-Laborde, “Proposal and design of a photonic in-fiber fractional Hilbert transformer,” *IEEE Photonics Technology Letters*, **22** (1), 33–35 (2010).
- [221] R. Slavík, S. Doucet, and S. LaRochelle, “High-performance all-fiber Fabry-Perot filters with superimposed chirped Bragg gratings,” *Journal of Lightwave Technology*, **21** (4), 1059–1065 (2003).
- [222] A. Carballar (1999) *Estudio de redes de difracción en fibra para su aplicación en comunicaciones ópticas*, Ph.D. thesis, Universidad Politecnica de Madrid.
- [223] Z. Li, X. Zhang, and Y. J., “Optical single-sideband modulation using a fiber-Bragg-grating-based optical Hilbert transformer,” *IEEE Photonics Technology Letters*, **23** (9), 558–560 (2011).
- [224] J. Azaña, “Proposal of a uniform fiber Bragg grating as an ultrafast all-optical integrator,” *Optics Letters*, **33** (1), 4–6 (2008).
- [225] R. Slavík, Y. Park, N. Ayotte, S. Doucet, T. J. Ahn, S. LaRochelle, and J. Azaña, “Photonic temporal integrator for all-optical computing,” *Optics Express*, **16** (22), 18 202–18 214 (2008).
- [226] M. H. Asghari and J. Azaña, “Design of all-optical high-order temporal integrators based on multiple-phase-shifted Bragg gratings,” *Optics Express*, **16** (15), 11 459–11 469 (2008).
- [227] Y. Park, T. J. Ahn, Y. Dai, J. Yao, and J. Azaña, “All-optical temporal integration of ultrafast pulse waveforms,” *Optics Express*, **16** (22), 17 817–17 825 (2008).

- [228] R. Ashrafi, M. R. Dizaji, L. Romero Cortés, J. Zhang, J. Yao, J. Azaña, and L. R. Chen, “Time-delay to intensity mapping based on a second-order optical integrator: application to optical arbitrary waveform generation,” *Optics Express*, **23** (12), 16 209–16 223 (2015).
- [229] M. T. Hill, H. J. S. Dorren, T. De Vries, X. J. M. Leijtens, J. H. Den Besten, B. Smalbrugge, Y. S. Oei, H. Binsma, G. D. Khoe, and M. K. Smit, “A fast low-power optical memory based on coupled micro-ring lasers,” *Nature*, **432** (7014), 206–209 (2004).
- [230] M. Ferrera, Y. Park, L. Razzari, B. E. Little, S. T. Chu, R. Morandotti, D. J. Moss, and J. Azaña, “On-chip CMOS-compatible all-optical integrator,” *Nature Communications*, **1** (29), 29 (2010).
- [231] R. Schmogrow, M. Winter, M. Meyer, D. Hillerkuss, S. Wolf, B. Baeuerle, A. Ludwig, B. Nebendahl, S. Ben-Ezra, J. Meyer, M. Dreschmann, M. Huebner, J. Becker, C. Koos, W. Freude, and J. Leuthold, “Real-time Nyquist pulse generation beyond 100 Gbit/s and its relation to OFDM,” *Optics Express*, **20** (1), 317–337 (2012).
- [232] M. A. Muriel and A. Carballar, “Internal field distributions in fiber Bragg gratings,” *IEEE Photonics Technology Letters*, **9** (7), 955–957 (1997).
- [233] M. A. Muriel, A. Carballar, and J. Azaña, “Field distributions inside fiber gratings,” *IEEE Journal of Quantum Electronics*, **35** (4), 548–558 (1999).
- [234] J. Capmany, M. A. Muriel, and S. Sales, “Synthesis of 1D Bragg gratings by a layer-aggregation method,” *Optics Letters*, **32** (17), 2312–2314 (2007).
- [235] P. Yeh *Optical waves in layered media*, John Wiley and Sons, New York (1988).
- [236] G. Bjork and O. Nilsson, “A new exact and efficient numerical matrix theory of complicated laser structures: properties of asymmetric phase-shifted DFB lasers,” *Journal of Lightwave Technology*, **LT-5** (1), 140–146 (1987).
- [237] S. O. Kasap *Optoelectronics devices and photonics: principles and practices*, Prentice-Hall, New Jersey (2001).
- [238] J. Capmany, M. A. Muriel, S. Sales, J. J. Rubio, and D. Pastor, “Microwave V-I transmission matrix formalism for the analysis of photonic circuits: application to fiber Bragg gratings,” *Journal of Lightwave Technology*, **21** (12), 3125–3134 (2003).

## Appendix A

# Auxiliary mathematical demonstrations for the analysis of time-domain Vander-Lugt filters

This Appendix contains auxiliary mathematical derivations that complete the theoretical study of the design of spectral holograms for their use in time-domain Vander-Lugt filters, presented in Chapter 5. In particular, we derive the equations that model the signal at the output of the system in Fig. 5.3. Also, we prove the need for adding an odd-symmetry auxiliary quadratic phase term to the fundamental spectral hologram of the target transfer function.

Figure 5.3 shows the scheme for carrying out time-domain spectral shaping (TDSS). As detailed in Section 5.3, the input signal is a transform-limited Gaussian pulse defined as  $e_S(t) = \hat{e}_S(t) \exp\{j\omega_0 t\}$ , where  $\hat{e}_S(t) = \exp\{-t^2/2T_0^2\}$  is its complex envelope,  $T_0$  is the half width at  $1/e$  maximum and  $\omega_0$  is the carrier frequency. This input signal is dispersed in a medium with transfer function

$$H_{\ddot{\Phi}}(\omega') = \exp\left\{-j\frac{\ddot{\Phi}\omega'^2}{2}\right\}, \quad (\text{A.1})$$

where  $\omega' = \omega - \omega_0$ ,  $\omega$  is the optical angular frequency and  $\ddot{\Phi}$  is the chromatic dispersion of the medium. The dispersed signal is amplitude modulated by an RF signal  $H_{hc}(t)$ , and the Fourier transform of the signal at the output of the modulator is

$$E_M(\omega') \propto [E_S(\omega') \cdot H_{\ddot{\Phi}}(\omega')] \otimes h_{hc}(\omega), \quad (\text{A.2})$$

Next, we derive the complex envelope of the signal at the output of a time-domain Vander-Lugt system implemented using a simple spectral hologram and a prechirped spectral hologram. The results and conclusions obtained from the following mathematical derivations have been employed in descriptions of Chapter 5.

## A.1 Time-domain Vander-Lugt filter using a simple spectral hologram

Let us first assume that the spectral hologram used as a modulating signal is defined as derived in Section 5.1, i.e.,

$$H_{hc}(t) \propto H_F(t) \exp\{-j\omega_p t\} + H_F^*(t) \exp\{j\omega_p t\}, \quad (\text{A.3})$$

where  $H_F(t)$  is a temporal signal with a complex envelope proportional to the spectrum of the impulse response of the target filter,  $h_F(t)$ , assuming a time-frequency proportionality factor  $t = \ddot{\Phi}\omega$ ; and  $\omega_p$  is a shift parameter employed to avoid any spectral overlapping between the two terms in the RHS of Eq. A.3 (Eq. 5.8). The signal at the output of the modulator has a spectral response defined as

$$\begin{aligned} E_M(\omega') &\propto \int_{-\infty}^{\infty} h_F(\Omega - \omega_p) \exp\left\{-\frac{1}{2}T_0^2(\omega' - \Omega)^2\right\} \exp\left\{-j\frac{\ddot{\Phi}}{2}(\omega' - \Omega)^2\right\} d\Omega \\ &\quad + \int_{-\infty}^{\infty} h_F^*(-\Omega - \omega_p) \exp\left\{-\frac{1}{2}T_0^2(\omega' - \Omega)^2\right\} \exp\left\{-j\frac{\ddot{\Phi}}{2}(\omega' - \Omega)^2\right\} d\Omega. \end{aligned} \quad (\text{A.4})$$

Let us call the first integral in the RHS of Eq. A.4 as  $I_1$  and the second integral as  $I_2$ . Also, we assume that the spectrum of  $H_{hc}(t)$  is confined to a small spectral range such that  $T_0\omega_m \ll 1$ , where  $\omega_m$  is the maximum frequency of  $H_{hc}(t)$ .

$$\begin{aligned} I_1 &= \int_{-\infty}^{\infty} h_F(\Omega - \omega_p) \exp\left\{-\frac{1}{2}T_0^2\omega'^2\right\} \exp\left\{-\frac{1}{2}T_0^2\Omega^2\right\} \exp\left\{T_0^2\omega'\Omega\right\} \\ &\quad \cdot \exp\left\{-j\frac{\ddot{\Phi}}{2}\omega'^2\right\} \exp\left\{-j\frac{\ddot{\Phi}}{2}\Omega^2\right\} \exp\left\{j\ddot{\Phi}\omega'\Omega\right\} d\Omega \\ &= \exp\left\{-\frac{1}{2}T_0^2\omega'^2\right\} \exp\left\{-j\frac{\ddot{\Phi}}{2}\omega'^2\right\} \int_{-\infty}^{\infty} h_F(\Omega - \omega_p) \\ &\quad \cdot \exp\left\{-\frac{1}{2}T_0^2\Omega^2\right\} \exp\left\{T_0^2\omega'\Omega\right\} \exp\left\{-j\frac{\ddot{\Phi}}{2}\Omega^2\right\} \exp\left\{j\ddot{\Phi}\omega'\Omega\right\} d\Omega. \end{aligned} \quad (\text{A.5})$$

Note that the first exponential term in the RHS of Eq. A.5 is equal to  $E_S(\omega')$  and the second exponential term is equal to  $H_{\ddot{\Phi}}(\omega')$ . The maximum value that the variable  $\Omega$  can take inside the integral is  $\omega_m$ , as  $h_F(\Omega - \omega_p)$  is zero outside the range of frequencies for which  $h_{hc}(\omega)$  is defined. Then,  $T_0^2\Omega^2 \leq (T_0\omega_m)^2$  and the exponential term  $\exp\{-T_0^2\Omega^2/2\} \simeq 1$ . On the other hand, the variable  $\omega'$  is the domain of definition of the convolution integral between a Gaussian-like spectrum and the function  $h_{hc}(\omega)$ . Observing Eq. A.5, we can conclude that the exponential terms dependent on  $\omega'$  are defined for  $\omega' \leq (2\pi/T_0 + \omega_m)$ . Therefore,  $T_0^2\omega'\Omega \leq T_0^2\omega_m(2\pi/T_0 + \omega_m) = 2\pi T_0\omega_m + (T_0\omega_m)^2 \ll 1$ , and the exponential term  $\exp\{T_0^2\omega'\Omega\}$  can be also approximated as 1. Equation A.5 can then be written as

$$I_1 = \exp\left\{-\frac{T_0^2\omega'^2}{2}\right\} \exp\left\{-j\frac{\ddot{\Phi}}{2}\omega'^2\right\} \int_{-\infty}^{\infty} h_F(\Omega - \omega_p) \exp\left\{-j\frac{\ddot{\Phi}\Omega^2}{2}\right\} \exp\left\{j\ddot{\Phi}\omega'\Omega\right\} d\Omega. \quad (\text{A.6})$$

Applying the same approximation in the integral  $I_2$ , the spectrum of the modulated signal is

$$\begin{aligned}
 E_M(\omega') &= E_S(\omega') H_{\ddot{\Phi}}(\omega') \int_{-\infty}^{\infty} [h_F(\Omega - \omega_p) + h_F^*(-\Omega - \omega_p)] \exp\left\{-j \frac{\ddot{\Phi}}{2} \Omega^2\right\} \exp\{j \ddot{\Phi} \omega' \Omega\} d\Omega \\
 &= E_S(\omega') H_{\ddot{\Phi}}(\omega') \int_{-\infty}^{\infty} h_{hc}(\Omega) \exp\left\{-j \frac{\ddot{\Phi}}{2} \Omega^2\right\} \exp\{j \ddot{\Phi} \omega' \Omega\} d\Omega \\
 &= E_S(\omega') H_{\ddot{\Phi}}(\omega') \cdot \left[ H_{hc}(\omega') \otimes \exp\left\{-j \frac{1}{2} \ddot{\Phi} \omega'^2\right\} \right], \tag{A.7}
 \end{aligned}$$

where we have considered the term  $\exp\{j \ddot{\Phi} \omega' \Omega\}$  as the kernel of an inverse Fourier transformation. The variables related by this Fourier transformation are  $\Omega \leftrightarrow t = \ddot{\Phi} \omega'$ .

Next, the amplitude modulated signal propagates through a dispersion medium with transfer function

$$H_{-\ddot{\Phi}}(\omega') = \exp\left\{j \frac{\ddot{\Phi} \omega'^2}{2}\right\}. \tag{A.8}$$

The resulting signal at the output of the system has a spectral response

$$E_{out}(\omega') = E_S(\omega') \cdot \left[ H_{hc}(\omega') \otimes \exp\left\{-j \frac{1}{2} \ddot{\Phi} \omega'^2\right\} \right]; \tag{A.9}$$

or equivalently, its temporal envelope is

$$\begin{aligned}
 \hat{e}_{out}(t) &= \hat{e}_S(t) \otimes h_{hc}(t) \exp\left\{-j \frac{t^2}{2\ddot{\Phi}}\right\} \\
 &= \hat{e}_S(t) \otimes \left[ h_F(t - \ddot{\Phi} \omega_p) \exp\left\{-j \frac{t^2}{2\ddot{\Phi}}\right\} + h_F^*(-t - \ddot{\Phi} \omega_p) \exp\left\{-j \frac{t^2}{2\ddot{\Phi}}\right\} \right]. \tag{A.10}
 \end{aligned}$$

Hence, under the above-presented condition ( $T_0 \omega_m \ll 1$ ), the output signal envelope of a TDSS system with a modulating signal proportional to the spectral hologram defined in Section A.3 is, within a quadratic phase factor, proportional to the convolution between the input signal and the target impulse response. Therefore, this system would enable the synthesis of non-symmetrical, but intensity-only pulse shapes, due to the fact that the output phase would be distorted by the above-mentioned quadratic phase.

## A.2 Time-domain Vander-Lugt filter using a prechirped spectral hologram

In order to cancel out the undesired quadratic phase term in the resulting waveform (Eq. A.10), an additional quadratic phase term proportional to  $H_{-\ddot{\Phi}}(\omega)$  needs to be added to the spectrum of  $H_{hc}(t)$ . In other words, it is necessary to prechirp the spectral hologram. The phase term added to  $h_{hc}(\omega)$  has to be an odd function so that the modulating temporal signal is real-valued. The

resulting prechirped spectral hologram has the following spectral response,

$$h_{hc}(\omega) \propto h_F(\omega - \omega_p) \exp \left\{ j \frac{\ddot{\Phi} \omega^2}{2} \right\} + h_F^*(-\omega - \omega_p) \exp \left\{ -j \frac{\ddot{\Phi} \omega^2}{2} \right\}. \quad (\text{A.11})$$

Substituting Eq. A.11 into Eq. A.2,  $E_M(\omega)$  can be written as

$$\begin{aligned} E_M(\omega') &\propto \int_{-\infty}^{\infty} h_F(\Omega - \omega_p) \exp \left\{ j \frac{\ddot{\Phi} \Omega^2}{2} \right\} \exp \left\{ -\frac{T_0^2}{2} (\omega' - \Omega)^2 \right\} \exp \left\{ -j \frac{\ddot{\Phi}}{2} (\omega' - \Omega)^2 \right\} d\Omega \\ &+ \int_{-\infty}^{\infty} h_F^*(-\Omega - \omega_p) \exp \left\{ -j \frac{\ddot{\Phi} \Omega^2}{2} \right\} \exp \left\{ -\frac{T_0^2}{2} (\omega' - \Omega)^2 \right\} \exp \left\{ -j \frac{\ddot{\Phi}}{2} (\omega' - \Omega)^2 \right\} d\Omega. \end{aligned} \quad (\text{A.12})$$

Again, the two integral terms of Eq. A.12 are called  $I_1$  and  $I_2$ , respectively. Also, it is assumed that the spectrum of  $H_{hc}(t)$  satisfies that  $T_0 \omega_m \ll 1$ , with  $\omega_m$  being the maximum frequency of  $H_{hc}(t)$ . The integral  $I_1$  can be derived as

$$\begin{aligned} I_1 &= \int_{-\infty}^{\infty} h_F(\Omega - \omega_p) \exp \left\{ j \frac{\ddot{\Phi} \Omega^2}{2} \right\} \exp \left\{ -\frac{1}{2} T_0^2 \omega'^2 \right\} \exp \left\{ -\frac{1}{2} T_0^2 \Omega^2 \right\} \exp \left\{ T_0^2 \omega' \Omega \right\} \\ &\cdot \exp \left\{ -j \frac{\ddot{\Phi}}{2} \omega'^2 \right\} \exp \left\{ -j \frac{\ddot{\Phi}}{2} \Omega^2 \right\} \exp \left\{ j \ddot{\Phi} \omega' \Omega \right\} d\Omega \\ &= \exp \left\{ -\frac{1}{2} T_0^2 \omega'^2 \right\} \exp \left\{ -j \frac{\ddot{\Phi}}{2} \omega'^2 \right\} \int_{-\infty}^{\infty} h_F(\Omega - \omega_p) \\ &\cdot \exp \left\{ -\frac{1}{2} T_0^2 \Omega^2 \right\} \exp \left\{ T_0^2 \omega' \Omega \right\} \exp \left\{ j \ddot{\Phi} \omega' \Omega \right\} d\Omega. \end{aligned} \quad (\text{A.13})$$

The quadratic phase term used to prechirp the spectral hologram compensates the quadratic phase term  $\exp\{-j \ddot{\Phi} \Omega^2 / 2\}$  inside the first integral in Eq. A.13. Hence, by employing a similar treatment as in the previous Section, the convolution integral of Eq. A.13 can be approximated as

$$I_1 = \exp \left\{ -\frac{1}{2} T_0^2 \omega'^2 \right\} \exp \left\{ -j \frac{\ddot{\Phi}}{2} \omega'^2 \right\} \int_{-\infty}^{\infty} h_F(\Omega - \omega_p) \exp \left\{ j \ddot{\Phi} \omega' \Omega \right\} d\Omega. \quad (\text{A.14})$$

Next, we apply the same approximation in the integral  $I_2$ ,

$$\begin{aligned} I_2 &= \int_{-\infty}^{\infty} h_F^*(-\Omega - \omega_p) \exp \left\{ -j \frac{\ddot{\Phi} \Omega^2}{2} \right\} \exp \left\{ -\frac{1}{2} T_0^2 \omega'^2 \right\} \exp \left\{ -\frac{1}{2} T_0^2 \Omega^2 \right\} \exp \left\{ T_0^2 \omega' \Omega \right\} \\ &\cdot \exp \left\{ -j \frac{\ddot{\Phi}}{2} \omega'^2 \right\} \exp \left\{ -j \frac{\ddot{\Phi}}{2} \Omega^2 \right\} \exp \left\{ j \ddot{\Phi} \omega' \Omega \right\} d\Omega \\ &= \exp \left\{ -\frac{1}{2} T_0^2 \omega'^2 \right\} \exp \left\{ -j \frac{\ddot{\Phi}}{2} \omega'^2 \right\} \int_{-\infty}^{\infty} h_F^*(-\Omega - \omega_p) \exp \left\{ -j \ddot{\Phi} \Omega^2 \right\} \exp \left\{ j \ddot{\Phi} \omega' \Omega \right\} d\Omega. \end{aligned} \quad (\text{A.15})$$

Finally, the spectrum of the signal at the output of the amplitude modulator (Eq. A.12) can be written as

$$\begin{aligned}
 E_M(\omega') \propto & \exp\left\{-\frac{1}{2}T_0^2\omega'^2\right\} \exp\left\{-j\frac{\ddot{\Phi}}{2}\omega'^2\right\} \int_{-\infty}^{\infty} h_F(\Omega - \omega_p) \exp\left\{j\ddot{\Phi}\omega'\Omega\right\} d\Omega \\
 & + \exp\left\{-\frac{1}{2}T_0^2\omega'^2\right\} \exp\left\{-j\frac{\ddot{\Phi}}{2}\omega'^2\right\} \int_{-\infty}^{\infty} h_F^*(-\Omega - \omega_p) \exp\left\{-j\ddot{\Phi}\Omega^2\right\} \exp\left\{j\ddot{\Phi}\omega'\Omega\right\} d\Omega.
 \end{aligned} \tag{A.16}$$

This integral can be solved by considering  $\exp\{j\ddot{\Phi}\omega'\Omega\}$  as the kernel of an inverse Fourier transformation, where the variables related by the Fourier transform are  $\Omega \leftrightarrow t = \ddot{\Phi}\omega'$ . Then, we obtain,

$$E_M(\omega') \propto E_S(\omega') H_{\ddot{\Phi}}(\omega') \cdot \left[ H_F(\omega') \exp\{j\ddot{\Phi}\omega_p\omega'\} + H_F^*(\omega') \exp\{-j\ddot{\Phi}\omega_p\omega'\} \otimes \exp\{-j\ddot{\Phi}\omega'^2/4\} \right]. \tag{A.17}$$

The propagation of this modulated signal through a dispersion medium with transfer function  $H_{-\ddot{\Phi}}(\omega')$  compensates the quadratic phase term  $H_{\ddot{\Phi}}(\omega')$  and the resulting signal has a temporal complex envelope,

$$\hat{e}_{out}(t) \propto \hat{e}_S(t) \otimes h_F(t - \ddot{\Phi}\omega_p) + \hat{e}_S(t) \otimes (h_F^*(-t - \ddot{\Phi}\omega_p) \exp(-jt^2/\ddot{\Phi})). \tag{A.18}$$

This result, shown in Chapter 5 as Eq. 5.11, demonstrates that the output of the system is composed of two delayed, non-overlapped terms, and one of them (first term in the RHS of the equation) is proportional to the desired temporal waveform in both amplitude and phase. Therefore, the use of a prechirped spectral hologram in a TDSS configuration enables the synthesis of non-symmetrical and complex-valued pulse shapes.



## Appendix B

# Design of arbitrary filters based on fiber Bragg gratings

The numerous advantages of fiber Bragg gratings (FBGs) have made them a fundamental component technology of high interest for a myriad of applications in optical communications and sensor systems [11, 77–92]. In the linear regime, i.e., when the intensity of the propagating electromagnetic wave is not sufficiently high to excite nonlinear effects, FBGs operate as optical band-pass filters in reflection and, consequently, as band-stop filters in transmission. Besides their numerous advantages, described in Chapters 1 and 5, one of the most distinctive features of FBGs is the extraordinary flexibility they offer to achieve almost any desired band-pass spectral filtering characteristic (in amplitude or/and phase) when working in reflection. To achieve the target grating spectral response, nearly all the grating physical parameters can be varied, e.g., the induced refractive index modulation, the length, and/or the period chirp [54]. A great deal of research has been carried out to develop methods to predict the behavior of electromagnetic fields in periodic media. In particular, in the case of FBGs, algorithms able to provide the reflective spectral response  $H_R(\omega)$  from the grating's refractive index profile  $n_{FG}(z)$ , also known as analysis algorithms [53, 54, 70–72], and vice versa, i.e., algorithms that provide the required  $n_{FG}(z)$  from a targeted  $H_R(\omega)$ , or synthesis algorithms [73–76], have been developed and they are widely employed nowadays for the design of efficient optical filters based on this technology.

Among the different existing techniques to carry out the analysis and synthesis of FBGs, in this Thesis we have devoted special attention to two of them; namely one technique based on coupled-mode theory (CMT) [53, 54, 75], and one based on the multi-layer (ML) method [232–234]. These two techniques (CMT and ML) have been employed in this Thesis for the design of the optical signal processors presented in Section 5.4 of Chapter 5. Both algorithms provide numerical solutions to perform analysis and synthesis of arbitrary FBGs in an accurate and intuitive fashion.

In this Appendix, we present a comprehensive mathematical description of the algorithms for the analysis and synthesis of FBGs based on the CMT and the ML methods. Then, we discuss their applicability considering the type of FBG to be examined (i.e., tapered, chirped, phase-shifted, superimposed, etc. [54]).

## B.1 Analysis of fiber Bragg gratings

In this Section, we describe the two previously mentioned algorithms for carrying out analysis of FBGs, namely those based on CMT and ML methods. These algorithms provide the complex spectral response in reflection,  $H_R(\omega)$ , and transmission,  $H_T(\omega)$ , of a particular grating structure,  $n_{FG}(z)$ . Two hypotheses are considered for the development of both algorithms. First, we consider a uni-dimensional variation (along the  $z$ -axis) of the refractive index in the core of a single mode fiber (SMF), which follows Eq. 1.9 (see also Eqs. B.3 and B.13). Secondly, it is assumed that the electric fields propagating through the grating are ideal monochromatic plane waves [53, 54, 72, 232].

CMT provides an analytic solution for the propagation of the electromagnetic fields along a uniform FBG, i.e., an FBG whose refractive index modulation and period are constant along the grating's length. In this case, the grating's transmissive and reflective spectral responses can be directly obtained, as explained below. If a non-uniform FBG is to be analyzed, the CMT-based algorithm makes use of the transfer-matrix method (TMM). TMM is a powerful tool for the analysis of periodic structures, consisting in the division of the whole structure into simpler sections that can be defined by  $2 \times 2$  transfer matrices. Then, the complete response of the system can be simply obtained from the multiplication of all the transfer matrices. Thus, in the case of a non-uniform FBG, the complete grating is divided into layers containing few periods, and each layer is described by the  $2 \times 2$  transfer matrix corresponding to a uniform FBG. On the other hand, the ML-based algorithm also employs the TMM, in this case for the study of any arbitrary perturbation. The grating structure is divided into layers shorter than the smaller period, in such a way that each layer can be considered as a dielectric medium with constant refractive index. Then, the complete grating response is obtained from the alternative multiplication of  $2 \times 2$  transfer matrices corresponding to media with constant refractive index and interfaces between two dielectrics with different refractive indexes.

Once the grating's spectral responses in reflection,  $H_R(\omega)$ , and transmission,  $H_T(\omega)$ , are known, other interesting parameters can be readily obtained. These responses, usually referred as reflective and transmissive field coefficients, respectively, are generally complex and therefore, they can be written as  $H_R(\omega) = |H_R(\omega)| \exp\{j \phi_R(\omega)\}$  and  $H_T(\omega) = |H_T(\omega)| \exp\{j \phi_T(\omega)\}$ . The reflectivity and the transmissivity of the FBG are obtained as  $R(\omega) = |H_R(\omega)|^2$  and  $T(\omega) = |H_T(\omega)|^2$ , respectively. Besides, the group delays in reflection and transmission can be also obtained from the reflective and transmissive coefficients, as

$$\tau_R(\omega) = -\frac{\partial \phi_R(\omega)}{\partial \omega}; \quad (\text{B.1})$$

$$\tau_T(\omega) = -\frac{\partial \phi_T(\omega)}{\partial \omega}. \quad (\text{B.2})$$

The length of the layers into which the grating is divided makes the ML method a general and accurate technique that is able to analyze any arbitrary perturbation with high level of precision. However, the required computation workload is extremely heavy for gratings longer than e.g.  $\sim 1$  cm. On the other hand, CMT cannot detect grating variations at the period level, and therefore it is only applicable in certain specific cases. Still, CMT-based algorithm is accurate for most of the common cases of practical interest (apodized or chirped gratings) and it is much more efficient in terms of computation time, what make it the preferable choice whenever it can be applied.

### B.1.1 Coupled-mode theory (CMT)

Coupled-mode theory is a simple and efficient tool for obtaining quantitative information about the spectral dependence of fiber gratings. It is a widely spread technique that relates electromagnetic waves propagating in opposite directions along the grating structure using coupled differential equations. The CMT has been extensively used for the analysis of periodic structures because of its simplicity and flexibility. Here, we do not provide a derivation of the CMT from the Maxwell's equations, as it can be found in numerous references [53, 70–72], but we just use its results to build the CMT-based FBG analysis algorithm.

In case the perturbation of the refractive index is defined by a uniform cosenoidal function (i.e., the refractive index modulation and the grating period are constant along the grating length), CMT provides an analytic solution to model the dynamics of the electromagnetic waves propagating along the perturbed structure. In this case, the refractive index perturbation at the core of an SMF can be written as

$$n_{FG}(z) = n_{av} + \Delta n_{max} \cdot \cos \left\{ \frac{2\pi}{\Lambda} z \right\}, \quad (\text{B.3})$$

where  $n_{av}$  is the “dc” index change spatially averaged over a grating period,  $\Delta n_{max}$  is the maximum refractive index change, and  $\Lambda$  is the period of the grating perturbation, being all of them constant values. This FBG is confined over a length  $L$ , i.e.,  $n_{FG}(z)$  is defined for  $z \in [0, L]$ . Due to the variation of the refractive index in the medium, the light is reflected in a distributed fashion. The relative phase of each reflected signal is determined by the wavelength of the light and the grating period. The reflected waves along the periodic structure interfere constructively in a narrow band around one particular wavelength, namely the Bragg wavelength  $\lambda_0$ , which is given by the Bragg condition

$$\lambda_0 = 2n_{av}\Lambda. \quad (\text{B.4})$$

The Bragg condition can be obtained from Eq. 1.10, assuming  $\beta_2 = -\beta_1$  and  $m = 1$ . At other wavelengths, the multiple reflections interfere destructively and cancel each other out, and as a result, light is transmitted through the grating. The solution of the coupled-mode equations provides the expressions of the complex amplitudes of the waves that propagate forward and backwards on the perturbed structure. The boundary conditions required for the solution of the equation system are the values of the optical waves at the extremes of the grating, as shown in Fig. B.1 [53, 72].

$$\begin{aligned} E^+(z, \omega) = & \frac{\exp(-j\beta_0 z)}{\gamma \cosh(\gamma L) + j(\Delta\beta/2) \sinh(\gamma L)} \\ & \cdot \left\{ \left[ \gamma \cosh(\gamma(L-z)) + j(\Delta\beta/2) \sinh(\gamma(L-z)) \right] E^+(0, \omega) \right. \\ & \left. - \left[ j\kappa \sinh(\gamma z) \exp(j(\Delta\beta/2)L) \right] E^-(L, \omega) \right\}, \quad (\text{B.5}) \end{aligned}$$

$$\begin{aligned}
E^-(z, \omega) = & \frac{\exp(j\beta_0 z)}{\gamma \cosh(\gamma L) + j(\Delta\beta/2) \sinh(\gamma L)} \\
& \cdot \left\{ \left[ -j\kappa^* \sinh(\gamma(L-z)) \right] E^+(0, \omega) \right. \\
& \left. - \left[ \gamma \cosh(\gamma L) + j(\Delta\beta/2) \sinh(\gamma z) \right] \exp(j(\Delta\beta/2)L) E^-(L, \omega) \right\}, \quad (\text{B.6})
\end{aligned}$$

where \* stands for conjugation, the propagation constant is

$$\beta_0 = \frac{\pi}{\Lambda}, \quad (\text{B.7})$$

and the parameter  $\gamma$  is defined as

$$\gamma^2 = |\kappa|^2 - \left( \frac{\Delta\beta}{2} \right)^2. \quad (\text{B.8})$$

The parameter  $\kappa$  is the coupling coefficient of the grating, which provides the relative amount of power coupled between two modes per unit length, and it is defined as

$$\kappa = \frac{\omega \Delta n_{max}}{2c_0} \exp \left\{ j 2\pi \int_0^z \left( \frac{1}{\Lambda(z')} - \frac{1}{\Lambda_0} \right) dz' \right\}. \quad (\text{B.9})$$

On the other hand, the detuning  $\Delta\beta$  is given by the following expression,

$$\Delta\beta = 2\beta - \frac{2\pi}{\Lambda} = 2\frac{n_{av}}{c_0}(\omega - \omega_0), \quad (\text{B.10})$$

where  $\omega_0 = 2\pi c_0/\lambda_0$  is the Bragg angular frequency.

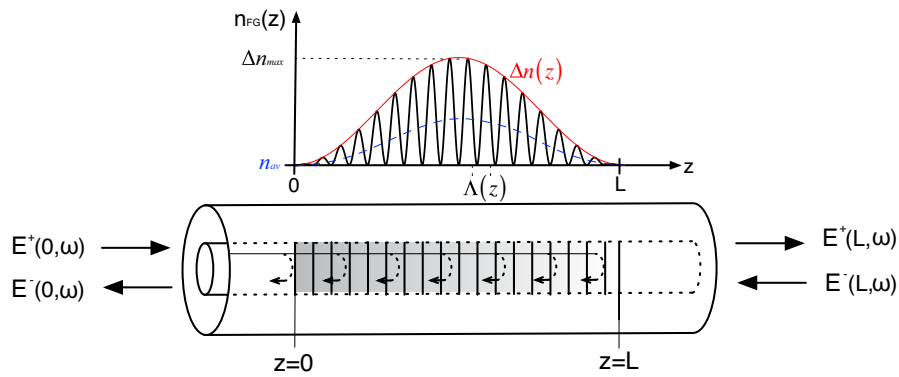


Figure B.1 – Nomenclature for the optical waveforms at the two extremes of an FBG of length  $L$ .

From the expressions of the optical waves propagating through the grating, it is straightforward to obtain the reflection and transmission spectral responses of the uniform FBG, which are

$$H_R(\omega) = \frac{E^-(0, \omega)}{E^+(0, \omega)} \Big|_{E^-(L, \omega)=0} = \frac{-j \kappa^* \sinh(\gamma L)}{\gamma \cosh(\gamma L) + j(\Delta\beta/2) \sinh(\gamma L)}; \quad (\text{B.11})$$

$$H_T(\omega) = \frac{E^+(L, \omega)}{E^+(0, \omega)} \Big|_{E^-(L, \omega)=0} = \frac{\gamma \exp(-j \beta_0 L)}{\gamma \cosh(\gamma L) + j(\Delta\beta/2) \sinh(\gamma L)}. \quad (\text{B.12})$$

This theory can be extended to allow the treatment of non-uniform gratings, i.e., gratings with a non-uniform refractive index modulation or period. The induced refractive index of a non-uniform FBG can be then expressed as in Eq 1.9, that is,

$$n_{FG}(z) = n_{av} + \Delta n(z) \cdot \cos \left\{ \int_0^z \frac{2\pi}{\Lambda(z')} dz' \right\}. \quad (\text{B.13})$$

This problem does not have an analytic solution based on CMT, and therefore, it has to be solved using numerical methods. The typically used method is based on transfer matrices (i.e., the TMM). The whole grating is divided into layers containing several periods, and each layer is considered as a uniform grating, as shown in Fig. B.2. The transfer matrix of a uniform FBG of length  $\delta l_i$  is

$$\begin{bmatrix} E^+(z_i, \omega) \\ E^-(z_i, \omega) \end{bmatrix} = \begin{bmatrix} M_{i,11} & M_{i,12} \\ M_{i,21} & M_{i,22} \end{bmatrix} \begin{bmatrix} E^+(z_i + \delta l_i, \omega) \\ E^-(z_i + \delta l_i, \omega) \end{bmatrix} = [M_{U,i}] \begin{bmatrix} E^+(z_i + \delta l_i, \omega) \\ E^-(z_i + \delta l_i, \omega) \end{bmatrix}. \quad (\text{B.14})$$

The elements of the matrix  $\mathbf{M}_{U,i}$  can be obtained from the analytic expression of the waves  $E^+(z, \omega)$  and  $E^-(z, \omega)$  (Eqs. B.5 and B.6), as

$$M_{i,11} = \frac{\gamma \cosh(\gamma \delta l_i) + j(\Delta\beta/2) \sinh(\gamma \delta l_i)}{\gamma} \exp(j \beta_0 \delta l_i) \quad (\text{B.15a})$$

$$M_{i,12} = \frac{j \kappa \sinh(\gamma \delta l_i)}{\gamma} \exp(-j \beta_0 \delta l_i) \quad (\text{B.15b})$$

$$M_{i,21} = \frac{j \kappa^* \sinh(\gamma \delta l_i)}{\gamma} \exp(j \beta_0 \delta l_i) \quad (\text{B.15c})$$

$$M_{i,22} = \frac{\gamma \cosh(\gamma \delta l_i) - j(\Delta\beta/2) \sinh(\gamma \delta l_i)}{\gamma} \exp(-j \beta_0 \delta l_i). \quad (\text{B.15d})$$

Then, each section is described by a transfer matrix, and the total grating response is calculated by multiplying each matrix in the proper order:

$$[M_{FBG}] = [M_{U,1}] \cdot [M_{U,2}] \cdots [M_{U,i}] \cdots [M_{U,N-1}] \cdot [M_{U,N}], \quad (\text{B.16})$$

where  $N$  is the number of sections and  $\mathbf{M}_{U,i}$  is the transfer matrix of the  $i$ -th section. The reflection and transmission coefficients can be obtained as

$$H_R(\omega) = \left. \frac{E^-(0, \omega)}{E^+(0, \omega)} \right|_{E^-(L, \omega)=0} = \frac{M_{FBG,21}}{M_{FBG,11}}, \quad (\text{B.17})$$

$$H_T(\omega) = \left. \frac{E^+(L, \omega)}{E^+(0, \omega)} \right|_{E^-(L, \omega)=0} = \frac{1}{M_{FBG,11}}. \quad (\text{B.18})$$

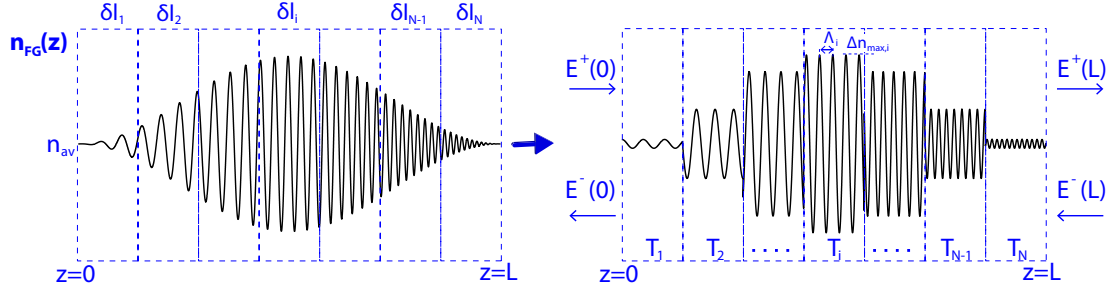


**Figure B.2** – Schematic of the division into layers of a non-uniform FBG for its analysis using CMT. The complete grating structure is divided into layers containing few periods, and each layer is treated as a uniform FBG. The analysis of the complete structure is done based on TMM. The propagating waves' dependence with the angular frequency has been omitted in the figure for simplicity.

Generally, the number of sections ( $N$ ) needed for the piecewise-uniform calculation is determined by the required accuracy. Still,  $N$  may not be made arbitrarily large, since the CMT approximations that lead to Eqs. B.5 and B.6 are not valid when a uniform grating section is only a few grating periods long [54]. Thus, we require  $\delta l_i \gg \Lambda_{max}$ ,  $\Lambda_{max}$  being the longer period in the grating structure. This method provides accurate results for FBGs containing arbitrary apodization profile, period profile or phase shifts. To implement the piecewise-uniform method for apodized and chirped gratings, we simply assign constant values  $\gamma$ ,  $\kappa$  and  $\Delta\beta/2$  to each uniform section, where these might be the  $z$ -dependent values of these parameters evaluated at the center of each section. For phase-shifted gratings, we insert a phase-shift matrix  $\mathbf{M}_{ps}$  between the factors  $\mathbf{M}_i$  and  $\mathbf{M}_{i+1}$  in the product in Eq. B.14 for a phase shift after the  $i$ -th section. The phase-shift matrix is of the form

$$[M_{ps}] = \begin{bmatrix} \exp\left(-\frac{i\phi_i}{2}\right) & 0 \\ 0 & \exp\left(\frac{i\phi_i}{2}\right) \end{bmatrix}, \quad (\text{B.19})$$

where  $\phi_i$  is the shift in the phase of the grating itself [54].

One of the main advantages of CMT combined with TMM is that it provides accurate results for the majority of FBGs of practical interest (i.e., apodized, chirped or phase-shifted) with relatively low computational time. However, CMT-TMM is not applicable for the analysis of special grating structures, such as superimposed gratings [158] or gratings with non-constant  $n_{av}$ .

### B.1.2 Multi-layer based on transfer-matrix method (ML-TMM)

The algorithm of ML-TMM represents a general and accurate model to analyze FBGs. This analysis algorithm has been widely employed not only for the characterization of FBGs, but also thin film filters [235] or periodic perturbations in optical waveguides [236]. It employs a sampling rate of the refractive index modulation that is below the grating period, as shown in Fig. B.3. This sampling rate allows analyzing FBGs with any type of nonuniformity, including a non-cosinoidal or even non-periodic perturbation. Moreover, it enables the calculus of the wave distributions at any point of the grating device, so it is possible to study the dynamics of operation of the FBG [232, 233]. The main drawback of ML-TMM is that, due to the high sampling rate, the required computation workload becomes extremely heavy for gratings longer than  $\sim 1$  cm.

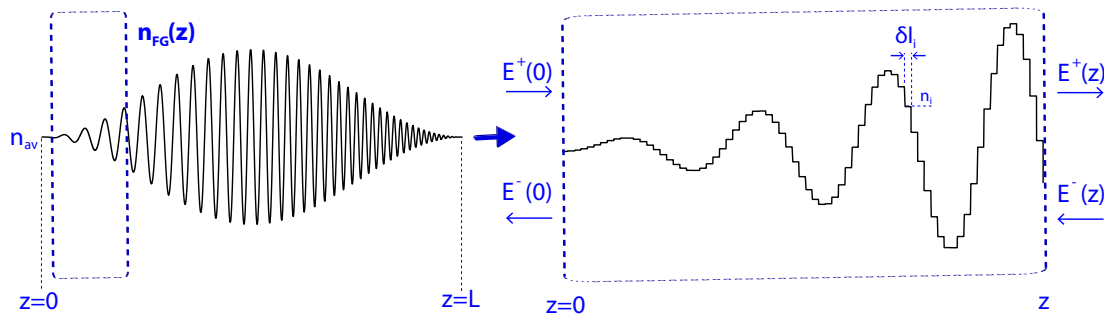


**Figure B.3** – Schematic for division into layers of a non-uniform FBG for its analysis using ML-TMM. The complete grating structure is divided into layers with a length at least one order of magnitude shorter than the minimum value of the period, and each layer is treated as medium of constant refractive index. The analysis of the complete structure is done based on TMM. The optical waves' dependence with the angular frequency has been omitted in the figure for simplicity.

Similarly to the previous case, we consider a unidimensional refractive index variation  $n_{FB}(z)$  (Eq. B.13). ML-TMM divides the complete grating into sections, but in this case the length of each section  $\delta l_i$  is sufficiently short so that it can be considered as a medium with constant refractive index, typically  $\delta l_i \ll \Lambda_{min}$ , with  $\Lambda_{min}$  the shorter period found in the grating. The segmented structure can be treated as a multi-layer system composed of an alternation of two different elements: (i) a dielectric medium of constant refractive  $n_i$  index and length  $\delta l_i$ , and (ii) a interface between two dielectric media of different refractive indexes  $n_i$  and  $n_{i+1}$ . Each of these elements can be characterized using a  $2 \times 2$  transfer matrix, and then, the transfer matrix of the complete structure can be obtained from the multiplication of these individual matrices.

The transfer matrix that characterizes the interface between two dielectric media of different, constant refractive index (Fig. B.4(a)) can be derived from the conditions of continuity of the tangential components of the electric and magnetic fields in this interface [235, 237]. Assuming normal incidence,

$$\begin{bmatrix} E^+(z_i^-, \omega) \\ E^-(z_i^-, \omega) \end{bmatrix} = \frac{1}{2n_i} \begin{bmatrix} n_i + n_{i+1} & n_i - n_{i+1} \\ n_i - n_{i+1} & n_i + n_{i+1} \end{bmatrix} \begin{bmatrix} E^+(z_i^+, \omega) \\ E^-(z_i^+, \omega) \end{bmatrix} = [M_{I,i}] \begin{bmatrix} E^+(z_i^+, \omega) \\ E^-(z_i^+, \omega) \end{bmatrix}. \quad (\text{B.20})$$

Assuming the propagation of a plane wave along the  $z$  axis on a lossless medium with constant refractive index  $n_i$  and length  $\delta l_i$  (Fig. B.4(b)), the transfer matrix that characterizes this medium

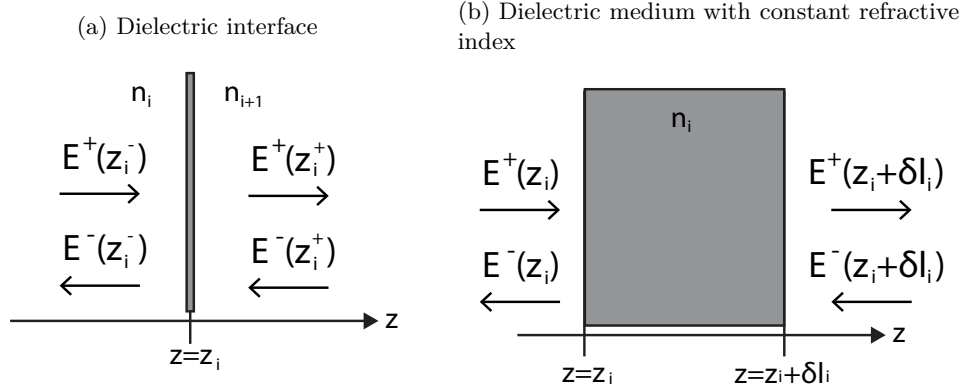


**Figure B.4** – Schematic of the two elements that compose the whole grating structure for its analysis following ML-TMM.

is

$$\begin{aligned}
 \begin{bmatrix} E^+(z_i, \omega) \\ E^-(z_i, \omega) \end{bmatrix} &= \frac{1}{2n_i} \begin{bmatrix} \exp(j k_0 n_i \delta l_i) & 0 \\ 0 & \exp(-j k_0 n_i \delta l_i) \end{bmatrix} \begin{bmatrix} E^+(z_i + \delta l_i, \omega) \\ E^-(z_i + \delta l_i, \omega) \end{bmatrix} \\
 &= [M_{M,i}] \begin{bmatrix} E^+(z_i + \delta l_i, \omega) \\ E^-(z_i + \delta l_i, \omega) \end{bmatrix}, \tag{B.21}
 \end{aligned}$$

where  $k_0 = \omega/c_0$  is the wavenumber in vacuum.

The transfer matrix of the complete grating  $\mathbf{M}_{FBG}$  can be obtained as

$$[M_{FBG}] = [M_{I,1}] \cdot [M_{M,1}] \cdots [M_{I,i}] \cdot [M_{M,i}] \cdots [M_{I,N}] \cdot [M_{M,N}] \cdot [M_{I,N+1}]. \tag{B.22}$$

The first transfer matrix  $\mathbf{M}_{I,1}$  characterizes the interface between the unperturbed medium  $n_0$  and the first layer of the grating, while the last matrix  $\mathbf{M}_{I,N+1}$  characterizes the interface between the last layer of the grating and the unperturbed fiber core. Finally, the reflective and transmissive field coefficients  $H_R(\omega)$  and  $H_T(\omega)$  can be obtained from the elements of the transfer matrix  $\mathbf{M}_{FBG}$  using the Eqs. B.17 and B.18.

As introduced above, ML-TMM is a general algorithm that can be employed for the characterization of any arbitrary refractive index perturbation, including those gratings profiles to which CMT-TMM cannot be applied. Moreover, this algorithm also provides the internal electric field distributions of an FBG versus the distance along the grating and light frequency [232, 233]. The study of the microscopic characteristics of FBGs allows a better understanding of the macroscopic behavior of these devices. However, due to the high number of operations that needs to be performed for the characterization of an FBG (multiplication of  $> 20$  matrices per period), the required computation workload makes this algorithm unpractical for the analysis of relatively long FBGs. Therefore, in this Thesis, its use has been restricted for those cases where the previous method (CMT-TMM) cannot be used.

## B.2 Synthesis of fiber Bragg gratings

The FBG design usually starts from the specification of the required spectral transfer function upon reflection and must produce both the device length and the required variation of the period and amplitude of the sinusoidal perturbation of the refractive index. This problem of inferring the grating profile from a specified spectrum is referred to as the inverse scattering or grating synthesis problem [75].

In this Section, two techniques for synthesizing FBGs are described, namely those based on CMT and ML methods, combined with TMM. These two methods are built following a methodology similar to that of the corresponding analysis tool. Thus, the CMT-based synthesis tool provides discrete values for the grating apodization and period profiles, with a sampling rate given by the specified length of the layers in which the grating structure is to be divided. On the other hand, the ML-based synthesis algorithm provides the total grating refractive index modulation, i.e.,  $n_{FG}$ , due to the fact that the length of the pre-defined layers is at least one order of magnitude lower than the period, which can be estimated from the Bragg frequency.

### B.2.1 Coupled-mode theory (CMT)

This technique provides the local coupling coefficient  $\kappa(z)$  from the reflection coefficient  $H_R(\omega)$ . The obtained  $\kappa(z)$  encodes all the information about the refractive index modulation  $\Delta n(z)$  and the grating period  $\Lambda(z)$ , following Eq. B.9. The advantage of the method described here is that it utilizes the direct solution of exactly the same coupled-mode equations that are used in grating analysis and thus has a straightforward description [74, 75].

The inverse Fourier transform of the reflective coefficient,  $h_R(t)$ , can be expressed as a sum over all the possible space-time propagation paths between the  $(z, \tau)$  points  $(0, 0)$  and  $(0, \tau)$ , where  $\tau$  is a truncated time variable. Each path contains information of the scattering events occurred in it. The impulse response can be written as

$$h_R(\tau) = -\frac{1}{2}\kappa\left(\frac{\tau c_0}{2n_{av}}\right) + h_{tr}(\tau), \quad (\text{B.23})$$

where  $h_{tr}(\tau)$  is the impulse response at time  $\tau$  corresponding to a medium which has been truncated at  $z = (\tau c_0 / (2n_{av}))^-$ , having a coupling function  $\kappa_{tr}(z)$  defined by

$$\kappa_{tr}(z) = \begin{cases} \kappa(z) & 0 \leq z < (\tau c_0 / (2n_{av})) \\ 0 & (\tau c_0 / (2n_{av})) \leq z \end{cases}. \quad (\text{B.24})$$

Equation B.23 allows us to reconstruct the value of the coupling function  $\kappa(z_i)$  at the space point  $z_i$  from knowledge of both the impulse response  $h_R(\tau)$  at  $\tau = 2z_i n_{av} / c_0$  and the value of the coupling function  $\kappa(z)$  at previous  $z < z_i$ . For the reconstruction process to be accurate, the impulse response  $h_{tr}(\tau)$  of the truncated medium must be calculated taking into account all the multiple reflections [74].

To implement this algorithm efficiently, the propagation problem has to be discretized. Then, we built a layered medium that is equivalent to the grating structure within a certain degree of approximation. This layered medium will then be described in terms of transfer matrices that relate the counterpropagating waves  $E^+(z, \omega)$  and  $E^-(z, \omega)$  at different locations along the grating.

The solution of the propagating equation for a uniform medium of length  $\delta l_i$  and constant coupling coefficient  $\kappa$  can be expressed in term of the well-known transfer matrix  $M_{U,i}$ ,

$$\begin{aligned} \begin{bmatrix} E^-(z_i + \delta l_i, \omega) \\ E^+(z_i + \delta l_i, \omega) \end{bmatrix} &= \begin{bmatrix} \cosh(\gamma \delta l_i) - j \frac{\kappa}{\gamma} \sinh(\gamma \delta l_i) & \frac{\kappa}{\gamma} \sinh(\gamma \delta l_i) \\ \frac{\kappa^*}{\gamma} \sinh(\gamma \delta l_i) & \cosh(\gamma \delta l_i) + j \frac{\kappa}{\gamma} \sinh(\gamma \delta l_i) \end{bmatrix} \begin{bmatrix} E^-(z_i + \delta l_i, \omega) \\ E^+(z_i + \delta l_i, \omega) \end{bmatrix} \\ &= [M_{U,i}] \begin{bmatrix} E^-(z, \omega) \\ E^+(z, \omega) \end{bmatrix}. \end{aligned} \quad (\text{B.25})$$

Equation B.25 describes the distributed nature of the reflection from a grating that occupies the space interval  $(z_i, z_i + \delta l_i)$ . The use of this approximation is very advantageous in terms of efficiency, reducing drastically the computation time with respect the method based on ML-TMM, described later in this Appendix. Let us assume that we have already constructed the first  $S$  layers of the grating  $\{\kappa(0), \dots, \kappa(S\delta l_i)\}$  and consequently, the accumulated transfer matrix  $\mathbf{M}'_{FBG}(S\delta l_i, \omega)$ . The impulse response  $h_{tr}(\tau)$  (Eq. B.23) corresponding to this matrix matches accurately the target impulse response  $h_R(\tau)$  for the time interval  $[0, 2S\delta l_i]$ . The steps to calculate the next coupling coefficient  $\kappa((S+1)\delta l_i)$  are as follows. First, from  $\mathbf{M}'_{FBG}(S\delta l_i, \omega)$ , we calculate the impulse response  $h_{tr}(\tau)$  of the truncated grating  $[0, S\delta l_i]$  at  $\tau = 2(S+1)\delta l_i n_{av}/c_0$ . Then, we compute the difference  $\Delta h_R(\tau)$  between the target impulse response  $h_R(\tau)$  and the truncated impulse response  $h_{tr}(\tau)$  at  $\tau = 2(S+1)\delta l_i n_{av}/c_0$ . The next step is to calculate  $\kappa((S+1)\delta l_i)$  so as to match the impulse response  $h_R(\tau)$  at  $\tau = 2(S+1)\delta l_i n_{av}/c_0$  with the desired degree of accuracy. This involves solving the equation

$$\begin{aligned} \Delta h_R \left( \frac{2(S+1)\delta l_i n_{av}}{c_0} \right) &= \frac{-\kappa((S+1)\delta l_i) \tanh(|\kappa((S+1)\delta l_i)| \cdot \delta l_i)}{2} \frac{\delta l_i}{|\kappa((S+1)\delta l_i)| \cdot \delta l_i} \\ &\quad \cdot \prod_{m=0}^S [\cosh(|\kappa(m\delta l_m)|)]^{-2}, \end{aligned} \quad (\text{B.26})$$

which is the discrete counterpart of Eq. B.23. Finally, we should compute the new accumulated transfer function  $\mathbf{M}'_{FBG}((S+1)\delta l_i, \omega)$  and carry out the same sequence of steps to identify the next layer [74].

This algorithm represents an efficient layer-peeling algorithm for the design of complex fiber gratings. As its complexity scales with the square of the number of points in the grating, it provides enhanced performance for the design of long gratings.

## B.2.2 Multi-layer based on transfer-matrix method (ML-TMM)

The synthesis method based on ML-TMM presents the advantages of generality and accuracy over the previously described method. CMT-TMM algorithm provides the coupling coefficient  $\kappa(z)$  from the grating's reflective field coefficient  $H_R(\omega)$ , which provides information about the grating

apodization profile  $\Delta n(z)$  and period variation  $\Lambda(z)$ . The method presented in this Section, on the other hand, directly provides the grating refractive index profile,  $n_{FG}(z)$ . Therefore, this method can be applied to synthesize grating structures with local defects or discontinuities of the order of the local period, e.g., phase shifted gratings or superimposed gratings. Also, this synthesis tool is useful for detecting defects in a fabricated device.

ML-TMM is based on the reconstruction of the local refractive index  $n_{FB}(z)$  and the Fourier equivalent scattering, produced at discrete points with a spatial resolution below the local period ( $\delta l_i \ll \Lambda$ ), as opposed to discrete layer peeling CMT-TMM where layers are of the order of tens of grating periods. This minimum discretization step also allows for the synthesis of very strong gratings since the reflection spectrum is sampled with the minimum bandwidth resolution [234].

The starting point is the sampling of the grating reflective impulse response with a rate  $\Delta t$ ,

$$h_R(t) = \mathcal{F}^{-1}\{H_R(\omega)\} = \sum_{p=0}^{\infty} h_{RS}(p)\delta(t - 2p\Delta t), \quad (\text{B.27})$$

where  $\Delta t$  is chosen to be equal to the round-trip delay in a layer of length  $\delta l$ , which is the spatial resolution set for the synthesis process,  $\Delta t = n_{av}\delta l/c_0$  (see Fig. B.5(a)).

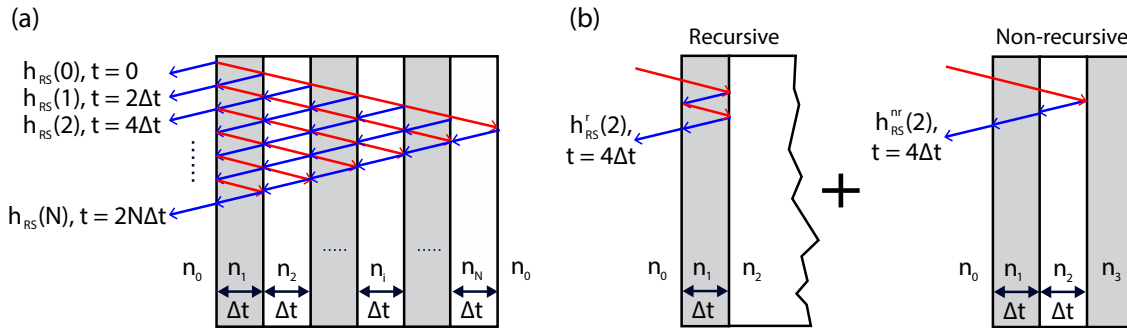


**Figure B.5** – (a) Layout of the division of the FBG in layers and the contribution to the total sampled impulse response; (b) The calculation of the refractive index of each layer is obtained from the non-recursive component of the impulse response in this layer. To this purpose, the total sampled impulse response is decomposed into the recursive component and the non-recursive component, where the total impulse response and its non-recursive component are known.

The algorithm to obtain the refractive index modulation of the FBG is described as follows [234]. First, from the value of the first sample of the impulse response  $h_{RS}(0)$  it is straightforward to calculate  $n_1$  (we take  $n_0$  for the unperturbed refractive index of the waveguide, which is known in advance):

$$n_1 = n_0 \left[ \frac{1 - h_{RS}(0)}{1 + h_{RS}(0)} \right]. \quad (\text{B.28})$$

Observing Fig. B.5(a), we have that

$$h_{RS}(1) = t_{01}r_{12}t_{10}, \quad (\text{B.29})$$

where  $t_{xy}$  represents the field transmission coefficient under normal incidence for the transition between dielectric  $x$  and dielectric  $y$ , and  $r_{xy}$  represents the field reflection coefficient under normal incidence for the transition between dielectric  $x$  and dielectric  $y$ . Then, the reflection coefficient  $r_{12}$

can be obtained from the sampled reflective impulse response as

$$r_{12} = \frac{h_{RS}(1)}{t_{01}t_{10}} = \frac{(n_0 + n_1)^2 h_{RS}(1)}{4n_0n_1}. \quad (\text{B.30})$$

The value of the refractive index in the second layer  $n_2$  is calculated as

$$n_2 = n_1 \left[ \frac{1 - r_{12}}{1 + r_{12}} \right]. \quad (\text{B.31})$$

It can be observed in Fig. B.5(b) that, starting from the third coefficient of the impulse response,  $h_{RS}(2)$ ,  $h_{RS}(t)$  can be obtained as the sum of a recursive contribution (left part) and a non-recursive one (right part). In particular, the non-recursive part of  $h_{RS}(2)$  is given by

$$h_{RS}^{nr}(2) = t_{01}t_{12}r_{23}t_{21}t_{10} = r_{23} \prod_{i=0}^1 \left( \frac{4n_i n_{i+1}}{(n_i + n_{i+1})^2} \right), \quad (\text{B.32})$$

where all the parameters are known except for  $r_{23}$  which is essential to obtain  $n_3$  since

$$n_3 = n_2 \left[ \frac{1 - r_{23}}{1 + r_{23}} \right]. \quad (\text{B.33})$$

This parameter  $r_{23}$  is obtained from the recursive part  $h_{RS}^r(2)$ . Assuming that the grating perturbation is finished at the second layer, i.e., the second layer is infinitely long, and applying the analysis techniques based on the V-I transmission matrix [238], we have

$$r_{23} = \frac{h_{RS}^{nr}(2)}{\prod_{i=0}^1 \frac{4n_i n_{i+1}}{(n_i + n_{i+1})^2}} = \frac{h_{RS}(2) - h_{RS}^r(2)}{\prod_{i=0}^1 \frac{4n_i n_{i+1}}{(n_i + n_{i+1})^2}}. \quad (\text{B.34})$$

Once  $r_{23}$  is known, the value of  $n_3$  is obtained using Eq. B.33. The generalization for a time instant  $2(S-1)\Delta t > 2\Delta t$ , which results on the computation of the refractive index of layer  $S$ , i.e.,  $n_S$ , is straightforward. This procedure must be repeated until the last sample of  $h_{RS}(N)$ .

### B.3 Discussion on the applicability of CMT and ML techniques and conclusions

The suitability of the two described techniques to analyze/synthesize FBGs has already been discussed in the corresponding Sections on this Appendix. Table B.1 summarizes which of these two methods is applicable to several kinds of FBGs. In general, CMT is suitable for most FBGs of practical interest, namely apodized, chirped or phase-shifted FBGs (or with a combination of these features). Therefore, the higher efficiency of this method in terms of computation time makes it the preferable technique in the cases in which it can be applied. The ML method, on the other hand, is more precise, enabling the detection of grating defects or perturbations within the period

regime. Moreover, it also provides the internal dynamics of the FBGs, which is useful for a better understanding of the FBGs' operation.

**Table B.1 – Types of FBGs and suitable method to analyze/synthesize each type.**

Type of FBG	CMT-TMM	ML-TMM
Apodized structures	✓	✓
Chirped structures	✓	✓
Phase-shifted structures	✓	✓
Structures with non-constant $n_{av}(z)$	✗	✓
Superimposed structures	✗	✓



# Appendix C

## Associated publications

### C.1 Journal articles

- [1] M. R. Fernández-Ruiz, J. Huh, and J. Azaña, “Time-domain Vander-Lugt for in-fiber complex (amplitude and phase) optical pulse shaping,” *Optics Letters*, **41**, 10 2121-2124 (2016).
- [2] M. R. Fernández-Ruiz, L. Lei, M. Rochette, and J. Azaña, “All-optical wavelength conversion based on time-domain holography,” *Optics Express*, **23**, 22 847–22 856 (2015).
- [3] M. R. Fernández-Ruiz and J. Azaña, “Temporal phase conjugation based on time-domain holography,” *Optics Letters*, **40**, 127–130 (2015).
- [4] M. R. Fernández-Ruiz, L. Wang, A. Carballar, M. Burla, J. Azaña, and S. LaRochelle, “THz-bandwidth photonic Hilbert transformers based on fiber Bragg gratings in transmission,” *Optics Letters*, **40**, 41–44 (2015).
- [5] M. R. Fernández-Ruiz, A. Carballar, and J. Azaña, “Arbitrary time-limited optical pulse processors based on transmission fiber Bragg gratings,” *IEEE Photonics Technology Letters*, **26**, 1754–1757 (2014).
- [6] M. R. Fernández-Ruiz, A. Carballar, and J. Azaña, “Design of ultrafast all-optical signal-processing devices based on fiber Bragg gratings in transmission,” *Journal of Lightwave Technology*, **31**, 1593–1600 (2013).
- [7] M. R. Fernández-Ruiz, M. Li, M. Dastmalchi, A. Carballar, S. LaRochelle, and J. Azaña, “Picosecond optical signal processing based on transmissive fiber Bragg gratings,” *Optics Letters*, **38**, 1247–1249 (2013).
- [8] M. R. Fernández-Ruiz, M. Li, and J. Azaña, “Time-domain holograms for generation and processing of temporal complex information by intensity-only modulation processes,” *Optics Express*, **21** (8), 10314–10323 (2013).

## C.2 International conference papers

- [1] M. R. Fernández-Ruiz, J. Huh, and J. Azaña, “Fiber-optics reconfigurable arbitrary (complex) picosecond pulse shaping/coding by time-domain amplitude-only spectrum modulation,” in *Optical Fiber Communication (OFC)*, March 2016, Anaheim, California. Paper Th3H.2.
- [2] M. R. Fernández-Ruiz, and J. Azaña, “High speed processing of complex-modulation signals based on time-domain holography,” in *Photonics in Switching (PS)*, September 2015, Florence, Italy. Paper WeIII2. **Invited presentation.**
- [3] M. R. Fernández-Ruiz, A. Carballar, and J. Azaña, “Hilbert transformers based on fiber Bragg gratings in transmission,” in *Photonics North*, June 2015, Ottawa, Canada. Paper OP-Quantum 9-11-5.
- [4] M. R. Fernández-Ruiz, and J. Azaña, “Wavelength-preserving temporal phase conjugation based on intensity-only detection and modulation devices,” in *Optical Fiber Communication (OFC)*, March 2015, Los Angeles, California. Paper M2E.5.
- [5] M. R. Fernández-Ruiz, A. Carballar, and J. Azaña, “Ultrafast (THz-bandwidth) photonic Hilbert transformer based on a fiber Bragg grating in transmission,” in *Bragg Gratings, Photosensitivity, and Poling in Glass Waveguides (BGPP)*, July 2014, Barcelona, Spain. Paper BM3D.5.
- [6] M. R. Fernández-Ruiz, and J. Azaña, “Time-domain holograms for high-speed optical signal generation and processing,” in *Opto-Electronics and Communication Conference and Australian Conference on Optical Fiber Technology (OECC)*, July 2014, Melbourne, Australia. Pages 1053-1055. **Invited presentation.**
- [7] M. R. Fernández-Ruiz, A. Carballar, and J. Azaña, “Design of ultrafast all-optical Nth-order differentiators based on fiber Bragg gratings operating in transmission,” in *CLEO: Science and Innovations*, June 2014, San Jose, California, USA. Paper JW2A.42.
- [8] M. R. Fernández-Ruiz, A. Carballar, and J. Azaña, “Ultrafast arbitrary (non-minimum-phase) optical pulse processors based on Bragg gratings in transmission,” in *OPTOEL*, July 2013, Alcalá de Henares, Madrid, Spain. Pages 245 – 248.
- [9] M. R. Fernández-Ruiz, M. Li, M. Dastmalchi, A. Carballar, S. LaRochelle and J. Azaña, “Picosecond flat-top pulse-shaper based on linearly-chirped fiber Bragg gratings in transmission,” in *CLEO: Science and Innovations*, June 2013, San Jose, California, USA. Paper CF2G.6.
- [10] M. R. Fernández-Ruiz, M. Li, and J. Azaña, “Time-domain holography,” in *IEEE Photonics Conference (IPC)*, September 2012, Burlingame, California, USA. Paper WCC 4.
- [11] M. R. Fernández-Ruiz, J. Azaña, and A. Carballar, “Ultrafast all-optical Nth-order differentiators based on transmission fiber Bragg gratings,” in *IEEE Photonics Conference (IPC)*, September (2012), Burlingame, California, USA. Paper WCC3.
- [12] M. R. Fernández-Ruiz, M. Li, and J. Azaña, “Generation of arbitrary complex optical data streams using a single amplitude-only (Mach-Zehnder) modulator,” in *European Conference and exhibition on Optical Communication (ECOC)*, September 2012, Amsterdam, The Netherlands. Paper We.3.E.3.

- [13] M. R. Fernández-Ruiz, A. Carballar, and J. Azaña, “Design of picosecond flat-top optical pulse generator using a linearly-chirped fiber Bragg grating in transmission,” in *OSA Bragg Gratings, Photosensitivity and Poling (BGPP)*, June 2012, Colorado Springs, Colorado, USA. Paper BW4E.3.
- [14] M. R. Fernández-Ruiz, A. Carballar, and J. Azaña, “Design of an ultra-fast first-order integrator based on waveguide Bragg gratings,” in *IEEE Photonics Conference (IPC)*, October 2011, Arlington, Virginia, USA. Paper ThO.4.

### C.3 Book chapters

- [1] M. R. Fernández-Ruiz, R. Ashrafi, A. Carballar, S. LaRochelle, and J. Azaña: All-optical pulse shaping in the sub-picosecond regime based on fiber grating devices, (Ch. 9) in *Shaping light in nonlinear optical fibers*, Wiley and Sons, in preparation.

## C.4 Other publications not directly related with the Thesis

### C.4.1 Journal articles

- [1] Bo Li, M. R. Fernández-Ruiz, and J. Azaña, “Highly contrast linear optical pulse compression using a temporal hologram,” *Optics Express*, **23** (5), 6833-6845 (2015).
- [2] M. Burla, M. Li, L. Romero Cortés, X. Wang, M. R. Fernández-Ruiz, L. Chrostowski, and J. Azaña, “Terahertz-bandwidth photonic fractional Hilbert transformer based on a phase-shifted waveguide Bragg grating on silicon,” *Optics Letters*, **39** (21), 6241-6244 (2014).
- [3] H. P. Bazargani, M. R. Fernández-Ruiz, and J. Azaña, “Tunable, nondispersive optical filter using photonic Hilbert transformation,” *Optics Letters*, **29** (17), 5232-5235 (2014).

### C.4.2 Conference papers

- [4] A. Carballar, M. R. Fernández-Ruiz, and J. Azaña, “Design of photonic Hilbert transformers based on impulsive response specifications,” in *IEEE Photonics Conference (IPC)*, October 2015, Reston, Virginia, USA. Paper WG1.4.
- [5] R. Maram, M. R. Fernández-Ruiz, and J. Azaña, “Design of an FBG-based phase-only (all-pass) filter for energy-efficient all-optical clock recovery,” in *OSA Bragg Gratings, Photosensitivity and Poling (BGPP)*, July 2014, Barcelona, Spain. Paper BM4D.7.
- [6] H. P. Bazargani, M. R. Fernández-Ruiz, and J. Azaña, “Bandwidth-tunable optical filters based on photonic Hilbert transformation,” in *IEEE Photonics Conference (IPC)*, September 2013, Bellevue, Washington, USA. Paper ThG1.2.

- [7] H. P. Bazargani, M. R. Fernández-Ruiz, and J. Azaña, “Tunable optical filter using photonic Hilbert transformation,” in *Signal Processing in Photonics Communications (SPPCom)*, July 2013, Rio Grande, Puerto Rico, USA. Paper SPM4D.
- [8] M. R. Fernández-Ruiz, and A. Carballar, “Comprehensive and general method for the analysis and synthesis of fiber Bragg gratings,” in *Workshop on Fibre and Optical Passive Components (WFOPC)*, July 2011, Montreal, Quebec, Canada.
- [9] M. R. Fernández-Ruiz, and A. Carballar, “Minimum-phase reconstruction for getting the specifications of a fiber Bragg grating,” in *Workshop on Fibre and Optical Passive Components (WFOPC)*, July 2011, Montreal, Quebec, Canada.